# Design optimization of a novel inter-satellite downlink for small satellites to (mega-)constellations.

Jos van ’t Hof

TU Delft

This page intentionally left blank.

# Design optimization of a novel inter-satellite downlink for small satellites to (mega-)constellations.

by

Jos van 't Hof

to obtain the degree of Master of Science
at the Delft University of Technology,
to be defended publicly on Monday July 5, 2021 at 15:00.


| | | |
|---|---|---|
| Student number: | 4624181 | |
| Project duration: | July 8, 2019 – July 5, 2021 | |
| Thesis committee: | Dr. S. Speretta, | TU Delft, Space Systems Engineering, supervisor |
| | Dr. A. Cervone, | TU Delft, Space Systems Engineering |
| | MSc. MBA K. Cowan, | TU Delft, Astrodynamics and Space Missions |




TU Delft

This page intentionally left blank.

# Acknowledgements

Multi-tasking is tiring, finishing two MSc. degrees during a pandemic even more so. Starting this adventure of a double MSc. degree back in 2016 was exciting and do doing it at the TU Delft was one of the best decisions I made. The experience I gained and friends I made along the way made this ambitious plan absolutely worth it. I did not anticipate when I started studying that I would launch a sounding rocket from the South of Spain, do an internship at a heavy lift launch vehicle company (which I am now working at) and a second one at a nano satellite company. The knowledge I gained during both studies kick-started my career and the experienced I had will be everlasting.

I however also did not anticipate how long the 'final stretch' was going to be. Having to split a combined thesis into two separate stand-alone projects did not reduce the amount of work I had on my plate. Given the circumstances however it was the path of least resistance. Although the scope and content exceeded intention with at least an order of magnitude, I am proud to stay close to my original intent with both projects. With two lengthy reports and two conference papers (and hopefully soon two master's degrees) I am looking forward to being done graduating.

I could not have done this without the support of countless people around me. I would like to thank Visweswaran (Vishu) Karunanithi for helping me refine the ideas of this project and co-write my first conference paper on the topic. Warren Gebbett and the team at SES for the insightful discussions on non-geostationary satellite systems. My daily supervisor Stefano Speretta for supporting me (remotely) in this thesis as well as being a great conversation partner on satellite RF communications. My girlfriend for having to deal with me waking up early and working late to finish this report, and finally I would like to thank my family for supporting me throughout my studies. What an exciting journey it has been!

*Jos van 't Hof*
*Seattle, May 2021*

This page intentionally left blank.

# Summary

Technological advancements and miniaturization of space hardware now allows small satellites, having a mass below 500 kg, to perform missions that used to only suite larger class satellites. However, low downlink data rates are limiting the scientific and commercial return for small satellite missions. As the payload capabilities and mission complexity of the small satellites increases, higher payload downlink capability is required [1], [2] creating the need for higher performing downlink architectures.

This thesis investigated a novel downlink communication architecture for Earth orbiting small satellites in which data is relayed through non-geostationary orbit (NGSO) (mega-)constellations. Companies such as Telesat, SpaceX, OneWeb and O3b are building constellations aimed to provide broadband connectivity from space [3]. Some of their constellation proposals are called mega-constellations by the large number of satellites used to provide global coverage. The satellites in these NGSO (mega-) constellations have their orbits, field-of-views, spot beams and frequency re-use schemes optimized for ground coverage. This leaves gaps in low Earth orbit (LEO) where a small satellite is not in view of the constellation satellite. This results in interesting challenges for the proposed LEO-to-NGSO data-relay downlink system, requiring consideration of the orbital dynamics between the satellites as well as the the design trade-offs for the communication system in order to evaluate the concept and estimate its performance.

An analysis into the small satellite market shows an increase in missions using constellations of small satellites for Earth Observation (EO), Remote Sensing (RS) and Internet-of-Things (IoT)/Machine-to-Machine (M2M). In these categories, the EO missions are producing a significant amount of data in LEO up to 80 GByte per orbit per satellite [2] with constellations growing beyond 100 satellites. Recent publications show that the payload downlink systems on these small satellites are outperforming those on larger class satellites by size, mass and throughput. It is expected that the need will grow for higher payload downlink performance for EO and IoT/M2M satellites.

Concept missions were setup and analysed for each of these two potential use-cases of the NGSO data-relay downlink. A visibility and contact time analysis for eight upcoming LEO and medium Earth orbit (MEO) (mega-)constellations showed that the higher altitude LEO mega-constellations, those with orbital shells at 1500 km altitude such as Telesats constellation, offered coverage with long duration inter-satellite passes. The MEO constellations offered the longest contact opportunities reaching up to 50 minutes of continuous coverage from a single satellite. The Telesat LEO mega-constellation and the O3b mPOWER MEO constellation were selected to perform a design optimization of a data-relay downlink for the two concept missions.

A vectorized orbital simulator and a multi-objective genetic algorithm optimization framework were developed to analyse the performance and design characteristics of the proposed NGSO data-relay downlink. The vectorized orbital simulator provides all contact opportunities in which two satellites have line-of-sight for a given simulated period. This data is used in the design optimization that considers all components of the small satellite payload downlink system including the modulator, modulation and coding scheme, power amplifier and the antenna. This optimization framework is also able to show the requirements on other satellite subsystems to support a data-relay downlink such as those on the power system and the attitude determination and control system.

Four scenarios were analysed using the data-relay optimization framework, a EO use-case and a IoT/M2M use case for two target constellations, the Telesat LEO constellation and the O3b mPOWER MEO constellation. Each scenario was considered individually over a mission period of three orbits. The design optimization for EO missions showed that when using a data-relay downlink with the Telesat mega-constellation, a higher throughput per orbit can be achieved for the same energy consumption per orbit. The data-relay downlink for that mission would use a 35 dBi deployable reflect array antenna that is combined with the solar array. The transmitter would have a peak total power dissipation of 40

W using the 32-amplitude and phase-shift keying (APSK) 9/10 forwards error correction (FEC) mode of the DVB-S2 standard and 300 MHz of transmission bandwidth.

For the IoT/M2M use-case it was found that using a data-relay downlink with the Telesat mega-constellation could offer a lower latency between the time data is collected from sensors on the ground to delivery to the user. This design would use 4.8 dBi low-gain patch antenna to minimize the need for pointing the satellite. The transmitter would have a peak total power dissipation of 30 W using the 8-APSK 9/10 FEC mode of the DVB-S2 standard and 5 MHz of transmission bandwidth.

The scenarios run with the O3b mPOWER constellation showed that similar numbers are achievable however the increased distance from LEO-to-MEO requires more energy consumption and a higher gain antenna that would take up a large portion of the available volume on the targeted small satellite platforms. In all optimizations, the generated design for the data-relay downlink are possible using the current state-of-the-art small satellite communication technologies.

# Contents

This page intentionally left blank.

# 1 Introduction

This thesis investigates a novel downlink communication architecture for Earth orbiting small satellites. Earth orbiting satellites have been used for many purposes such as Earth observation, communications, weather monitoring and navigation. Technological advancements and miniaturization of space hardware now allows small satellites, having a mass below 500 kg, to perform missions that used to only suite larger class satellites. However, low downlink data rates are limiting the scientific and commercial return for small satellite missions. As the payload capabilities and mission complexity of the small satellites increases, higher payload downlink capability is required [1], [2] creating the need for higher performing downlink architectures.

The class of small satellites has become increasingly popular due to CubeSats which are nano-satellites with standardized form factor of 10 x 10 x 10 cm cubes, also called units or simply 1U cubes. These satellites started around the year 2000 as simple technology demonstrators developed by universities to stimulate education and now have developed into a separate market sector involving universities, industry and space agencies [4]. As shown in table 1.1, small satellites have lower mass, reduced cost and reduced build time in comparison to large or medium class satellites. With increasing capabilities and reducing costs, the use of small satellites in constellations is now actively explored by companies in the industry. There already exist successful (start-up) companies that commercialize constellations of nano-satellites in LEO, such as Planet (Earth observation, >387 satellites launched) and SPIRE (remote sensing, >120 satellites launched) [5]. In addition, companies such as Hiber, Fleet, Lacuna Space and Kepler have started launching their first nano-satellites into LEO or very low Earth orbit (VLEO) to provide IoT and M2M connectivity [6]–[9] using nano-satellite constellations.

Examples of small satellite payloads are optical imagers, radars or communication systems. These payloads generate data throughout the orbit of the satellite and this data needs to be transferred the ground. In the early days, spy satellites such as those from the CORONA and GAMBIT family would send their images to ground by dropping film buckets from orbit that would re-enter into the atmosphere to be picked up by the US navy [10]. Nowadays, all communication from and to a satellite is send by either radio frequency (RF) or optical communication links.

Table 1.1: Classification of small satellites, based of [11] including values from [12].

| | Class | Mass [kg] | Cost [US $] | Time to build | Antenna Gain | Power [W] |
|---|---|---|---|---|---|---|
| | Conventional | >1000 | 0.1 - 2 B | >5 years | Very high | 1000 |
| | Medium | 500 - 1000 | 50 - 100 M | 4 years | Very high | 800 |
| Small | Mini | 100 - 500 | 10 - 50 M | 3 years | High | 53.2 |
| Small | Micro | 10 - 100 | 2 - 10 M | 1 year | Medium | 35 |
| Small | Nano | 1 - 10 | 0.2 - 2 M | 1 year | Medium | 7 |
| Small | Pico | 1 - 1.3 | 20 - 200 K | < 1 year | Low | 2 |
| Small | Femto | < 0.1 | 0.1 - 20 K | < 1 year | Low | 0.006 |

The developments towards constellations of small satellites will significantly increase the amount of data that is generated in LEO. However, the throughput of traditional direct RF communication links between a satellite and a ground station is limited to the duration in which the satellite is in view and the transmission rate of the satellite. Current EO small satellite missions are already experiencing this limitation and are therefore heavily investing in the mission ground segment and developing new commination technology to maximize the data-rate of the payload downlink transmitter on the satellite [1], [2].

At the same time another revolution in satellite-based connectivity is going on with the rise of non-geostationary orbit (NGSO) satellite constellations. Companies such as Telesat, SpaceX, OneWeb and O3b are building constellations aimed to provide broadband connectivity from space [3]. Some of their constellation proposals are called ”mega-constellations” by the large number of satellites used to provide global coverage. The satellites in these NGSO (mega-)constellations operate in LEO region (around 500 to 1500 km altitude) and/or MEO region (around 8000 to 14000 km altitude). The proposals for the aforementioned small satellite constellations for Earth observation and IoT/M2M connectivity operate around 500 km altitude and are therefore passing under and through the field-of-view of the (mega-)constellation satellites. This brings the opportunity for a novel data-relay architecture where the LEO small satellites relay their payload data to the NGSO (mega-)constellation satellites. Investigating the feasibility of such a data-relay architecture for small satellites is the topic of this work.

## 1.1. LEO to NGSO data-relay architecture

This novel NGSO data-relay architecture was first proposed by Karunanithi et. al. [4] and could offer advantages to downlink payload data. Figure 1.1 illustrates the differences between a direct-to-ground downlink, a cross-link downlink and the proposed NGSO data-relay downlink architecture. A direct-to-ground downlink operates in a store-and-forward fashion, the satellite will collect and store payload data throughout the orbit and will downlink this data once in view of a ground station. The throughput per orbit here is limited by the number of ground stations, the duration of the satellite passes and the transmit data rate of the satellite. When there are more satellites operating in a constellation the overall throughput may be increased by the use of inter-satellite communication links or cross-links between in-plane travelling satellites. In this cross-link architecture payload data may be forwarded to a neighbouring satellite until a satellite is reached that is in-view of a ground station. A ring network

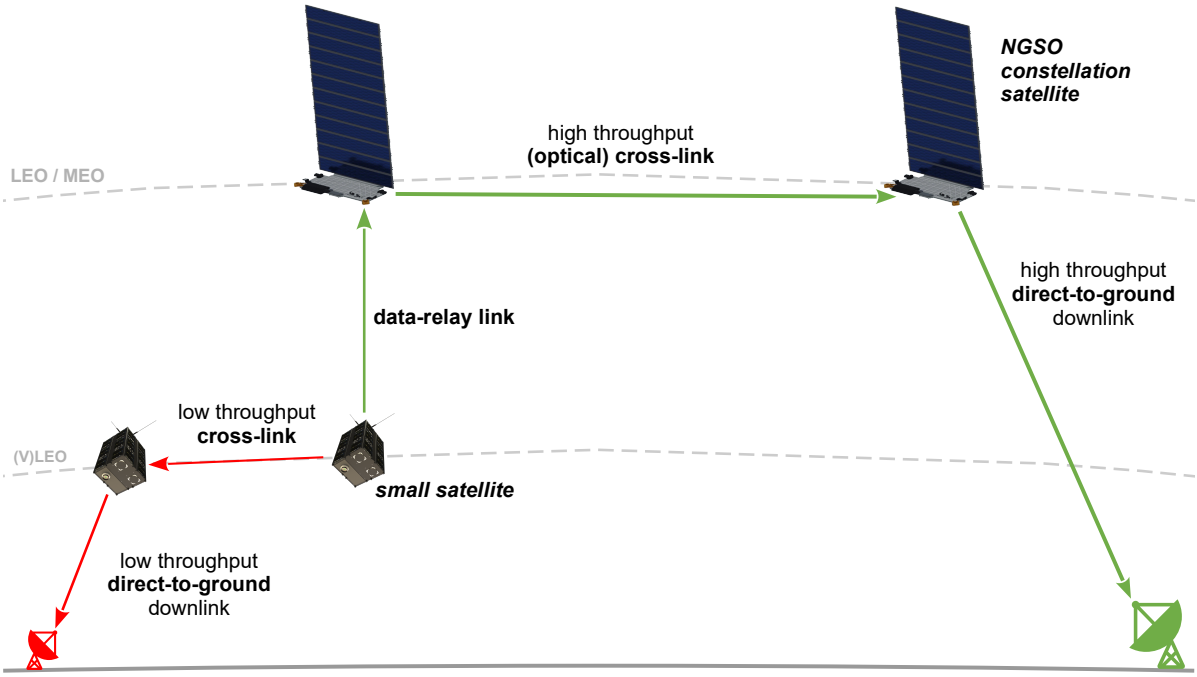


Figure 1.1: Illustration of three downlink communication architectures: a direct-to-ground downlink, an in-plane cross-link and a data-relay link. This project considers data-relay links with non-geostationary orbit (NGSO) satellites in (mega-)constellations that aim to provide global broadband connectivity from space. *Starlink models from Fluoritt* [13]

may be formed when enough satellites are placed in the same orbit at equally spaced distances. In this ring network the downlink is always available as long as one satellite is in-view of a ground station. This however requires a second communication system for the inter-satellite cross-links that is always active whenever any satellite in the constellation desires to downlink data. Having this second communication system would therefore be significantly increasing the power budget on the small satellite.

In the proposed NGSO data-relay architecture each small satellite would have only a single transmitter that is used to downlink payload data. This transmitter is used for a one-way transmission to the NGSO satellite to create a data-relay link. The small satellite would effectively carry a (modified) user-terminal as would be used by customers on the ground to connect to the broadband service provided by the NGSO constellation. In practice, the actual link would likely have to be bi-directional (see chapter 4) to allow for handshaking/link-management if a new user wants to use the broadband service. However, the return link or uplink (from the small satellite perspective) is considered not to be the limiting in the proposed data-relay architecture for small satellites, as a low data-rate return link would suffice to for handshaking/link-management purposes. The forward link or data-relay downlink (from the small satellite perspective) investigated in this study is what limits the capabilities of small satellite missions by the amount of payload data that can be downlinked and how often this link is available.

After the data is relayed, the NGSO (mega-)constellation takes care of routing the data to the ground by forwarding it through its high throughput (optical) cross-links (if existing) to eventually downlink the data to their ground station. As the NGSO (mega-)constellations provide global coverage more contact time with the small satellites could be achieved. In addition, the RF links would not be affected by atmospheric attenuation as would be the case in a direct-to-ground downlink. Overall this could increase the throughput per orbit that could be achieved for small satellite missions. In addition, the proposed architecture could lower overall mission costs by reducing the ground segment investment to only telemetry and command ground-stations.

## 1.2. Thesis goal

There is a need for small satellite communication technology that can increase payload downlink performance in small satellite (constellation based) missions. A downlink communication architecture where small satellites in LEO would relay their payload data to NGSO (mega-) constellations that provide broadband connectivity from space could offer more contact time with the satellite and higher throughput per orbit. This thesis project is set up to investigate the possibility of this data-relay commination architecture and assess the potential performance and technical feasibility:

*The main goal of this thesis project is to investigate the feasibility for a small satellite data-relay communication architecture using non-geostationary orbit (mega-)constellations as the primary means to downlink payload data from low Earth orbit.*

## 1.3. Challenges of NGSO data-relays

Using commercial satellite constellations to relay small satellite data has been explored before. In 2016 the VELOX-II satellite showed successful in-orbit operation of an inter-satellite data relay terminal to connect with Inmarsats geostationary Earth orbit (GEO) constellation [14]–[16]. Similarly a consortium of European companies including NanoAvionics is planning to use LEO-to-GEO data-relays for a global Internet of Things constellation [17]. A LEO satellite is visible from GEO throughout a large part of the orbit and therefore a large contact time per orbit can be maintained in such an architecture. However, the large distance from LEO-to-GEO (>35000 km) limits the achievable data-rate to a few hundred kilobytes per second [14].

The proposed LEO-to-NGSO data-relay architecture might have the opposite challenges. The inter-satellite distances are shorter and could therefore allow for higher data-rates. However, the satellites in the NGSO (mega-)constellations have their orbits, field-of-views, spot beams and frequency re-use schemes optimized for ground coverage as was shown in a paper by Del. Portillo et. al. [3]. This leaves gaps in LEO where the small satellite is not in view of a constellation satellite, similar to as seen in the analysis of multi-layer satellite networks by Li et. al. [18]. Therefore an investigation is to be performed to determine how often a small satellite is in-view of the NGSO (mega-)constellation satellites and contact can be made to relay data. Then these contact opportunities should be evaluated to see if a communication system could be designed that achieves significant throughput per orbit.

As the inter-satellite distances are small and the satellites are travelling in different planes, it is expected that the contact opportunities will be of short duration but appear frequent due to the amount of satellites in the (mega-)constellations. Direct evaluation and design of a communication system on the small satellite will be challenging an for such complex system. Therefore, to determine the actual performance that can be obtained in this architecture a design optimization is performed for the data-relay downlink (sub-)system on the small satellite. This design should take optimal use of the contact opportunities with the NGSO constellation satellites to maximize throughput while maintaining within the capabilities of small satellite communication hardware.

There are other technical challenges associated with NGSO (mega-)constellations that are related to this work, such as the routing through a mesh-network of satellites and hand-overs from one satellite to the other. This has been explored in research [19]–[22] and is related to this study but not chosen as the primary focus. Where possible the NGSO (mega-)constellations are specified on a system level and their technical operation is abstracted to maintain scope for this work.

## 1.4. Research questions

To achieve the goal of this thesis the performance of the proposed NGSO data-relay architecture needs to be evaluated. The specifications of NGSO (mega-)constellations are fixed by their primary mission goal; providing broadband connectivity for users on ground from space. This evaluation therefore comes down to an orbital dynamics analysis to determine the contact opportunities between the small satellite and the NGSO (mega-)constellation satellites, and determination of the performance of the communication system on the small satellite that makes optimal use of these contact opportunities to achieve the goals of the small satellite mission.

The first research question relates to identification of which small satellite missions could benefit from the proposed NGSO data-relay architecture:

**R1** - *Which (kind of) small satellite mission could benefit from a NGSO data-relay downlink?*

To answer this question, first research needs to be done to investigated what the capabilities and limitations are of state-of-the-art small satellite communication systems (sub-research question 1.1), what the benefits and drawbacks are of the proposed LEO-to-NGSO data relay communication system are (sub-research question 1.2) and finally what is needed on the small satellite to support a data-relay downlink system (sub-research question 1.3).

The second research question relates to evaluation of the upcoming NGSO (mega-)constellations for the NGSO data-relay architecture:

**R2** - *Which NGSO (mega-)constellations could be used for relaying data from a small satellite?*

For this research question it needs to be determined what the properties of these constellations are (sub-research question 2.1), what data throughput could be achieved with each constellation (sub-research question 2.2) and what the requirements for the data-relay downlink system are to communicate with the constellation (sub-research question 2.3).

The third research question focusses on how to use optimization techniques to generate a design for the data-relay downlink on the small satellite:

**R3** - *How to use optimization techniques to generate an optimized design for a data-relay downlink on a small satellite?*

The optimization of the data-relay downlink on the small satellite needs to make optimal uses of the contact opportunities with the NGSO constellation satellites. To do so it needs to be determined: what the inputs, outputs and constraints to optimize against are (sub-research question 3.1), how to incorporate orbital dynamic models and link budget models into the optimization (sub-research question 3.2), and what optimization techniques could be used to optimize the design (sub-research question 3.3).

The fourth and final research question relates to using and evaluating the optimized data-relay downlink designs for different small satellite missions:

**R4** - *What are the design characteristics and performances of an optimum NGSO data-relay downlink for a small satellite mission?*

To answer this question first it should be determined what is considered optimal performance for the communication system on each small satellite mission that is evaluated (sub-research question 4.1). The optimization should show how different performance parameters such as power/energy consumption trade-off against throughput or latency (sub-research question 4.2). Finally, the optimized designs should be compared with the current state-of-the-art communication systems to evaluate possible gaps in technology and directions for follow-up research (sub-research question 4.3).

## 1.5. Report structure

The content of this thesis report is divided into ten chapters. Chapter 2 outlines the methodology that is used in project to answer the research questions. Chapter 3 presents the results of a literature study into (upcoming) small satellite missions an their communication technologies with a focus on those having high payload downlink requirements. Chapter 4 presents the results of a literature study into (upcoming) NGSO (mega-)constellations and their specifications. Chapter 5 will define the concept missions based on the contents of the previous two chapters that are analysed in the rest of this thesis, and gives a detailed description of the communication architecture and system boundary to define the scope of the analysis in this work. Chapter 6 describes the purpose-built simulator that was developed for simulating data-relay links in scenarios with a large amount of objects. Chapter 7 will show the first order results of a visibility analysis using the data-relay simulator between a small satellite orbit and the NGSO (mega-)constellations. Chapter 8 describes the optimization framework that was developed for optimization of the data-relay communication system on the small satellites. Chapter 9 describes the results of the design optimization for each of the evaluated concept missions and NGSO (mega-)constellation. Finally, chapter 10 will give the conclusions and recommendations for the project.

This page intentionally left blank.

# 2

# Methodology

This chapter presents the methodology that is employed in this thesis project to evaluate the feasibility for the small satellite NGSO data-relay downlink communication architecture. An overview of the activities is presented in section 2.1 of this chapter. Each of the research questions stated in section 1.4 of the introduction is addressed in at least one of these activities. The linkage between the research questions, primary research activities and chapters in this report is presented in section 2.8 of this chapter.

## 2.1. Overview of activities

An overview of the activities that compose the methodology employed in this is shown in fig. 2.1. The goal of the thesis is to investigate the feasibility of a small satellite communication system that uses NGSO (mega-)constellations as a data-relay for payload data. To investigate the feasibility a design study is to be performed for the data-relay downlink system on the small satellite that considers the orbital dynamics, link budgets and satellite constraints. The design study is performed by means of a design optimization evaluating several small satellite concept missions and NGSO (mega-) constellations. An optimization approach is chosen because of the complexity of the system due to the large amount of satellites and link opportunities to consider. The activities in the methodology cover the generation of input data for the optimization, development of the analysis and optimization models and verification of the results. The outcomes of the activities will answer the sub-research questions.

Six primary activities are defined in the work of this thesis. shown in fig. 2.1. A market analysis (1.) will provide an overview of possible NGSO (mega-)constellations and examples of existing/upcoming small satellite missions for the use-case definition. It will also provide an overview of small satellite communication hardware to later be used for design comparison. The use-case / concept mission definition (2.) will define the small satellite missions and NGSO (mega-)constellations that are evaluated in the design optimization(s). Optimization objectives, orbital parameters and downlink requirements will flow down from these mission definitions. An orbital mechanics simulation (3.) of the small satellite and the satellites in the (mega-)constellation will provide the actual input data sets for the optimization; contact opportunities (moments in which line-of-sight is obtained) and link parameters (direction, range, etc.). In the design optimization (4.) several (parametrized) models are developed that can be used in a (multi-objective) optimization. Using these models the optimization outputs are calculated. These outputs define the specification and performance of the optimized design which will then be verified (5.) against the requirements from the concept mission and the specifications of state-of-the-art communication hardware. Finally, the results of the design optimization will be evaluated and the concept of a small satellite data-relay using NGSO (mega-)constellations will be assessed (6.).

The next sections will discuss each of the six activities in more detail. For each of the activities a motivation is given, a description of inputs, outputs and methods, descriptions and requirements for the end-products (tools, code, etc.) that is to be developed, verification steps if applicable, how the activity is to be documented and where in this report the results are discussed.

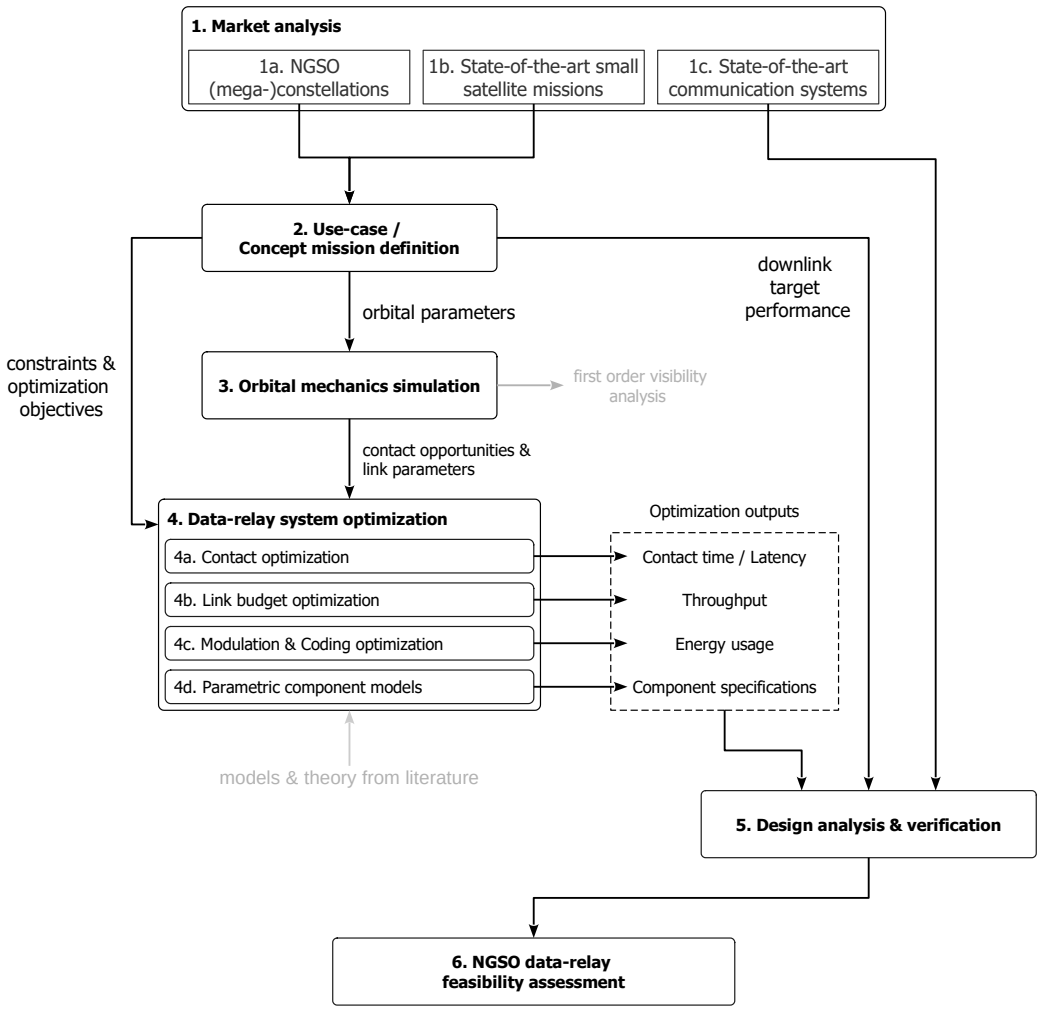


Figure 2.1: Overview of the methodology employed in this thesis project. Six primary activities are identified to generate an optimized design for a small satellite data-relay downlink system and asses its feasibility and performance.

## 2.2. Market analysis

The first step in evaluating the proposed data-relay concept is to understand potential use-cases and design possibilities. Therefore a market analysis is to be performed to create an create an overview of small satellite missions, NGSO (mega-)constellations and the current state-of-the-art in small satellite communication hardware applicable to the concept. Future needs may be identified by obtaining this overview of current capabilities and trends in small satellite missions. This then allows for definition of the kinds of small satellite missions that could benefit from the data-relay system and what the target performance of the system should be to match future needs. An overview of NGSO (mega-)constellations will show which constellations evaluate for the data-relay system. The overview of state-of-the-art communication hardware will show what is currently capable with small satellite communication hardware, and will effectively determine the design space for the optimization.

This information will be collected by performing a literature study. Sources include scientific publications such those from as popular small satellite conferences like the International Astronautical Congress (IAC) [23] and the Small Satellite Conference [24], public specifications from the companies including data-sheets and public filings to the Federal Communications Commission (FCC) that companies are required to make for spectral licenced operation in the United States.

There shall be three outputs to this market analysis; a table of small satellite missions properties with payload downlink needs, a table of NGSO (mega-)constellation with relevant properties, and several tables of state-of-the-art communication hardware (i.e. transmitters, antennas, etc.). In addition, for each category a short summary explaining observed trends and potential challenges will be given.

Part of this market analysis has been performed in the literature study prior to this thesis [25]. From this literature study, an overview and analysis in small satellite missions, with a focus on payload

downlink capabilities, and small satellite communication technology is provided in chapter 3, and an overview and analysis of NGSO (mega-)constellations is given in chapter 4.

## 2.3. Use-cases / Concept mission definition

The next step is to converge to a set of use-cases for the data-relay concept to be analysed in the rest of the investigation. To limit the scope of the work only a couple use-cases with different needs are analysed further. These use-cases will be defined as concept missions. Each concept mission shall define a baseline for a specific small satellite mission that has particular payload downlink needs.

The concept missions will be based on the trends in small satellite missions, capabilities and needs that were identified in the market analysis activity. Each concept mission description shall consist of a mission specification, optimization criteria and performance targets for the payload downlink, and a NGSO constellation specification. The mission specifications determines the fixed values and constraints the design optimization should comply to. These are for example the available size, mass and power for the downlink system or the orbital parameters of the satellite. The optimization objectives specify the criteria the design shall be optimized for. These could be for example throughput per orbit or latency. The performance targets give a target value for these optimization objectives. These targets are chosen to match or exceed state-of-the-art performance of small satellite communication technology and satisfy future needs that were identified. Finally, the NGSO constellation specification determines the fixed values and constraints the design optimization should comply to in order to be compatible with the target NGSO constellation. The mission specifications, optimization criteria, performance targets and NGSO constellation specifications shall be captured in a set of tables with a parameter description and parameter value or range. The formulation and definition of concept missions is described in chapter 5.

## 2.4. Orbital mechanics simulation

The design of the data-relay downlink is primarily driven by the contact opportunities (moments in which line-of-sight is obtained) and link parameters (direction, range, etc.). These follow from the orbital mechanics between the small satellite and the NGSO (mega-)constellation satellites. In the investigation of this project the orbits of the small satellites are chosen to be similar to state-of-the-art small satellite missions following from the market analysis activity. Therefore the orbital parameters of the small satellite are fixed in the analysis and will not be part of the optimization. The optimization will consider a set of contact opportunities and link parameters as the input for the optimization. The orbital mechanics simulation is therefore an activity performed prior to the actual design optimization of the data-relay downlink.

From the contact opportunities found by the orbital mechanics simulation a first order visibility analysis may already be performed. For example the total coverage for the small satellite could be determined, i.e. as the total possible amount of contact time per orbit that can be achieved. Or the distribution in duration of the time of contact during each contact opportunity may be defined. Based on this first order analysis some NGSO (mega-)constellations may be ruled out for further investigation simply because the total contact time per orbit or average duration of the contact opportunities is too low to achieve meaningful throughput.

As some of the NGSO (mega-)constellations may contain over 4.000 satellites (see chapter 4) a purpose-built orbital mechanic simulation will be developed that can handle simulation of large object counts and find the contact opportunities and link parameters within a reasonable amount of computation time. The orbital mechanics simulator shall use the orbital parameters of the concept missions and NGSO (mega-)constellations to propagate the positions of the satellites over time. Then based on the specified (FoVs) it will determine to which NGSO satellites have a line-of-sight with the small satellite of interest. At each time step the locations of the satellites in each line-of-sight pair shall be recorded. This output data will then used as the input for the design optimization. To verify the operation of the orbital mechanics simulator it shall be verified against commercial orbital mechanics simulators using test-cases with a small number of satellites.

The orbital mechanics simulator will be developed in Python. A description of the design and operation of the simulator will be provided in chapter 6 of this report and its source code will be uploaded to a Github repository [26]. A first-order visibility analysis on the contact opportunities with the NGSO (mega-)constellations is provided in chapter 7.

## 2.5. Data-relay downlink optimization

The contact opportunities need to be analysed and data-relay downlink needs to be designed for the small satellite that can make optimal use of these contact opportunities. Finding an optimal design is complex because of the multitude of different contact opportunities that occur through the orbit of the small satellite. Therefore to aid in this design synthesis optimization algorithms may be used. These algorithms could consider the optimal selection of the contact opportunities, transmitter and antenna configurations, and modulation/coding schemes. In addition, different criteria for the optimization could be considered for each different concept mission such as throughput per orbit, latency or total energy usage.

The optimization framework shall consider four main aspects that are developed from models and theory from literature:
(a) *Contact optimization* - the framework shall consider which contact opportunities to use in order to get the best performance for each concept mission.
(b) *Link budget optimization* - the framework shall consider the parameters of the components in the (to be designed) transmitting and (NGSO specified) receiving systems to determine if the signals are received with enough power to establish a link.
(c) *Modulation & Coding optimization* - the framework shall consider different modulation & coding schemes which drive parameters such the link data-rate, required power levels and efficiencies.
(d) *Parametric component models* - the framework shall consider (parametric) models of the components to determine key component parameters such as gain, output power, efficiency, size and mass.

Multi-objective optimization techniques can be used to show the trade-off between several optimization objectives. Therefore the optimization framework will not only show which designs are optimal for certain concept missions, but also how different objectives such as throughput per orbit and energy usage per orbit trade-off. The framework shall provide for each optimal design the component specifications (i.e size, mass, transmitter power, antenna gain) and an estimation of the performance (i.e. throughput, latency and energy usage).

The data-relay downlink optimization framework will also be developed in Python. A description of the design and operation of the simulator will be provided in chapter 8 of this report and its source code will be uploaded to a Github repository [26].

## 2.6. Design analysis & verification

After synthesis of the optimal data-relay downlink designs for each concept mission an analysis and verification step will be performed. Two aspects will be considered. First, the set of designs will be analysed to see if any fulfils the target performance for each concept mission and where particular key trade-off might be found. Second, a check is performed to if the design is realistic by comparing the specification and performance of its components with that of the state-of-the-art small satellite communication systems found in the market analysis. If the generated designs significantly out-perform the state-of-the-art this might indicate that the optimization is missing some constraints or models. This verification step will be performed as an iterative process throughout the thesis to refine the optimization approach. The goal is to have the synthesized data-relay downlink designs within the current capabilities of small satellite hardware and not require significant technological improvements.

The output of the design analysis and verification step shall be a narrowed list or range of design parameter that would most likely suit the concept mission definition. Or show that with current hardware or the NGSO constellations it is not possible to achieve the desired performance and where improvement are to be made.

Chapter 9 will analyse the results of the design optimization for each of the concept missions and narrow the options for the data-relay downlink for the concept missions.

## 2.7. Feasibility assessment

Finally a feasibility assessment will be performed for the NGSO (mega-)constellation data-relay concept for small satellites. The feasibility assessment will be made based on two aspects: 1) the performance of the data-relay concept for each of the baselined concept mission specifications evaluate see if (future) downlink needs are met, and 2) a comparison of the optimized design specification with the current state-of-the-art small satellite communication hardware to evaluate deficiencies in current

technologies to make the concept feasible. This feasibility assessment is included in chapter 9 of this report.

## 2.8. Summary of research activities

The matrix in table 2.1 shows the link between the research questions, the six main activities of this thesis project and the chapters of this project. The blue crosses show in which activities the (sub-)research question is addressed. The numbers in the far right column show the chapters addressing the (sub-)research questions. A summary of the answers to the research questions will be given in the conclusions chapter 10 of this report.

Table 2.1: Overlap between (sub-)research questions, project activities and report chapters

| | 1. Market analysis | 2. Use-case definition | 3. Orbital simulation | 4. System optimization | 5. Design verification | 6. Feasibility assessment | Chapter(s) |
|---|---|---|---|---|---|---|---|
| **Research question 1:** Which (kind of) small satellite mission could benefit from a NGSO data-relay downlink? | X | X | | | X | X | 3,5,9 |
| What are the current capabilities and limitations of state-of-the-art communication systems on small satellites? | X | | | | | | 3 |
| What are the benefits and drawbacks of a NGSO data-relay architecture? | | X | | | | X | 5,9 |
| What are the requirements on the small satellite to support such a communication system? | | | | | X | | 9 |
| **Research question 2:** Which NGSO (mega-)constellations could be used for relaying data from a small satellite? | X | X | X | X | | | 4,7,9 |
| What are the properties of (upcoming) NGSO (mega-)constellations? | X | | | | | | 4,7,9 |
| What link performance can be achieved with each of the constellations? | | | X | X | | | 7,9 |
| What are the requirements for the small satellite communication system to communicate with the constellation? | X | | | X | | | 4,9 |
| **Research question 3:** How to use optimization techniques to generate an optimized design for a data-relay downlink on a small satellite? | | | X | X | | | 6,7,8 |
| What are the inputs, outputs and constraints to the optimization? | | | | X | | | 8 |
| How to incorporate orbital dynamic models and link budget models in the optimization? | | | X | X | | | 6,7,8 |
| What optimization algorithms can be used to optimize the design of the communication system? | | | | X | | | 8 |
| **Research question 4:** What are the design characteristics and performances of an optimum NGSO data-relay downlink for a small satellite mission? | | | | X | X | X | 5,8,9 |
| What is considered optimal performance for the communication system? | | | | X | X | X | 5,9 |
| How do the different performance parameters trade-off in the design of the data-relay downlink? | | | | | X | X | 8,9 |
| How does the design compare with respect to state-of-the-art small satellite communication systems? | | | | | X | | 9 |

This page intentionally left blank.

# 3

# State-of-the-art small satellite missions and communication technologies

This chapter will present a literature study on small satellite missions and communication technology. Section 3.1 presents a market analysis of state-of-the-art small satellite missions. From this overview, baseline missions are formulated later in chapter 5 that are used to analyse the potential of the NGSO data-relay downlink by a design optimization. The section also discusses the commercial potential and alternatives to the proposed NGSO data-relay downlink. Section 3.2 will present an overview of state-of-the-art (small-)satellite communication systems. This section will start by giving some background into the components that make up a typical (downlink) communication system. The section will then present a detailed overview of the state-of-the-art of the major components including transmitters and antennas. The use of this overview is two fold; it is used to formulate parametric models for the components in the data-relay downlink optimization in chapter 8, and it is used in chapter 9 to compare the results of the design optimization with existing technology.

## 3.1. Small satellite market analysis

The timeline in fig. 3.1 by Karunanithi et. al. [4, IEEE Aerospace presentation] shows how CubeSat nano-satellites started around the year 2000 from simple technology demonstrators developed by universities to stimulate education to now have developed into a market sector involving universities, industry and space agencies. The latest trend seen are proposals for constellations of nano-satellites as the cost of Commercially Of The Shelf (COTS) hardware and launch costs decrease.

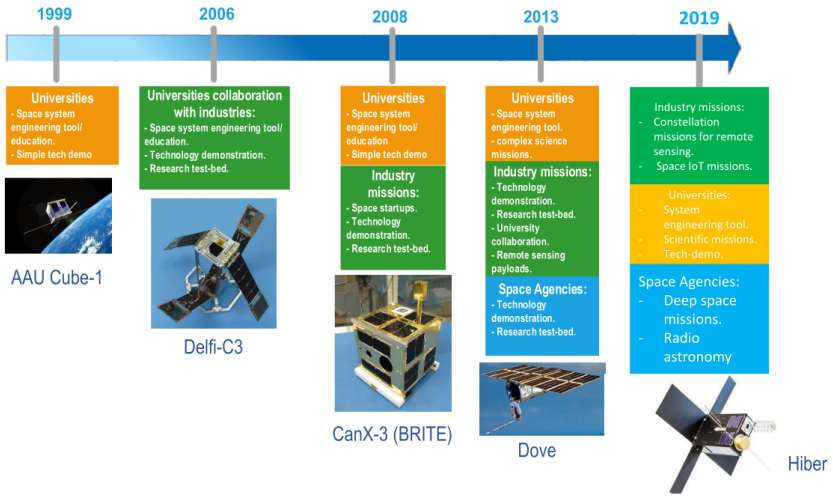


Figure 3.1: Nano-satellite missions including CubeSats have evolved from simple technology demonstrators to constellation missions as the costs of COTS satellite hardware and launch costs decreases [4, IEEE Aerospace presentation]

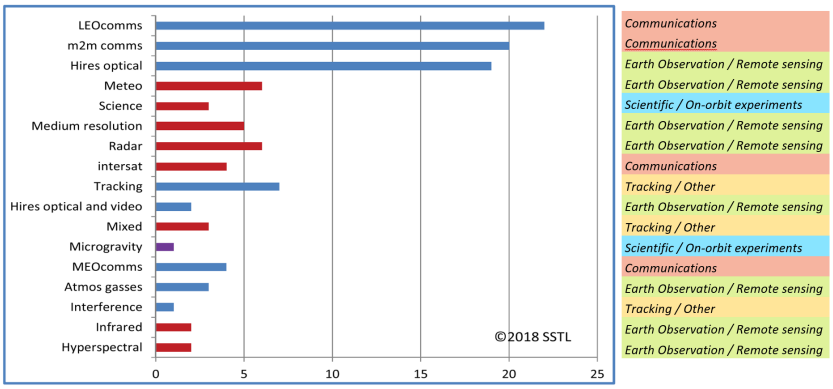


Figure 3.2: Applications for proposed small satellite constellations from [27]. Added to the figure on the right are some of the areas in which these applications are developing.

A 2018 study by SSTL provides an overview of proposals for applications of small satellite constellations [27] shown in the graph of fig. 3.2. In this graph, four areas can be indicated in which these constellation applications are developing (added to the right side of the figure). These four areas are; Earth Observations / Remote Sensing, Communications, Scientific / On-orbit experiments and Tracking. In general, it can be concluded from the amount of small satellite constellation proposals that the amount of data generated in (low Earth) orbit will be greater than ever. From the studied literature in this review it was found that within the four application areas two areas will contribute the most to this increase in data, namely Earth Observations / Remote Sensing and Communications. These two areas will see increased data generation because of the miniaturization of high-performance instruments and an increasing demand for connectivity for Internet of Things and Machine to Machine communications. The proposed constellations in these areas are therefore interesting candidates for the proposed LEO-to-NGSO data-relay downlink.

In sections section 3.1.1 and section 3.1.2 these two areas are discussed, and existing missions and proposals are presented. A focus is placed on the current solutions employed for downlinking the onboard generated payload data. Section 3.1.3 will summarize the two areas as two distinct use cases and highlights how each could benefit from a data-relay downlink. Finally, section 3.1.4 will conclude with a short discussion on the commercial potential for a data-relay system for small satellites by showing proposals for similar systems, and will look into some of the alternatives for data-relays systems, such as high speed direct optical links and shared ground networks.

### 3.1.1. Earth observation & remote sensing small satellite missions

Earth observations and remote sensing missions use (optical) instruments and sensors to investigate the Earth and its atmosphere. The increase in data generated for these applications goes hand in hand with the miniaturization of COTS hardware. Sensors have become smaller, lighter, more affordable and consume less power, allowing for higher resolution images or measurements to be taken from smaller (nano-satellite) platforms. This enables missions of small satellite constellations for the same price as a single larger satellite, while keeping a relatively high sensor performance each satellite in the constellation. The result is a significant increase in data generated on the now multiple satellites in a constellation and a bigger challenge to get all this data down to ground.

Table 3.1 shows a selection of existing and near future (constellations of) small satellites for Earth observation and remote sensing. With companies such as Planet, Spire and BlackSky, planning to have around 100 satellites in orbit the amount of data that will be generated by small satellites will increase significantly the coming years. Planet has proven the business model for small satellite earth observation constellations by maintaining the largest Earth observation constellation of 120+ nanosatellites operational in orbit [2] showing that it is commercially possible for other companies to do the same.

It is difficult to estimate the total amount of data generated on the satellites from just the publicly available numbers. The to be downlinked data is strongly dependent on how the satellites are used operationally, i.e. how much pictures they take during their orbit, number of ground station and if the data is compressed or selectively downlinked. In two publications from Planet and Astro Digital

an exact number of maximum throughput is given of 80 Gbyte and 3.2 Gbyte per pass respectively. These numbers give a clear performance target for a data-relay system in order to compete with a direct link solution. For the other satellites, no numbers on data downlink were found. However, it is possible to give an indication by looking at the size of the onboard storage and maximum downlink speed, both more commonly published numbers. Larger onboard storage allows for more data to be gathered before a need for downlinking. With selective downlinking (only selecting the interesting images for transmission and discarding the rest) or compression algorithms, the total amount of data can be reduced. However, the only way to increase throughput per orbit is to achieve higher data rates during a pass or increase the number of ground stations.

Table 3.1: Overview of (small) satellites used for Earth Observations. Three larger satellite families from DigitalGlobe, NASA and CNES are added for comparison.

| Company | Size / Weight | Type | Latest launch | Orbit | Operational/ planned sats | Downlink rate [Gbps] | Storage [GB] | Architecture/ # of GS | Ref |
|---|---|---|---|---|---|---|---|---|---|
| Planet<br>*Dove* | 3U / 5.8 kg | MS | 2020 | 500 km<br>98 deg | 150 | 1.674 | 2000 | Direct link - X-band<br>2 GS | [28], [2] |
| SPIRE<br>*Lemur* | 3U / 4.6 kg | RO/AIS/<br>ADS-B | 2019 | 500 km<br>var. deg | 80/150 | ? | ? | Direct link - S-band<br>>5 GS | [29], [30] |
| BlackSky<br>*Global* | ? / 56 kg | OPT | 2019 | 500 km<br>98 deg | Apr-60 | ? | ? | ?<br>? | [31], [32],<br>[33], [34] |
| Astro Digital<br>*Corvus* | 6U / 11 kg | MS | 2018 | 550 km<br>98 deg | May-25 | 0.32 | 1000 | Direct link - Ka-band<br>1 GS | [1], [35] |
| GeoOptics<br>*CICERO* | 6U / 10 kg | RO | 2018 | 500 km<br>72 deg | Jun-24 | 0.002 | ? | Direct link - X-band<br>? GS | [36] |
| JAXA<br>Compact *SAR* | 0.7x0.8x0.9 / 130 kg | SAR | ? | ? | 1 2 | | 768 | Direct link - X-band | [37] |
| *DigitalGlobe*<br>*QuickBird-2*<br>*Ikonos-2*<br>*GeoEye-1*<br>*WorldView-1/2*<br>*WorldView-3* | <br>1.6x3m / 951 kg<br>1.8x1.6m / 817 kg<br>4.4x2.7m / 1955 kg<br>4.3x2.5m / 2800 kg<br>5.7x2.5m / 2810 kg | MS | <br>2001<br>1999<br>2008<br>2009<br>2014 | <br>600 km<br>to<br>700 km<br>98 deg | 5 | <br>0.320<br>0.320<br>0.740<br>0.800<br>1.200 | <br>16<br>8<br>150<br>275<br>275 | Direct link - X-band<br>? GS | [38], [39],<br>[40], [41],<br>[42], [43],<br>[34] |
| NASA<br>*Landsat-7*<br>*Landsat-8*<br>*Landsat-9* | 2.8x4.3m / 2200 kg<br>? / 2780 kg<br>? | MS | 1999<br>2013<br>P2023 | 700 km<br>98 deg | 3 | 0.300<br>0.440<br>? | 47.25<br>390<br>? | Direct link - X-band<br>? GS | [44], [45],<br>[46] |
| CNES<br>*Spot 5* | 3.4x3.1x6m / 3030 kg | MS | 2015 | 832 km<br>98 deg | 1 | 0.1 | 11.25 | Direct link - X-band<br>? GS | [47] |

*OPT – Optical imaging*
*MS – Multi spectral imagining*
*RO – Radio Occultation*
*AIS – Automatic Identification System*
*ADS-B – Automatic Dependent Surveillance – Broadcast*
*SAR – Synthetic Aperture Radar*
*? – Missing data*

As shown in Table 3.1 most of the EO satellites use a direct link on X-band to downlink the payload data. Only the Astro Digital Corvus spacecraft use a direct link Ka-band achieving a 320 Mbps peak data rate [1]. A paper by Katona et. al from the German DLR shows that moving to Ka-band or higher bands using direct links or data-relay links will allow for an order of magnitude capacity increase for large class EO satellites [48]. A later 2018 paper by the same authors show the ongoing developments for a Ka-band demonstrator setup [49]. Although there are no announced plans by any of the small EO satellite companies for a data-relay architecture, Planet has made an FCC filing for testing a C-band link which could be used for an intersatellite link [50]. However, it is unclear if this would be for a potential data-relay link or crosslinks between the Dove satellites.

Three conclusions can be drawn from the data presented in this section. First, the maximum data rates of small satellites can achieve is now on the same level or higher as the larger EO satellites such as the DigitalGlobe WorldView-3 satellite. This rapid development in achievable data rates is not seen in the larger class satellites, as for those satellites it only seems as if the amount of storage has increased over the years. This performance increase is well displayed by the development in the Planet High Speed Downlink transmitter going from a data rate of 0.01 Mbps to over 1000 Mbps in only 8 years [2]. Second, the size of storage on-board of small satellites does not seem to be an issue as terabytes of storage is possible on nano-satellites such as the Dove and Corvus. The increase in storage indicates a rise in performance and collected data by these satellites. Finally, there exist active developments for higher throughput systems with a trend towards Ka-band and alternative architectures such as crosslinks or data-relays for both small and large class satellites.

Although the examples presented in this section are mostly of constellations of small satellites for EO, there are several standalone small satellite missions that could benefit from a data-relay system, such as the 6U RainCube satellite for precipitation radar [51]. The proposed LEO-to-NGSO data-relay system could allow these missions to achieve high downlink throughputs throughout their orbits without having to invest in multiple ground stations.

### 3.1.2. Internet of Things / Machine to Machine small satellite missions

Proposals for small satellites for communications have grown significantly because of an increase in the demand for connectivity. Part of this demand originates from people in rural and developing areas that are currently underserved by terrestrial internet connectivity. This is the primary market for the NGSO constellations which will be discussed in chapter 4. A second demand however rises from the increase in Internet-of-Things (IoT) and Machine-to-Machine (M2M) applications. These applications include for example tracking of livestock and ship containers, or monitoring remote sensors for weather forecasting and smart grids. These applications do not require a high data rate but are at remote locations where there is no terrestrial communication infrastructure available. In addition, these applications are often low power, working from a small battery or possibly a small solar panel which makes them less applicable for the NGSO constellations that require a user terminal with a 0.5 meter dish or phased array equivalent (chapter 4).

Start-up companies are catering to this demand with dedicated IoT/M2M constellation missions that provide service from space using communication protocols designed for these low power & remote applications. The satellites in these constellations receive the data from the IoT/M2M sensors throughout their orbit and will downlink it to an internet connected ground station, in a store-and-forward fashion. Companies such as Hiber, Fleet, Lacuna Space and Kepler have started launching their first satellites for constellations in LEO or VLEO that can connect with sensors world-wide [6], [8], [52], [53].

Hiber is planning a constellation of 48 satellites and launched two demonstrator 6U nano-satellites to LEO. The satellites can receive packets of 1400 bits lasting no longer than 400 milliseconds from the user terminals and can also broadcast firmware updates and data to the user terminals [54]. Although Hiber is currently using 6U nano-satellites their final constellation will use smaller 3U nano-satellites.

Lacuna Space is planning a similar IoT/M2M to LEO approach however then using the LoRa(WAN) protocol that is popular for IoT devices [55]. This protocol can achieve speeds up to 11 kbps and Lacuna Space has demonstrated the link on a hosted payload on a M6P satellite from NanoAvionics [55]. Lacuna Space is planning 3U nano-satellites for their full constellation of 32 satellites.

Fleet Space is taking a different approach; their users will connect through LoRa(WAN) with a Fleet Portal that will pass their data via a satellite to the internet. Their customers applications therefore not directly connect to the satellites in space. Fleet has put their first 1.5U and 3U nano-satellites in orbit but are planning to use the constellations of Iridium and Inmarsat until their constellation of 100 satellites is operational [52], [56].

Astrocast is planning a similar network as Hiber for IoT/M2M applications that require a few kilo bytes of connectivity a day or less. Their low-power module can establish a bi-directional connection with satellites in LEO over a L-band link [57]. Astrocast has launched two 3U satellites towards completing their full constellation of 64 satellites and have contracted the hardware for six ground stations [58], [59].

Hiber, LacunaSpace, Fleet Space and Astrocast will all use a store-and-forward scheme for their IoT/M2M satellites, having one or multiple ground stations that will connect the satellites to the internet using a direct link either on the same frequency as their users (Astrocast on L-band) or on a separate feeder link (Hiber on S-band [54]). Kepler Communications is exploring an alternative architecture. Their constellation of 140 satellites will use direct feeder links to ground stations on Ku-band but will also have Ka-band crosslinks between the satellites to create a network in the constellation. This allows a satellite to directly forward its data to another satellite if it is not in view of a ground station. Kepler Communications is also targeting a higher speed link with their users (up to 150 Mbps) and are planning to provide data-relay services for other satellites in LEO [53]. After hosting the payloads of LacunaSpace and BlinkSpace, NanoAvionics is planning to provide their constellation of 6U M6P or 12U M12P satellites as a service for IoT/M2M providers. The Global IoT constellation will consist of 72 satellites that will have crosslinks and/or a data-relay with GEO direct-to-home satellites [17].

Although IoT/M2M services from LEO small satellites has gained popularity the idea of providing (low rate) internet from space is older. From 2002 to 2014 Aprize has launched 12 25x25x25cm

AprizeSats each weighing 13 kg, making them fall just out of the nano-satellite category. The AprizeSats collect low rate data (up to a few kbps) throughout their orbit and can collect larger amount of data (several Mbps) for specific users when requested. The AprizeSats also collect and distribute Automatic Identification System (AIS) data used for tracking and managing ship traffic [60], [61]. A little older is the OG2 constellation of Orbcomm, launched between 2010 and 2015, as a second-generation of satellites dedicated to M2M communications. The OG2 satellites use the SN-100 bus and have a size of 1 x 1 x 0.5 meter, weighing 172 kg. The satellites provide a two-way communication link up to 4 Mbps on VHF and an AIS terminal. Including the first generation satellites a total of 50 satellites were launched, however only 12 satellites remain operational due to failures [62].

Table 3.2: Overview of planned and existing (small) satellite constellations used for IoT/M2M

| Company / *Satellite* | Size / Weight | Type | Latest launch | Orbit | Launched / planned | User Uplink rate [Mbps] | Downlink rate [Mbps] | Downlink architecture | Ref |
|---|---|---|---|---|---|---|---|---|---|
| Hiber<br>*Hiber 1 & 2* | 6U / 7.23 kg | IoT/M2M | 2018 | ~500 km<br>98 deg | 2 / 48 | 0.0035 | 4.30 | DL - S-band<br>2 GS | [54], [6] |
| Lacuna Space<br>*demo on M6P*<br>*LacunaSat-1* | ? / ?<br>3U / ? | IoT/M2M | 2017 | ? | 0 / 32 | 0.01 | ? | ? | [8], [55] |
| Fleet Space<br>*Proxima 1*& 2<br>*Centauri 1 & 2*<br>*future planned* | //1.5U / ?<br>3U / ?<br>6U & 12U | IoT/M2M | 2018 | 500 km<br>~90 deg | 4 / 100 | ? | ? | ? | [5], [63], [64], [52] |
| Astrocast SA<br>*Astrocast* | 3U / 4 kg | IoT/M2M | 2018 | ~600 km<br>~98 deg | 2 / 80 | ? | ? | DL - L-band<br>6 GS | [5], [58] [59] |
| Kepler Communications<br>*Kepler 1 & 2* | 3U / <5 kg | Data/Relay | 2018 | ~500 km<br>~98 deg | 2 / 140 | 150 | 120 | DL - Ku-band<br>CL - Ka-band<br>2 GS | [53], [9] |
| NanoAvionics GIoT<br>*M6P*<br>*M6P / M12P* | 6U / ?<br>6U or 12U / ? | IoT/M2M | 2017 | ~500 km<br>98 deg | 3 / 72 | ? | ? | CL - ?<br>GEO-DR<br>- Ku/Ka-band | [17], [65] |
| Aprize<br>*AprizeSat* | 25x25x25cm<br>/ 13 kg | M2M/AIS | 2014 | 690 km<br>98 deg | 12 / 48 | >1.00 | >1.00 | DL - S-band<br>AIS - VHF | [60], [61] |
| Orbcomm (OG2)<br>*OG2 / SN-100 bus* | 1x1x.5m<br>/ 172 kg | M2M/AIS | 2015 | 750 km<br>52 deg | 50 / 52 | 4.00 | 310.00 | DL - UHF<br>AIS - VHF | [62], [66], [67] |
| Iridium Next | ? / 860 kg | Voice/Data<br>/Relay | 2019 | 780 km<br>86 deg | 66 / 66 | 8000 | ? | DL -<br>CL - Ka-band | [68] |
| GlobalStar | ? / 450 kg | Voice/Data | 2007 | 1440 km<br>52 deg | 48 / 48 | 9.6 | ? | DL - C-band | [69] |

DL – Direct link
CL – Cross link
GEO-DR – GEO data-relay
AIS – AIS information collection & broadcast
# GS – Number of (planned) ground stations
? – missing data

Table 3.2 shows an overview of some of the planned and existing (small) satellite constellations for IoT and M2M data. Small satellites for IoT/M2M applications are a competitive field, it is therefore difficult to find detailed information on the exact architectures of the satellites communication and storage system. FCC filings and public datasheets of the systems used by Kepler, Hiber and Orbcom help defining the data generated on these satellites but exact numbers on data generated/collected by the satellites is not available. This gap in knowledge opens opportunity for research to find the how much data these constellations generate, for example by a user demand model as set up by I. Del Portillo in his analysis on mega-constellations [3]. Then based on the demand model, multi-objective optimization algorithms can be used as is done by C. Jilla to optimize the design of a distributed system that maximizes performance (billable user data) and cost [70].

A simple upper limit estimation can be made by looking at the maximum downlink rates in table 3.2. In a store-and-forward architecture, the user data uplinked to the satellite between ground station passes cannot be greater than what can be downlinked during a ground station pass, assuming no compression is used, and all data is to be uploaded to the internet. The maximum amount of user generated data is then roughly the pass duration of the satellite over its ground stations multiplied by its maximum downlink rate. As most of these constellations are in high inclination orbits, ground stations at the poles offer the most contact time, about 400s on average per pass [2]. This would result into a maximum data per orbit per polar ground station between 215 Mbyte per orbit (case Hiber 4.3 Mbps down) and 6 Gbyte (case Kepler 120 Mbps down). Knowing nano-satellites can reach several

hundreds to a thousand bits per second downlink rates and downlinking tens of gigabytes per pass (i.e. DOVE and Corvus see section 3.2.2) it seems that there is (currently) not enough demand for the IoT/M2M satellites to require a high throughput or that the costs for high rate communication systems do not result in more profit. However, some of the proposals include multiple ground stations at multiple locations such as Hiber with two locations (Delft, The Netherlands & Svalbart, Norway) [54] and Astrocast with six planned locations with multiple antennas [58]. A reason for multiple ground stations for IoT/M2M constellations could be that the latency of the store-and-forward architecture is limited by the time between satellite reception of a user packet and the satellite revisiting the ground station. Solutions for this problem are crosslinks as planned by Kepler Communications to create a network between the satellites, a geostationary data-relay satellite that can see a large portion of the satellite orbit or, as proposed in this work, a data-relay with non-geostationary constellations.

### 3.1.3. Summary of use-cases

Two distinct small satellite use-cases for the proposed data-relay architecture with non-geostationary constellations for downlinking LEO payload data have been identified; constellations for Earth Observation (EO) and constellations for Internet-of-Things (IoT) and Machine-to-Machine (M2M) communication. Current proposals and missions for both use-cases consider primarily satellites in a 500 km to 700 km (Sun-synchronous) orbit, making it theoretically possible to establish a data-relay link with satellites in higher low Earth orbits (i.e. 1000 km to 2000 km), medium earth orbits and geostationary orbits. The distances for a LEO-to-LEO data-relay would be roughly the same as for a direct link to ground but do not suffer from atmospheric attenuations. For LEO-to-MEO and LEO-to-GEO the distance would be greater, resulting in more path loss, but they would offer longer (continuous) contact times with the satellite. Earth observation constellations (but also standalone missions) could benefit

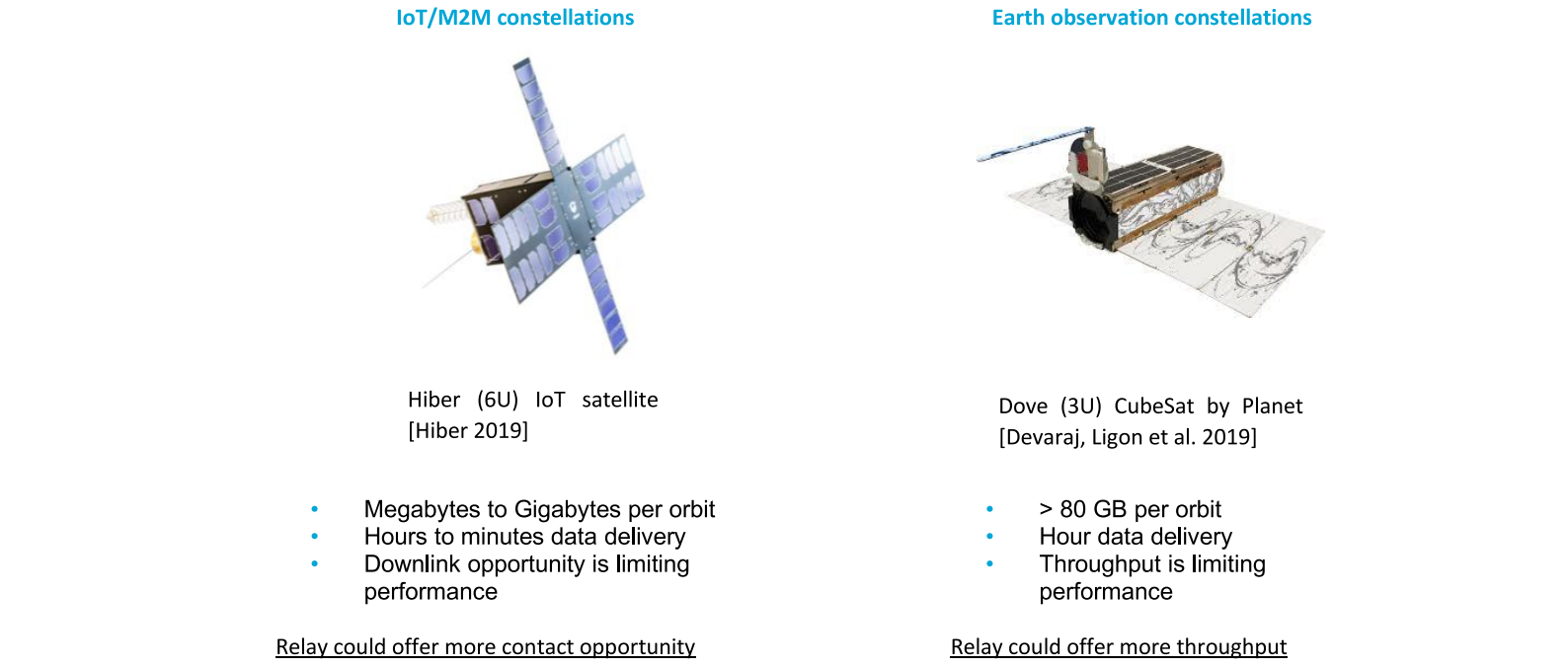


Figure 3.3: The LEO-to-NGSO data-relay architecture could offer more contact time with the satellites in LEO. IoT/M2M missions could benefit from this by allowing the latency to be reduced while EO missions could benefit from the increase in throughput per orbit.

from the proposed LEO-to-NGSO data-relay architecture because it offers significantly more contact time (although not continuous) with the satellite than would be possible with a single ground station. Instead of transmitting all payload data during infrequent ground station passes with high data rates to maximize throughput, the satellites could off-load their data throughout their orbit. For IoT/M2M missions the same benefit holds and more contact time offers more throughput per orbit. However, as was shown in section 3.1.2, the throughput is not necessarily the bottleneck for these missions. Since most of these IoT/M2M missions uses store-and-forward architectures, the average latency for the users to

receiver their data is directly related to the number of ground stations and their locations across the globe. The proposed LEO-to-NGSO data-relay architecture could relive this limitation by offering more contact opportunity with the satellite, even though it might be non-continuous for i.e. the LEO-to-LEO case. In chapter 5 these two use-cases are used to define baseline concept missions that are used in the rest of this work to analyse the potential of the NGSO data-relay downlink.

### 3.1.4. Commercial potential and alternatives to the NGSO data-relay architecture

Previous sections have shown use-cases that could benefit from a LEO-to-NGSO data-relay architecture. Several companies have recognised the (business) potential of providing data-relay services from non-geostationary orbits and are in the early stages of developing their concepts. Kepler Communications is one of the companies that is planning a small satellite constellation in LEO for high bandwidth and IoT/M2M data. However, their 2016 FCC filing also mentions a 25.25 – 27.5 GHz Ka-band RF links use for inter-satellite communication within the network of their satellites and with other NGSO satellites [53].

Similarly, the US based company Stara Space is “making downloading satellite data simple” by allowing third party satellites to transfer data through their network of LEO satellites [71]. Their first two PocketQubes of 5x5x15cm were launched in 2019 to demonstrate intersatellite communications. However little is known about these satellites other than that Alba Orbital has built the satellites and brokered their launch [72]. The Unicorn-2 platform of Alba Orbital includes UHF and S-band modules that can downlink up to 200 kbps [73].

Another start-up named Analytical Space is planning to launch a satellite relay network constellation. They launched their first 6U experimental satellite named RADIX in 2018 which had multiple communication systems onboard, including a GomSpace SDR TR-600 software defined radio, wideband antennas, a parabolic antenna and a laser communications terminal [74]. Their second experimental satellite Meshbed will include a phased array communication on 2 GHz and 5 GHz [75].

Finally, there is the company Audacy that was the first to be granted operation of their constellation of three satellites in MEO to provide data-relay services for satellites in lower orbits [76]. Audacy was proposing K-band and V-band communications that would offer high bandwidth and long visibility times with the satellites of its users. Audacy was the most advanced of these four companies but filed for bankruptcy in 2020 [77], section 4.2.2 will elaborate on their proposed system.

It is also important to look at some of the alternatives to a data-relay communication architecture and several examples are explored in research and industry. The first alternative to consider is the use of optical laser downlinks links instead of traditional radio frequency downlinks. Laser communications could offer small satellites gigabits per second of data downlink [78] without having to go through the costly and slow processes of applying for spectral licencing. Optical laser links however do not work in clouded conditions requiring several ground stations for timely downlink of data [2]. In addition, optical laser technology for the ground segment and space segment is at this moment expensive and has a low readiness level. A second alternative architecture is to establish crosslinks between the satellites in the constellation. Radio frequency or (optical) inter-satellite links between the satellites in the constellation can be used to create a network. In case one satellite in the constellation wishes to downlink its data, it can forward it to the next satellite until the data arrives at a satellite in view of a ground station. This might reduce the latency for store-and-forward schemes, but the total throughput is still limited by the number of ground stations and the speed of the direct link. In addition, most of the EO and IoT/M2M constellations of table 3.1 and table 3.2 have their satellites in a single plane. Meaning that in order to always provide this networking capability the crosslinks between the satellites should stay up all the time, consuming significant amounts of power on the satellites. Finally, although constellations for EO and IoT/M2M will be the largest data generators in space, crosslinks are not a solution for stand-alone small satellite missions. A final alternative can be identified that would offer an increase in contact time and bandwidth for all different kinds of missions. Ground station networks can be created if ground stations are shared between missions. Instead of having a dedicated ground station for a constellation or mission, the ground stations could use standardized protocols and frequencies to downlink data from any satellite that is within view. This would give a standalone satellite mission access to multiple ground stations across the world allowing more contact time with the satellite. The SATNOGS project is an amateur initiative for such a ground station network [79]. In addition, Amazon Web Services is commercializing this concept with their AWS Ground Station [80]. Shared ground station networks would be the most effective solution to deal with increase in data generation in space. However, even

though these services can be successfully commercialized, it is likely that companies will still invest in and use their own ground stations for security reasons or simply to get the competitive edge in data throughput for their system.

## 3.2. Small satellite communication technologies

Small satellites often have two or more communication systems on board. Figure 3.4 shows the example of the 6U Hiber IoT/M2M CubeSat that has a low data rate communication system for Tracking Telemetry and Command (TT&C), a high data rate downlink system to transmit payload data and a third system for bi-directional communication with the IoT user terminals on the ground [54].

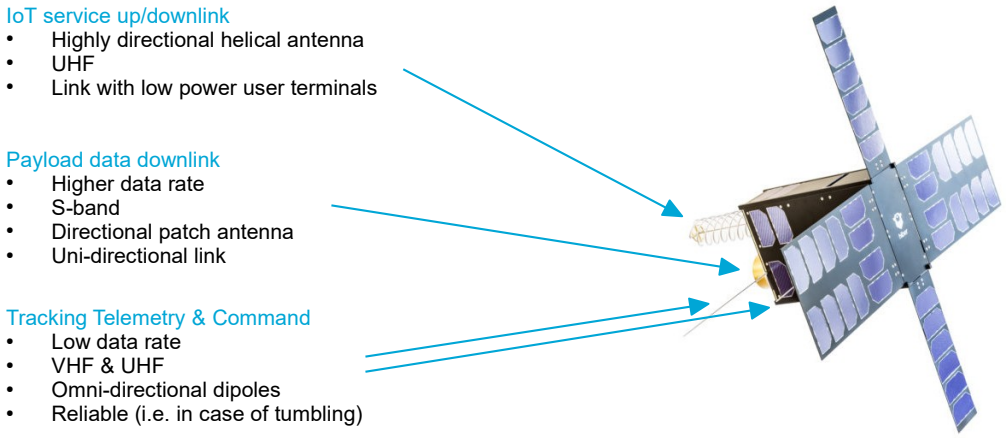


Figure 3.4: Hiber 6U CubeSat with three communication systems. The third communication system on for IoT service up/downlink is unique to the mission of Hiber [6], [54]

The task of the satellite payload downlink communication system (from now on called the payload downlink system) is to transmit the data that is generated onboard of the satellite to a ground station on Earth (direct link) or to another satellite (inter-satellite link). Figure 3.5 shows a block diagram of a typical signal chain of a payload downlink system. Throughout literature different nomenclature is used for the payload downlink system and its parts. Devaraj et. al [2] use the word radio to refer to their High Speed Downlink 2 system on the satellite side and the word transmitter when referring to the system excluding the antennas. Leveque et. al [1] use the word transmitter to describe their complete system on the satellite side including the antenna. In this work 'communication system' or 'system' is used to refer to all the blocks shown in fig. 3.5. The word transmitter is used when referring to the blocks in fig. 3.5 between the CPU and the antenna. To avoid ambiguity the word radio is not used in this work unless it is specifically used in referenced literature.

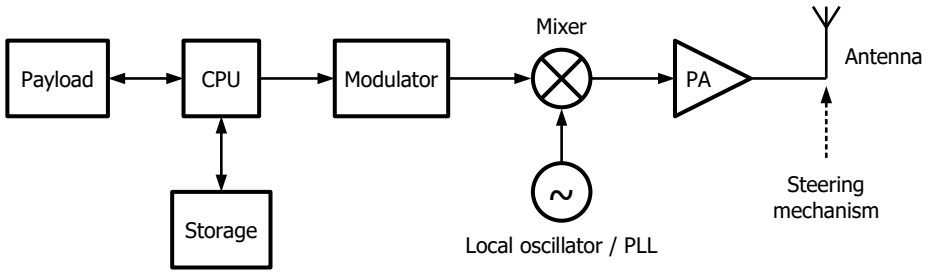


Figure 3.5: Block diagram of a typical payload downlink communication system.

In the payload downlink system the data stream from the payload is processed by a central processing unit (CPU). This processor could be separate from the on-board computer and dedicated for payload data processing, possibly using compression algorithms to reduce the size of the data or add

an error correction code to improve data integrity during storage. When the downlink is not available (i.e. when a ground station is not in view) data generated by the payload will be stored in the onboard storage. When in view of the ground station the CPU will recall the data from storage, packetize it and stream it to the modulator.

The modulator takes the (packetized) data stream on its input data port (i.e. an Ethernet port in [1], [2], [81]) and encodes and modulates the digital data on an analog signal specified according to a communication protocol or standard such as DVB-S2 (see Section 3.2.1). A popular architecture for the modulator is that of the software defined radio (SDR) such as the IQ wireless XLink transceiver [82] or the Gomspace NanoCom SDR-MK3 [83]. In an SDR most blocks needed for modulation, coding and waveform shaping are completely implemented in software. This allows the transmitter to be reconfigurable and allow for operation using different protocols and frequencies. An SDR has a dedicated processor and memory for the digital processing of the signals and therefore it can also significantly contribute to the total power consumption of the transmitter.

The analog modulated signal generated by the modulator is centred around an intermediate frequency (IF). In a the super-heterodyne transmitter[1] this IF will be upconverted in the mixer or upconverter to the carrier frequency, also called the radio frequency (RF) [84]. The upconverter is responsible for the frequency reconfigurability for the satellite including band and or user channel selection. Adaptive control of the local oscillator (LO) frequency can correct for Doppler shifts that appear due to the end points in the link moving with respect to each other. In some cases the modulator is a physically separated unit from the rest of the transmitter such as in the Hi-BEAM DVB-S2 modem [81] and only connected by the IF cable. However, in the small form factor of CubeSats, the modulator is integrated with the rest of the transmitter and possibly the antenna such as in [1]. The paper by Devaraj et al. mentions that the availability of commercially of the shelf (COTS) mixers at Ka-band is limited compared to X-ban [2]. However the Ka-band transmitter by McNicholas et al. seem to prove otherwise as they have used off-the-shelf monolithic microwave integrated circuits (MMIC) in their design [84].

Before transmission by the antenna, the signal needs to be amplified by a power amplifier (PA) to increase its power level. The PA is a critical component for the overall power consumption of the system. The efficiency of the PA determines how much power is used to increase the power level of the signal and how much is dissipated in heat. Energy efficient PA design is an active field of development in microelectronics. A survey by Wang et. al. [85] provides an excellent overview in the state-of-the-art in PA design from 500 MHz to 1.5 THz.

After amplification the signal is converted to a (radiating) electromagnetic wave by the antenna and transmitted through space. The antenna provides a gain in transmitted power by directing the electromagnetic wave in the direction the ground station or relaying satellite. Some systems include a pointing mechanism for the antenna allowing it to be steered towards a target without changing the orientation of the spacecraft. The block diagram shown in fig. 3.5 is typical for a unidirectional RF communication system. An alternative for RF communication is optical communication where electromagnetic waves in the optical spectrum (300 GHz to 3000 THz) are used to carry the information. Optical communication for small satellites is an active field of development and some missions have flown demonstrating this technology [86]. At this moment optical communication has a low technology readiness level (TRL) [78] and the NGSO constellations discussed in chapter 4 currently do not offer an optical user uplink. Therefore, optical communication hardware is not the focus of this study.

The following sections will present some of the state-of-the-art in small satellite communication systems. Section 3.2.1 will start with presenting modulation and encoding schemes that are currently popular for payload downlink transmission. Section 3.2.2 will describe the state-of-the-art in small satellite transmitters and section 3.2.3 will do the same for small satellite antennas. This chapter will conclude a survey of existing and proposed (small satellite) missions that employ inter-satellite link systems in section section 3.2.4.

### 3.2.1. Modulation and coding

Modulation is the process of mapping an (digital) stream of data onto an (analog) waveform. Modern modulation schemes map the data onto the phase and amplitude of a carrier signal. Each amplitude and phase combination is called a symbol and the possible symbols of a modulation scheme are displayed in constellation diagrams such as the ones shown in fig. 3.6a. In these diagrams the radius from the

[1] Alternative architectures such as direct modulators or RF digital to analog converters exist where the output frequency of the modulator is that of the carrier. Discussion of different architectures for transmitters is beyond the scope of this study.

centre determines the amplitude of the carrier wave and the rotation from the x-axis determines the phase of the carrier wave.

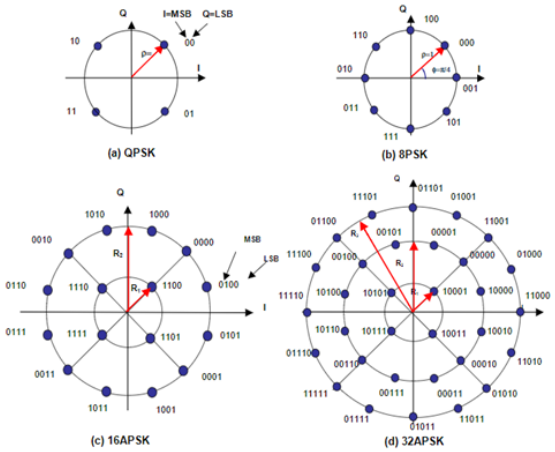


(a) Bit to symbol mapping in the four constellations used in the DVB-S2 standard [87], [88]

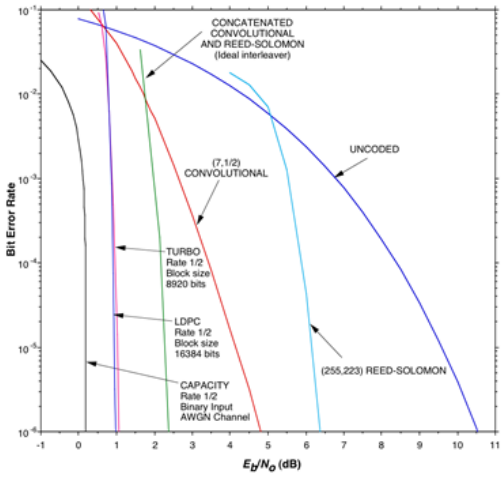


(b) Required bit-energy-to-noise ratio $E_b/N_0$ to achieve a bit error rate for selected error codes using binary phase-shift keying (BPSK) modulation in an additive white gaussian noise channel [89]

Figure 3.6: Symbols used in the DVB-S2 protocol (left) and theoretical performance of forward-error-correction codes (right).

At the receiver the symbols are demodulated into bits to recover the data. During transmission the received constellations however get distorted due to noise in the channel and (non-linear) effects of the transmitter and receiver. Error correction codes are added to the original stream of data to correct these errors. In general, there are two approaches to error detection and correction: backwards error correction (BEC) and FEC. In BEC, the packet is re-transmitted when it is detected to be incorrect at the receiver. This requires a bi-directional link with the satellite to request packets for retransmission. In FEC, the packet contains additional information to correct errors without the need of retransmission. This however means an overhead of bits are added to the data stream to correct the data if needed at the receiver. This reduces the effective data rate through the link but gives a more robust communication.

Error correction codes can be compared by their bit-error rate (BER) curves as shown in fig. 3.6b. These curves show the required bit-energy-to-noise ratio ($E_b/N_0$) to achieve a certain BER performance with a specified modulation scheme and channel. For the mathematical background on bit error probability calculations the reader is referred to chapter 7 of the book Digital and Analog Communication Systems by L. Couch [27]. The performance of an error correction code can be evaluated by its coding gain; the reduction in required bit-energy-to-noise ratio for a given BER with respect to uncoded data shown in dark blue line in fig. 3.6b. There also exists a upper limit to coding performance defined by the channel capacity theorem. This theorem shows that the capacity of a channel (in bits per symbol) reduces for an increase in BER as shown in [90]. By using this BER dependent capacity in the Shannon-Hartley theorem limiting curve can be calculated shown in black in fig. 3.6b.

The modulation and coding (MODCOD) used during transmission is determined by a protocol (or a standard that defines which protocol to use). The performance of a MODCOD can be expressed in several ways. Below are three primary performance indicators:

**Spectral efficiency** the number of bits per second that can be send per Hz of bandwidth [bits/s/Hz] for the given modulation scheme.

**Signal-to-noise threshold** the signal-to-noise ratio that is needed to achieve a certain BER for the given modulation scheme.

**Implementation costs** the computational power needed to modulate and demodulate the signals, but also the power required to for example amplify the signal without too much distortion.

There are three families of standards for high-rate modulation and coding schemes for satellite systems; those specified by the Consultative Committee for Space Data Systems (CCSDS), those

specified by the European Commission for Space Standardization (ECSS) and those specified by the European Telecommunications Standards Institute (ETSI). Table 3.3, table 3.4 and table 3.5 show the applicable standards for these three families of communication protocols.

Table 3.3: CCSDS databooks and standards related to (high-rate) communications

| Standard | Description | Ref |
|---|---|---|
| CCSDS 131.2-B-1 | Flexible Advanced Coding and Modulation scheme for High Rate Telemetry Applications | [91] |
| CCSDS 130.11-G-1 | SCCC–Summary of Definition and Performance | [92] |
| CCSDS 131.3-B-1 | CCSDS Space Link Protocols over ETSI DVB-S2 Standard | [93] |
| CCSDS 130.12-G-1 | CCSDS Protocols over DVB-S2–Summary of Definition, Implementation, and Performance. | [94] |
| CCSDS 401.0-B-30 | Radio Frequency and Modulation Systems–Part 1: Earth Stations and Spacecraft | [95] |
| CCSDS 413.0-G-3 | Bandwidth-Efficient Modulations–Summary of Definition, Implementation, and Performance | [96] |
| CCSDS 131.0-B-3 | TM Synchronization and Channel Coding | [97] |
| CCSDS 130.1-G-2 | TM Synchronization and Channel Coding–Summary of Concept and Rationale. | [89] |

Table 3.4: ECSS standards related to (low-rate) communications

| Standard | Description | Ref |
|---|---|---|
| ECSS-E-ST-50-01C | Space data links – Telemetry synchronization and channel coding (31 July 2008) | [98] |
| ECSS-E-ST-50-05C | Rev.2 Radio frequency and modulation (4 October 2011) | [99] |
| ECSS-E-ST-50C | Communications (31 July 2008) | [100] |
| ECSS-E-HB-50A | Communications guidelines (18 November 2008) | [101] |

Table 3.5: ETSI standards on DVB-S2 and DVB-S2X

| Standard | Description | Ref |
|---|---|---|
| ETSI EN 302 307-1 V1.4.1 (2014-11) | Digital Video Broadcasting (DVB); Second generation framing structure, channel coding and modulation systems for Broadcasting, Interactive Services, News Gathering and other broadband satellite applications; Part 1: DVB-S2 | [102] |
| ETSI TR 102 376-1 V1.2.1 (2015-11) | Digital Video Broadcasting (DVB); Implementation guidelines for the second generation system for Broadcasting, Interactive Services, News Gathering and other broadband satellite applications; Part 1: DVB-S2 | [87] |
| DVB BlueBook A171-1 | Digital Video Broadcasting (DVB); Implementation guidelines for the second generation system for Broadcasting, Interactive Services, News Gathering and other broadband satellite applications; Part I (DVB-S2) | [88] |
| ETSI EN 302 307-2 V1.2.1 (2020-05) | Digital Video Broadcasting (DVB); Second generation framing structure, channel coding and modulation systems for Broadcasting, Interactive Services, News Gathering and other broadband satellite applications; Part 2: DVB-S2 Extensions (DVB-S2X) | [103] |
| ETSI TR 102 376-2 V1.1.1 (2015-11) | Digital Video Broadcasting (DVB); Implementation guidelines for the second generation system for Broadcasting, Interactive Services, News Gathering and other broadband satellite applications; Part 2: S2 Extensions (DVB-S2X) | [104] |
| DVB BlueBook A171-2 | Digital Video Broadcasting (DVB); Implementation guidelines for the second generation system for Broadcasting, Interactive Services, News Gathering and other broadband satellite applications; Part 2: S2 Extensions (DVB-S2X) | [105] |

From a communications system level perspective the spectral efficiency and signal to noise threshold are often used to capture the performance of each of different MODCODs in a standard. Figure 3.7 shows these performance parameters plotted against each other. In general, a higher spectral efficiency requires more symbols in the modulation scheme and a higher signal to noise ratio to close the link. This information, available directly from the standard, is implemented in the optimization models of this thesis (see chapter 8). For this work only the DVB-S2 standard is considered as the current state-of-the-art satellites, Dove and Corvus, use this protocol to achieve high-rate data downlink. Using a widely implemented standard helps finding COTS transmitter and receiver hardware making the choice of DVB-S2 also a cost-effective solution for payload downlinks. It is therefore also supported in the CCSDS protocols [94].

A future study may compare the different high-rate protocols using the models developed in this work. In particular, the use of the computationally low demanding SCCC encoding with overlapping MODCODs in the CCSDS [92] [91] would be interesting for this use case. Similarly, the DVB-S2X standard would be of interest as it adds 'very low' signal-to-noise ratio (VL-SNR) modulation and coding schemes, targetted for moving vehicles like trains and cars, which could be used instead to create low-rate (but high accumulated throughput) links to MEO or GEO data-relay satellites.

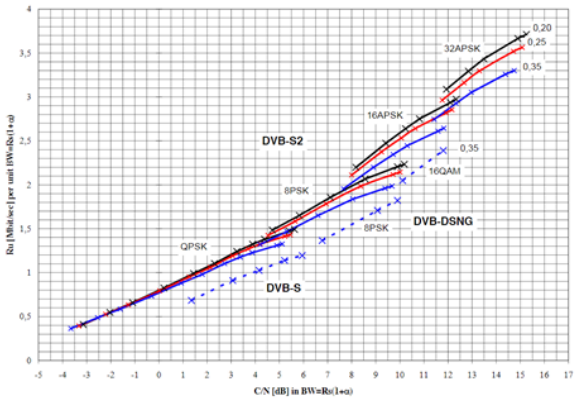


(a) Spectral efficiency against carrier to noise ratio for DVB-S2 [102]

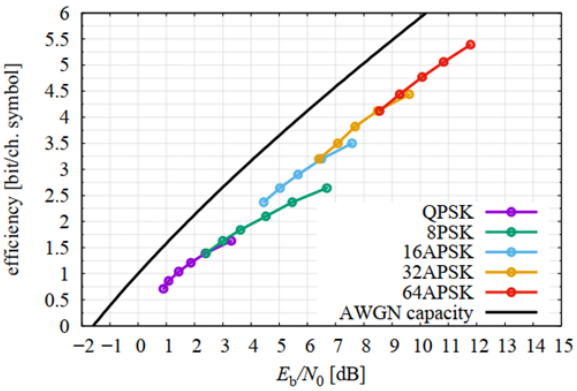


(b) Spectral efficiency against bit-energy-to-noise ratio $E_b/N_0$ in an AWGN channel for the SCCC scheme recommended in 131.2-B-1 from [92] showing near Shannon limit operation and a wide range of spectral efficiencies.

Figure 3.7: Spectral efficiency against bit-energy-to-noise ratio for the DVB-S2 (left) and CCSDS (right). Both standard have overlapping formats for each modulation scheme allowing for smooth transitions in VCM or ACM operation.

### 3.2.2. Transmitters

The RF transmitter in a downlink communication system typically consist of a modulator, a up-converter (mixer) and a power amplifier. Important performance specifications of transmitters include:

**Data rate** the (maximum) bits per second the transmitter can transmit.

**RF output power** the (maximum) radio-frequency signal power the transmitter can generate

**Efficiency** the amount of power consumed per bit or per unit RF power

**Size, weight and cost** the size, weight and cost of the transmitter

This section presents an overview of the performance of current state-of-the-art in small satellite transmitters. The goal is to find a trend in the key performance specifications such as data rate, RF power and efficiency. The State of the Art Small Spacecraft Technology reports of NASA [78], [106] contains excellent chapters on Communications in VHF, UHF, L, S, X, Ku/Ka and optical bands. This part of the review will present an up to date overview on RF transmitters operating at X-band and above.

Figure 3.8 shows an illustration of the bands nano-satellites currently use (and proposed missions) from nanosats.eu [38]. What can be seen is that VHF and UHF remain popular, this is because most satellites use omnidirectional antennas in this band for robust TT&C (i.e. in case of tumbling during early operations). S-band and X-band are popular for high data rate down link communications and only a few satellites are using frequencies above X-band. Of the 66 satellites using Ka-band approximately 30 are Corvus/Landmapper (proposals) from the company Astro-Digital [5]. This shows that Ku-band and above is a novel area for small satellite communications.

Table 3.6 shows a selection of the state-of-the-art in small satellite transmitters in X-band and above. Transmitters on X-band for small satellites and CubSats/nanosats are now widely available with over a dozen companies developing COTS transmitters in this band. The maturity of transmitters in this band can be seen from two aspects. On one hand there exist transmitters that have undergone strong miniaturization such as the designs of the IQ Wireless, AAC Clyde and COMSpace transmitters [82], [83], [107], [108]. These transmitters offer a data rate of several Mbps in a small form factor of around 0.1U. On the other hand, in the same band there also exists the highest performing transmitters (in maximum data rate) at this moment including the Planet HDS2 achieving more than 1 Gbps [2] and the Hodoyoshi 4 transmitter offering 0.5 Gbps [109]. Finally, this band also includes the exotic example of the IRIS V2.1 Deep Space Transponder that flew on the MarCO satellites [110] showing that transmitters in this band exists in a small form factor, are high performing and can be designed to operate in the harsh environment of deep space.

One band higher in the Ku/Ka-band developments are speeding up. There is more bandwidth available in this band however COTS components are less available [111]. This results in only four

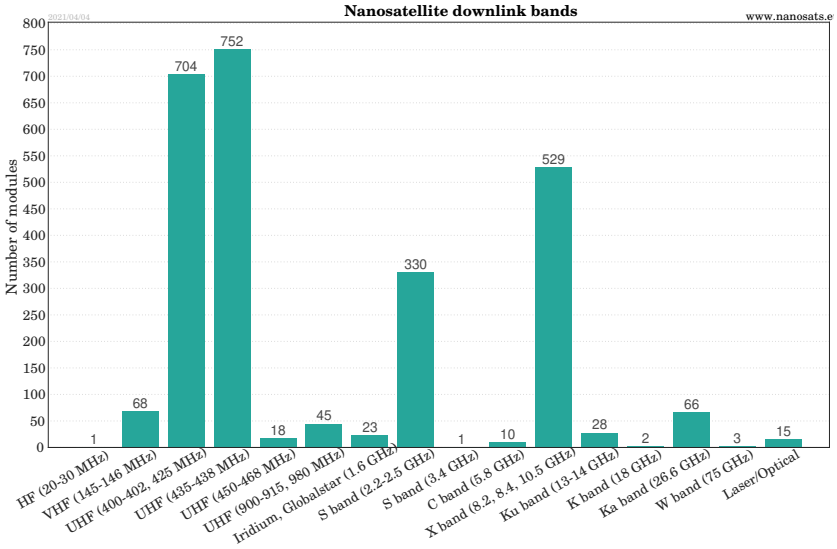


Figure 3.8: Downlink bands used by nano-satellites from Nanosats.eu [38]

transmitters in this band to be included in Table 9. The highest performing in this band is the Ka-Band transmitter from Astro Digital that is flying on the Corvus/Landmapper spacecraft [1], [84], [111] achieving 320 Mbps. This transmitter uses an integrated upconverter, amplifier and antenna from SAGE Millimeter [112] with an integrated DVB-S2 modulator all within 1U of space. The only other transmitter in this band that can be considered of a TRL greater than 6 is the SWIFT-KTX from Tethers Unlimited Inc. [113]. The last two transmitters in this band are the New Space Systems SDR Ka-band / S-band transceiver [114] and the ISARA tone-generator [115]. Only little information is available of the New Space Systems transceiver apart from a mention in NASA's report and a limited datasheet. The ISARA tone-generator is part of a recent in-orbit reflect array demonstrator. It is included in this overview for its RF efficiency metric and to show the ongoing developments in this frequency band.

Table 3.6: Selection of state-of-the-art small satellite transmitters in X-band and Ka-band

| Description | Operating band / (Frequency) | Bandwidth [MHz] | Data rate [Mbps] | RF power [W] | DC power [W] | Size [U] | Mass [kg] | Highest MOD | Ref. |
|---|---|---|---|---|---|---|---|---|---|
| Ka-band transmitter Gen. 3 Astro Digital | Ka-band (26.8 GHz) | 86.4 | 320.6 | 0.6 | 20 | 1.00 | 1.00 | 32-APSK | [1], [111] [84], [112] |
| SWIFT-KTX Thethers Unlimited Inc. | K-Band/Ka-Band (18 – 23 GHz or 23 – 28 GHz) | 500 | 100 | 2 | 25 | 0.33 | 0.50 | 16-APSK | [113] |
| ISARA | Ka-band (26 GHz) | n.a. | n.a. | 0.5 | 10 | 0.50 | 0.19 | n.a. | [115] |
| New Space Systems SDR Transciever | Ka-band (26.5 - 40 GHz) | ? | 10 | 2 | 30 | 0.5 | 0.6 | QPSK | [114] |
| Planet HDS2 | X-band (8025 – 8400 MHz) | 300 | 1674 | 2 | 50 | 0.25 | ? | 32-APSK | [2] |
| Hodoyoshi 4 transmitter | X-band (8160 MHz) | 125 | 538 | 2 | 22 | 1.05 | 1.30 | 64-APSK | [109] |
| IRIS V2.1 Deep Space Transponder | X-band (8400 – 8500 MHz) | 8.44 | 6.25 | 3.8 | 33.7 | 0.56 | 1.20 | BPSK | [110] |
| XLINK IQ Wireless GmbH | X-band (8025 – 8500 MHz) | 475 | 25 | 0.5 | 15 | 0.16 | 0.20 | 8-PSK | [82] |
| PULSAR-XTX AAC Clyde | X-band (8025 – 8375 MHz) | 300 | 50 | 2 | 15 | 0.10 | 0.13 | QPSK | [107] |
| NanoCom XT8250 GOMSpace | X-band (8000 – 8500 MHz) | 500 | 225 | 3 | 28.5 | 0.10 | 0.32 | 32-APSK | [83], [108] |

n.a. - not applicable
? - unknown

Table 3.7 shows an overview of four performance indicators of the selected state-of-the-art transmitters. The four performance indicators are:

**Spectral efficiency** the number of bits per second the transmitter is able to transmit per Hertz of bandwidth. This number is calculated by dividing the maximum data rate by the used bandwidth. Increasing spectral efficiency requires a higher order modulation code, higher spectral efficiency is desired because (licenced) bandwidth is expensive.

**Power efficiency** the maximum RF power the transmitter can generate per watt of DC input power. A higher energy efficiency means less power is required in the power budget for the transmitter to close the link.

**Link efficiency** the amount of energy it takes to transmit one bit (from space to Earth). For this number the ratio of data rate and DC power is taken instead of the RF power as the performance of the transmitter is to be evaluated on a (satellite) system level and not just on a RF link level [116]. A higher data rate per power means less power is required to transmit a bit. It should be noted that this number is also depended on the performance of the ground station.

**Power density** the maximum RF power the transmitter can generate inside the volume it uses. As RF power generation (in the power amplifier) is an in-efficient process heat is generated inside the transmitter which requires proper thermal design. If a large power can be generated in a small volume (high power density) this indicates a higher performing design.

Table 3.7: Performance indicators of selected small satellite transmitters in X-band and Ka-band

| Description | Operating band / (Frequency) | Spectral efficiency [bit/s/Hz] | Power efficiency [%] | Link efficiency [Mbit/J] | Power density [W/U] | Ref. |
|---|---|---|---|---|---|---|
| Ka-band transmitter Gen. 3 Astro Digital | Ka-band (26.8 GHz) | 3.71 | 3.00 | 16.03 | 0.60 | [1], [111] [84], [112] |
| SWIFT-KTX Thethers Unlimited Inc. | K-Band/Ka-Band (18 – 23 GHz or 23 – 28 GHz) | 0.20 | 8.00 | 4.00 | 6.06 | [113] |
| ISARA | Ka-band (26 GHz) | n.a. | 5.00 | n.a. | 1.00 | [115] |
| New Space Systems SDR Transciever | Ka-band (26.5 - 40 GHz) | ? | 6.67 | 0.33 | 4.00 | [114] |
| Planet HDS2 | X-band (8025 – 8400 MHz) | 5.58 | 4.00 | 33.48 | 8.00 | [2] |
| Hodoyoshi 4 transmitter | X-band (8160 MHz) | 4.30 | 9.09 | 24.45 | 1.90 | [109] |
| IRIS V2.1 Deep Space Transponder | X-band (8400 – 8500 MHz) | 0.74 | 11.28 | 0.19 | 6.79 | [110] |
| XLINK IQ Wireless GmbH | X-band (8025 – 8500 MHz) | 0.05 | 3.33 | 1.67 | 3.13 | [82] |
| PULSAR-XTX AAC Clyde | X-band (8025 – 8375 MHz) | 0.17 | 13.33 | 3.33 | 20.00 | [107] |
| NanoCom XT8250 GOMSpace | X-band (8000 – 8500 MHz) | 0.45 | 10.53 | 7.89 | 30.00 | [83], [108] |

n.a. - not applicable
? - unknown

The differences between the state-of-the-art in X-band and Ku/Ka-band are well captured in Table 10. At this moment the highest performing X-band transmitters perform better than the Ku/Ka-band in terms of spectral efficiency. The Planet HDS2 uses separate data streams on left- and righthand circular polarizations [2] effectively doubling the spectral efficiency. The Hodoyoshi 4 instead uses a higher order modulation scheme (64-APSK) to achieve the higher spectral efficiency [109]. There is a notable difference in the energy efficiency of the two bands. For X-band the efficiency lies around 10%, with only the Planet HDS2 and XLINK having below 5% efficiency. For the HDS2 a large amount of power is used for the six DVB-S2 modulators in the transmitter, lowering the overall efficiency of this transmitter. For Ka-band the efficiency number drops to around 5%. This reduction in efficiency can also be seen in the power density specification where small miniaturized X-band transmitters score significantly higher than the Ka-band transmitters.

The impact of the decrease in power efficiency at Ka-band is a key point of interest for the proposed LEO-to-NGSO data-relay concept, especially considering the LEO-to-LEO variant. Because the NGSO constellations discussed in chapter 3 use Ku/Ka-band frequencies the efficiency will be lower than what is currently achieved on X-band. This means that more power will be used on the satellite for the downlink communication system. In addition, the duty cycle for transmission in the data-relay architecture will be higher than in the direct link architecture. As passes in the data-relay architecture occur more frequent throughout the orbit the downlink transmitter will be active more often. It might therefore be the case that there is not enough time in between transmissions for the solar cells to keep the batteries charged throughout the orbit. In order to evaluate the proposed data-relay architecture this increase in duty cycle should therefore be considered in the power budget.

### 3.2.3. Antennas

Small satellite antennas are an active field of development as they are enabling technologies for communication, radar and sensing applications. Antennas convert electrical signals to electromagnetic waves and vice versa. They also provide gain by shaping the electromagnetic radiation in a certain direction. Publications by S. Gao et. al. [117] and Y. Rahmat-Samii et. al. [118] provide a good overview of the state-of-the-art in small satellite antennas. In this section those overviews are extended with recent developments and some criteria on which to evaluate antenna systems are highlighted. The presented material in this section is focussed on designs of medium to high gain antennas (> 15 dBi) operating at X-band or higher (above 8.0 GHz) that have had or are close to flying on a demonstrator mission (TRL 5/6).

The small satellite antennas reviewed in this section can be placed into five categories: planar antennas, horn and lens antennas, reflect array antennas, mesh reflector antennas and inflatable antennas. Figure 3.9 shows examples for these five types of antennas and indicate some of their key properties. The following subsections will explain the characteristics of each antenna type in detail.

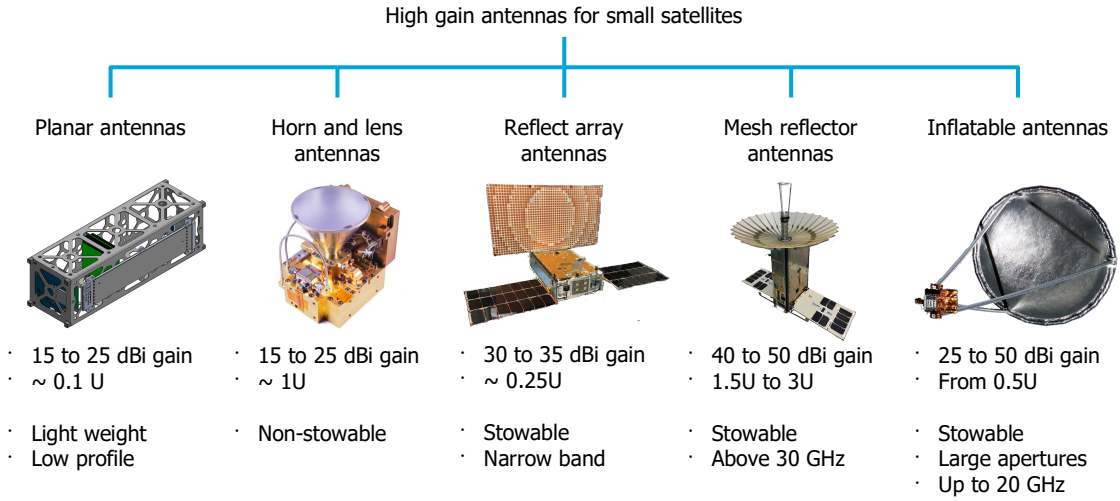


Figure 3.9: High gain antennas for small satellites can be categorized in 5 types. From left to right images show Kymeta Ka-band meta-material phased array antenna [119], Astro Digital / SAGE millimeter Ka-band horn antenna used on the Corvus satellites [1], MarCO X-band reflect array [120], Tendeg KaPDA Ka-band mesh reflector antenna on Raincube [121] and the large inflatable deployable antenna experiment [122].

#### Planar antennas

Planar antennas have radiating elements integrated into a flat panel surface, often a dielectric substrate or a metal surface. Their planar, light weight and low profile design allows these types of antennas to be integrated in unused surfaces of the small satellite. Tubbal et. al. [11] provide a great survey of planar antennas for small satellites including some performance enhancement techniques. The survey compares two sub-types of planar antennas; the microstrip patch antenna and the slot antenna. However, this category also includes some exotic types such as the bullseye antenna [123], wideband Fabry-Perot antennas [124] and grid oscillator antennas [125]. Because multiple planar antennas can

be placed on a single dielectric substrates it is affordable to create an array of radiating elements increasing the overall gain of the antenna. This is for example done in the designs of Patriotis et. al. [126] and Buttazoni et. al [127], [128] to create a high gain at K/Ka-band frequencies (>18 GHz) that take only a small area (one side of a 1U CubeSat).

### Horn and lens antennas

Horn antennas are versatile in satellite communication systems and provide a reasonable gain (15 to 25 dBi) and a wide bandwidth. A horn can be made linearly or circular polarized and can operate at millimeter wave frequencies. Horns are a popular choice for small satellite antennas, either used directly such as in the Ka-band transmitter of the Corvus spacecraft [1], [112] or as a feed antenna for a parabolic reflector. Horn antennas are also a popular choice when individual pointing is required using mechanical steering as shown in fig. 3.10a. A disadvantage of the horn antenna is the large volume it occupies. The small antenna in fig. 3.10a provides 15 dBi gain while the larger only provides 18 dBi for its significant increase in occupied space.

In lens antennas the electromagnetic waves are guided through a dielectric or metal medium. The waves are focussed in a similar way as in an optical lens. An interesting recent example of a lens antenna is the water drop lens antenna by Fonseca et. al. [129]. This low-profile antenna operates at Ka-band frequencies and can be electronically steered. The antenna has a high aperture efficiency and with its low profile this results into a high gain for a small volume.

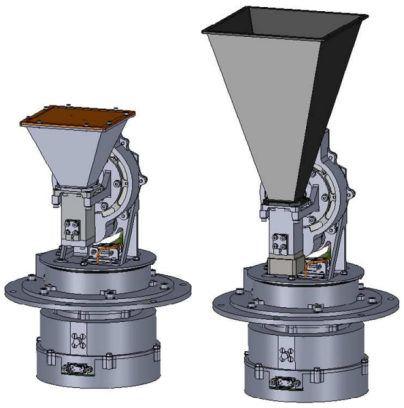

(a) First and second generation horn antenna with pointing mechanism from SSTL [130]

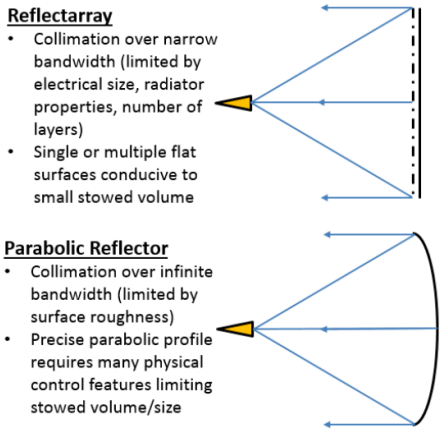


(b) Comparison between reflect array and parabolic reflector from [131]

Figure 3.10: Example of horn antennas (left) and difference between reflect-array antennas and parabolic reflectors (right)

### Reflect array antennas

Reflect array antennas use an array of passive (non-driven) elements to collimate the electromagnetic waves over a large area. Their principle of operation is similar to that of a parabolic reflector as illustrated in fig. 3.10b. The reflect array antenna has proven its strengths with the 6U MarCO satellites that are the first interplanetary CubeSats [120], [132]. Their reflect arrays were used to relay data back from the InSight mission to Earth on X-band. The planar design of reflect arrays allows them to be integrated into the structure of the satellite and possibly deployed, folding out similar to solar arrays. The ISARA mission (a follow up of the MarCO satellites) includes a Ka-band reflect array integrated into the back of the solar array of the 3U satellite [133], [134]. Just as planar antennas, a reflect array can be made from dielectric substrate/PCB materials and are therefore inexpensive antennas. A disadvantage of the reflect array antenna is its narrow band of operation [131].

### Mesh reflector and inflatable antennas

A high gain can be achieved using mesh reflector or inflatable antennas. Both types use a parabolic reflector to increase the aperture and gain of the antenna. With this increased aperture gains up to 50 dBi can be achieved such as with the KaTENna 3-meter aperture antenna [135]. Creating large structures in space is challenging as launching a solid 3-meter diameter structure on its own is impractical and expensive. Therefore, mesh reflector and inflatable antennas are deployable systems that fold

(or inflate) into a large reflecting structure. A lot of research is done on inflatable antennas including 1997 space shuttle demo missions by NASA [122] and more recent research on a CubeSat concept by Babuscia et. al. [136]–[140]. Inflatable antennas allow for a large antenna gain with only a small stored volume, however they suffer from two major drawbacks. The first one is that inflatable antennas require pressurized gas to inflate and should remain fully inflated in order to stay functional. Therefore, leaks caused by the deployment or by damage in-orbit are detrimental to this concept. The second drawback is that it is difficult to create inflatable antennas at high frequencies because of the low surface roughness requirement. A 1998 paper by Cassapakis et. al. [141] shows that the surface roughness of the inflatable structure becomes limiting above 20 GHz, making this concept less appropriate for Ka-band communications. Mesh reflectors do not have this drawback because of their consistent surface allowing for Ka-band operation. This was demonstrated by the antenna of RainCube [51] has a tested 43 dBi gain. The company behind this antenna design TenDeG, specialized in space deployables, is working on a 3m version for this antenna that could provide up to 50 dBi gain. The disadvantage of mesh reflectors is the large stowage volume required, making them only suitable for the larger CubeSats. Recent developments show an interesting combination of the reflect array antenna and deployable mesh antennas. A paper by P. K. Kelly [131] proposes a deployable reflect array antenna on a membrane similar to that of the KaTENna antenna. Allowing for a large aperture reflect array offering higher performance.

### Steering mechanisms

In general, there are three approaches to steering the antenna: spacecraft body pointing, mechanical steering and electrical steering. In body pointing, the whole spacecraft is steered to point the antenna to the target using the attitude control system of the spacecraft. This approach to pointing is of course applicable to any type of antenna, however simultaneous pointing of the antenna and the payload is not possible, which ma reduce the mission return, In addition, the steering speed and accuracy is limited by that of the attitude control system. To independently steer the antenna from the spacecraft a dedicated antenna steering mechanism is needed. For in mechanical steering mechanisms this is done using electric motors such as in the antenna pointing mechanisms of SSTL [130] shown in fig. 3.10a. However, these types of steering mechanisms are heavy, consume power and contain mechanical parts that could wear out over time. Alternatively, some antenna types are suitable for electronic steering, primarily phased array antennas but also more exotic types such as Kymeta's metamaterial antennas or the water drop lens antenna [142][129]. The elements of planar antennas arrays (phased arrays) can be driven with a relative phase shift allowing for the antenna beam to be steered without mechanical components [143]. This type of steering comes at the cost of decreased gain for higher steering angles, also called scanning losses or cosine losses. For any type of steering mechanism, the steering range, steering speed and steering accuracy are important and should be considered when calculating the throughput of the system.

### State-of-the-art overview

Table 3.8 shows an overview of the state-of-the-art in small satellite antennas most of which mentioned in the previous sections. Three specifications are included in this table: the gain of the antenna in dBi, the volume in CubeSat standardized units (U) of 10x10x10 cm and the mass of the antenna in kilograms. As antenna gain is one of the key performance indicators it is almost always mentioned in publications. However, volume and mass are often not mentioned unless the antenna is also commercially available, and a datasheet is published. Where possible the (stored) volume was calculated from specified dimensions. Reported mass numbers are only those that are mentioned in publications, no attempts were made to estimate masses. In addition to these three specifications, the deployability and steerability for each antenna is mentioned.

The antennas presented in this section are of different types, operate at different bands and some include steering mechanisms which add up mass and volume and a particular shape might suit one spacecraft better than the other. However, some trends can be observed when comparing gain against volume and gain against mass as is done in fig. 3.11. The gain against volume shows approximately how each type of antenna could perform. There is a linear trend where more volume results into more gain but because of the limited data and the non-equal comparison in frequencies this trend is somewhat weak. The reflect area and mesh reflector do well on this performance indicator. Because of the limited mass numbers available no comparison is drawn between the different types on the gain versus volume performance indicator.

Table 3.8: Overview of state-of-the-art small satellite antennas

| Description / Mission | Operating band / (Frequency) | Type | Gain [dBi] | Volume [U] | Mass [kg] | Deployable | Steerable | State | Ref |
|---|---|---|---|---|---|---|---|---|---|
| Planar active pashed array / GaNSAT | K-band (175 - 20.5 GHz) | Planar | 16 | ? | ? | No | Electronically ±70° | In-dev. | [117] [124] [144] [145] |
| Reconfigurable Transmit / Receive Antenna Array | K/Ka-band (20 - 32 GHz) | Planar (dual-band) | 15 | ? | ? | No | No | In-dev. | [126] |
| Reconfigurable Phased/ Antenna | Ka-band (35 - 40 GHz) | Planar (dual-band) | 24 | 0.01 | ? | No | No | In-dev. | [127] [128] |
| Bulls eye antenna | V-band (60-GHz) | Planar (bullseye) | 19.1 | 0.03 | ? | No | No | In-dev. | [123] |
| Kymeta Meta-Material CubeSat Antenna | Ka-band (27.0 GHz) | Planar (meta-material) | 24 | 0.15 | ? | No | Electronically ±45 | In-dev. | [119] |
| Boeing Tile Array | Ka-band (25.25 - 27.5 GHz) | Planar (phased array) | 28 | 3.91 | 1.8 | No | Electronically ±70° | In-dev. | [119] |
| SAGE millimeter / Astro-Digital Corvus | Ka-band (26.3 - 27.2 GHz) | Horn (lens corrected) | 24 | 0.48 | 0.17 | No | No | In-orbit | [1] [112] |
| Water drop lens | Ka-band (27.5 - 30.0 GHz) | Lens | 23.87 | 0.91 | ? | No | Electronically ±70° | In-dev. | [142] [129] |
| SSTL X-APM | X-band (8.0 - 8.5 GHz) | Horn | 15 | ? | 2.7 | No | Mechanically ±270° Az. ±110° El. | In-orbit | [130] |
| ISARA | Ka-band (26.0 GHz) | Reflect array | 33.5 | 0.72 | ? | Yes | No | In-orbit | [133] [134] |
| MarCO | X-band (8.425 GHz) | Reflect array | 29.2 | 0.24 | 0.93 | Yes | No | In-orbit | [120] [132] |
| DaHGR | X-band (10 GHz) | Reflect array | 34 | 1.50 | ? | Yes | No | In-dev. | [131] |
| KaPDA / RainCube | Ka-band (35.75 GHz) | Mesh reflector (Cassegrain) | 42.6 | 1.60 | 1.4 | Yes | No | In-orbit | [51] [146] |
| KaTENna | Ka-band (36.0 GHz) | Mesh reflector (offset-fde) | 49.2 | 3.00 | 2.5 | Yes | No | In-dev. | [147] |
| JPL-ASU | X-band (8.4 GHz) | Inflatable (dish reflector) | 24.1 | 0.50 | ? | Yes | No | In-dev. | [136][137] [138][139] [140] |
| Large Inflatable Deployable Antenna | X-band (11.1 GHz) | Inflatable (dish reflector) | 47.7 | ? | ? | Yes | No | Demo | [141] |

In-dev. - In development
Planned - Launch planned
Demo - Demonstrator flown
In-orbit - Antenna operating in orbit

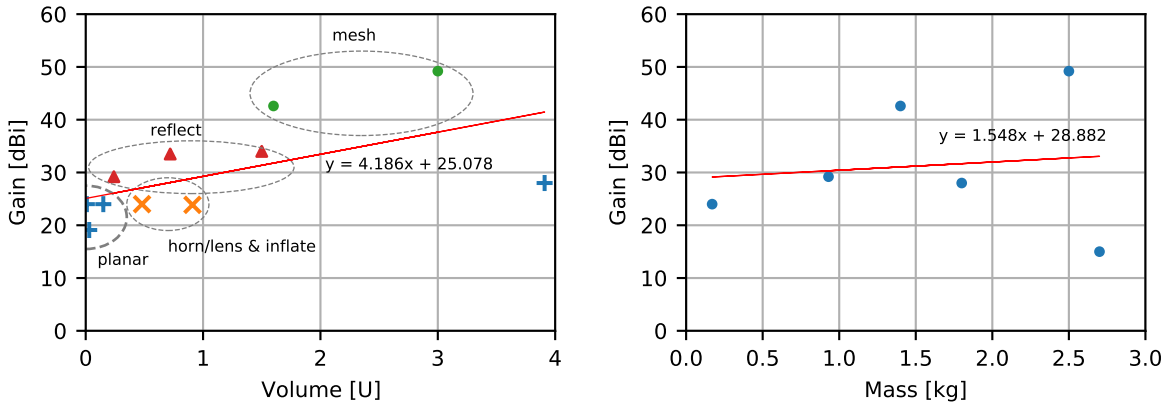


Figure 3.11: Comparison in antenna gain against volume and antenna gain against mass for state-of-the-art small satellite antennas.

### 3.2.4. Intersatellite links

Intersatellite link (ISL) have been used to relay data from other satellites in the past, both NASA and ESA have dedicated high data rate (optical) relay systems called Tracking and Data Relay Satellite System (TDRSS) and European Data Relay Satellite System (EDRS) in GEO that can be used to relay data from satellites, weather balloons or planes [148], [149]. ISLs have also been used to create crosslinks between satellites in constellations such as in the constellation of Iridium. In addition, ISLs have been used on interplanetary missions such as the Rosetta-Philae satellite & lander link during the mission to comet 67P/Churyumov–Gerasimenko [150] and recently intersatellite links have been used to relay data from the Mars InSight lander through the MarCo nano-satellites [132].

Although dedicated systems such as TDRSS and EDRS exists, recent proposals show interest in using existing GEO commercial fixed satellites services as a data-relay for LEO satellites, i.e. proposed by Kopp in [151]. This architecture is currently being explored for micro-satellite missions. For example the VELOX II satellite has demonstrated a data-relay with the commercial Inmarsat GEO constellation [15] and a consortium of European companies including NanoAvionics is planning to use LEO-to-GEO data-relays for a global Internet of Things constellation [17], [152]. Several nano-satellite (<10 kg) missions have been proposed or launched to experiment with inter-satellite links to the existing commercial LEO constellations of Iridium and Globalstar [153]. A short survey by Yoon et. al. shows several other small satellites demonstrating inter-satellite links [152].

Table 3.9 shows a selection of satellite technology and missions that have demonstrated or proposed the use of intersatellite links. The table shows that intersatellite links have found their use in several domains. nano-satellites such as TSAT, GEARRS-1&2 and SHARC are starting to use ISLs for low rate TT&C with existing LEO constellations and demonstrators for crosslink ISLs achieving Mbps rates. Larger (6U) nano-satellites such as the M6P of NanoAvionics and Velox-II satellite are exploring the option of a LEO-to-GEO intersatellite link although not achieving significantly higher rates. Rates of multiple Mbps can be found on the larger satellite systems such as TDRSS and EDRS or the cross-links in the Iridium Next constellation.

Table 3.9: Selection of satellite technology using or demonstrating intersatellite links

| Mission / Hardware | Relay | Distance | Band | Data rate | Status | Ref |
|---|---|---|---|---|---|---|
| TSAT, GEARRS1 *STX-2/3* | Globalstar | LEO-LEO / ~1000 km | L-band | 72 bps | Success | [154] |
| GEARRS2, SHARC *EyeStar-D2* | Globalstar | LEO-LEO / ~1000 km | L-band / S-band | 7 kbps | Success | [154]–[156] |
| TechEdSat-1,2,3p | Iridium/Globalstar | LEO-LEO / ~1000 km | L-band | 9.6 kbps | Proposed | [157] |
| CommCube 1 | GlobalStar | LEO-LEO / ~1000 km | L-band / S-band | 9.6 kbps | Proposed | [140] |
| CanX-4&5 | *ISL-demo* | 5 km | S-band | 10 kbps | Success | [152] |
| Diamond | *ISL-demo* | ? | S-band | 2 Mbps | Success | [152] |
| S-NET | *ISL-demo* | 400 km | S-band | 100 kbps | Success | [152] |
| NanoAvionics GoIT | ? | LEO-GEO / ~36000 km | Ku/Ka-band | ? | Proposed | [17], [152] |
| VELOX-II | Inmarsat | LEO-GEO / ~36000 km | L-band | 200 kbps | Success | [15] |
| LISA | ARTEMIS | LEO-GEO / ~36000 km | S-band / Ka-band | ? | Proposed | [158] |
| | TDRS | LEO-GEO / ~36000 km | S-band<br>S-band<br>Ku-band<br>Ka-band | 10 kbps (multiple access)<br>6 Mbps (single access)<br>300 Mbps (single access)<br>650 Mbps (single access) | Operational | [148] |
| | EDRS | LEO-GEO / ~36000 km | Ka-band<br>Optical | 300 Mbps<br>1.8 Gbps | Operational | [149], [159] |
| *Argo Modem* | EDRS | LEO-GEO / ~36000 km | Ka-band | 300 Mbps | ? | [160], [161] |
| Iridum Next | *crosslink* | LEO-LEO / 4500 km | Ka-band | 12.5 Mbps | Operational | [152] |
| Insight lander | MarCO | ~3500 km | UHF | 8 kbps | Success | [132] |
| Philae | Rosetta | ~200 km | S-Band | 16 kbps | Success | [150] |

The use of ISLs to for data-relay purposes or cross-links is actively explored in research and academia. However, LEO-to-LEO data-relay links have only been considered with previously existing LEO constellations such as Iridium and Globalstar that to not offer high enough data rates to be

competitive with the throughput of state-of-the-art payload downlink transmitters. The proposed LEO-to-LEO or LEO-to-MEO data-relays with broadband communication constellations would however have the potential to exceed the throughput that is currently possible on small satellite platforms using direct links. A throughput analysis for the LEO-to-NGSO data-relay is needed to evaluate the concept and its competitiveness with direct link systems.

# 4

# NGSO (mega-)constellations

This chapter will present an overview of current proposals for NGSO (mega-)constellations, including LEO (mega-)constellations and MEO constellations. Recently, the interest in non-geostationary orbit (NGSO) constellations to provide global broadband connectivity from space has increased. Satellite constellations in low Earth orbit (LEO) or medium Earth orbit (MEO) have less latency than geostationary Earth orbit (GEO) satellites and the decrease in distance allows for lower power communication systems on the satellite and the ground. However, the satellites see a smaller part of the surface of the Earth than a satellite in GEO and therefore more satellites and more ground stations (or crosslinks between the satellites) are needed to provide global coverage. Decreased launch costs and improved small satellite technologies allow for novel concepts including a large 'mega-constellations' of over 1000 satellites, millimeter wave communications and laser crosslinks. The markets for these NGSO constellations are rural and developing areas that are currently underserved by terrestrial communication networks. However, several challenges are pointed out by Su [38] for these constellations including integration with terrestrial infrastructure, interference with existing systems, dynamic routing and resource management.

NGSO constellations are not a new concept and there have been several companies since the late 1990 that tried to commercialize LEO constellations for broadband connectivity as Iridium and Teledesic. The recent developments however show new light for NGSO constellations with several companies such as SpaceX, OneWeb, Telesat and O3b having launched their first satellites. This chapter will take a technical look at the proposed architectures and the potential for small satellites to use these constellations for relaying their payload data.

The use of LEO mega-constellations as a data relay for small satellites was first suggested by Karunanithi [4]. In this chapter a broader scope is taken and NGSO constellations in MEO are also considered. For a first order analysis of the proposed LEO-to-NGSO data relay the following specifications of the constellations are of interest:

- Orbital parameters of the constellation including number of satellites, number of planes, inclinations and altitudes.
- Operation of the user beams of the satellites, such as operational field-of-view (FoV), number of beams and steerability of the beams.
- Frequency and protocols used for the user communication channels.

Although the companies like to keep specifics of their constellations private, they must provide some specifications in order to operate satellite systems in the United States. The companies therefore must file an application for their constellations at the FCC that administrates frequency coordination between all spectrum users in the United States. These filings provide good insights of the proposals of the companies; however they are known to contain optimistic numbers on communication system performance. The following sections will separately discuss LEO and MEO constellations on these aspects. Then a general overview is given and finally a short discussion is provided on research for multi-layered satellite networks.

## 4.1. LEO (mega-)constellations

The technical challenges of LEO constellations and novel proposals by companies such as SpaceX and Amazon have sparked the interest of academics. A 2019 paper by Del Portillo [3] compared specifications and throughput of the industries three frontrunners in LEO satellite mega-constellations, SpaceX, OneWeb and Telesat, and indicated the importance of inter-satellite links within the satellite network to achieve high throughput. Since then OneWeb has gone bankrupt after launching its first batch of satellites [162] and SpaceX has made several changes to its constellation, eventually lowering all satellites to 500 km [163], making a LEO-to-LEO data-relay challenging. The following sections will shortly discuss the proposals of companies planning LEO (mega-)constellations.

### 4.1.1. Telesat

In November 2016 Telesat Canada filed its first application for a LEO constellation of 117 satellites operating in Ku/Ka-band [164]. In March 2017 Telesat has requested approval for a separate LEO constellation operating in V-band [165]. In May 2020 Telesat requested to modify the original proposal of 117 satellites in two phases to a total of 1671 satellites [166]. This latest constellation consists of two sub-constellations, one of polar orbits in 27 planes inclined at 98.98° with each 13 satellites per plane and one of inclined orbits in 40 planes inclined at 50.88° with 33 satellites per plane. The polar sub-constellation will be at an altitude of 1015 km altitude while the inclined sub-constellation will be at 1325 km altitude. The configuration of the constellation is shown in fig. 4.1. According to Telesats

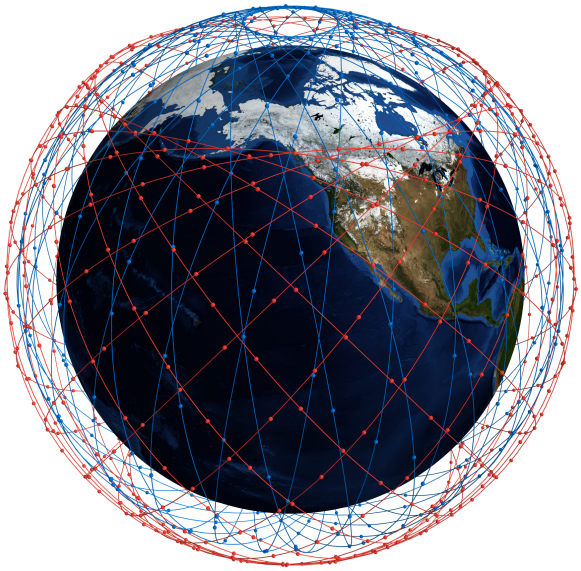

Figure 4.1: Telesat LEO mega-constellation of 1671 satellites as described in [166].

original application, the satellites will serve users that can see the satellite down to an elevation angle of 10° [164]. This gives an operating FoV on each satellite around ±55°. Users will initiate communication with the satellite through the satellites fixed wide-area beam. After the initiation, the satellite will provide the communication with the user with its shapeable and steerable user-beams of which there are at least 24 available on each satellite [166].

The user uplink band is 17.8 – 20.2 GHz (Ka-band) with a theoretical maximum bandwidth of 500 MHz. The user downlink band is 27.5 – 30 GHz with a theoretical maximum bandwidth of 850 MHz. The constellation uses optical ISLs that allows any two adjacent satellites to communicate regardless of their orbital planes. This allows a satellite to forward its data to a satellite that is in view of an internet connected ground station.

### 4.1.2. OneWeb

In April 2016 OneWeb filed its first application for a LEO constellation of 720 satellites [167]. In March 2017 OneWeb filed an application for a V-band extension to the constellation with 1280 satellites in MEO when fully deployed [168]. In March 2018 OneWeb requested to double the number of planes in the initial LEO constellation to 36 and the number of satellites per plane to 55 increasing the total amount of satellites to 1980 [169]. However in an December 2018 interview OneWeb's founder said the company is scaling back the LEO constellation to around 600 satellites [170]. OneWeb's original LEO constellation proposal of 720 satellites as defined in [167] would have 18 polar orbital planes at an altitude of 1200 km and an inclination of 87.9° with 40 satellites per plane. The configuration of the constellation is shown in fig. 4.2. Each of OneWeb's satellites will serve users that can see the

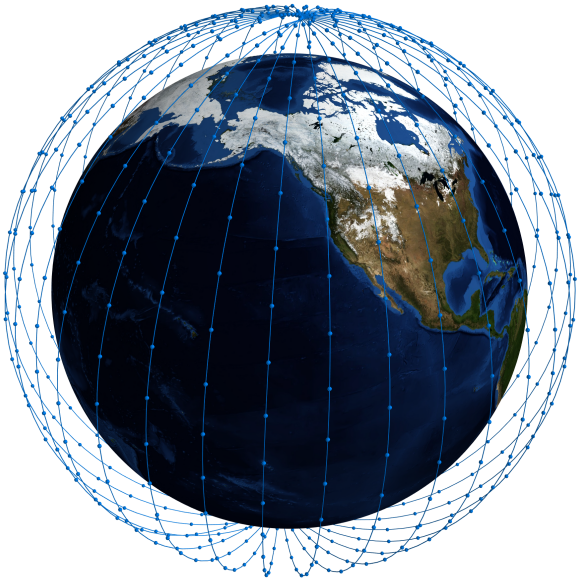

Figure 4.2: OneWeb LEO mega-constellation of 720 satellites as described in [167]

satellite down to an elevation angle of 25°. This gives the 1200 km altitude satellites an FoV of around 40°. The 16 user beams of OneWeb's satellites are however fixed and elliptical, therefore a circular FoV is a simple approximation of the actual FoV. The user uplink band is 14.0 – 14.5 GHz with a bandwidth of 125 MHz. The user downlink band is 10.7 – 12.7 GHz with a bandwidth of 250 MHz. The OneWeb satellites do not have an inter-satellite link and should therefore always be in line of sight of a ground station. OneWeb launched 74 satellites before filing for bankruptcy in February 2019. Troubles raising funding, the technical challenging aspects of a LEO constellation and finally the outbreak of the COVID-19 pandemic forced the start-up to close its doors [162] and require new investments to continue operation [171].

### 4.1.3. SpaceX Starlink

In November 2016 SpaceX filed its first application for a LEO constellation of 4425 satellites [172]. In March 2017 SpaceX has requested approval for a VLEO extension to this constellation with an additional 7518 satellites [173]. This hybrid constellation would consist of three shells in VLEO between 335.9 km and 345.6 km altitude, and five shells in LEO between 1100 km and 1325 km altitude. In November 2018 SpaceX requested to lower the altitude of the satellites in the lowest LEO shell in the original 2016 constellation of 4425 satellites to 550 km [174] and change the number of planes and satellites per plane in this lower shell later in August 2019 [175]. However, in an April 2020 application SpaceX requests lowering all shells to 540 km to 570 km [163]. This change would lower all Starlink satellites to roughly the same altitude of the small satellites considered for the data-relay system. This could make the possibility for a data-relay challenging as the inter-satellite passes will be of short duration. Therefore two applications of the SpaceX constellation are considered in this work, the August 2019 specification that has some shells at higher LEO altitudes and the April 2020 specification that has all shells in the lower LEO altitudes.

The August 2019 specification of SpaceX's constellation consists of 5 shells totalling 4409 satellites [175]. The first shell is inclined at 53° at an altitude of 550 km with 72 planes and holding 22 satellites each. The second shell is inclined at 53.8° at an altitude of 1110 km with 32 planes holding 50 satellites each. The third shell is inclined at 74° at an altitude of 1130 km with 8 planes holding 50 satellites each. The fourth shell is inclined at 70° at an altitude of 1325 km with 6 planes holding 75 satellites each. The fifth shell is inclined at 81° at an altitude of 1275 km with 5 planes holding 75 satellites each.

The April 2020 modification of SpaceX's constellation keeps the 5 shells totalling 4408 satellites [163]. The first two of the shells are inclined at 53° and 53.2° at an altitude of 550 km and 540 km with 72 planes holding 22 satellites each. Then a medium inclined shell with an inclination of 70° at 570 km altitude has 36 orbital planes with 20 satellites per plane. The final two shells provide coverage over the poles with an inclination of 97.6° at 560 km altitude with 6 and 4 planes each and 58 and 43 satellites per plane respectively.

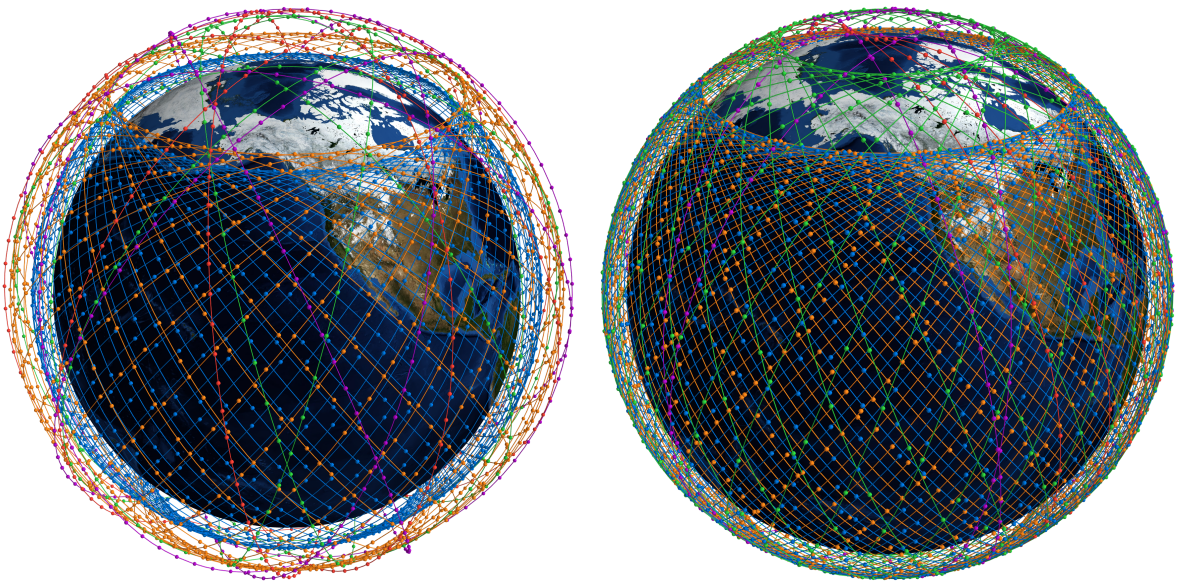

(a) SpaceX Starlink constellation as specified on August 2019 with 4409 satellites [163] still having higher LEO shells.

(b) SpaceX Starlink constellation as specified on April 2020 with 4408 satellites [163] only lower LEO shells.

Figure 4.3: SpaceX Starlink constellation as specified on August 2019 (left) and April 2020 (right).

The satellites will serve users with 8 steerable and shapeable spot beams per satellite down to a minimum elevation angle of 25° giving the satellites an operating FoV of around 56°. The user uplink band is 12.75 – 14.5 GHz with a theoretical maximum bandwidth of 500 MHz. The user downlink band is 27.5 – 30 GHz with a theoretical maximum bandwidth of 1 GHz. The SpaceX satellites will use optical inter-satellite links between the satellites in the constellation [172].

SpaceX has launched 955 satellites towards the first Starlink constellation as of November 2020 [176]. They have also recently applied for a Gen2 next-generation constellation of 30.000 satellites to address the surging demand in broadband connectivity [177].

### 4.1.4. Kuiper Systems

Amazon filed its application for operation of a LEO constellation of 3236 satellites in July 2019 under the company Kuiper Systems LCC [178]. The Kuiper constellation will consist of three orbital shells of 590 km, 640 km and 630 km orbit inclined at 33.0°, 42.0° and 51.9° respectively. The number of planes per shell and satellites per plane are equal in the three shells, being 28, 36 and 34 respectively. The FCC filing shows that the Kuiper constellation is optimized for coverage in the United States between +10° and +60° latitude, providing less coverage on the Southern hemisphere. Kuipers first FCC filing comes three years later than the first filings of Telesat, SpaceX and OneWeb and since then no additional filings have been made. The satellites in the Kuiper constellation will serve users down to an elevation angle of 35° resulting in an operating FoV of around 48.2°. The satellites have 16 steerable and shapeable user beams operating for user uplink between 28.35 – 30 GHz and for user downlink

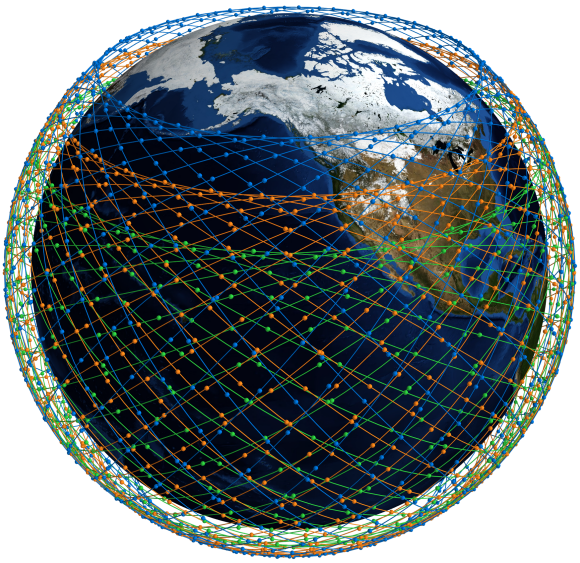

Figure 4.4: Kuiper Systems LEO constellation of 3236 satellites as specified in [178]

between 17.7 – 20.2 GHz in both directions with a maximum channel bandwidth of 500 MHz. The FCC filing also mentions the use of low-density parity check (LDPC) codes for forward error correction on the link.

### 4.1.5. Astrome Spacenet

Astrome Space Technologies has not filed FCC filings for its constellation. However they released two papers related to their constellation design in June 2019 [179] and July 2019 [180]. Astrome's SpaceNet constellation is designed to provide coverage between ±38° latitude with 198 satellites from LEO [180]. The constellation has 11 orbital planes at an altitude of 1530 km and an inclination of 30° with each 18 satellites per plane [179]. Each of Astrome's satellites has a FoV of ±37° and uses digital beam forming to create multiple steerable spot beams [179]. The user uplink band is 81.0 – 86.0 GHz and the user downlink band is 71.0 – 76.0 GHz. Each satellite will have six RF inter-satellite links at 66.0 – 71.0 GHz to communicate with all neighbouring satellites [179].

Figure 4.5: Astrome Spacenet LEO constellation of 198 satellites [179], [180]

## 4.2. MEO constellations

MEO is home to the constellations for navigation systems such as GLONAS, Galileo and GPS. Recently traditional GEO satellite network operators such as SES/O3b have been developing constellations in MEO to provide satellite connectivity with lower latency.

### 4.2.1. O3b mPower

O3b was founded in 2007 to build a satellite networking constellation in MEO to provide voice and data communications to the “other three billion” people that were unconnected or poorly connected to the internet. In 2016 the company became fully owned by backer SES but its satellites still carry the name O3b. The second generation of satellites, O3b mPower, is planned for launch in 2021. This constellation will consist of 42 satellites of which 32 are in a equatorial plane at 8062 km altitude and 10 are in two inclined 70° planes [181]. The satellites in the constellation serve users down to an

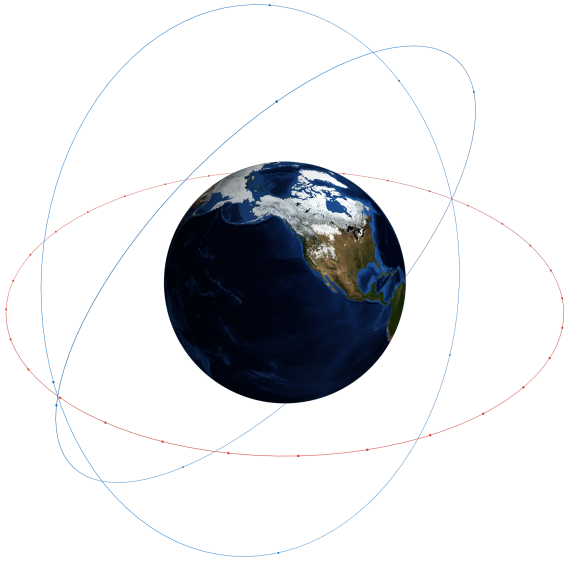

Figure 4.6: O3b constellation of 42 satellites in MEO [181]

elevation angle of 5° using 10 steerable spotbeams, resulting in a FoV of ± 26°. The new O3b mPower satellites will use a different antenna technology that will be able to provide “thousands of user beams per satellite” [182]. The user uplink band of the satellites is 27.75 – 28.96 GHz with a maximum available bandwidth of 300 MHz and the user downlink band is 17.95 – 19.95 GHz with a maximum available bandwidth of 500 MHz.

### 4.2.2. Audacy

In December 2016 Audacy filed its application for a MEO constellation of three satellites [76]. Audacy’s constellation is specifically designed as a data relay constellation for spacecraft in lower orbits. The constellation consist of three satellites at 13900 km altitude at 25° inclination spaced 120° apart. The relay satellites have a split FoV operating area with an inner ring and an outer ring that are filled with spot beams. The inner ring is nadir pointing while the outer ring surrounds the earth up to 1500 km. The gaps in between the two beams of one relay satellite is filled with that of the other two [76]. Estimated from the figures in the FCC filing the FoV of the inner ring is approximately ±16.55° and the outer ring is from approximately 18.29° to 21.22°.

The relay satellites operate in K-band and V-band, the user uplink and downlink bands are 22.95 – 33.00 GHz with a maximal bandwidth of 600 MHz. The relay satellites also have dedicated spot beams for advanced users in a 10000 km field of view. The uplink and downlink bands are 22.55 – 32.8 GHz with a maximal bandwidth of 500 MHz for a single user. The relay satellites have RF inter-satellite links in the V-Band to forward data if one of the satellites cannot establish a connection to a ground station [76]. Audacy’s constellation was specifically focussed on providing services to other satellites in orbit, but the concept was too ahead of its time as customers for the service do not exist yet. This eventually led to the company filing for bankruptcy in 2019 [77].

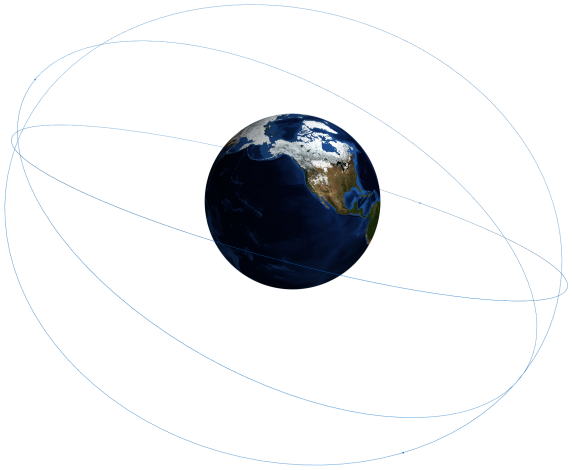

Figure 4.7: Audacy constellation of 3 satellites in MEO [76]

## 4.3. Overview

Table 4.1 shows an overview of the NGSO constellations in the previous discussed sections. The previous chapter showed that small satellite missions tend to go for polar (sun-synchronous) polar orbits at around 500 km altitude. As the antennas of the NGSO constellations are nadir pointing, they need to be in a higher orbit to see the small satellites in a 500 km orbit. When the orbital altitude difference is small, the duration for which a small satellite is visible for a of the NGSO satellite is short, making the possibility for a data relay difficult. The constellations of Kuiper and SpaceX's latest proposal that only have shells around 600 km are therefore less suitable for a LEO-to-LEO data relay. On the other hand, the MEO constellations of O3b and Audacy are at a much higher altitude and therefore would have a higher free space path loss requiring more power to be transmitted in order to close the (inter-satellite) link budget.

The constellations in Telesat's proposal, SpaceX's older proposal, OneWeb proposal and Astrome's proposal at first glance seem to be the best options for the proposed data relay concept. The intersatellite distance will be around 500 km to 700 km during the closest pass which is similar to the distance from LEO to ground. However, the LEO-to-LEO link would not suffer from atmospheric attenuation. A downside however is the limited field of view of the satellites in these constellations. This limitation would result into short non-continuous contact opportunities between the satellites.

Most of the NGSO constellations of table 4.1 use Ku/Ka-bands for the user uplink and downlink. In the proposed LEO-to-LEO data relay concept the small satellite in LEO would use the user uplink band for data downlink using a similar modem as a user would on the ground. Only the constellation of Astrome is considering the use of V-band frequencies for the user up and downlink, Telesat, SpaceX and OneWeb did file applications for V-band operations [58, 61, 65] as it offers higher bandwidths. Since then no news has come out about plans in this band and it does not seem that V-band services to users are a priority for any of the operators at this moment.

Only Kuiper Systems provides an indication on which modulations scheme to use as they mention low-density parity check codes for forward error correction on their link which is a commonly used encoding of the DVB-S2 standard. However, the DVB-S2 standards have been traditionally used for bend-pipe systems where the satellite would simply perform a frequency shift on the uplink and downlink channels to the feeder channels that are connected to a ground station. Because the proposals of Telesat and Starlink use laser crosslinks to create networks between the satellites, it is possible that their satellites, will a regenerative system, in which incoming data is demodulated, routed and re-modulated on board of the satellite.

Table 4.1: Overview of NGSO constellations

| Name | Altitude | $i$ | Number of: | | | User bands & (Bandwidth): | | Beam Type | FoV[1] |
|---|---|---|---|---|---|---|---|---|---|
| | | | Planes | Sats | Total | Uplink | Downlink | | |
| **Telesat [166]** | 1015 km<br>1325 km | 99.0°<br>50.9° | 27<br>40 | 13<br>33 | 1671 | 17.8 - 20.2 GHz (≤500 MHz) | 27.5 - 30.0 GHz (≤850 MHz) | Steerable & shapeable spot beams | ±58.15°<br>±52.03° |
| **OneWeb [167]** | 1200 km | 87.9° | 18 | 40 | 720 | 10.7 - 12.7 GHz (≤250 MHz) | 14.0 - 14.5 GHz (≤250 MHz) | Fixed elliptical beams | ±35.35° |
| **SpaceX Starlink 2019 [175]** | 550 km<br>1110 km<br>1130 km<br>1275 km<br>1325 km | 53.0°<br>53.8°<br>74.0°<br>81.0°<br>70.0° | 72<br>32<br>8<br>5<br>6 | 22<br>50<br>50<br>75<br>75 | 4409 | 12.8 - 14.5 GHz (≤500 MHz) | 10.7 - 12.7 GHz (≤1 GHz) | Steerable & shapeable spot beams | ±44.84°<br>±40.72°<br>±40.59°<br>±39.67°<br>±39.36° |
| **SpaceX Starlink 2020 [163]** | 550 km<br>540 km<br>570 km<br>560 km<br>560 km | 56.54°<br>56.67°<br>56.29°<br>56.42°<br>56.42° | 72<br>72<br>36<br>6<br>4 | 22<br>22<br>20<br>58<br>43 | 4408 | 12.8 - 14.5 GHz (≤500 MHz) | 10.7 - 12.7 GHz (≤1 GHz) | Steerable & shapeable spot beams | ±56.50° |
| **Kuiper [178]** | 590 km<br>610 km<br>630 km | 33.0°<br>42.0°<br>51.9° | 28<br>36<br>34 | 28<br>36<br>34 | 3236 | 28.35 - 30.0 GHz (500 MHz) | 17.7 - 20.2 GHz (500 MHz) | Steerable & shapeable spot beams | ±48.50° |
| **Astrome Spacenet [179], [180]** | 1530 km | 30.0° | 11 | 18 | 198 | 81.0 - 86.0 GHz (<500 MHz) | 71.0 - 76.0 GHz (≤500 MHz) | Digital beam-forming spot beams | ±37.00° |
| **O3b [183]** | 8062 km<br>8062 km | 0.0°<br>70.0° | 1<br>2 | 32<br>5 | 42 | 27.75 - 28.96 GHz (<300 MHz) | 17.95 - 19.95 GHz (<500 MHz) | Steerable spot beams | ±26.00° |
| **Audacy [76]** | 13900 km | 25.0° | 3 | 1 | 3 | 22.95 - 33.0 GHz (≤600 MHz) | 22.95 - 33.0 GHz (≤600 MHz) | Digital beam-forming spot beams | ±37.00°[2] |

[1] A calculation of each constellations field-of-view can be found in `notebooks/FOV_calculations.ipynb`
[2] There is a gap in the FoV of the relay satellites of Audacy between 16.55° and 18.29°

Figure 4.8 shows the operating range of a single satellite in each of the NGSO (mega-)constellations projected on the surface of the Earth. As can be see of the figures, the coverage of the satellites in the LEO constellations are smaller than those of the MEO constellations. From this it is clear to see why having the satellites at a lower altitude requires a larger number of satellites in the constellation. The Starlink constellation of SpaceX compensates for this by having high operating field-of-view accomplished by a large steering range of the antenna phased arrays. The area of operation defines where communication with a satellite can be achieved, this coverage reduces at higher altitudes. This means that if the NGSO constellation provides full coverage on the surface, gaps in coverage will appear at higher altitudes. Having a high ground coverage per satellite the MEO constellations of O3b and Audacy will likely provide better coverage at higher altitudes that the LEO.

## 4.4. Summary

This chapter presented an overview of the current (proposals) for NGSO (mega-)constellations. Both LEO (mega-)constellations an MEO constellation proposals were presented that have or are close to launching their first satellites. An overview of orbital configuration was given, showing that the LEO constellations are planning to have satellites in shells around 500 km altitude (SpaceX, Kuiper Systems) or around 1200 km altitude (Telesat, OneWeb, Astrome). The MEO constellations are a factor seven to twelve times higher in altitude which will significantly impact the link budget for a data-relay with these constellations. The constellations at 500 km altitude will have a reduced coverage for current nano-satellite and small satellite missions that orbit around the same altitude. This coverage analysis will be performed later in chapter 7 and the best candidates for the NGSO data-relay concept will be chosen for further analysis.

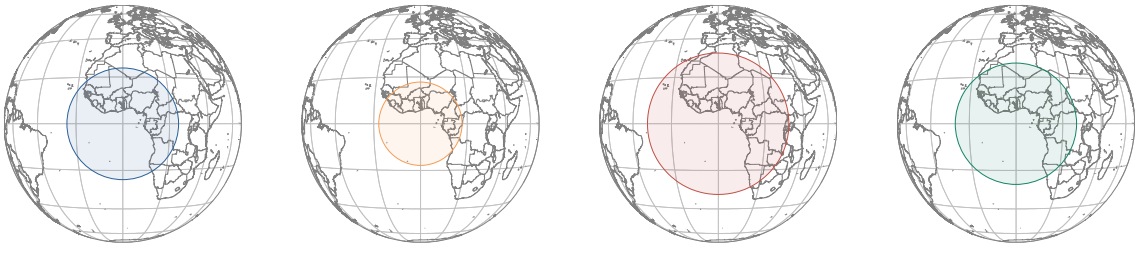

(a) Telesat (b) OneWeb (c) SpaceX Starlink (d) Kuiper Systems

(e) Astrome (f) O3b (g) Audacy

Figure 4.8: Operating areas of (steerable and shape-able) antenna beams for different NGSO constellations.

This page intentionally left blank.

# 5

# Use-case and architecture definition

This chapter will describe the NGSO data-relay downlink architecture and use-cases that are analysed in the rest of this thesis. The architecture description will define the system boundary, assumptions and the aspects of the design that will be considered in the design optimization. Section 5.1 describes in more detail the NGSO data-relay downlink architecture. The section defines the system boundary that is investigated in this work and it defines the constraints for the system in relation to small satellite missions and NGSO (mega-)constellations. It will also describe the general concept of operations for a small satellite mission using the data-relay downlink and identifies the key quality of service requirements the data-relay downlink should fulfil. Then in section 5.2 and section 5.3 the specifics for the IoT/M2M and EO small satellite missions are discussed. For both missions a baseline mission is defined that captures the use-case for the NGSO data-relay downlink for further analysis. Finally, in section 5.4 a summary is provided for these two potential use-cases for the NGSO data-relay downlink including an overview of the requirements and constraints, and several reference missions used for comparison.

## 5.1. Downlink architecture

The NGSO data-relay downlink is an architecture for a distributed space system where the data downlink component of the small satellite mission utilises a second space system (the NGSO constellation) that has its own separate primary mission (broadband connectivity on Earth). This data-relay architecture could offer advantages such as more contact-time with the satellite, a higher throughput per orbit, lower data-generation-to-date-delivery latency and reduced ground segment costs.

Figure 5.1 shows the context diagram for the distributed space system using an NGSO data-relay downlink. The complete system consists of a ground segment for the TT&C of the small satellite, the

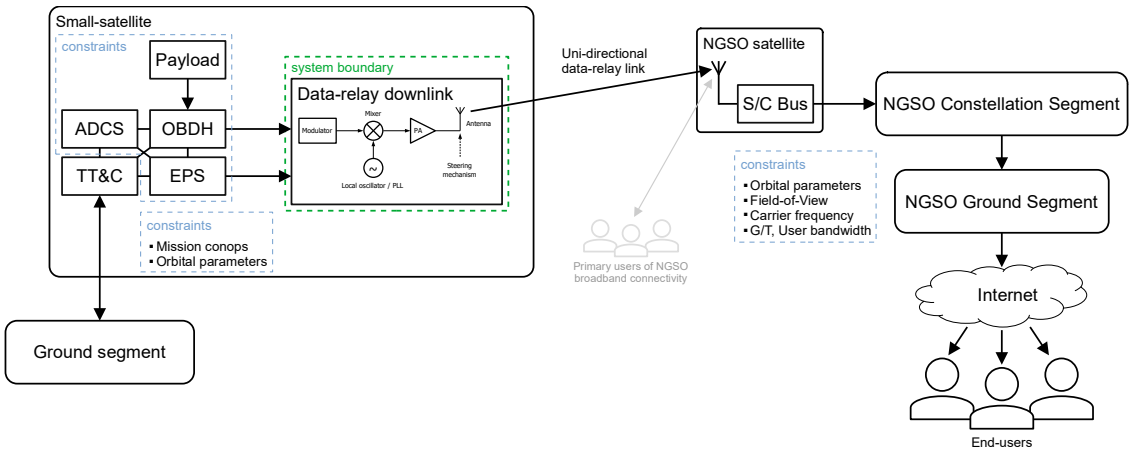


Figure 5.1: Context diagram for the NGSO data-relay downlink for small satellites. The green system boundary is the boundary of what is investigated in this thesis. The blue constraints are considered to influence the design and analysis of the data-relay downlink but are not part of the design space.

small satellite, the NGSO satellite and (mega-)constellation, the NGSO ground-segment connected to the internet, and the end-users of the data from the small satellite payload.

In this distributed system the data generated by the payload on-board of the small satellite is transferred off the satellite using a uni-directional data-relay link to a satellite of an NGSO constellation. This NGSO constellation has as primary mission to provide broadband connectivity to users on Earth, however this aspect of the NGSO system is not considered in this work. The NGSO satellite will then take care of bringing the data down to the ground, using the same channels as for the broadband user data, by routing it through the NGSO constellation (if cross-links are available) to then downlink it to a ground-station. The ground station is connected to the internet to make the data available to end-users.

### 5.1.1. System boundary, constraints and requirements

The system boundary for the design of the NGSO data-relay downlink in this work is shown in green in fig. 5.1. The system boundary represents a small portion of the overall distributed system. However, constraints from each of the segments are taken into account in the analysis and design of the components within the data-relay downlink. It is assumed that the data-relay downlink is only used to downlink payload data and a separate TT&C communication system is used for commanding the satellite.

The data-relay downlink components are assumed to be those of a typical payload downlink communication transmitter, discussed in section 3.2, consisting of a modulator, up-converter (mixer), power-amplifier, antenna and (optional) antenna steering mechanism. This transmitting chain is directly connected to the On-board Data Handling (OBDH) computer of the small satellite which provides the data stream that needs to be downlinked, and connected to the Electric Power System (EPS) which provides power to the data-relay downlink system.

#### Small satellite constraints

Several constraints to the NGSO data-relay downlink are applied by the small satellite properties. These consist of size, mass and power limits, but also constraints on the accuracy of the attitude determination and control system (ADCS) in orientation knowledge and pointing, including the rate at which the orientation of the spacecraft can be changed. It is assumed that the orbital parameters are determined by the small satellite mission and cannot be changed to support the data-relay downlink. Only the orientation of the satellite may be changed to track a NGSO satellite for the data-relay link if the satellite is not orientated for other mission aspects such as for payload pointing. This final constraint is put by the mission concept of operations (conops).

#### NGSO constraints

The NGSO (mega-)constellation and its satellites properties apply several constrains to the design of the NGSO data-relay downlink. The first two constraints follow from the orbital parameters and service/operating field-of-view for each satellite. If the small satellite is not in-view of any NGSO satellite, the data-relay downlink cannot be used. It is also assumed that the user frequencies, user bandwidths and receiver properties are fixed by the specifications of the NGSO. The data-relay downlink on the small satellite should therefore function as a user-terminal on the ground and no additional hardware changes on the NGSO satellite are required.

It is assumed that the communication protocols and modulation schemes can be freely chosen as chapter 4 showed that this information is not publicly available for the NGSO (mega-)constellations. Whether the NGSO satellites operate as bend-pipes or regenerative, it is assumed that any protocol and modulation may be used within the allocated user bandwidths. Furthermore, no spectral restrictions are considered.

#### Mission Concept of Operations constraints

Figure 5.2 shows the baseline concept of operations that is used for analysis and design of the NGSO data-relay downlink on the small satellite. The satellite is assumed to do either of three operations: 1. recharge the batteries by pointing the solar panels/body towards the Sun, 2. collect payload data by pointing a (non-steerable) payload in a particular direction or 3. track a NGSO satellite to relay data. This baseline concept of operations assume that these three operations take place separately. However, if for example the satellite maintains adequate power levels while pointing its payload nadir and its data-relay downlink system zenith, it is possible that the satellite can collect payload data and

relay if there is a NGSO satellite in-view. If this is not the case, the duty cycle at which NGSO data-relay downlink operates (possibly requiring reorientation) should be low enough to allow for the other two operations to occur during the mission.

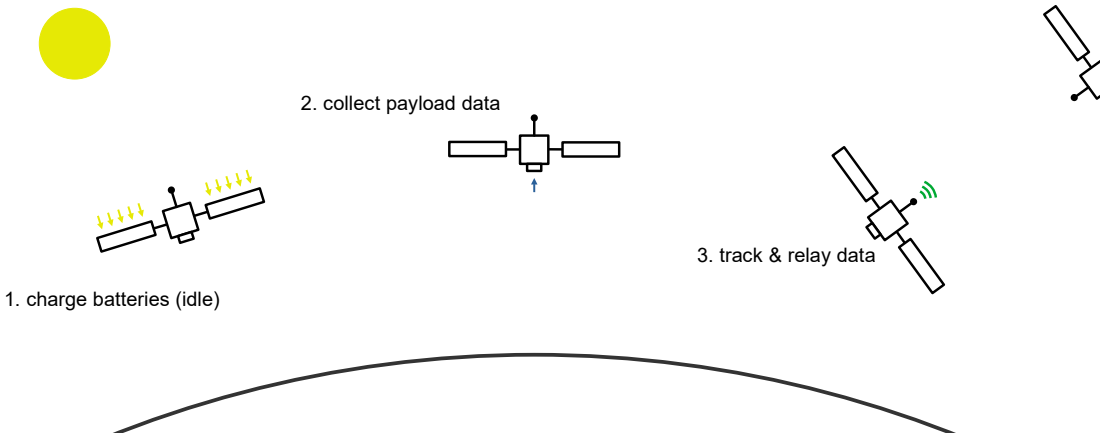


Figure 5.2: Concept of operations for a small satellite with a NGSO data-relay downlink.

### Quality of Service requirements

Finally, some Quality of Service requirements are to be identified to asses the performance of the NGSO data-relay downlink and to evaluate it against current alternatives. These requirements do not solely capture the performance of the communication system in terms of data-rate/spectral efficiency, but are translated to mission capabilities. For this purpose two requirements are used, the total throughput per orbit, and the latency from payload data generation to end-user delivery. The two use-cases described in the next sections have different Quality of Service requirements. For each concept, either latency or total throughput per orbit, allows for a higher mission return.

## 5.2. Use-case: IoT/M2M

The first use-case that could potentially use the NGSO data-relay downlink concept is a small satellite mission that collects IoT or M2M data from sensors on the ground. Figure 5.3 shows the sequence diagram of the interactions in the IoT/M2M use-case. The sequence diagram contains six participants; an IoT/M2M sensor, a small satellite (constellation), an NGSO constellation, an NGSO ground-station, an online storage platform, and a user of the IoT/M2M data.

The IoT/M2M sensor on the ground, stationary or mobile, collects data from its low-rate sensors (1.) while operating autonomously. The sensor will continue collecting and storing sensor data on its on-board storage (2.) while waiting for a contact opportunity (3.) with a small satellite of the IoT/M2M constellation. Once a satellite comes in view[1] (4.) the sensor starts transmitting its collected sensor data (store-and-forward) to the IoT/M2M small satellite (5.). Uplinking the data to the satellite can be done by the sensors individually, as is done with the system of Hiber [6], [54] or Lacuna Space [55]. Or multiple sensors can first forward their data to a gateway which then forwards the data to the satellite, as is done with the system of Fleet [7].

The small satellite will similarly store the data (6.) and collect data from other sensors it encounters throughout the orbit while waiting (7.) for a contact opportunity with the NGSO constellation. Once in view of a NGSO satellite (8.) the small satellite forwards the data it has collected from the IoT/M2M sensors to the NGSO constellation (9.).

The NGSO satellite that received the data from the small satellite will now route (10.) the data through the constellation (if cross-links are available like in the SpaceX or Telesat constellations) until

[1] There are several options for determining when the small satellite is in view for uplink of data such as using a pre-programmed fixed schedule in the IoT/M2M sensor or a identification signal transmitted by the small satellite. The exact method of link negotiation is considered beyond the scope of this work.

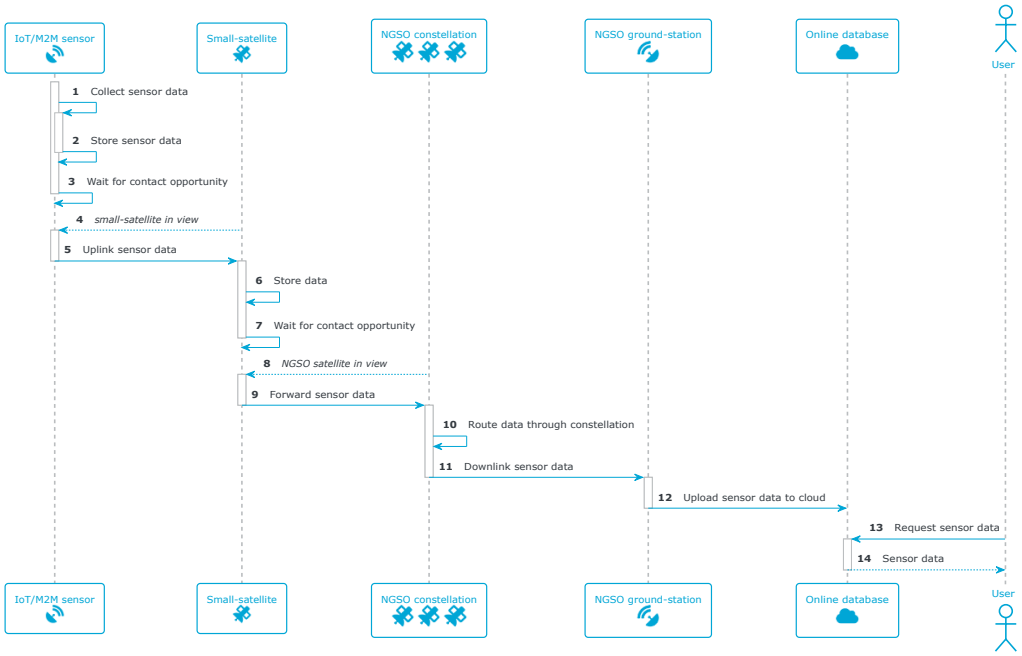


Figure 5.3: Sequence diagram for the collection and distribution of IoT/M2M data using small satellites and a NGSO data-relay downlink

the data has reached a satellite that is in-view of a ground station and the data can be downlinked (11.). The ground station is assumed to be connected to the internet and will upload the sensor data to a online databases (12.). This online database can then be accessed by the user of the IoT/M2M data, a person or a machine (13. - 14.).

### 5.2.1. Spacecraft properties

Two small satellites for IoT/M2M are used to form the baseline spacecraft properties for an mission, the TUBiX-10 by the TU Berlin [184] for the S-NET mission and the Hiber satellite [54]. Both satellites have recently launched to perform their IoT/M2M mission and are representative for the state-of-the-art in small satellites for IoT/M2M.

The TUBiX-10 is a 8U satellite-bus with a mass of (max) 12 kg. It has a peak power generation of 50 W and battery storage of 150 Wh. The satellite has a 3 axis attitude-determination and control system with an determination accuracy of < 1.0°, control accuracy of < 5.0° and control rate of 15°/s. The Hiber satellite is slightly smaller being an 6 U satellite with a mass of 7.23 kg. Power generation and attitude-determination and control performance for the Hiber satellite are unknown. Therefore the performance of the TUBiX-10 bus is base-lined. Both satellites have non-steerable solar panels and the spacecraft is nadir pointing with the antenna systems to service users on the ground.

The Hiber and S-NET satellites are placed in a Sun-synchronous orbit, at 585 km for the S-NET satellite and 600 km for the Hiber satellites. The Hiber constellation uses 8 orbital planes at 97.8 degrees inclination. For the baseline IoT/M2M mission the orbital configuration of the Hiber satellites is assumed having 24 satellites in 8 planes separated 22.5° each in right ascension.

There are no exact numbers available on the amount of data generated on the satellites. It is therefore assumed that the maximum data generated is roughly equal to what can be downlinked through one (polar) ground-station. The Hiber Satellite has the highest downlink data rate on its ISIS S-band transmitter of 8 Mbps [185]. The maximum data that can be downlinked during a 400 s pass with a ground-station is therefore 400 Megabyte. With 24 active satellites this makes 9.6 Gigabyte per orbit for the whole constellation. The 20 W power consumption of ISIS S-band transmitter is base-lined for the maximum power consumed by the NGSO data-relay downlink for the IoT/M2M mission.

### 5.2.2. Quality-of-Service requirements

The quality of service of a NGSO data-relay downlink for IoT/M2M constellations will be primarily determined by the latency from sensor data generation (1.) to sensor data delivery (14.). A lower latency is desired because it would allow for higher update rates moving towards near-real time updates

from the IoT/M2M sensors.

The main contribution to latency in the system happens while waiting for IoT/M2M sensor to come in view of the small satellite (3.) and while waiting for the small satellite to come into view of an NGSO satellite (7.). With the size of the data-packets of IoT/M2M applications it is expected that uplinking the data to the small satellite (5.) and forwarding the data (9.) will be a matter of seconds. Similarly, routing (10.), downlinking (11.) and uploading (14.) will be a matter of milliseconds. These are therefore not significant contributors to the overall latency.

The latency caused while waiting for a small satellite to come into view (3.) can be reduced by reducing the revisit time, for example by having more satellites in the IoT/M2M constellation and optimizing the orbits of the satellites for ground coverage. This is considered beyond the scope of this work. The latency while waiting for a contact opportunity with a NGSO constellation (3.) can be influenced by the design of the data-relay downlink. At a given time one or multiple NGSO constellation satellites may be in-view, and it would be up to the data-relay downlink to pick the best based on duration, contact angles, etc. For a IoT/M2M mission the best picks are those that minimize this latency. The achievable end-to-end latency (from 1. to 14.) is assumed to be in the order of minutes to provide for high-end IoT/M2M applications. A first order estimate for the required latency from data-reception to forwarding (from 5. to 9.) to achieve this is assumed to be less than or equal to one minute.

The downlink throughput per orbit is considered of less importance as the total data generated by a single IoT/M2M sensor will remain in the order of kilo-bits per second. The total data generated per orbit will increase linearly as the number of IoT/M2M sensors increases. But with several small satellites in an constellation it is not expected that each satellite will generate more than a few gigabit per orbit. A first order estimate for the required throughput per orbit for an IoT/M2M mission is assumed to be 2.5 Gigabyte per satellite per orbit.

## 5.3. Use-case: Earth Observation

The second use-case that could potentially use the NGSO data-relay downlink concept is the small satellite EO mission, either as a stand-alone single satellite EO mission, or a constellation of EO satellites. Figure 5.4 shows the sequence diagram of the interactions in the EO use-case. The sequence diagram contains five participants; a small satellite (constellation) with imaging payloads, an NGSO constellation, an NGSO ground-station, an online storage platform, and a user of the EO data.

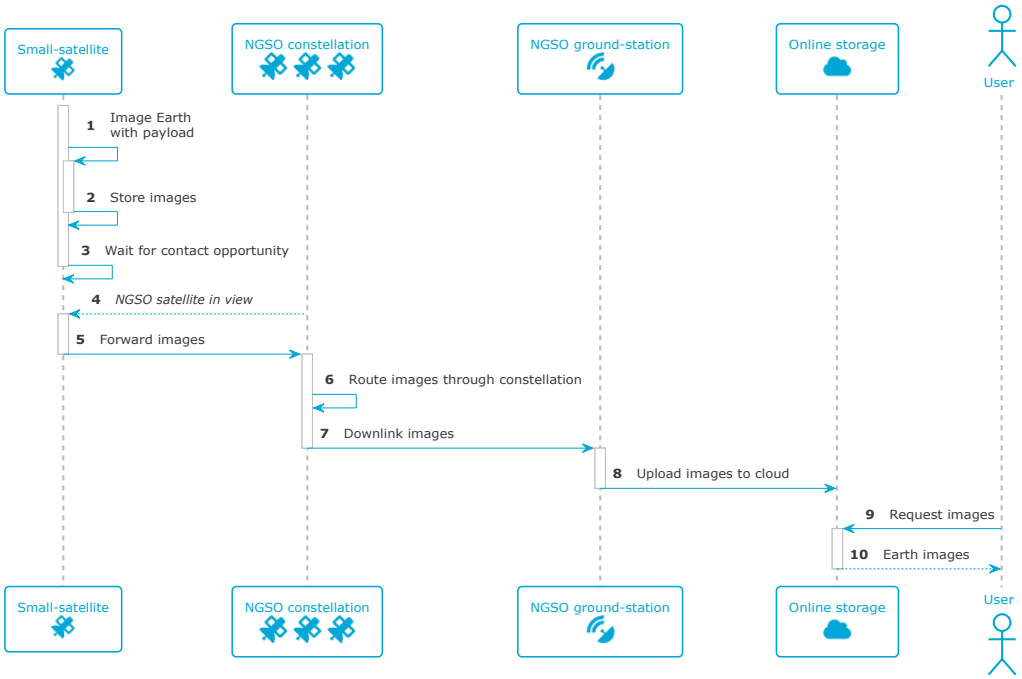


Figure 5.4: Sequence diagram for collection and distribution of Earth observation data using small satellites and a NGSO data-relay downlink

The sequence for the EO use-case is similar to that of the IoT/M2M use-case only now the source of the generated data is onboard the small satellite as the imaging payload. The payload first acquires an (spectral/optical/radar) image of the Earth (1.) this images is temporarily stored on the on-board storage of the small satellite (2.) and the satellite waits for a NGSO satellite to come in view (3.). While waiting, the small satellite could continue to collect and store payload data until the on-board storage is full.

Once a NGSO satellite is in view (4.) the small satellite will forward its stored images to the NGSO satellite (5.). The NGSO satellite that received the data from the small satellite will now route (6.) the data through the constellation (if cross-links are available like in the SpaceX or Telesat constellations) until the data has reached a satellite that is in-view of a ground station and the data can be downlinked (7.). The ground station is assumed to be connected to the internet and will upload the sensor data to a online databases (8.). This online database can then be accessed by the user of the IoT/M2M data, a person or a machine (9. - 10.).

### 5.3.1. Spacecraft properties

The two small satellites that used to form the baseline spacecraft properties for an EO mission are the Dove satellites by Planet [2], and the Corvus-BC satellite by Astro Digital [1]. These two satellites are representative for state-of-the-art in small satellite for Earth observation. Their optical (Dove) and multi-spectral imaging (Corvus) payloads are one of the highest performing in class, resulting into a high on-board data generation and need for high transmission rates.

The Dove satellites are 3U satellites with a mass of 5.8 kg. The satellites have a peak power generation of 50 W with a 80 Wh battery. Information on the performance of the attitude-determination and control system on the Dove satellites is unknown. The Corvus-BC spacecraft is a 6U satellite with a mass of 11 kg. It has a peak power generation of 40 W and a 48 Wh battery. Its attitude-control and determination system is 3-axis with an determination accuracy of $< 0.03°$, a control accuracy of $< 0.05°$ and a maximum control rate of 6°/s. Both satellites have non-steerable solar panels and are nadir pointing with the imaging payloads to the ground.

The Dove and Corvus satellites are in a Sun-synchronous orbit, at 500 km and 550 km respectively at in inclination of 98 degrees. The Dove constellation consists of 120+ satellites in this single orbital plane. This configuration is assumed for the baseline EO mission.

The Dove satellites currently have the highest performing downlink transmitter. With their X-band transmitter system the satellite is capable of transmitting roughly 80 GB per pass with their ground station. Assuming the use of one ground station (location) this would mean a throughput of 80 GB per orbit per satellite. The 50 W power consumption of Dove X-band transmitter is base-lined for the maximum power consumed by the NGSO data-relay downlink.

### 5.3.2. Quality-of-Service requirements

The quality of service of a NGSO data-relay downlink for EO constellations will be primarily determined by the throughput per orbit that can be achieved. A higher throughput allows for more and higher quality images to be taken and increase the mission return.

The throughput per orbit will primarily be determined by the number of contact opportunities(4.), their duration and the data rate at which the small satellite can transmit while forwarding the data (5.). Since the NGSO constellations are intended for broadband connectivity on Earth and the overall data-rate will be in the order of Terabits per second [3], it is assumed that the throughput of the NGSO constellations will not be limiting in the overall throughput. The current state-of-the-art throughput per orbit for EO satellites is 80 GB per orbit for the Dove satellite [2]. The NGSO data-relay downlink should at least match this number but preferably be higher to make the system a better alternative. Therefore, the first order estimate for the required throughput per orbit for an EO mission is assumed to be 120 Gigabyte per satellite per orbit.

The latency from the moment an image is taken (1.) until it is available for the user to view (10.) is considered of less importance. This assumption is made because the current latency, assuming one polar ground station such as for the Dove satellites [2], is one orbital period, roughly 1.5 hours. Instead the key-requirement is throughput as the papers by Devaraj et. al. [2] and Leveque et. al. [1] state that low data throughput is limiting mission return from small satellites. The NGSO data-relay downlink could reduce latency as the small satellites will have contact opportunities throughout their orbit but this is not the main priority for the system. A first order estimate for the required latency from the moment

an image is taken to when its available to the user (from 1. to 10.) is assumed to be less than or equal to one and a half hours.

## 5.4. Baseline small satellite missions overview

Two use-cases were identified that could potentially use the NGSO data-relay downlink concept as their primary means for downlinking payload data, a IoT/M2M and a Earth Observation (EO) small satellite mission. Two baseline missions were defined that are used for further analysis in this work. Table 5.1 shows an overview of the properties and requirements for the baseline IoT/M2M and Earth Observation (EO) small satellite missions.

The IoT/M2M mission is assumed to consist of a constellation of 24 satellites in 8 equally separated Sun-synchronous polar orbital planes at 600 km. The satellites are expected to be 6U or 8U with a mass between 7 to 14 kg. The peak power generation assumed to be 50 W using non-steerable solar panels and a battery capacity if 150 Wh. Attitude determination and control performance is assumed to be in the order of degrees and the satellites are expected to be nadir pointing while collecting payload data.

The EO mission is assumed to consist of a constellation of 120 satellites in one Sun-synchronous orbital plane at 500 km. The satellites are assumed to be 3U or 6U with a mass between 6 to 12 kg. The peak power generation assumed to be 50 W using non-steerable solar panels and a battery capacity of 60 Wh. Attitude determination and control performance is assumed to be in the order of tenths of degrees and the satellites are expected to be nadir pointing while collecting payload data.

Five key-requirements are considered for the NGSO data-relay downlink that are dependent on the baseline missions; size, mass, peak power consumption, throughput per orbit and latency. The NGSO constellations described in chapter 4 use high frequencies in the Ka-band and Ku-bands for the user uplinks. Small satellite transmitters at high frequencies are relatively new technology and as shown in chapter 3 only a hand-full of transmitters exist for these frequencies, the transmitter of the Corvus-BC spacecraft being the current highest performer. Therefore the size and mass of this transmitter is baselined as the requirement for the NGSO data-relay downlink, fitting a 1U form-factor with a mass equal or less than 2 kg [1]. A lower throughput per orbit of 2.5 GB per orbit is acceptable for the IoT/M2M mission therefore a lower peak power consumption requirement of 20 W (equal to an ISIS TXS transmitter [185]). A lower power consumption will also reduce the overall energy consumption per orbit of the data-relay downlink in case a high duty cycle is required to reach the latency requirement of less than or equal to 1 minute. For the EO mission a higher throughput is required, greater or equal than 120 GB per orbit, but the latency requirement is reduced to equal or less than 1.5 hours. Therefore the peak power requirement of the transmitter is relaxed to less than or equal to 50 W (equal to an Dove HSD2 transmitter [2]).

Table 5.1: Overview of the parameters of the two baseline small satellite missions analysed in the rest of this work; an IoT/M2M mission and an Earth Observation (EO) mission.

| | **IoT/M2M** | **EO** |
|---|---|---|
| *Constellation parameters* | | |
| Active satellites | 24 | 120 |
| Maximum data generated per 24h | 9.6 GB | 300 TB |
| Orbital parameters: | | |
| altitude | 600 km | 500 km |
| inclination | 97.8° | 98.0° |
| number of planes | 8 | 1 |
| RAAN increment | 22.5° | n.a. |
| *Spacecraft properties* | | |
| Size | 6U to 8U | 3U to 6U |
| Mass | 7 - 14 kg | 6 - 12 kg |
| Peak power generation | 50 W | 45 W |
| Battery capacity | 150 Wh | 60 Wh |
| Solarpanels | non-steerable | non-steerable |
| Attitude determination | < 1° | < 0.03° |
| Attitude control accuracy | < 5° | < 0.05° |
| Attitude control rate | 15 °/s | < 6°/s |
| Pointing during payload operation | nadir | nadir |
| *NGSO data-relay downlink requirements* | | |
| Size | Fits 1U form factor | |
| Mass | ≤ 2 kg | |
| Peak power consumption | ≤ 20 W | ≤ 50 W |
| Throughput per orbit | ≥ 2.5 GB | ≥ 120 GB |
| Latency tolerance | ≤ 1 minute | ≤ 1.5 hour |
| *Current solutions* | | |
| Maximum data rate | 8 Mbps | 1.6 Gbps |
| Downlink duty cycle | 14.5% | 14.5% |
| Contact time per orbit per (polar) ground station | ≈400s | ≈400s |
| Throughput per orbit | 400 MB | 80 GB |
| Example spacecraft | TUBiX-10<br>Hiber | Dove<br>Corvus |

# 6

# NGSO data-relay orbital simulator

In this chapter the NGSO data-relay orbital simulator is described that was purpose-built to simulate the orbital dynamics between typical small satellite orbits and the satellites of a NGSO (mega-) constellation. The choice for developing this software was made because the simulation considers a large number of satellites and therefore computational performance is of importance. In addition, licenses for commercial packages (such as Analytical Graphics Systems Tool Kit (STK)) were not available and the packages were considered not performant enough to simulate the large number of satellites required for this project in a reasonable time. The purpose-built data-relay orbital simulator was designed for fast computation in determining the positions and line-of-sight between multiple satellites. The simulator is written in Python building on existing open source packages such as `Astropy` [186] and `Poliastro` [187] and uses code acceleration by compiling parts of the code to C using the `Numba` package [188].

In section 6.1 of this chapter the top-level requirements for the data-relay orbital simulator are outlined and explained. Section 6.2 introduces the line-of-sight problem and highlights several challenges for simulation of a large number of satellites. Section 6.3 provides a top-level overview of the data-relay orbital simulator, a description of the general operation of the simulator and a description of how simulation scenarios are constructed. The remainder of the chapter dives deeper into the design and verification of th algorithms in the data-relay orbital simulator. Section 6.4 discusses the orbital propagator algorithms that are implemented for fast computation of the positions of the satellites at a given time instance. Section 6.5 discusses the algorithms that were implemented for fast determination of the line-of-sight between simulation objects. In section 6.6 the results of the data-relay orbital simulator are validated for a simple scenario against a commercial orbital simulator package. A description of the post-processing steps taken to prepare the output dataset for the communication system optimization is given in section 6.7. And finally, this chapter will conclude with a summary, recommendations and discussion for the data-relay orbital simulator in section 6.8.

## 6.1. NGSO simulator requirements

This section will outline some high-level requirements that were set-up to guide the development of the data-relay orbital simulator. As explained in the methodology of chapter 2 the data-relay orbital simulator will generate the input data set that is used for the optimization of the data-relay downlink system on the small satellite. This dataset will consist of the contact opportunities that arise during the orbit of the small satellite. A contact opportunity is defined as a moment in time where the small satellite has line-of-sight with a satellite in the NGSO (mega-)constellation and the opportunity exists to establish a link if desired. To find the contact opportunities the data-relay orbital simulator should simulate the orbital positions of the small satellite and the NGSO constellation satellites over a given period of time and compute when the small satellite is in view of the NGSO constellation satellites. The first requirement for the data-relay orbital simulator is therefore:

**DROS-1** The data-relay orbital simulator shall compute the contact opportunities between a small satellite and the satellites of a NGSO (mega-)constellation during a given period.

Chapter 4 showed that some NGSO (mega-)constellations have more than 4400 satellites. Orbit propagation and line-of-sight determination with this number of satellites is non-trivial. As mentioned in the introduction of this chapter this challenge led to the decision to develop a purpose build simulator for this project. The second driving-requirement is therefore:

**DROS-2** The data-relay orbital simulator shall be capable of simultaneous simulation of at least 5000 satellites.

A large enough input dataset should be considered for the design optimization. This will prevent bias in the optimization where the design is only optimal for certain on-orbit period and not necessarily for a whole mission. For now it is assumed that 7 days of simulation time (roughly 100 orbital periods at 500 km circular orbit) is enough to satisfy the size of the dataset needed for the optimization. The time-step resolution of the optimization is also important as it will define the moments in time at which the link budget is to be calculated and the resolution at which gaps in coverage are detected. As the satellites will be moving in different planes a relatively small time resolution (with respect to the orbital period) is desired. In this case a 1 second time-step resolution is considered adequate to later in the optimization be able to accurately compute the link budgets. The third requirement covers simulation time and time-step resolution is:

**DROS-3** The data-relay orbital simulator shall be capable of computing 7 days of simulation time with a 1 second time-step resolution within reasonable computational time.

The fourth requirement specifies the expected format of the output dataset. The design optimization will consider the link budgets and therefore needs the link parameters including as range and relative position over time during the contact opportunity. Range can be computed from the orbital positions in an Earth centred inertial frame (ECIF), however the relative position should consider the orientation of the small satellite and should therefore be exported in a satellite fixed frame (SFF). In addition, the relative velocity should be considered to evaluate parameters such as Doppler shift. Therefore the fourth requirement is:

**DROS-4** The data-relay orbital simulator shall output a list of contact opportunities at each time-step containing positions and velocities in ECI and SF reference-frames of the pairs of satellites that have line-of-sight.

Finally, in order to get insight in the results the data-relay orbital simulator should include visualisations for the orbital motion of the satellites and contact opportunities:

**DROS-5** The data-relay orbital simulator shall generate two-dimensional and three-dimensional visualisations of the orbital motion of the satellites and contact opportunities.

## 6.2. The line-of-sight problem & simulation challenges

Finding the contact opportunities for the small satellite can be considered as repeatedly solving a line-of-sight problem. This problem is illustrated in fig. 6.1. The problem considers two satellites, the small satellite (denoted subscript $sc$) in a low orbit and the data-relay satellite (denoted subscript $dr$) in a higher orbit. Each satellite is considered to have an operating field of view (FoV) for the communication system highlighted in the red and blue cones. This is the area in which the satellite can ”see” other objects. In RF communications, visibility of another object comes down to whether or not the antenna provides gain in the direction of the other object. If directional antennas are used a first-order abstraction can be made assuming the FoV is defined as a cone with an angle equal to the half-power beam width of the antenna. This half-power beam width defines the angle between the points where the antenna provides half the gain with respect to the peak gain of the main lobe [189, p. 62]. In fig. 6.1 the small satellite has a highly directive antenna that has therefore a lower half-power beam width and a smaller FoV. In principle, the FoV cone extends to infinity, having the range for the RF link limited by the performance of the transmitter and receiver. In case the spacecraft can rotate or the antenna can be individually pointed the FoV cone can be considered as the maximum rotation or pointing angle of the communication system.

To solve the line-of-sight problem, the first step is to determine the positions of the satellites (at a time instance of interest) within a common frame of reference, i.e. the ECIF. Then the line-of-sight

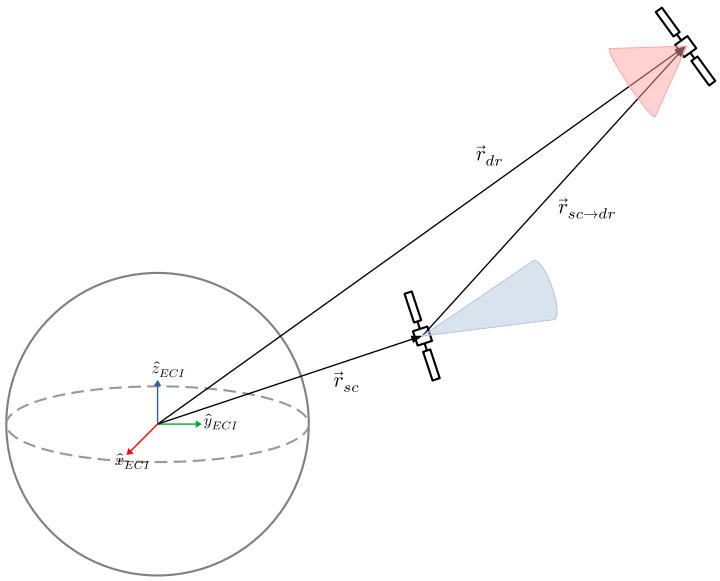


Figure 6.1: Illustration of the line-of-sight problem, the problem considers whether or not two satellites can see each other (and achieve communication). The problem comes down to determining if the other satellite is within the field of view (FoV) of the given satellite and vice-versa. In this example no line-of-sight is obtained because the small satellite (denoted $sc$) cannot "see" the data-relay satellite (denoted $dr$) as the line-of-sight vector $\vec{r}_{sc\to dr}$ lies outside the FoV of the small satellite.

vector from one satellite to the other is computed by a vector subtraction of the position vectors of the two satellites. In order to have a line-of-sight this vector should not be obstructed by other objects, i.e. the attractor, and the vector should lie within the FoV cones. In the example of fig. 6.1 the line-of-sight vector is not obstructed. It lies within the FoV of the data-relay satellite which can therefore "see" the small satellite. But it does not lie within the FoV of the small satellite which therefore cannot "see" the data-relay satellite and no line-of-sight is obtained in this example. The line-of-sight problem can therefore be considered as a problem with four steps:

1. Compute positions of the satellites in a common reference frame
2. Compute the line-of-sight vector from one satellite to the other satellite
3. Determine if the line-of-sight vector is not obstructed by other objects
4. Determine if the line-of-sight vector lies within the field-of-view of each satellite

A line-of-sight is obtained between a pair of satellites if the answers to 3. and 4. are yes. When line-of-sight is obtained the possibility of communication should be further evaluated by considering the link parameters, and the performance of the transmitting system on the small satellite and the receiving system on the data-relay satellite. This step will be performed during the design optimization for which the framework is described in chapter 8. The output of the data-relay simulator will therefore be a list of contact opportunities for further evaluation that occur during the orbits where line-of-sight is obtained between two satellites.

Several challenges arise when the line-of-sight problem has to be solved repeatedly for a large number of satellites over a long simulation time with a small time-step resolution. The following sections briefly discuss these challenges to support the decisions made in the design of the NGSO data-relay orbital simulator.

### 6.2.1. Orbital positions as a function of time for a large number of satellites

The first challenge in solving the line-of-sight problem in NGSO (mega-)constellations is to efficiently calculate the orbital positions of the satellites at each time step. Chapter 4 showed that the satellites in the NGSO constellations are in circular orbits and have station-keeping abilities to compensate for perturbations and maintain the specified orbits. Chapter 3 showed that it is common for the small satellites to be in Sun-synchronous orbits. In both cases, the position of the satellites is governed by

the two-body problem in which the relative motion between a body $k$ (the attractor) at the origin and body $i$ is described as [190, p. 70]:

$$\frac{d^2\vec{r}}{dt^2} = -\frac{\mu}{r^3}\vec{r} \tag{6.1}$$

where $\vec{r}$ is the vector pointing from body $k$ to $i$ with magnitude $r = |\vec{r}|$ and the gravitational parameter $\mu$ that depends on the universal gravitational constant $G$ and the masses of both bodies $m_k$ and $m_i$ as $\mu = G(m_k + m_i)$[1].

Equation (6.1) is a non-linear second order differential equation that governs the motion (position and velocity) of body $i$ orbiting body $k$. Here lies the challenge of solving the orbital positions of a large number of objects as function of time as for each time-step the differential equation of eq. (6.1) needs to be solved $N$ times where $N$ is the number of satellites considered. For the large number of satellites in the NGSO (mega-)constellations this becomes a computationally intensive problem.

For this project however several assumptions can be made for the required accuracy of the orbital propagation. The target simulation period of seven days is relatively short, therefore perturbations that are not included in eq. (6.1) will only have a limited effect in this short duration. In addition, the satellites in the LEO (mega-)constellations will likely drift simultaneously with the targeted small satellite (if they are not station-kept) and therefore will not change the contact opportunities by much. The required accuracy is thereby low and the assumption of two-body motion with limited[2] to no perturbations is sufficient to achieve the goals of this research. The primary challenge is to effectively simulation the contact opportunities between a large number of satellites. Section 6.4 will describe vectorized orbit propagation and position/velocity computation algorithms that are used in the data-relay orbital simulator for fast computational speeds.

### 6.2.2. Simulation memory usage and computational speed

The orbital position and velocity of a satellite is often stored as a state-vector in the frame of reference. This state-vector has six components, three for position and three for velocity:

$$\vec{r} = r_x\hat{\imath} + r_y\hat{\jmath} + r_y\hat{k} \qquad \vec{v} = v_x\hat{\imath} + v_y\hat{\jmath} + v_y\hat{k} \tag{6.2}$$

where the vectors $\hat{\imath}$, $\hat{\jmath}$ and $\hat{k}$ are the unit vectors of the ECIF. The second challenge comes with storing these state-vectors in memory between computation steps. In computing the typical size for a single precision floating point number (`numpy.float32`) is 32-bits [191]. Which means that storing one state-vector having six components for one satellite at one time step takes at least 192-bits or 24-bytes. Scaling up this problem to a simulation time of seven days with a time step of 1 second results into 14515200-bytes or 14-megabytes for storing the state-vector of a single satellite over one week. Which means that for 5000 satellites this would take 72576-megabytes or 72.6-gigabytes.

As this amount of memory exceeds that of a typical computer it is not feasible to first compute the positions of the satellites on throughout the simulation time for all time steps up to the simulation time of seven weeks before computing the line-of-sight vectors. There are several ways to overcome this challenge such as processing the data up in small batches and writing intermediate results to a hard drive to reduce memory usage. However, this is not a particularly elegant solution for the line-of-sight problem when considering the data-relay architecture with NGSO mega constellations. The only interesting state-vectors to store at a time step are those of the satellites that have line-of-sight. For each time step more than half of the satellites in the NGSO (mega-)constellations will be on the other side of the Earth. Therefore, if the line-of-sight problem can be computed fast to decide which state-vectors to store in the contact opportunities the memory usage of the simulation can be greatly reduced.

### 6.2.3. Geometry computations

The last two steps to solving the line-of-sight problem is to determine if the line-of-sight vector is unobstructed and lies within the FoVs of each satellite. These steps require some geometry computations which with the large amount of satellites also become computationally intensive. As stated in the previous section, it would be beneficial to be able to quickly perform this computation step to determine

[1] If $m_k >> m_i$ then $\mu \approx Gm_k = k$ where $k$ is the gravitational constant of the attractor. For Earth $k_{Earth} \approx 3.986 \cdot 10^{14} m^3/s^{-2}$

[2] See section section 6.4.5 for a basic implementation of a J2 perturbation.

which satellite state-vectors are worth storing before moving to the next time step. Section 6.5 will describe the algorithms used to compute if the line-of-sight vector is obstructed.

## 6.3. Simulator top-level description

Figure 6.2 shows a top-level overview of the data-relay orbital simulator. The simulator takes a user defined scenario as input that can be build from different objects such as single satellite, planes of satellites or a constellation of satellites that specified by their classical orbital elements. The scenario is initialized with settings specifying start & stop date-time, time-step and which line-of-sight pairs are to be analysed. These line-of-sight pairs could be any two objects in the simulator, for example satellite-to-satellite or satellite-to-constellation pairs.

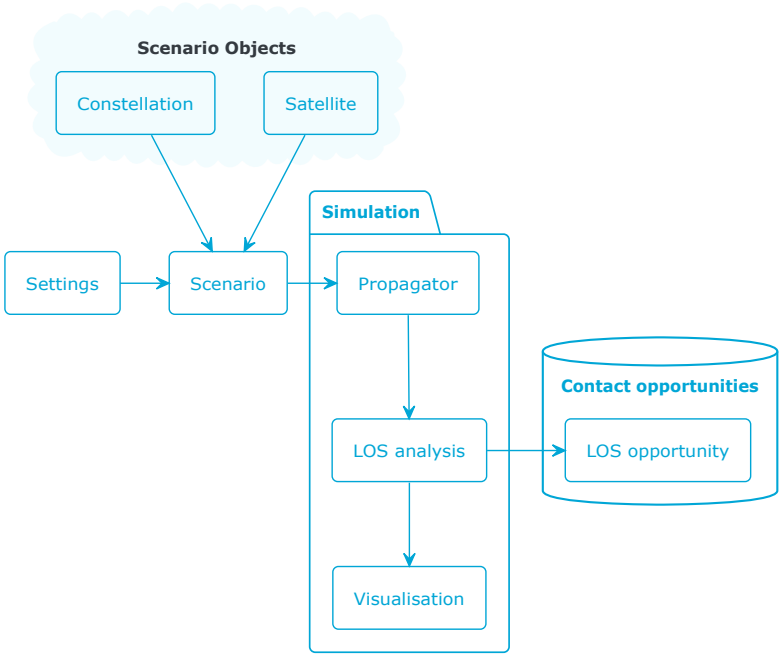


Figure 6.2: Top-level overview of the data-relay orbital simulator

After the scenario is defined it can be simulated. The simulator consist of an orbital propagator module, a line-of-sight analysis module and a visualisation module. The propagator module propagates the position of the satellites in the scenario through each of the time steps. The line-of-sight analysis module computes which of the pairs of satellites have line-of-sight at each time step and stores this information as in a database of contact opportunities. The state of the scenario can be visualised in a two-dimensional and three-dimensional representations showing the positions of the satellites and which satellites have line-of-sight.

### 6.3.1. General operation

The data-relay orbital simulator is specifically designed for simulation of (mega-)constellations with a large number of satellites. It differentiates from other orbital simulators by the order in which the computations are performed and the use of vectorization.

To minimize memory usage during the simulation the data-relay orbital simulator uses a just-in-time approach. In this approach, all the computation steps necessary to find the contact opportunities are performed before moving to the next time-step. After performing the computation for a single time step only the state-vectors for the satellite pairs in the contact opportunities are stored and the rest of the data is discarded. All computation therefore happens in a main loop, that iterates over each time step. This differs from an ahead-of-time approach where the orbital positions at all time steps are computed and stored first before moving to line-of-sight computation.

The just-in-time approach is combined with vectorized algorithms for each of the computational steps in the simulator. This includes a vectorized algorithm for the orbital propagator and vectorized

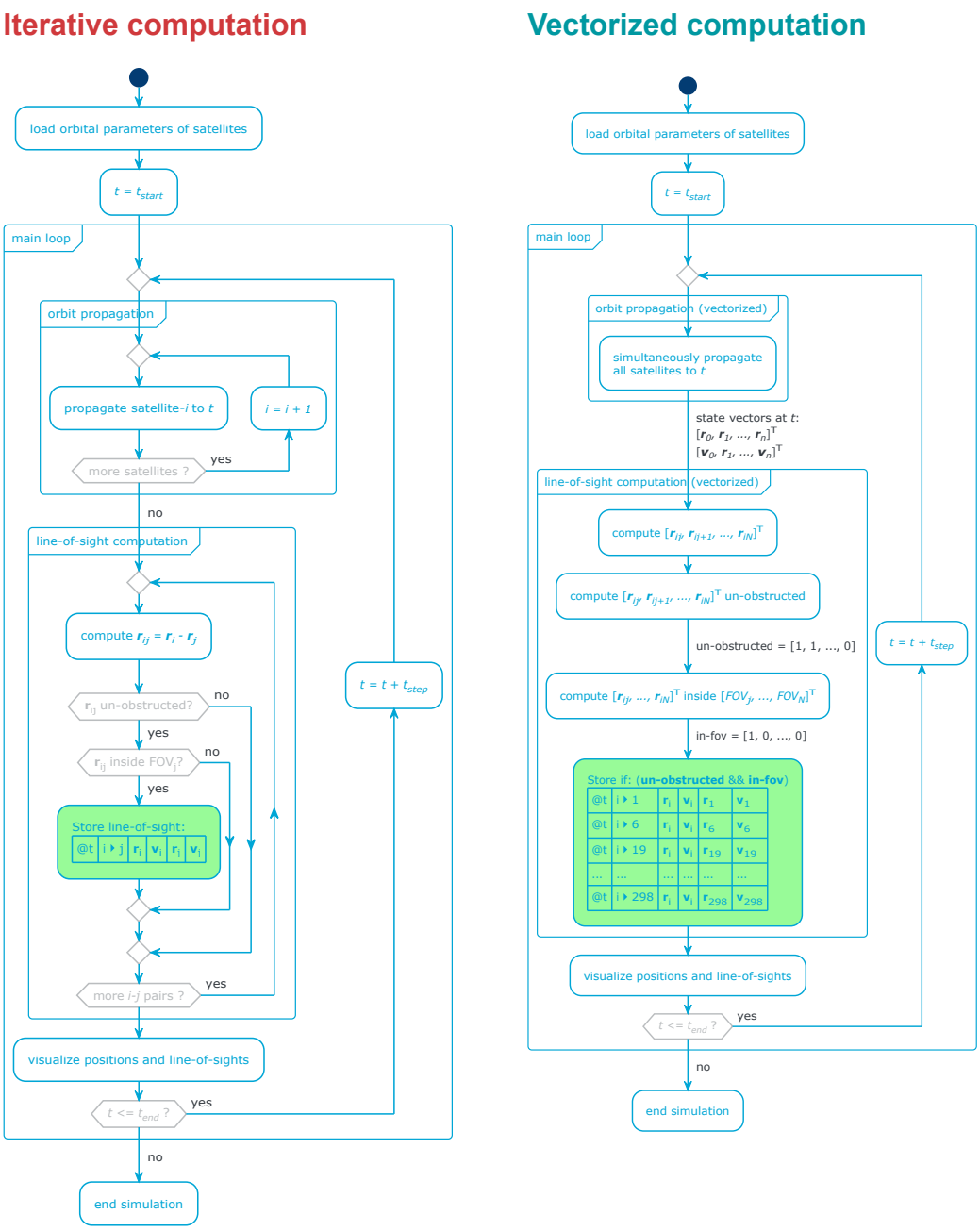


(a) Iterative computation with inner loops

(b) Vectorized computation without inner loops

Figure 6.3: The data-relay orbital simulator uses vectorized computation as shown on the right for the orbital propagation and line-of-sight computation algorithms

algorithms of the geometry computations for the line-of-sight analysis. Figure 6.3 shows the general operation of the data-relay orbital simulator with iterative computation and vectorized computation. In the iterative case the main loop of the simulation contains two inner loops with three main algorithms: an algorithm for the orbital propagation of the satellite, an algorithm to compute if the line-of-sight vector is obstructed (by the Earth) and an algorithm to compute if the the line-of-sight vector lies within the field-of-view of the satellites. First the positions of all the satellites in the scenario are propagated to the new time-step. Then for each line-of-sight pair the line-of-sight vector $r_{ij}$ is computed and by computational geometry it is checked whether this vector is un-obstructed and lies within the field-of-view. If so, this pair is stored in the contact opportunity dataset at this time step with the state-vectors for both satellites and the next pair is computed. The iterative approach repeatedly calls in the inner loops to propagate

each satellite and compute line-of-sight for each pair making the computation sequential. It would therefore make iterative approach computationally slow with the simulation time directly proportional to the number of satellites.

Instead vectorized algorithms were developed for each computational step. A orbital propagator is used that can compute the position of all satellites at once using matrix computations that are fast on typical processors. Similarly the computation of the geometrics for Earth obstruction and field-of-view are implemented in a vectorized algorithm and all pairs are evaluated at once to determine which are stored. This greatly reduces the computation time per time step, allowing the computations (and visualisations) to be performed just-in-time. The data-relay orbital simulator is written in Python and uses the Numba package to compile parts of the algorithms to C to gain an even higher performance [188]. This results in an computation time of about 30 minutes for a simulation time of 7 days for one target and a constellation of 4000+ satellites. By only storing the state-vectors of the satellites in a line-of-sight pair and discarding the rest the memory usage during the simulation is minimized. Less than 2 GB of memory is used during the simulation and the output files are around 500 MB.

The data-relay orbital simulator considers the FoV of one of the satellites to be unconstrained and fully spherical. Although it can operate with both satellites having a constraint field-of-view, in the simulations for this work it is initially assumed that the small satellite has an unconstrained field-of-view. Later in the optimization part of chapter 8 the field-of-view of the small satellites will be constraint in relation to the specifications of the communication system during the design optimization.

### 6.3.2. Scenario definition and orbital parameter storage

A scenario in the data-relay orbital simulator is defined prior to running a simulation. A scenario can be build by the user by adding objects such as satellites, satellite planes and constellations. After defining the objects in the scenario analyses can be specified such as a spatial coverage analysis or line-of-sight analysis. The scenario objects are stored in a tree-structure. Each element in the tree describes one (for a single satellite) or multiple sets (plane or constellation) of orbital parameters. Figure 6.4 shows an example of a scenario definition containing two small satellites in 400 km and 500 km orbits and the SpaceX Starlink constellation as specified in [175].

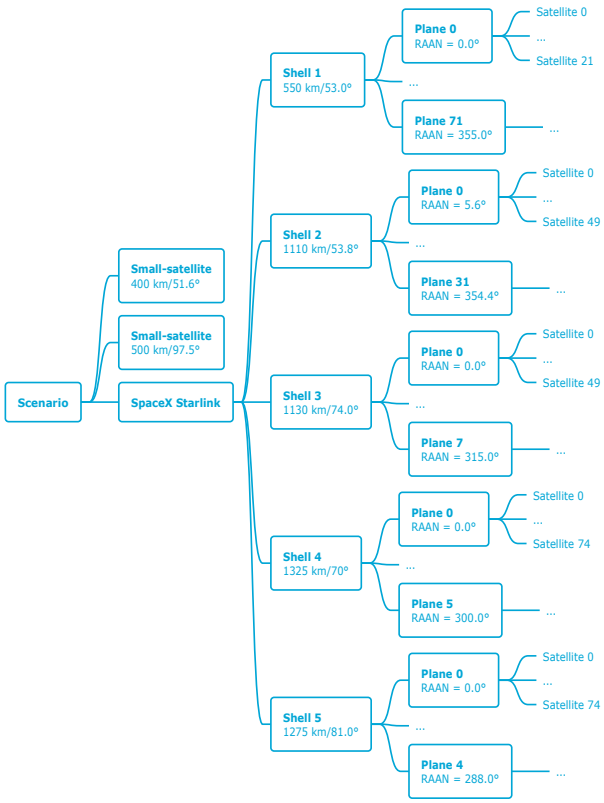


Figure 6.4: Example of a scenario definition for the data-relay orbital simulator stored in a tree-memory structure. This scenario consists of two small satellites in 400k and 500 km orbits and the SpaceX Starlink constellation as described in [175]

The satellites in the Starlink constellation are first grouped by their shell and then their orbital plane. By doing so the analyses in the data-relay orbital simulator can be used with respect to the whole constellation, a shell, an orbital plane or a single satellite in the constellation. Upon start of the simulation the tree of scenario objects is flattened into array of orbital parameters. The definition of the six (classical) orbital parameters that are used are shown in table 6.1.

Table 6.1: Definition of the classical orbital elements

| Element | Symbol | Variable in Python | Unit |
|---|---|---|---|
| semi-major axis | $a = \frac{p}{1-e^2}$ | `a` | [km] |
| eccentricity | $e$ | `ecc` | [-] |
| inclination | $i$ | `inc` | [rad] |
| right ascension of the ascending node | $\Omega$ | `raan` | [rad] |
| argument of perigee | $\omega$ | `argp` | [rad] |
| true anomaly at epoch | $\theta$ | `nu0` | [rad] |

After flatting 1D (column) array are obtained for each of the six orbital parameters[3]:

$$\boldsymbol{p} = \begin{bmatrix} p_0 & p_1 & \dots & p_N \end{bmatrix}^T \tag{6.3}$$

$$\boldsymbol{e} = \begin{bmatrix} e_0 & e_1 & \dots & e_N \end{bmatrix}^T \tag{6.4}$$

$$\boldsymbol{i} = \begin{bmatrix} i_0 & i_1 & \dots & i_N \end{bmatrix}^T \tag{6.5}$$

$$\boldsymbol{\Omega} = \begin{bmatrix} \Omega_0 & \Omega_1 & \dots & \Omega_N \end{bmatrix}^T \tag{6.6}$$

$$\boldsymbol{\omega} = \begin{bmatrix} \omega_0 & \omega_1 & \dots & \omega_N \end{bmatrix}^T \tag{6.7}$$

$$\boldsymbol{\theta} = \begin{bmatrix} \theta_0 & \theta_1 & \dots & \theta_N \end{bmatrix}^T \tag{6.8}$$

These six arrays of orbital parameters facilitate vectorized computation of the state-vectors for position $\vec{\boldsymbol{r}}$ and velocity $\vec{\boldsymbol{v}}$ and line-of-sight during the simulation. The tree memory structure allows for easy creation of the scenario definition and dereferencing of the orbital elements to each of the satellites in an object-oriented manner.

## 6.4. Vectorized orbit propagation

The orbits considered in the simulator are governed by the fundamental equation of relative two-body motion eq. (6.1). These orbits are often referred to as Keplerian orbits and follow elliptical paths around their attractor. The data-relay orbital simulator includes a two-body orbit propagator to find the positions and velocities of the satellites in the scenario at each time-step. In order to minimize computation time for the propagation of 5000 satellites a vectorized implementation is used. The following sections will first discuss the fundamental equations for the orbital position and velocity as function of time after which the vectorized implementation of the propagator is presented.

### 6.4.1. The orbit equation

The position and velocity of Keplerian orbits can be described in the perifocal frame by using polar coordinate system as shown in fig. 6.5. In this coordinate system the position of the satellite is defined by the length $r$ of the position vector $\vec{r}$ from the focal point and the angle from the apsis line $\theta$ called the true anomaly. The velocity $\vec{v}$ of the satellite can be composed into a radial component $\vec{v}_r$ and a tangential component $\vec{v}_\perp$. As the perifocal frame lies up with the orbital plane of the satellite, the satellite is travelling in plane and the position and velocity do not have transverse components.

The length $r$ of the position vector depends on the mean anomaly and can be derived from the fundamental equation of relative two-body motion eq. (6.1) by using the angular moment. This derivation can be found in Curtis [190, p. 74 - 79]. The length of the position vector is described by the orbit

[3] In this report a bold-face notation is used to indicate an 1D *array* of scalar values, i.e. $\boldsymbol{x} = [x_0, x_1, \dots, x_N]^T$. An arrow notation is used to indicate a *vector* with xyz components, i.e. $\vec{r} = [x, y, z]^T$. In case of an *array of vectors* a bold-face arrow notation is used, i.e. $\vec{\boldsymbol{r}} = [[x_0, y_0, z_0]^T, [x_1, y_1, z_1]^T, \dots, [x_N, y_N, z_N]^T]^T$. This array of vectors has size $N \times 3$.

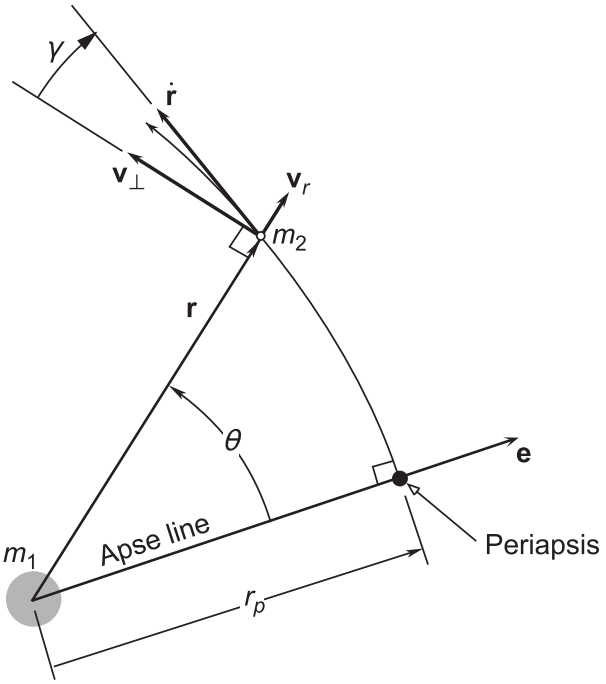


Figure 6.5: Definitions of the position and velocities in polar coordinates, from H. Curtis [190, Figure 2.13]

equation:

$$r = \frac{p}{1 + ecos\theta} \tag{6.9}$$

where $p$ is the parameter of the orbit[4] and $e$ the eccentricity of the orbit are constants and $\theta$ true anomaly which is the time varying quantity that changes $r$ through the path of the orbit. Similarly, the tangential component of the velocity is defined as [190, p. 80]:

$$v_\perp = \frac{\mu}{h}(1 + e \cdot cos\theta) \tag{6.10}$$

where $h$ is the angular momentum of the satellite and $\mu$ is the standard gravitational parameter. Finally, the radial component of the velocity is defined as [190, p. 81]:

$$v_r = \frac{\mu}{h} ecos\theta. \tag{6.11}$$

The equations eq. (6.9), eq. (6.10) and eq. (6.11) define the position and velocity in the perifocal frame as a function of the true anomaly $\theta$. Finding the position of a satellite at a specific time or propagating the position of the satellite from the defined epoch to time-of-flight, is for Keplerian orbits equivalent to finding the the true anomaly $\theta$ at that time and computing the position and velocity using these equations. For a perfectly circular orbit this becomes straightforward as the eccentricity equals zero ($e = 0$) making the position and velocity components constant, and the true anomaly $\theta$ is directional proportional by the orbital period $T$ to the time-of-flight $t$: $\theta = \frac{2\pi}{T}t$. The goal is however to support all elliptical orbits having $e < 1$ and the next section will discuss how the true anomaly $\theta$ can be found as function of time for all elliptical orbits.

### 6.4.2. Kepler's equation

In order to define the true anomaly $\theta$ it is helpful first define the mean anomaly for the elliptical orbit that varies monotonically to the time-of-flight $t$ and is proportional to the orbital period [190, eq. 3.8]:

$$M_e = n \cdot t \tag{6.12}$$

[4] Historically the parameter of the orbit is called the semi-latus rectum [190, p. 81] and equal to the ratio of the angular momentum squared and the standard gravitational parameter: $p = \frac{h^2}{\mu}$

where $n = 2\pi/T$ is the mean motion which can be calculated as:

$$n = \frac{2\pi}{T} = \sqrt{\mu\left(\frac{1-e^2}{p}\right)^3} \tag{6.13}$$

with orbital period $T$ equal to [190, eq. 2.82]:

$$T = \frac{2\pi}{\mu^2}\left(\frac{h}{\sqrt{1-e^2}}\right)^3. \tag{6.14}$$

The mean anomaly is a fictitious quantity that increases with the average angular velocity (the mean motion) of $2\pi/T$ and is equal to the true anomaly for circular orbits.

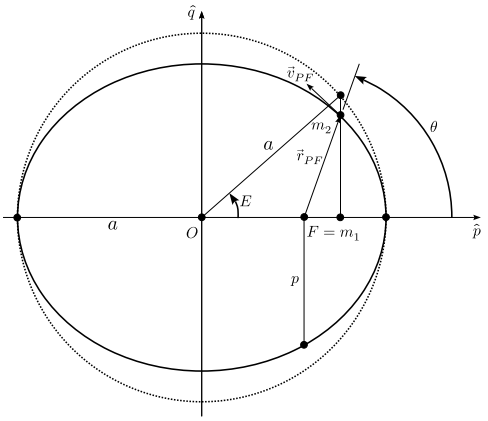


Figure 6.6: Definition of the eccentric anomaly angle $E$, the true anomaly $\theta$, parameter of the orbit $p$ and state-vectors in the perifocal frame. Adapted from Howard Curtis [190, Figure 3.3]

A second useful quantity to define is the eccentric anomaly angle $E$ shown in fig. 6.6. The eccentric anomaly can be related to the true anomaly $\theta$ as [192, p. 160]:

$$E = 2\tan^{-1}\left(\sqrt{\frac{1-e}{1+e}}\tan\frac{\theta}{2}\right) \tag{6.15}$$

$$\theta = 2\tan^{-1}\left(\sqrt{\frac{1+e}{1-e}}\tan\frac{E}{2}\right) \tag{6.16}$$

The use of the mean anomaly and the eccentric anomaly becomes clear after introducing the key equation to finding the true anomaly as function of the time-of-flight, Kepler's equation [192, eq. 3.14]:

$$M_e = E - e\sin E \tag{6.17}$$

The mean anomaly relates to the time-of-flight as per eq. (6.12), Kepler's equation eq. (6.17) links the mean anomaly to the eccentric anomaly and the eccentric anomaly relates to the true anomaly. The combination of these three equations allows for determination of the true anomaly of a two-body elliptical orbit as function of the time-of-flight, and thereby determine the orbital position and velocity as a function of the time-of-flight.

The Kepler's equation in eq. (6.17) is transcendental for the eccentric anomaly and therefore it cannot be directly solved. This is known as Kepler's problem and finding the eccentric anomaly from the mean anomaly requires the use of iterative methods such as Newton's method. Alternatively, Kepler's equation can be approximated by different function that allows for direct solving of the eccentric anomaly. By using such an approximation it is not necessary to perform iterations making such an algorithm suitable for vectorization and fast computation. The algorithm by F. Landis Markley [193] is such an non-iterative algorithm that solves Kepler's equation. This algorithm was used in a vectorized implementation in the propagator of the data-relay orbital simulator. The next section will discuss this implementation.

### 6.4.3. Markley propagator

The algorithm of F. Landis Markley solves Kepler's equation by using a fifth-order refinement of the solution of a cubic equation [193]. The maximum relative error of this algorithm is less than $10^{-18}$, which exceeds the capacity of double-precision[5] computer arithmetic, i.e. it exceeds the precision of how numbers stored and manipulated in computers.

The algorithm of Markley starts with a Padé approximation for $\sin E$ that is dependent on a parameter $\alpha$ [193, eq. 2]:

$$\sin E \approx \sigma(\alpha, E) = \frac{6\alpha - (\alpha - 3)E^2}{6\alpha + 3E^2} E. \tag{6.18}$$

Substitution of this algorithm into Kepler's equation of eq. (6.17) gives the cubic equation to be solved [193, eq. 4]:

$$[3(1-e) + \alpha e]\, E^3 - 3M_e E^2 + 6\alpha(1-e)E - 6\alpha M_e = 0. \tag{6.19}$$

The value for $\alpha$ is chosen as:

$$\alpha(e, M_e) = \frac{3\pi^2 + 1.6\pi(\pi - |M_e|)/(1+e)}{\pi^2 - 6} \tag{6.20}$$

which gives a relative error in the order of $10^{-4}$ when used to compute the eccentric anomaly in the elliptical range ($0 \leq e \leq 1$).

The first order solution to Kepler's equation using the cubic equation of eq. (6.19) can be found as [193, eq. 15]:

$$E_1 = \frac{1}{d}\left(\frac{2rw}{w^2 + wq + q^2} + M_e\right) \tag{6.21}$$

with [193, eq. 5, 9, 10, 14]:

$$d = 3(1-e) + \alpha e \tag{6.22}$$

$$q = 2\alpha d(1-e) - {M_e}^2 \tag{6.23}$$

$$r = 3\alpha d(d - 1 + e)M_e + {M_e}^3 \tag{6.24}$$

$$w = \left(|r| + \sqrt{q^3 + r^2}\right)^{2/3} \tag{6.25}$$

This first-order solution would have a relative error of $10^{-4}$. The aim of the paper by Markley was to find a computational method yielding errors smaller thatn the least significant bit of a double-precision floating point number. By using a fifth order refinement based on the zeros of the polynomial approximation [193, eq. 21]:

$$f(E) = E - e\sin E - M_e \tag{6.26}$$

a relative error smaller than $10^{-18}$ can be achieved. The fifth-order refined estimate of the eccentric anomaly is given by [193, eq. 29]:

$$E_5 = E_1 + \delta_5(E_1) \tag{6.27}$$

where the fifth order correction $\delta_5$ is computed as [193, eq. 22-28]:

$$\delta_5(E) = \frac{f(E)}{f'(E) + \frac{1}{2}\delta_4(E)f''(E) + \frac{1}{6}\delta_4^2(E)f'''(E) + \frac{1}{24}\delta_4^3(E)f''''(E)}, \tag{6.28}$$

$$\delta_4(E) = \frac{f(E)}{f'(E) + \frac{1}{2}\delta_3(E)f''(E) + \frac{1}{6}\delta_3^2(E)f'''(E)}, \tag{6.29}$$

$$\delta_3(E) = \frac{f(E)}{f'(E) - \frac{1}{2}\delta_3(E)f''(E)/f'(E)}, \tag{6.30}$$

$$f'(E) = 1 - e\cos E, \tag{6.31}$$

$$f''(E) = e\sin E, \tag{6.32}$$

$$f'''(E) = e\cos E = 1 - f'(E), \tag{6.33}$$

$$f''''(E) = -e\sin E = -f''(E). \tag{6.34}$$

[5] A double-precision type i.e. a `numpy.float64` is 64-bits in size[191], double that of the example in section 6.2.2

The suitability of Markley's algorithm for vectorized computation comes from the fixed number of refinement iterations used in order to obtain sufficient accuracy for double-precision floating point computations. The refinement equations eq. (6.29) to eq. (6.34) require only two (slow) trigonometric function evaluations ($\sin E$ and $\cos E$). In addition, all equations in the algorithm operate on scalars only making them suitable for vectorization, i.e. all equations are shaped as $y = g(x)$ which means they can easily be altered to use one-dimensional arrays to get $\boldsymbol{y} = g(\boldsymbol{x})$, where $\boldsymbol{x} = [x_1, x_2, ..., x_n]$.

The implementation of the open source `poliastro` Python orbital mechanics package of Markley's algorithm was used as a starting point [187]. Minor alterations were made and tested (see [194]) to allow the function to be called using one-dimensional arrays for the orbital parameters. These arrays are constants defined by the classical orbital parameters. They are initialised from the scenario definition (see section 6.3.2) and do not change in the main-loop of the simulation. Therefore only variable that changes in the main-loop is the time-of-flight for which the new true anomaly is to be computed. To further increase the computational speed of the orbital propagator the algorithm is compiled to C using the Numba Python package [188].

### 6.4.4. Vectorized state-vector computation

After propagating the value of the true anomaly to the specified time-of-flight, the new state-vectors of the satellites can be computed. Similarly to the propagation this is done in a vectorized implementation to avoid inner-loops and achieve high performance. This computation is performed in two steps, first the state-vectors are computed in the perifocal frame of fig. 6.5 after which a transformation is applied to get the state-vectors in the Earth centred inertial frame (ECIF).

The positions and velocities in the perifocal frame are calculated from the gravitational parameter $\mu$, the parameter of the orbit $p$, the eccentricity $e$and the propagated true anomaly $\theta$. Following eqs. (6.9) to (6.11), the magnitudes of the position and velocity in the perifocal frame can be defined as:

$$r_{PF} = (1 - e\cos\theta)^{-1} p \tag{6.35}$$

$$v_{PF} = \frac{\mu}{h} = \sqrt{p^{-1}\mu}. \tag{6.36}$$

The pqw-components of the position vector in the perifocal frame are calculated as follows:

$$r_p = r_{PF}\cos\theta \tag{6.37}$$

$$r_q = r_{PF}\sin\theta \tag{6.38}$$

$$r_w = 0 \tag{6.39}$$

$$\vec{r}_{PF} = \begin{bmatrix} r_p & r_q & r_w \end{bmatrix} \tag{6.40}$$

Similarly for the pqw-components for the velocity vector in the perifocal frame:

$$v_p = v_{PF}(-\sin\theta) \tag{6.41}$$

$$v_q = v_{PF}(e + \cos\theta) \tag{6.42}$$

$$v_w = 0 \tag{6.43}$$

$$\vec{v}_{PF} = \begin{bmatrix} v_p & v_q & v_w \end{bmatrix}. \tag{6.44}$$

The w-component for both the position and velocity vector is zero because the satellite moves in the perifocal frame. The state-vectors in the perifocal frame spanned by vectors ($\hat{p}$,$\hat{q}$,$\hat{w}$), can be transformed to the ECIF spanned by the vectors ($\hat{i}$,$\hat{j}$,$\hat{k}$) by using a chain of (3-1-3) rotation matrices [187] with angles $-\omega$, $-i$ and $-\Omega$:

$$\begin{bmatrix} \hat{i} \\ \hat{j} \\ \hat{k} \end{bmatrix} = \begin{bmatrix} \cos\Omega & -sin\Omega & 0 \\ \sin\Omega & cos\Omega & 0 \\ 0 & 0 & 1 \end{bmatrix} \begin{bmatrix} 1 & 0 & 0 \\ 0 & \cos i & -\sin i \\ 0 & \sin i & \cos i \end{bmatrix} \begin{bmatrix} \cos\omega & -\sin\omega & 0 \\ \sin\omega & \cos\omega & 0 \\ 0 & 0 & 1 \end{bmatrix} \begin{bmatrix} \hat{p} \\ \hat{q} \\ \hat{w} \end{bmatrix}. \tag{6.45}$$

Although these rotation matrices are an elegant formulation of the transformation it is not suited for fast computation. A fast computation can be obtained by recognizing that the transformation in eq. (6.45) is

constant as $\omega$, $-i$ and $\Omega$ are constants and therefore the result only has to be calculated once[6]. Then the transformation can simply be vectorized by writing out the relations:

$$\begin{bmatrix} \hat{i} \\ \hat{j} \\ \hat{k} \end{bmatrix} = \begin{bmatrix} p_i & q_i & w_i \\ p_j & q_j & w_j \\ p_k & q_k & w_k \end{bmatrix} \begin{bmatrix} \hat{p} \\ \hat{q} \\ \hat{w} \end{bmatrix} \tag{6.46}$$

having:

$$p_i = \cos\omega\cos\Omega - \sin\omega\sin\Omega\cos i \tag{6.47}$$
$$p_j = \cos\omega\sin\Omega + \sin\omega\cos\Omega\cos i \tag{6.48}$$
$$p_k = \sin\omega\sin i \tag{6.49}$$
$$q_i = -\sin\omega\cos\Omega - \cos\omega\sin\Omega\cos i \tag{6.50}$$
$$q_j = -\sin\omega\sin\Omega + \cos\omega\cos\Omega\cos i \tag{6.51}$$
$$q_k = \cos\omega\sin i \tag{6.52}$$
$$w_i = \sin\Omega\sin i \tag{6.53}$$
$$w_j = -\cos\Omega\sin i \tag{6.54}$$
$$w_k = \cos i. \tag{6.55}$$

The values $p_i$, $p_j$, $p_k$, $q_i$, $q_j$, $q_k$, $w_i$, $w_j$ and $w_k$ can be calculated once at the beginning of the simulation for each satellite in the scenario thereby avoiding the trigonometric evaluations in the main loop. Defining 1D arrays to combine the transformation coefficients for $N$ satellites:

$$\boldsymbol{p}_i = \begin{bmatrix} p_{i,1} & \dots & p_{i,N} \end{bmatrix}^T \quad \boldsymbol{q}_i = \begin{bmatrix} q_{i,1} & \dots & q_{i,N} \end{bmatrix}^T \quad \boldsymbol{w}_i = \begin{bmatrix} w_{i,1} & \dots & w_{i,N} \end{bmatrix}^T \tag{6.56}$$
$$\boldsymbol{p}_j = \begin{bmatrix} p_{j,1} & \dots & p_{j,N} \end{bmatrix}^T \quad \boldsymbol{q}_j = \begin{bmatrix} q_{j,1} & \dots & q_{j,N} \end{bmatrix}^T \quad \boldsymbol{w}_j = \begin{bmatrix} w_{j,1} & \dots & w_{j,N} \end{bmatrix}^T \tag{6.57}$$
$$\boldsymbol{p}_k = \begin{bmatrix} p_{k,1} & \dots & p_{k,N} \end{bmatrix}^T \quad \boldsymbol{q}_k = \begin{bmatrix} q_{k,1} & \dots & q_{k,N} \end{bmatrix}^T \quad \boldsymbol{w}_k = \begin{bmatrix} w_{k,1} & \dots & w_{k,N} \end{bmatrix}^T. \tag{6.58}$$

Starting from the individual pqw-components, the positions in the ECIF are computed as:

$$\boldsymbol{r}_i = \boldsymbol{r}_p \odot \boldsymbol{p}_i + \boldsymbol{r}_q \odot \boldsymbol{q}_i + \boldsymbol{r}_w \odot \boldsymbol{w}_i \tag{6.59}$$
$$\boldsymbol{r}_j = \boldsymbol{r}_p \odot \boldsymbol{p}_j + \boldsymbol{r}_q \odot \boldsymbol{q}_j + \boldsymbol{r}_w \odot \boldsymbol{w}_j \tag{6.60}$$
$$\boldsymbol{r}_k = \boldsymbol{r}_p \odot \boldsymbol{p}_k + \boldsymbol{r}_q \odot \boldsymbol{q}_k + \boldsymbol{r}_w \odot \boldsymbol{w}_k \tag{6.61}$$

$$\vec{\boldsymbol{r}}_{ECI} = \begin{bmatrix} \vec{r}_{ECI,1} \\ \vdots \\ \vec{r}_{ECI,N} \end{bmatrix} = \begin{bmatrix} \boldsymbol{r}_i & \boldsymbol{r}_j & \boldsymbol{r}_k \end{bmatrix} \tag{6.62}$$

and similarly for the velocities in the ECIF:

$$\boldsymbol{v}_i = \boldsymbol{v}_p \odot \boldsymbol{p}_i + \boldsymbol{v}_q \odot \boldsymbol{q}_i + \boldsymbol{v}_w \odot \boldsymbol{w}_i \tag{6.63}$$
$$\boldsymbol{v}_j = \boldsymbol{v}_p \odot \boldsymbol{p}_j + \boldsymbol{v}_q \odot \boldsymbol{q}_j + \boldsymbol{v}_w \odot \boldsymbol{w}_j \tag{6.64}$$
$$\boldsymbol{v}_k = \boldsymbol{v}_p \odot \boldsymbol{p}_k + \boldsymbol{v}_q \odot \boldsymbol{q}_k + \boldsymbol{v}_w \odot \boldsymbol{w}_k \tag{6.65}$$

$$\vec{\boldsymbol{r}}_{ECI} = \begin{bmatrix} \vec{v}_{ECI,1} \\ \vdots \\ \vec{v}_{ECI,N} \end{bmatrix} = \begin{bmatrix} \boldsymbol{v}_i & \boldsymbol{v}_j & \boldsymbol{v}_k \end{bmatrix} \tag{6.66}$$

where $\odot$ is the element-wise multiplication operator.

[6] Assuming no perturbations

**Vectorized orbit propagation algorithm**

The equations presented in section 6.4.4 lend themselves well to vectorized computation as they are all element-wise operations on scalar values. Therefore, the resulting position and velocity arrays of vectors having size $N \times 3$ can be computed using just element-wise operations on the initial arrays of orbital parameters ($\boldsymbol{p}$, $\boldsymbol{e}$, $\boldsymbol{i}$, $\boldsymbol{\Omega}$, $\boldsymbol{\omega}$) and the propagated true anomalies ($\boldsymbol{\theta}$).

**Algorithm 1:** Vectorized propagation of true anomaly and computation of state-vectors

**Input:** $\boldsymbol{\mu}, \boldsymbol{p}, \boldsymbol{e}, \boldsymbol{i}, \boldsymbol{\Omega}, \boldsymbol{\omega}, \boldsymbol{\theta}_0, tof$

**Output:** $\vec{\boldsymbol{r}} = \begin{bmatrix} \vec{r}_1 & \dots & \vec{r}_N \end{bmatrix}^T, \vec{\boldsymbol{v}} = \begin{bmatrix} \vec{v}_1 & \dots & \vec{v}_N \end{bmatrix}^T$

/* Lines 1-4 can be computed before main-loop ... */

1 $\boldsymbol{p}_i, \boldsymbol{p}_j, \boldsymbol{p}_k, \boldsymbol{q}_i, \boldsymbol{q}_j, \boldsymbol{q}_k, \boldsymbol{w}_i, \boldsymbol{w}_j, \boldsymbol{w}_k$ = `pwq_to_ijk_vectors`$(\boldsymbol{i}, \boldsymbol{\Omega}, \boldsymbol{\omega})$ // eqs. (6.48) to (6.55)

2 $\boldsymbol{E_0}$ = `theta_to_E`$(\boldsymbol{\theta}_0)$ // eq. (6.15)

3 $\boldsymbol{M_{e,0}}$ = `kepler_equation`$(\boldsymbol{E_0})$ // eq. (6.17)

4 $\boldsymbol{n}$ = `mean_motion`$(\boldsymbol{\mu}, \boldsymbol{e}, \boldsymbol{p})$ // eq. (6.13)

/* Lines 5-12 are computed vectorized during main-loop ... */

5 $\boldsymbol{M_e} = \boldsymbol{n} \cdot tof$ // eq. (6.12)

6 $\boldsymbol{E_1}$ = `markley_cubic`$(\boldsymbol{e}, \boldsymbol{M_e})$ // eqs. (6.20) to (6.25)

7 $\boldsymbol{E} = \boldsymbol{E_1}$ + `markley_refinement`$(\boldsymbol{E_1})$ // eqs. (6.27) to (6.34)

8 $\boldsymbol{\theta}$ = `E_to_theta`$(\boldsymbol{E})$ // eq. (6.16)

/* Compute state-vectors in the PFF eqs. (6.35) to (6.44) */

9 $\begin{bmatrix} \vec{r}_{PF,1} & \dots & \vec{r}_{PF,N} \end{bmatrix}^T, \begin{bmatrix} \vec{v}_{PF,1} & \dots & \vec{v}_{PF,N} \end{bmatrix}^T$ = `rv_pqw`$(\boldsymbol{\mu}, \boldsymbol{p}, \boldsymbol{e}, \boldsymbol{\theta})$

10 $\vec{\boldsymbol{r}}_{PF} = \begin{bmatrix} \vec{r}_{PF,1} & \dots & \vec{r}_{PF,N} \end{bmatrix}^T, \vec{\boldsymbol{v}}_{PF} = \begin{bmatrix} \vec{v}_{PF,1} & \dots & \vec{v}_{PF,N} \end{bmatrix}^T$ // Arrays of state-vectors in the PFF

/* Compute state-vectors in the ECIF eqs. (6.59) to (6.66) */

11 $\begin{bmatrix} \vec{r}_1 & \dots & \vec{r}_N \end{bmatrix}^T, \begin{bmatrix} \vec{v}_1 & \dots & \vec{v}_N \end{bmatrix}^T$ = `pqw_to_eci`$(\vec{\boldsymbol{r}}_{PF}, \vec{\boldsymbol{v}}_{PF}, \boldsymbol{p}_i, \boldsymbol{p}_j, \boldsymbol{p}_k, \boldsymbol{q}_i, \boldsymbol{q}_j, \boldsymbol{q}_k, \boldsymbol{w}_i, \boldsymbol{w}_j, \boldsymbol{w}_k)$

12 $\vec{\boldsymbol{r}} = \begin{bmatrix} \vec{r}_1 & \dots & \vec{r}_N \end{bmatrix}^T, \vec{\boldsymbol{v}} = \begin{bmatrix} \vec{v}_1 & \dots & \vec{v}_N \end{bmatrix}^T$ // Arrays of state-vectors in the ECIF

## 6.4.5. J2 perturbation

The data-relay orbital simulator includes a model for J2 perturbation to capture the first order secular rates of change in the $\Omega$, $\omega$ and true anomaly. A J2 perturbation was included because the some of the satellites of interest are launched in Sun-synchronous orbits that experience a orbital precession. This orbital precession might cause the orbital parameters of a small satellite to move relatively to the constellation over a long period, resulting contact opportunities with different satellites.

Only the first order secular rates (long-term trends) are modelled using the method of averaging of Gauss' planetary equations for the J2 perturbation [195, ch. 10.8] [196, ch. 23]. These first-order secular rates for the classical orbital elements (as function of the unperturbed orbital elements) are described by:

$$\frac{da}{dt} = \frac{de}{dt} = \frac{di}{dt} = 0 \tag{6.67}$$

$$\frac{d\Omega}{dt} = -\frac{3}{2} n J_2 \left(\frac{R}{p}\right)^2 \cos i \tag{6.68}$$

$$\frac{d\omega}{dt} = \frac{3}{4} n J_2 \left(\frac{R}{p}\right)^2 \left(5\cos^2 i - 1\right) \tag{6.69}$$

$$\frac{d\theta}{dt} = n\left(1 + \frac{3}{4} J_2 \left(\frac{R}{a}\right)^2 \left(1 - e^2\right)^{-3/2} \left(3\cos^2 i - 1\right)\right) \tag{6.70}$$

where $n$ is the unperturbed (constant) mean motion and $J2$ is the coefficient for the second zonal term

by the oblateness of the orbiting body.

When the J2 perturbation is included in the simulation, the secular rates in eq. (6.70) are multiplied with the time-of-flight and added to the unperturbed orbital parameters and propagated true anomaly prior to the vectorized state-vector computation of section 6.4.4. Figure 6.7 shows an example[7] of the long-term variation in the right ascension and argument of perigee for a satellite with initial orbital parameters $a = 8059.0km$, $e = 0.171$, $i = 28°$, $\Omega = 45°$, $\omega = 30$ and $\theta_0 = 40°$.

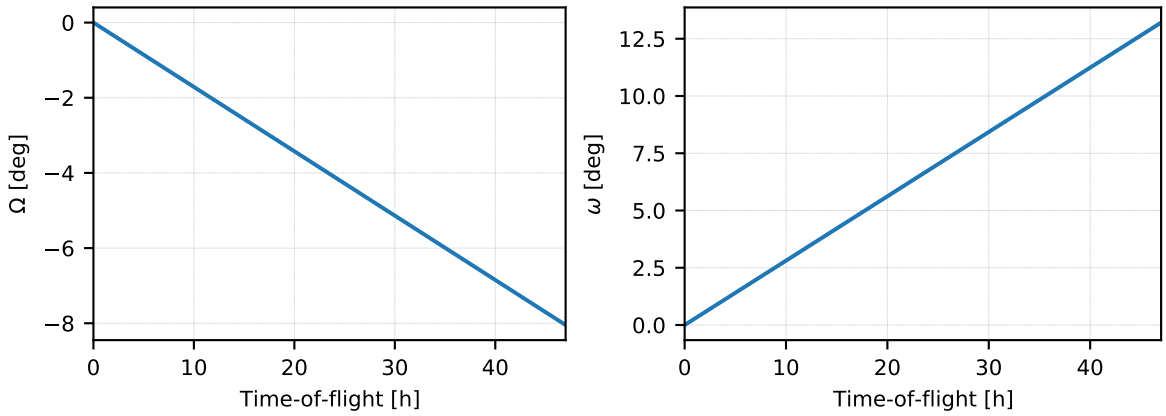


(a) J2 perturbation on the right ascension of the ascending node (b) J2 perturbation on the argument or perigee

Figure 6.7: A basic J2 perturbation model is implemented that captures the first order secular rates of change

## 6.5. Line-of-sight computation

The vectorized orbit propagation described in section 6.4 computes the positions of all satellites in the scenario at a given time instance. The next step is to compute the line-of-sight vectors between the satellites and determine if the small satellite is in view of a NGSO constellation satellite. At a given time instance most of the NGSO constellation satellites will be at the opposite side of the Earth. For these satellites the line-of-sight vector will be blocked by the Earth. This blockage is determined in the Earth blocking algorithm. For the remaining satellites it needs to be determined if the line-of-sight vector is within the operating field-of-view of the satellite. This is determined in the field-of-view algorithm.

### 6.5.1. Earth blocking algorithm

Figure 6.8 shows three satellites, data-relay satellite 1 ($dr1$), data-relay satellite 2 ($dr2$) and the small satellite ($sc$). Two line-of-sight vectors are drawn, one to data-relay satellite 1 ($\vec{r}_{sc \to dr1}$) and one to data-relay satellite 2 ($\vec{r}_{sc \to dr2}$). In this configuration the line-of-sight to satellite 2 is blocked by the Earth so this satellite can be ruled out for establishing the link.

Determining if the line-of-sight vector is blocked is a geometry problem that comes down to determining if the line-of-sight vector intersects the sphere. This geometry problem can be better understood when evaluated in the two-dimensional plane spanned by the position vectors of the two satellites. Figure 6.9 shows this geometry problem in two-dimensions. The point $D$ is the location of the relay satellite, the point $S$ is the location of the small satellite and the point $I$ is the closest point on the line $DS$ to the circle. By observing fig. 6.9 the problem comes down to determining if: 1) the closest point $I$ lies between the points $D$ and $S$, and 2) if the length of the line $OI$ is smaller than the radius of the circle. If both are true, then the line-of-sight is blocked by the sphere. If 1) is not true, the line-of-sight vector might intersect the sphere but not in between the satellites. If 2) is not true then the line-of-sight vector passes the Earth.

The mathematics behind this problem are described in [197]. In this case it is easiest to first determine if the point $I$ lies between the points $D$ and $S$, and then determine if the length of the vector $\vec{I}$ is smaller than the radius of the Earth. All points $\vec{P}$ on the line between the points $S$ and $D$ are described

[7] Equal to fig. 10.14 in [195]

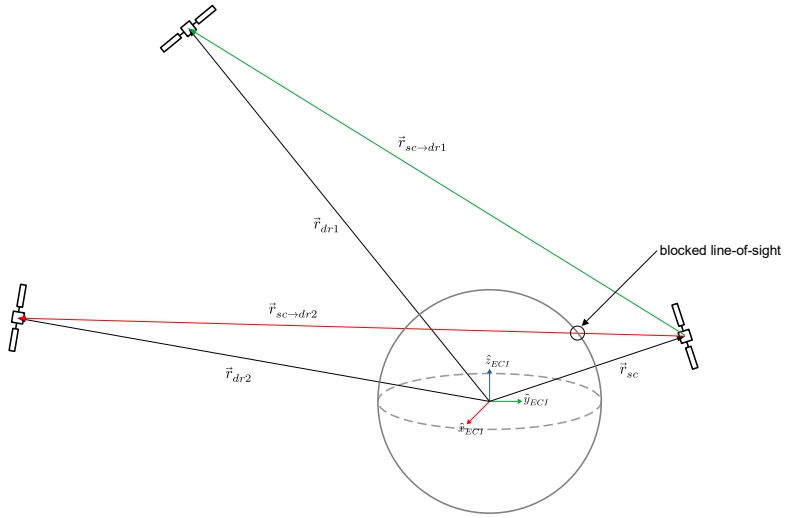


Figure 6.8: Example of blocking of the line-of-sight vectors by the Earth. The line-of-sight vector from the small satellite to data-relay satellite 2 ($\vec{r}_{sc\to dr2}$) is blocked by the Earth

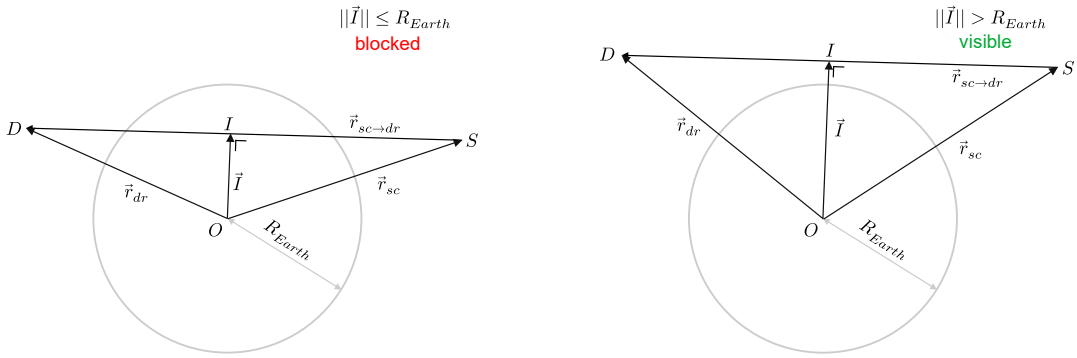


(a) Geometry in which line-of-sight vector is blocked by the Earth

(b) Geometry in which line-of-sight vector passes the horizon

Figure 6.9: The data-relay orbital simulator uses vectorized computation as shown on the right for the orbital propagation and line-of-sight computation algorithms

by:

$$\vec{P} = \vec{r}_{sc} + u \cdot \vec{r}_{sc\to dr}, \tag{6.71}$$

where $u$ is a scalar. For $u = 0$ eq. (6.71) equation gives the point $P = S$ and for $u = 1$ it gives the point $P = D$. Therefore, the value of $u$ should be $0 \leq u \leq 1$ for the closest point to the Earth $I$ if it were to lie between $S$ and $D$.

The closest point $\vec{I}$ to the Earth is perpendicular to the line-of-sight vector $\vec{r}_{sc\to dr}$ and therefore the dot product between these vectors should equal zero:

$$\vec{I} \cdot \vec{r}_{sc\to dr} = 0 \tag{6.72}$$

substituting eq. (6.71) into eq. (6.72) gives:

$$(\vec{r}_{sc} + u \cdot \vec{r}_{sc\to dr}) \cdot \vec{r}_{sc\to dr} = 0 \tag{6.73}$$

Solving eq. (6.73) for $u$ gives:

$$u = \frac{\vec{r}_{sc} \cdot \vec{r}_{sc\to dr}{}^{T}}{\|\vec{r}_{sc\to dr}\|^{2}}. \tag{6.74}$$

Now the position of point $I$ is defined as:

$$\vec{I} = \vec{r}_{sc} + u \cdot \vec{r}_{sc\to dr}. \tag{6.75}$$

If the point $I$ lies between $S$ and $D$, and the distance from the Earth is smaller than the radius of the Earth then the line-of-sight vector is blocked by the Earth. Therefore, the line-of-sight is blocked if:

$$\begin{gathered} 0 \leq u \leq 1 \\ \text{and:} \\ \left\|\vec{I}\right\| \leq R_{Earth} \end{gathered} \tag{6.76}$$

In this algorithm it the shape of the Earth is modelled as a perfect sphere with a constant radius $R_{Earth}$ instead of an oblate spheroid. In this study this assumption is sufficiently accurate as the field-of-view of the NGSO constellation satellites (as discussed in section 4.3) do not extend beyond the horizon. Therefore, line-of-sight vectors that just pass the surface of the Earth (and would be blocked in the case of an oblate spheroid) will not lie within the field-of-view of the NGSO constellation satellites and therefore will not be considered after the field-of-view computation.

**Vectorized Earth blocking algorithm**

The vectorized version of the algorithm is shown in algorithm 2. The algorithm takes the positions of all NGSO satellites as an array of vectors $\vec{\boldsymbol{r}}_{drs}$ of size $N_{dr} \times 3$ where $N_{dr}$ is the number of satellites in the NGSO constellation.

**Algorithm 2:** Earth blocking algorithm

**Input:** $\vec{\boldsymbol{r}}_{drs}, \vec{r}_{sc}$

**Output:** $[block_1, \ldots, block_{N_{dr}}]$ with $los_i \in \{0, 1\}$

1 $\vec{\boldsymbol{r}}_{sc\to drs} = \vec{\boldsymbol{r}}_{drs} - \vec{r}_{sc}$ // Compute line-of-sight vectors

2 $\boldsymbol{num} = \sum_{cols} \left(\vec{\boldsymbol{r}}_{sc\to drs} \odot \vec{r}_{sc}\right)$ // Vectorized numerator of eq. (6.74), $(N_{dr} \times 1)$

3 $\boldsymbol{denum} = \sum_{cols} \left(\vec{\boldsymbol{r}}_{sc\to drs} \odot \vec{\boldsymbol{r}}_{sc\to drs}\right)$ // Vectorized denumerator of eq. (6.74), $(N_{dr} \times 1)$

4 $\boldsymbol{u} = \boldsymbol{num} \oslash \boldsymbol{denum}$ // Element-wise division, $(N_{dr} \times 1)$

5 $\boldsymbol{I} = \vec{r}_{sc} + (\vec{\boldsymbol{r}}_{sc\to drs}{}^T \boldsymbol{u})^T$ // Vectorized closest interception points, eq. (6.75), $(N_{dr} \times 3)$

6 $\left\|\vec{\boldsymbol{I}}\right\| = \sqrt{\sum_{cols} \boldsymbol{I} \odot \boldsymbol{I}}$ // Norm of interception point distance of eq. (6.75), $(N_{dr} \times 1)$

7 $[block_1, \ldots, block_{N_{dr}}] = (0 \leq \boldsymbol{u})^T$ AND $(\boldsymbol{u} \leq 1)^T$ AND $\left(\left\|\vec{\boldsymbol{I}}\right\| < R_{Earth}\right)^T$

Figure 6.10 shows an example of the vectorized line-of-sight blockage computed in the data-relay orbital simulator. The line-of-sight blockage is computed from the cyan satellite to four other satellites,

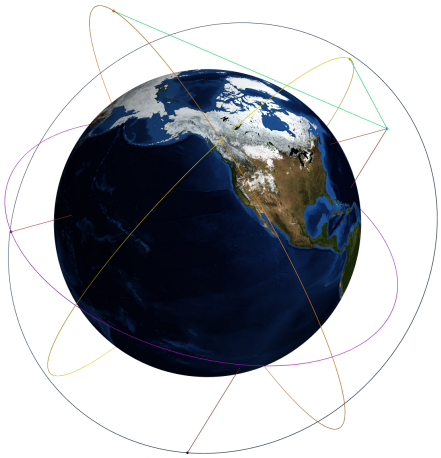

Figure 6.10: Line-of-sight blockage computed in the data-relay orbital simulator. The cyan satellite has line-of-sight (green) with the yellow and orange satellites, but not with the purple and black satellites as these line-of-sight vectors (red) are blocked by the Earth.

yellow, orange, blue and purple. The green lines show unblocked line-of-sight vectors (cyan-yellow, cyan-orange) and red lines show blocked line-of-sight vectors (cyan-purple, cyan-blue).

### 6.5.2. Field-of-view computation

The field-of-view of a satellite defines the operating angles of the communication system of the satellite. This could be by the shape of a (fixed) antenna gain pattern or by the maximum pointing angles of steered spot-beams. Objects inside the FoV can be serviced by the communication system on the satellite. Section 4.3 showed that the field-of-view ranges of the NGSO constellations can be modelled as a cone extending from the satellite towards nadir. If the line-of-sight vector lies within this cone then the satellite is visible and data may be transferred.

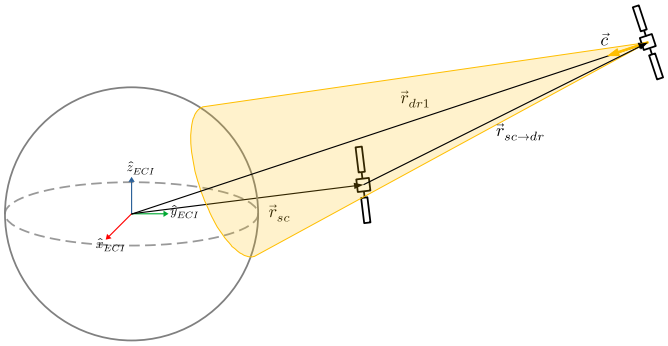


Figure 6.11: All NGSO constellations have their communication systems nadir pointing, servicing users on the ground. Thereby allowing for a simplification in the geometric computation of the field-of-view algorithm.

There are several possible ways to determine if the line-of-sight vector lies within the field-of-view. One way would be to take the vector in the ECIF and perform a coordinate transformation to the SFF of the NGSO satellite using a method such as Euler-angles, rotation matrices or quaternions. While this would be a versatile solution that allows the NGSO satellite to have any orientation it is also computationally intensive. Especially if over 5000 line-of-sight vectors have to be evaluated each time step, and each time step requires re-computation of the transformations.

An alternative computation is found by using a simplification. All NGSO constellation satellites are assumed to have their communication systems nadir pointing to service users on the ground as illustrated in fig. 6.11. Therefore, the pointing of each satellite is known in the ECIF as the satellites are pointing in the opposite direction of their position-vector $\vec{r}_{dr}$. This allows the field-of-view computation to be performed using geometry evaluation in a similar way as to the Earth blocking computation, without requiring coordinate frame transformations.

The field-of-view geometry problem can be better understood in the two-dimensional plane spanned by the position vectors of the two satellites. Figure 6.12 shows this geometry problem in two-dimensions. The point $D$ is the location of the data-relay satellite, the point $S$ is the location of the small satellite and

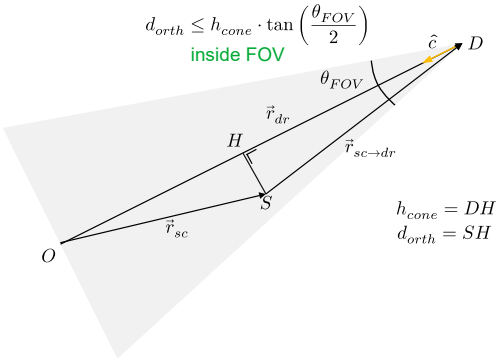


(a) Geometry for satellite inside field-of-view of data-relay satellite

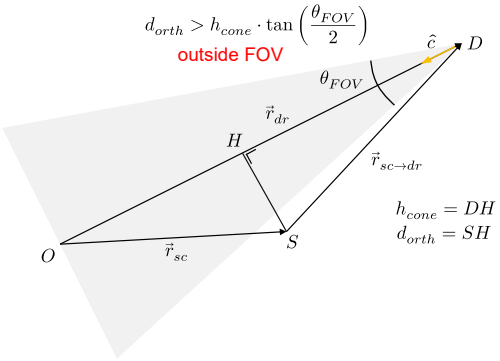


(b) Geometry for satellite outside field-of-view of data-relay satellite

Figure 6.12: The data-relay orbital simulator uses vectorized computation as shown on the right for the orbital propagation and line-of-sight computation algorithms

the point $H$ is the projection of the point $S$ on the line-segment $OD$. In this two-dimensional representation the field-of-view cone is a triangle (grey area) with angle $\theta_{FOV}$.

By observing fig. 6.12 the geometry problem comes down to determining if the segment $HS$ is smaller than the radius of the cone at a distance $DH$ from the tip of the cone. First the nadir pointing unit vector $\hat{c}$ from the data-relay satellite is found:

$$\hat{c} = -\vec{r}_{dr} / \|\vec{r}_{dr}\| \tag{6.77}$$

The distance $DH$ from the tip of the cone can be calculated by the projection (dot-product) of the unit vector $\hat{c}$ and the line-of-sight vector $\vec{r}_{sc\to dr}$:

$$h_{cone} = DH = \vec{r}_{sc\to dr} \cdot \hat{c}^T. \tag{6.78}$$

The orthogonal distance $DH$ is the norm of the difference between $d_{cone} \cdot \hat{c}$ and the line-of-sight vector:

$$d_{orth} = SH = \left\| (d_{cone} \cdot \hat{c}) - \vec{r}_{sc\to dr} \right\|. \tag{6.79}$$

Finally, the small satellite is within the field of view if:

$$d_{orth} \leq h_{cone} \tan \frac{\theta_{FOV}}{2}. \tag{6.80}$$

This algorithm requires only one trigonometric evaluation, the tangent of half the field-of-view, which is a constant and can therefore be computed prior to the simulation.

**Vectorized field-of-view algorithm**

The vectorized version of the field-of-view algorithm algorithm is shown in algorithm 3. The algorithm takes the position-vector of a single small satellite $\vec{r}_{sc}$, the positions of all NGSO satellites as an array of vectors $\vec{\boldsymbol{r}}_{drs}$ $(N_{dr} \times 3)$ in the NGSO constellation and the operating field-of-view as an array $\boldsymbol{\theta}_{FOV}$ $(N_{dr} \times 1)$ . It returns an array of length $N_{dr}$ with values true-or-false whether the satellite is in field-of-view of the respective data-relay satellite.

**Algorithm 3:** Field-of-view algorithm

**Input:** $\vec{\boldsymbol{r}}_{drs}, \vec{r}_{sc}$

**Output:** $[fov_1, \ldots, fov_{N_{dr}}]$ with $fov_i \in \{0, 1\}$

1 $\vec{\boldsymbol{r}}_{sc\to drs} = \vec{\boldsymbol{r}}_{drs} - \vec{r}_{sc}$ // Compute line-of-sight vectors, $(N_{dr} \times 3)$

2 $\hat{\boldsymbol{c}} = -\vec{\boldsymbol{r}}_{drs} \oslash \left\| \vec{\boldsymbol{r}}_{drs} \right\|$ // Computation of nadir pointing vectors, $(N_{dr} \times 3)$

3 $\boldsymbol{h}_{cone} = \sum_{cols} \left( \vec{\boldsymbol{r}}_{sc\to drs} \hat{\boldsymbol{c}}^T \right)$ // eq. (6.78), $(N_{dr} \times 1)$

4 $\boldsymbol{d}_{orth} = \left\| (\boldsymbol{h}_{cone}{}^T \cdot \hat{\boldsymbol{c}})^T - \vec{\boldsymbol{r}}_{sc\to dr} \right\|$ // Vectorized eq. (6.79), $(N_{dr} \times 1)$

5 $[fov_1, \ldots, fov_{N_{dr}}] = \boldsymbol{d}_{orth} \leq \boldsymbol{h}_{cone} \odot \tan \frac{\boldsymbol{\theta}_{FOV}}{2}$

Figure 6.13 shows an example of a satellite (cyan) entering the field-of-view of a constellation satellite (yellow). In the left picture the satellite is outside the conical field-of-view, indicated by the red-coloured line-of-sight vector. In the right picture the satellite is inside the conical field-of-view, indicated by the green-coloured-line of sight vector.

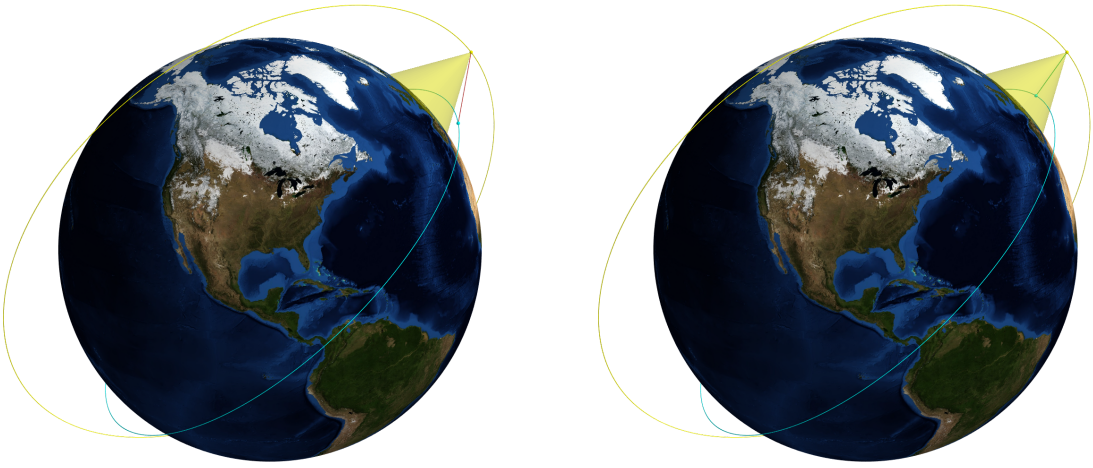

(a) Outside field-of-view (b) Inside field-of-view

Figure 6.13: Example showing a small satellite (cyan) entering field-of-view of a higher orbit satellite (yellow)

## 6.6. Verification

The orbital mechanics of the simulator was validated by comparing a simple scenario in the free version of Analytical Graphics Incorporated Systems Toolkit® 11 using its two body propagator. Figure 6.14 shows a side by side comparison of the simple scenario inside the two simulators. This scenario contains two satellites in circular orbits around Earth having orbital elements as defined in table 6.2.

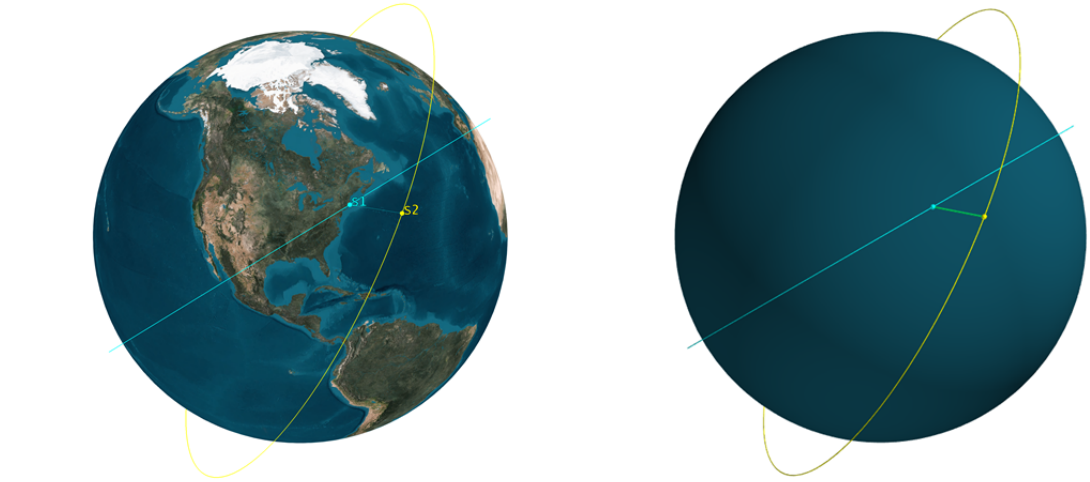


Figure 6.14: Side by side comparison of a simple scenario with AGI's Systems Toolkit® 11 (left) and the purpose build simulator (right)

To compare the two simulators the (inter-satellite) pass duration (the time in which there was a line of sight between the two satellites) between the two satellites are analysed. The higher orbit satellite has a constrained nadir pointing field of view that is varied in each of the cases. The lower orbit satellite has an unconstrained field of view. The analysis period is two hours starting at 1 September 2019 10:00:00.000 UTCG and the step size was set to 1 second.

Table 6.2: Orbital elements of the two satellites in the verification scenario

| | | Satellite 1 | Satellite 2 |
|---|---|---|---|
| Altitude | $h_a$ | 500 km | 1500 km |
| Eccentricity | $e$ | 1 | 1 |
| Inclination | $i$ | 45° | 60° |
| RAAN | $\Omega$ | 0° | 45° |
| True Anomaly | $\theta$ | 15° | 0° |
| Epoch | | J2000 | J2000 |

Table 6.3 shows the pass durations of the first pass encountered in the scenario. The pass duration found in the NGSO relay simulator corresponds to that in STK for all the cases. However, the adaptive step size computation in STK results to a much greater accuracy than is achieved with the fixed 1 second step size of the NGSO relay simulator.

Table 6.3: Orbital elements of the two satellites in the verification scenario

| FoV | STK Simulator | NGSO relay simulator |
|---|---|---|
| ± 60° | 1218.986 s | 1218 s |
| ± 45° | 463.702 s | 462 s |
| ± 30° | 246.319 s | 246 s |
| ± 15° | 100.317 s | 99 s |

For this work a step size of 1 second is considered acceptable and accurate enough. With this step size the NGSO relay simulator can find the pass durations with an accuracy of ±2s. The minimum duration for a usable inter-satellite pass will be determined by the overhead in setup and connection time of the communication protocol used by the NGSO constellations. This number is unknown for the considered NGSO constellations however it is assumed that it will be in the order of seconds and not milliseconds. Without knowing the exact duration of the setup times, simulating with a smaller step sizes is not considered useful at this time.

## 6.7. Post-processing

This section discusses some of the post-processing steps that happen after the orbital simulation to make the data suitable for further analysis and the data-relay optimization.

### 6.7.1. Output format

During the simulation the found contact opportunities are stored in memory using the `Pandas` library [198]. The data-frame that is stored resembles a table structure with two indexes $p$ and $n$ as shown in table 6.4.

Table 6.4: Example of the output format of the data-relay orbital simulator

| Index | | time-of-flight [s] | timestamp | strand | $\vec{r}_a$ | $\vec{v}_a$ | $\vec{r}_b$ | $\vec{v}_b$ |
|---|---|---|---|---|---|---|---|---|
| p | n | | | | | | | |
| 1 | 0 | 0.0 | 2019-01-01T00:00:00.00 | sat0-to-sat2 | | | | |
| 1 | 1 | 1.0 | 2019-01-01T00:00:01.00 | sat0-to-sat2 | | | | |
| ⋮ | ⋮ | ⋮ | ⋮ | ⋮ | | | | |
| 1 | 88 | 87.0 | 2019-01-01T00:01:27.00 | sat0-to-sat2 | | | | |
| 2 | 0 | 43.0 | 2019-01-01T00:00:43.00 | sat0-to-sat49 | | | | |
| 2 | 1 | 44.0 | 2019-01-01T00:00:44.00 | sat0-to-sat49 | | | | |
| ⋮ | ⋮ | ⋮ | ⋮ | ⋮ | | | | |
| 2 | 123 | 166.0 | 2019-01-01T00:02:46.00 | sat0-to-sat49 | | | | |

state-vectors

Each contact opportunity is stored by the strand name, the time-of-flight, timestamp and state-vectors of the satellites. The data is periodically written to the hard-drive to minimize memory usage during the simulation. The Hierarchical Data Format (HDF5) was chosen as it allows for appending [199] without having to load the compete data-set into memory. The first index $p$ keeps track of the number of the pass, incrementing when a new pass is found (i.e. when a line-of-sight is obtained with a satellite that had no line-of-sight in the previous time-step). The second index $n$ keeps track of the instances that occurred during the pass. In table 6.4 an example with two passes is shown, one with satellite 2 and one with satellite 49. In this example the passes are partially overlapping as the first pas ends at 87.0 seconds while the second starts at 43.0 seconds.

The data-set of contact opportunities can be extended with different parameters calculated from the state-vectors in each row such as the range, latitude/longitude and relative orientation in the satellite frame of reference (see next section). Other parameters such as the pass duration (the time from the pass start and the end of the pass) and gap duration (the time in between passes) can also be calculated by combining multiple rows in table 6.4. This is done in post-processing after the simulation has ended to reduce computation time in the main-loop of the simulation.

### 6.7.2. Changing frame of reference

The data-relay orbital simulator computes and exports the position vectors of the ECIF however for the design optimization it is of interest where the NGSO data-relay satellite is in the frame of reference of the small satellite. This is for example needed to determine how much the small satellite should rotate (or how much an antenna pointing system should rotate) to transmit in the direction of the data-relay satellite. Therefore a coordinate transformation is needed, fig. 6.15 illustrates the problem. The position of the transmitting small satellite $\vec{r}_{sc}$ and the position of the receiving data-relay satellite $\vec{r}_{dr}$ are both known in the ECIF as outputs of the orbital simulator. The ECIF is spanned by the unit vectors $(\hat{x}_{ECI}, \hat{y}_{ECI}, \hat{z}_{ECI})$. Simply using the line-of-sight vector $\vec{r}_{sc,dr}$ will not suffice as it does not take into account the rotation of the small satellite satellite. A transformation therefore is required to rotate the vector from the ECIF to a SFF spanned by the vectors $(\hat{x}_{SF}, \hat{y}_{SF}, \hat{z}_{SF})$.

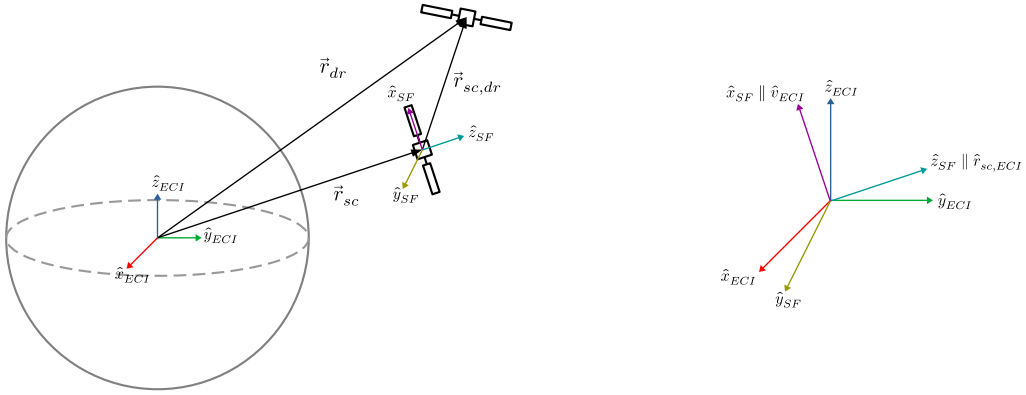


(a) Different orientations of the ECIF and satellite fixed (SF) frames. Here the SF frame is define with the $\hat{z}_{SF}$ axis pointing zenith and the $\hat{x}_{sff}$ pointing in the flight direction.

(b) Different orientations of the ECIF and SFF. Here the SFF is define with the $\hat{z}_{SF}$ axis pointing zenith and the $\hat{x}_{SF}$ pointing in the flight direction.

Figure 6.15: Output of orbital simulator.

In order to find this transformation first the orientation of the satellite needs to be defined in the ECIF. On an actual satellite this is done by the attitude determination system of the satellite based on the on-board sensors. In this simulation the orientation of the small satellite is assumed to have its z-axis ($\hat{z}_{SF}$) pointed towards zenith, therefore parallel to the (unit) position state-vector ($\hat{r}_{sc}$) and the x-axis ($\hat{x}_{SF}$) pointed towards the direction of flight, therefore parallel to the (unit) velocity state-vector ($\hat{v}_{sc}$). The small satellite y-axis can be defined as the cross-product between x-axis and negative z-axis to complete the right handed coordinate frame. As the position state-vector ($\vec{r}_{sc}$) and velocity state-vector ($\vec{v}_{sc}$) are defined in the ECIF as the state-vector outputs of the orbital simulator it is possible to formulate the rotation from the ECIF to the SFF as a rotation matrix.

The 3x3 rotation matrix that describes the rotation from a position in the ECIF ($\vec{p}_{ECI} = [x_{ECI}, y_{ECI}, z_{ECI}]^T$) to the corresponding position in the SFF ($\vec{p}_{SF} = [x_{SF}, y_{SF}, z_{SF}]^T$) is defined as:

$$\begin{bmatrix} x_{SF} \\ y_{SF} \\ z_{SF} \end{bmatrix} = \begin{bmatrix} a_x & a_y & a_z \\ b_x & b_y & b_z \\ c_x & c_y & c_z \end{bmatrix} \begin{bmatrix} x_{ECI} \\ y_{ECI} \\ z_{ECI} \end{bmatrix} \tag{6.81}$$

The rotation matrix $R_{ECI \to SF}$ can be found directly from the definition of the SFF axes of the satellite in the ECIF:

$$R_{ECI \to SF} = \begin{bmatrix} a_x & a_y & a_z \\ b_x & b_y & b_z \\ c_x & c_y & c_z \end{bmatrix} = \begin{bmatrix} \hat{v}_{sc} \\ \hat{r}_{sc} \\ \hat{v}_{sc} \times -\hat{r}_{sc} \end{bmatrix} \tag{6.82}$$

$$\hat{v}_{sc} = \frac{\vec{v}_{sc}}{\|\vec{v}_{sc}\|} \tag{6.83}$$

$$\hat{r}_{sc} = \frac{\vec{r}_{sc}}{\|\vec{r}_{sc}\|} \tag{6.84}$$

By this convention the rotation matrix $R_{ECI \to SF}$ is always well defined and easily obtainable from the state-vectors of the simulator. In some cases however it might be beneficial to convert this rotation matrix to a quaternion. Quaternions only use four variables instead of nine therefore reducing memory usage, they can be easily chained to for example include the orientation of an antenna on the small satellite, they can be interpolated and avoid Gimbal lock as with Euler angles [200]. In the post-processing applied here, the required reference frame transformation is determined by the rotation matrix as described above. Then the rotation matrix is transformed to a quaternion for storage and further processing.

Figure 6.16a shows the paths drawn by the line-of-sight vectors $\vec{r}_{sc,dr}$ for 10 passes of a 500 km altitude small satellite and an example NGSO constellation with satellites at 1000 km and 1250 km in the ECIF. After performing the transformation of reference frames the result in fig. 6.16b is obtained. By changing the coordinate frame, the paths drawn by the line-of-sight vector now correctly show the (inter-satellite) passes appearing above the small satellite at two different heights corresponding to the two orbital shells in this example. For example, in fig. 6.16b the blue and pink passes are with satellites in the 1250 km shell.

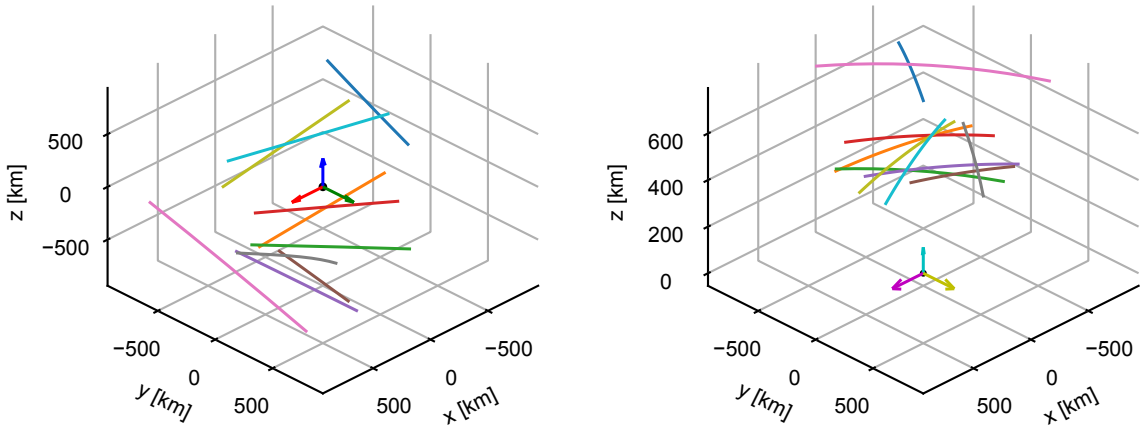


(a) Paths drawn by the line-of-sight $\vec{r}_{sc,dr}$ vectors in the ECIF

(b) Path drawn by the line-of-sight (inter-)satellite passes in the SFF

Figure 6.16: A change of reference frame using quaternion transformations allows for the (inter-)satellite passes to be observed in the satellite fixed frame (SFF)

After transformation from the ECIF to the SFF figures such as sky-plots can be made to visualise the (inter-satellite) passes of the contact opportunities similar to how satellite passes with a ground station are observed from the surface. A sky-plot is computing the elevation and azimuth of the line-of-sight vector and plotting this a polar plot. Figure 6.17 shows a range and sky plot of the first 10 passes appearing in the example.

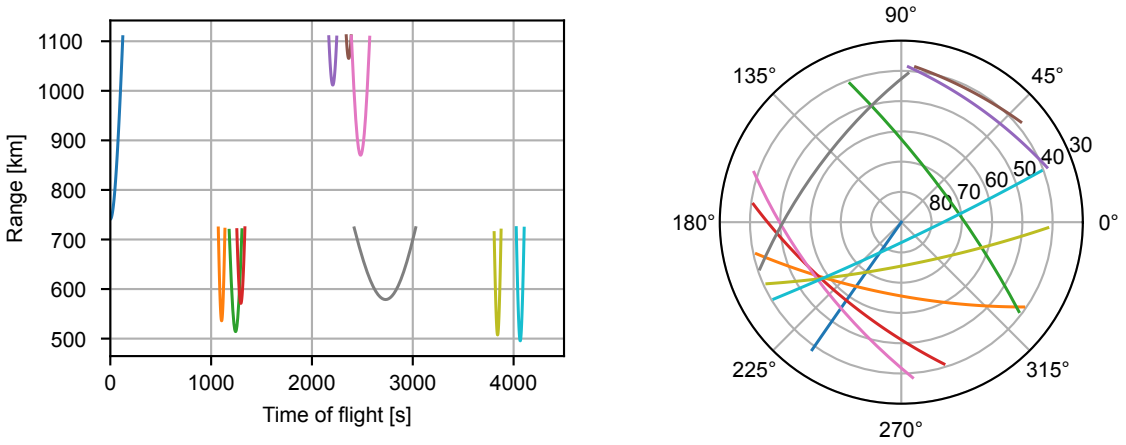


(a) Range of the first 10 inter-satellite passes

(b) Sky-plot of the first 10 inter-satellite passes

Figure 6.17: Range and sky-plots used to visualize the different (inter-satellite) passes that occur during the time of flight

## 6.8. Summary, discussion and recommendations

This chapter described the design of the NGSO data-relay orbital simulator that was purpose-built to find the contact opportunities between a small satellite and a NGSO (mega-)constellation. The data-relay orbital simulator takes a user defined scenario containing the orbital parameters of a satellite of interest and those of a NGSO (mega-)constellation and finds the contact opportunities between the two for a given period. These contact opportunities show which satellites have line-of-sight at a given moment in time. The data-relay orbital simulator can find the contact opportunities for a large number of satellites (> 5000) for a long simulation period (7 days) within acceptable simulation time and memory usage. This was achieved by implementing a vectorized two-body orbital propagator based on Markley's algorithm for solving Keplers equation [193]. This propagator uses a fifth-order refinement of the solution of a cubic equation, requires only minimal trigonometric evaluations and can be fully vectorized, allowing the orbital positions of the considered satellites to be calculated at once for a given time of flight. The simulator uses a just-in-time approach that minimizes memory utilization during the computation by evaluating for each time step which satellites have line-of-sight and only storing those satellite positions. The geometry computations for determining the line-of-sight pairs are performed in a similar vectorized manner. The data-relay orbital simulator can visualize the positions of the satellites in two-dimensional or three-dimensional views and export the state-vectors (position and velocity) to a file for post-simulation analysis. The NGSO data-relay orbital simulator was verified against commercial orbital simulation packages and showed to accurately find the durations of the contact opportunities. The data-relay optimization framework takes about 30 minutes for to simulate a constellation of 4400 satellites over a simulated period of 7 days using less than 2 GB of memory and output files around 500 MB.

### Discussion and recommendations

The operation of the data-relay optimization framework is based on vectorized and just-in-time computations. Table 6.5 shows an overview of the achieved performance with this simulator for some of the simulation runs for the data presented in the next chapter. As can be seen the data-relay orbital simulator takes about an hour to simulate a scenario of 4400 satellites with two satellites of interest for a period of 7 days. The output data file directly relates to the amount of contact opportunities that were found. In the case of table 6.5 the second file sizes correspond to a satellite at a higher altitude with less contact opportunities. The durations show to be reducing for less satellites within the constellation to about 7 minutes for a constellation with three satellites. This shows that although the simulator is vectorized, there is some overhead that results into a longer computation time when more satellites are simulated. In general, the performance shown in table 6.5 was considered sufficient for this study.

The computation method employed in the data-relay orbital simulator allows for fast computation and minimal memory usage. However, the highly optimized code limits its versatility and flexibility. A J2 perturbation was added to increase the fidelity of the orbital simulation and allow for a more represen-

Table 6.5: Overview of performance of the NGSO data-relay orbital simulator

| Constellation | Simulated time | Time step | Satellites | Analysis objects | Duration | Memory usage | Output data file size |
|---|---|---|---|---|---|---|---|
| Starlink 2019 | | | 4409 | | 01:11:15 | | 572 MB & 351 MB |
| Starlink 2020 | | | 4409 | | 01:04:02 | | 106 MB & 7.7 MB |
| Kuiper | 7 days | 1s | 3236 | 2 | 00:47:16 | < 2GB | 94.5 MB & 12.5 MB |
| O3b | | | 41 | | 00:10:36 | | 382 MB & 320 MB |
| Audacy | | | 3 | | 00:06:36 | | 106 MB & 101 MB |

tative simulation of Sun-synchronous orbits, although it was found that within 7 days of simulated time the effects of a J2 perturbation were only minimal. More advanced orbital propagators, i.e. those that aim to solve the governing differential equations (with perturbations) directly or those using iterative methods, are less suitable for vectorization. This limits the ability to evaluate different perturbations and the use of for example two-line elements.

Simulating the orbital dynamics of large constellations is an active topic of research. During this project work by Juan Luis Cano Rodríguez under the OpenSatCom initiative [201] benchmarked several implementations of the Simplified General Perturbations 4 (SGP4) propagator for cases like many satellites and many satellites, many dates using parallel multi-core processing. The SGP4 model allows for the use of two-line element sets and these implementations would be an interesting alternative to the vectorized implementation of this work. Using these implementations is recommended for future work.

This page intentionally left blank.

# 7

# Visibility and contact time analysis

In this chapter the NGSO data-relay orbital simulator is used to perform a first order visibility and contact time analysis for the proposed LEO-to-NGSO data-relay downlink architecture. As mentioned in earlier chapters of this report, the satellites in the NGSO (mega-)constellations have their orbits, field-of-views, spot beams and frequency re-use schemes optimized for ground coverage [3] leaving gaps in LEO where a small satellite would not be in view of a NGSO satellite. Similarly, due to the short inter-satellite distances and the satellites travelling in different planes, it is expected that the contact opportunities will be of short duration but frequent due to the amount of satellites in the NGSO (mega-)constellations.

The first order analysis in this chapter will give insight into these temporal characteristics of the contact opportunities that are encountered throughout the orbit of the small satellites. From these characteristics already, an assessment can be made if the proposed data-relay architecture is feasible from a contact time perspective for a small satellite orbit and NGSO constellation combination, without having to perform a complete communication system design optimization. In the case that a high throughput is desired (for example in the EO use-case) and the small satellite is only visible to the NGSO satellite for a small part of the orbit then a high data-rate communication link needs to be used to achieve a reasonable throughput per orbit. Similarly, the contact opportunities could be of such a short duration, the *pass duration*, that it would be difficult in practice to establish the link and achieve any throughput before line-of-sight is lost. In the case that a low-latency is desired (for example in the IoT/M2M use-case) the characteristics of the time in between contact opportunities, the *gap duration*, becomes important. If gap-duration is large then any IoT/M2M messages received during the gap will be delayed until the the small satellite is back in view of a NGSO constellation satellite.

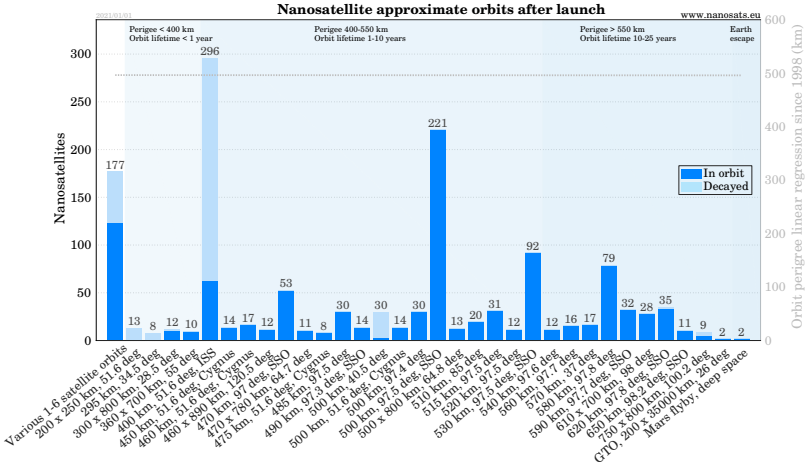


Figure 7.1: Overview of nano-satellite orbits from Nanosats.eu [5, January 2021]

For this first order analysed two typical small satellite orbits are investigated. Figure 7.1 shows

an overview of nano-satellite orbits after launch [5]. The two primary orbits in which nano-satellites are launched are a 400 km, 51.6° orbits launched from the International Space Station, and 500 km, 97.5° Sun-synchronous orbits. These two orbits are individually investigated for the NGSO (mega-) constellations discussed in chapter 4. Section 7.1 will first introduce the parameters that will be investigated in this chapter. Then section 7.2 will show the results for the LEO constellations, and section 7.3 will show the results for the MEO constellations. Finally, section 7.4 will show a summary of the results and discuss the applicability of the different constellations for the proposed NGSO data-relay downlink.

## 7.1. Parameters of interest

Several parameters are investigated in this first order analysis that describing on a high level the visibility and constant time characteristics between the small satellite orbit and the NGSO constellations. The paragraphs below introduce the parameters that are investigated for each of the NGSO (mega-) constellations at the two orbits.

**Spatial coverage** - this can be considered as the number of satellites in view at a particular location in the orbit, such as around the poles or the equator. This is similar to evaluating the coverage on the ground but then for spherical shells at the altitudes of interest (i.e. 400 km and 500 km). To visualise the spatial coverage at these altitudes the coverage can be mapped to ground coordinates, i.e. latitude and longitude, and overlayed on a map of the Earth. For ground coverage, this would show a densely covered map, which get sparser closer and closer to the orbital altitude of the NGSO constellation because of the limited field-of-view of each satellite. The spatial coverage is a snapshot in time of the positions of the satellites of the NGSO (mega-)constellation. As the satellites are moving the spatial coverage changes, possibly moving with the position of the small satellite. This is investigated in the visibility parameter.

**Visibility** - defined as the number of NGSO satellites that have the small satellite in field-of-view during the time of flight. At a given moment the small satellite could be in view of multiple-satellites or no satellites at all. If the small satellite is not in view of any satellite it has to store-and-forward any incoming data until line-of-sight is obtained. If the small satellite is in view of multiple-satellites a choice needs to be made to which satellite the data is relayed.

**Pass duration distribution** - the pass duration is defined as the amount of time of a contact opportunity between obtaining line-of-sight and losing it. The distribution of the pass durations shows the number of passes that occurred during the time-of-flight distributed in bins by their duration. This pass duration histogram can show what kind of passes are encountered in the particular small satellite orbit with the NGSO constellation, i.e. long but in-frequent or short but frequent passes or a combination of both. All contact opportunities are counted in this analysis even when they are overlapping, there is no choice made for which contact opportunity will be actually used.

**Gap duration distribution** - the gap duration is defined as the amount of time between losing all line-of-sight with current contact opportunities and obtaining line-of-sight with the next contact opportunity. Similar to the pass duration distribution, the distribution of the gap durations shows the number of gaps that occurred during the time-of-flight distributed in bins by their duration. This histogram of gap durations shows how long the small satellite has to operate in store-and-forward before encountering the next contact opportunity.

**Overall coverage with minimum contact time** - defined as the percentage of the orbital period of the small satellite in which contact is obtained with the NGSO constellation. The coverage effectively shows how much contact time is obtained per orbit, and when multiplied by a fixed data-rate it gives an estimated how much throughput could be obtained per orbit. The coverage can be made dependent on the minimum contact opportunity duration required to establish the link. For example, if it takes at-least 30 seconds to establish the link[1] then all contact opportunity durations are shortened by 30 seconds and contact opportunity of less than 30 seconds are discarded, possibly increasing the gap durations.

[1] Reasons why there would be a minimum required duration include: overhead by handshaking negotiations, pointing of the spot-beams on the NGSO satellite or synchronisation/acquisition time of the transmitted signal.

## 7.2. LEO constellations

The following sections show the results of the first order visibility and contact time analyses for the Telesat, OneWeb, SpaceX Starlink (both 2019 and 2020 configurations), Kuiper systems and Astrome mega-constellations. Each of the parameters of interest of section 7.1 is discussed individually in each of the sub-sub-sections.

### 7.2.1. Telesat

The constellation of Telesat is unique in having two shells, one inclined and one polar at relatively high altitudes of 1015 km and 1325 km. In addition, the field-of-view of the steerable and shapeable spot beams is relatively wide at around ±55.0° therefore possibly maintaining good coverage at the lower LEO altitudes. The Telesat satellites also have optical inter-satellite cross-links which means that any satellite could theoretically be used to relay data even if its not in view of a gateway ground station.

#### Spatial coverage

Figure 7.2 shows the number of Telesat satellites in view for two altitudes, 400 km and 500 km. The largest number of satellites in view are at ±50.9° (the maximum inclination of the 1325 km inclined shell of the constellation) with up to 20 satellites in view at 400 km. At both altitudes there are no gaps in the coverage between ±55° latitude. Therefore the Telesat constellation would provide continuous coverage at 400 km and 500 km between ±55° latitude. Only around 750 km altitude[2] gaps (no-satellites in view) start to appear between these latitudes. Beyond ±55° latitude the coverage is solely provided by the 1025 km polar shell of the constellation and less satellites are in view, up to 10 simultaneously with gaps in-between.

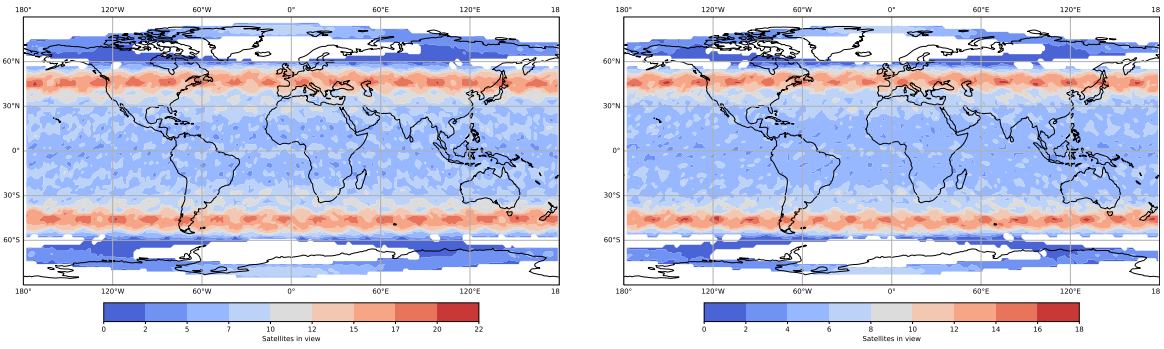


(a) Spatial coverage of the Telesat LEO constellation at 400 km altitude

(b) Spatial coverage of the Telesat LEO constellation at 500 km altitude

Figure 7.2: Spatial coverage (number of Telesat satellites in view) at altitudes of 400 km and 500 km

#### Visibility

Figure 7.3 shows the number of Telesat satellites in view throughout four hours for a small satellite at 400 km / 51.5° and a small satellite at 500 km / 97.5°. The satellite in the 400 km orbit is continuously in view of the Telesat constellation because its inclination is lower than 55°. The satellite in the 500 km has a near continuous view with the exception at the poles. This is as predicted by the spatial coverage of fig. 7.2 however occasionally, i.e. for $tof = (2750, 4800)\ s$, the satellites in Telesats polar orbits move together with the small satellite across the poles thereby maintaining visibility.

[2]Figures not printed.

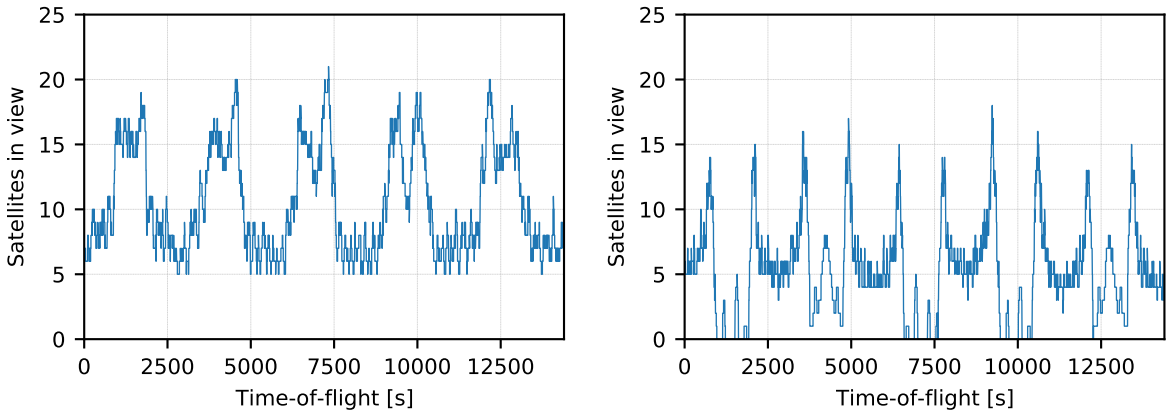


(a) Number of Telesat satellites in view for a small satellite in a 400 km orbit inclined at 51.6° over four hours

(b) Number of Telesat satellites in view for a small satellite in a 500 km orbit inclined at 97.5° over four hours

Figure 7.3: Number of Telesat satellites in view over a period of four hours.

### Pass duration distribution

Figure 7.4 shows the distribution of the pass durations during a period of seven days for the two small satellite orbits. The number of passes is slightly higher, around 20 000, for the satellite in the 500 km / 97.5° as it will also encounter passes in the polar regions. For both satellites there are more passes with the inclined Telesat satellites as these are more abundant (≈3.5 times more) in the constellation, and most passes have durations below 300 seconds. There are a few outliers for both orbits. For the 400 km / 51.5° orbit there are 600 inclined passes with a long duration of 1500 seconds (25 minutes). These passes are of long duration because the inclined satellites of Telesat are roughly at the same inclination. A satellite in the 400 km orbit is therefore continuously catching up with the next inclined satellite that is in a orbital plane close to its own, thereby creating long passes. A similar effect is seen for the 500 km / 97.5° orbit, but to a lesser extent with 50 to 100 polar passes with a duration of 1375 seconds (23 minutes). These outliers show that it would be beneficial to place the small satellites in orbital planes that coincide with those of the Telesat constellation.

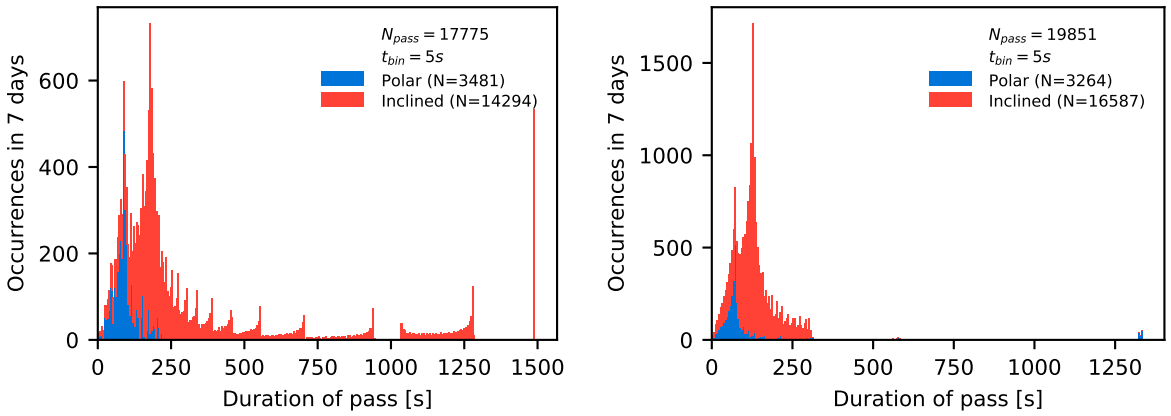


(a) Pass temporal distribution for a small satellite in an 400 km orbit inclined at 51.6°.

(b) Pass temporal distribution for a small satellite in an 500 km orbit inclined at 97.5°.

Figure 7.4: Distribution of pass durations with the Telesat (mega-)constellation for a small satellite in a 400 km inclined orbit (left) and a small satellite in a 500 km polar orbit (right) over a period of seven days

### Gap duration distribution

Figure 7.5 shows the distribution of the gap durations during a period of seven days for the two small satellite orbits. As predicted by the spatial coverage analysis a satellite in an 400 km / 51.5° orbit experiences a continuous coverage if all passes are used (see next section for discretization). For a satellite in an 500 km / 97.5° orbit the gaps appear with a duration up to 5 minutes, and mostly around 180 seconds. Following from the analysis in the previous sections these gaps appear at the polar regions and vary in length because occasionally the polar satellites of Telesat pass the polar region in sync with the small satellite.

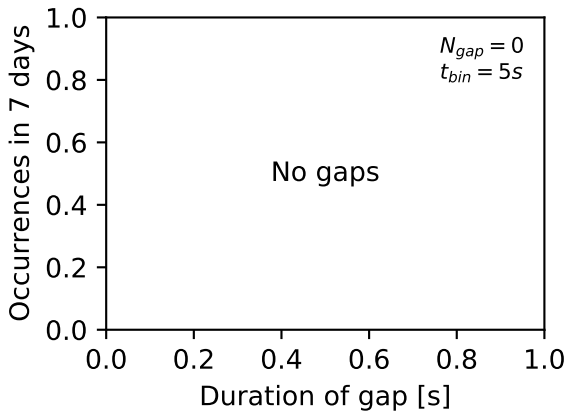


(a) Gap temporal distribution for a small satellite in an 400 km orbit inclined at 51.6°.

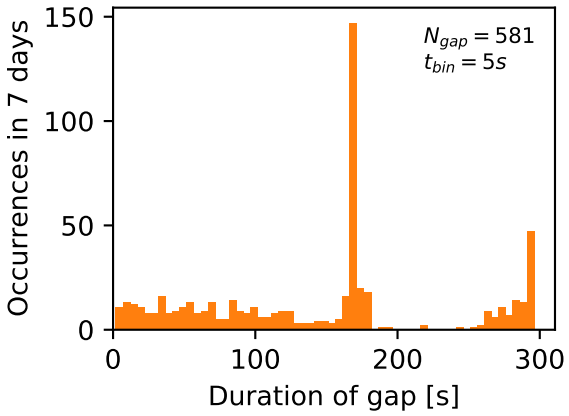


(b) Gap temporal distribution for a small satellite in an 500 km orbit inclined at 97.5°.

Figure 7.5: Distribution of gap durations with the Telesat (mega-)constellation for a small satellite in a 400 km inclined orbit (left) and a small satellite in a 500 km polar orbit (right) over a period of seven days

### Overall coverage with minimum contact time

Figure 7.6 shows the overall coverage as function of the minimum contact time over a period of seven days. A small satellite in a 400 km inclined orbit has a near continuous coverage ( 100%) including passes up to about one and a half minutes with the Telesat satellites. For longer minimum contact durations the coverage quickly drops to 80% at a minimum contact time of five minutes. A small satellite in a 500 km polar orbit has overall shorter passes with the Telesat satellites and starts with a overall coverage of 80%. The coverage gradually decreases towards less than 10% for a minimum contact time of five minutes.

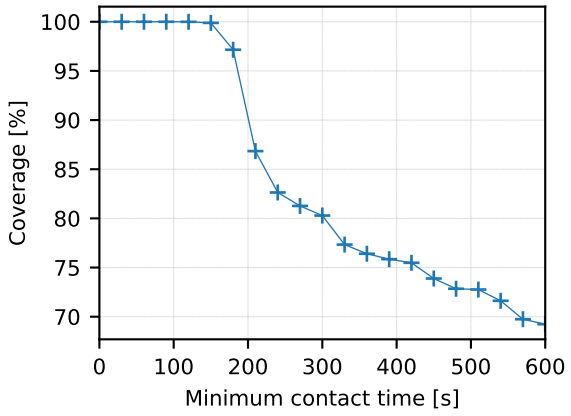


(a) Overall coverage against minimum contact time over a period of 7 days for a small satellite in an 400 km orbit inclined at 51.6°.

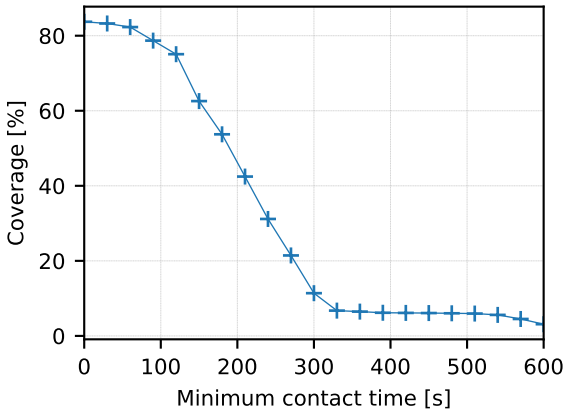


(b) Overall coverage against minimum contact time over a period of 7 days for a small satellite in an 500 km orbit inclined at 97.5°.

Figure 7.6: Coverage against minimum contact time needed for communications with the Telesat (mega-)constellation for a small satellite in a 400 km inclined orbit (left) and a small satellite in a 500 km polar orbit (right) over a period of seven days

### 7.2.2. OneWeb

The constellation of OneWeb is unique as it only uses polar orbital planes. The satellites in these 18 planes are at an altitude of 1200 km but have fixed beams with an overall narrow operating field-of-view of ±35.0°. The polar configuration provides a full coverage of the Earth on the ground, but the narrow operating field-of-view might lead to good coverage for polar small satellite orbits and bad coverage for any inclined small satellite orbit. In addition, the OneWeb satellites do not have inter-satellite cross-links and its FCC filing does not mention store-and-forward capability. Therefore it is likely that if a OneWeb satellite is not in-view of a gateway ground station (i.e. when its over an ocean) it cannot be used to relay data.

#### Spatial coverage

Figure 7.7 shows the number of OneWeb satellites in view for two altitudes, 400 km and 500 km. The largest number of satellites in view are at the polar regions, where the different polar planes of the OneWeb constellation come together. However, when moving away from the polar regions towards the equator, the coverage of the OneWeb satellites at these altitudes quickly reduces. Below ±60° significant gaps appear between the satellites and the coverage is dotted with only one satellite in view for both the 400 km altitude and the 500 km altitude. The narrow field-of-view of the OneWeb satellites only provides coverage right below the satellite. The coverage by different planes are also non-overlapping which means that when the small satellite is not in a plane close to that of one of the constellation of OneWeb, the coverage is likely greatly reduced. For small satellite missions with a singular orbital polar plane, such as the baselined Earth Observation mission, this might not be a problem and still a significant coverage can be maintained. However, for the small satellite missions with multiple orbital planes, such as the baselined IoT/M2M mission with eight orbital planes, a careful selection of the right ascension of each of the planes is to be made to ensure all planes have sufficient coverage.

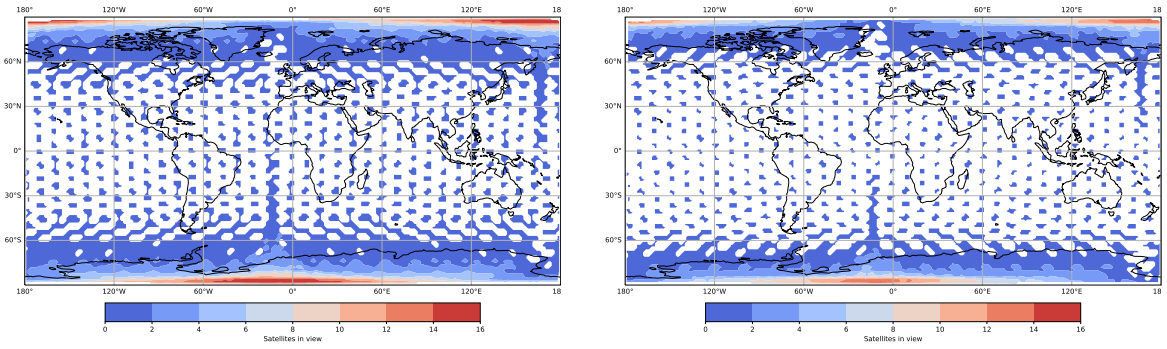


(a) Spatial coverage of the OneWeb LEO constellation at 400 km altitude

(b) Spatial coverage of the OneWeb LEO constellation at 500 km altitude

Figure 7.7: Spatial coverage (number of OneWeb satellites in view) at altitudes of 400 km and 500 km

#### Visibility

Figure 7.8 shows the number of OneWeb satellites in view throughout four hours for a small satellite at 400 km / 51.5° and a small satellite at 500 km / 97.5°. The small satellite in the 400 km orbit has at most one-satellite in view, but effectively hops from satellite-to-satellite, not obtaining a continuous visibility. The small satellite in the 500 km orbit is aligned with one of the planes of the OneWeb constellation. It is in view of up to 4 satellites when crossing the poles, but in between the poles at most one satellite is visible. As this small satellite is in an orbit aligned to that of the OneWeb constellation but has a higher orbital velocity, it is continuously catching up with the next satellite. The small satellite therefore stays slightly longer within the field-of-view of the OneWeb satellites than the satellite at 400 km orbit that is crossing the orbital planes of the constellation.

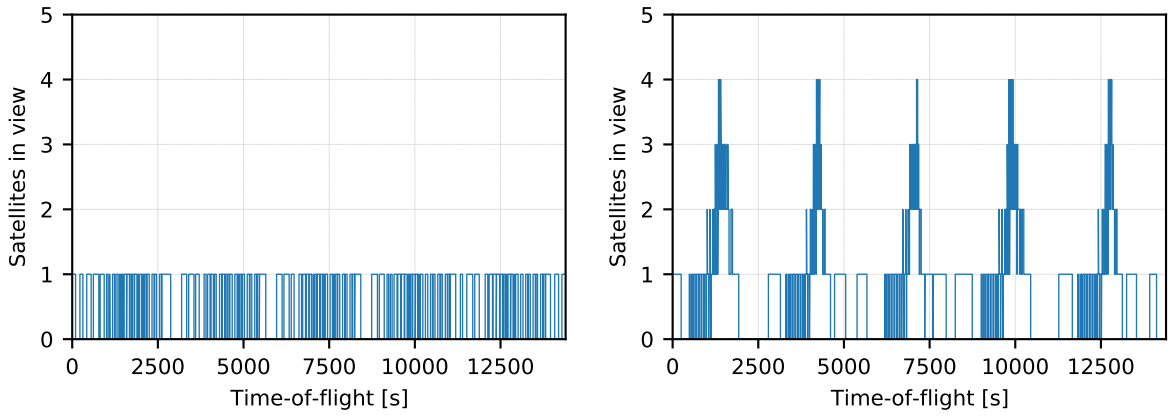


(a) Number of satellites in view for a small satellite in a 400 km orbit inclined at 51.6° over four hours

(b) Number of satellites in view for a small satellite in a 500 km orbit inclined at 97.5° over four hours

Figure 7.8: Number of OneWeb satellites that can view the small satellites over a period of four hours.

### Pass duration distribution

Figure 7.9 shows the distribution of the pass durations during a period of seven days for the two small satellite orbits. Most passes for both satellites at the 400 km and 500 km altitudes are of about a minute long. The number of passes for the small satellite at 500 km is slightly higher ( 6000) than that of the small satellite at 400 km ( 4000) as it encounters more satellites of the OneWeb constellation in the polar regions. The small satellite in the 400 km orbit does not encounter any passes longer that 200 seconds. For the small satellite in the 500 km orbit there are passes up to 500 seconds but these are less frequent.

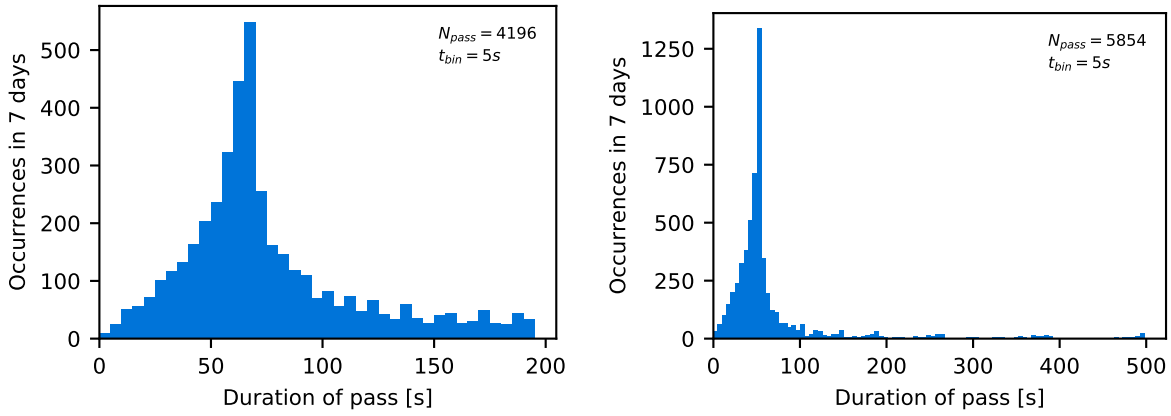


(a) Pass temporal distribution for a small satellite in an 400 km orbit inclined at 51.6°.

(b) Pass temporal distribution for a small satellite in an 500 km orbit inclined at 97.5°.

Figure 7.9: Distribution of pass durations with the OneWeb (mega-)constellation for a small satellite in a 400 km inclined orbit (left) and a small satellite in a 500 km polar orbit (right) over a period of seven days

### Gap duration distribution

Figure 7.10 shows the distribution of the gap durations during a period of seven days for the two small satellite orbits. Both the 400 km altitude and the 500 km altitude small satellites experience gaps in the coverage. For the 400 km altitude small satellite these are no longer than 330 seconds, with most having a duration around 60 seconds. While for the satellite at 500 km altitude the gaps can be as long as 1500 seconds but most less than 100 seconds.

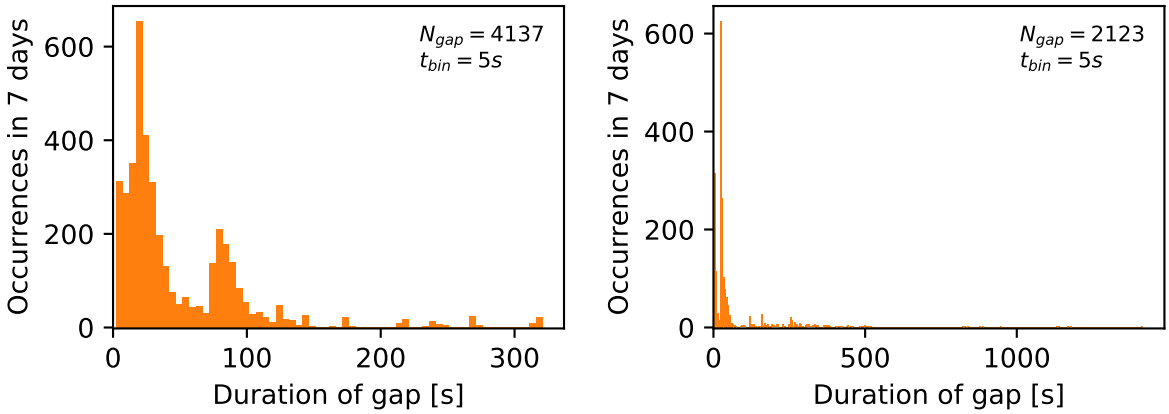


(a) Gap temporal distribution for a small satellite in an 400 km orbit inclined at 51.6°.

(b) Gap temporal distribution for a small satellite in an 500 km orbit inclined at 97.5°.

Figure 7.10: Distribution of gap durations with the OneWeb (mega-)constellation for a small satellite in a 400 km inclined orbit (left) and a small satellite in a 500 km polar orbit (right) over a period of seven days

### Overall coverage with minimum contact time

Figure 7.11 shows the overall coverage as function of the minimum contact time over a period of seven days. Both the 500 km polar and 400 km inclined small satellite orbits have a maximum coverage of about 60% over the seven day period. This however quickly drops as the minimum contact time is increased to less than 20% for both for a contact time longer than 100 seconds. There are no passes longer than 200 seconds for the 400 km inclined small satellite orbit. For the small satellite in the 500 km polar orbit the maximum is 500 seconds.

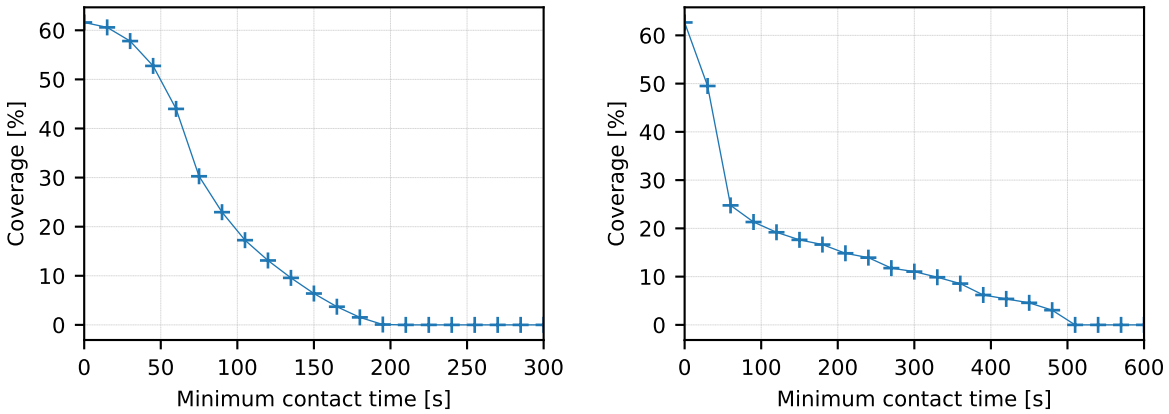


(a) Coverage against minimum contact time over a period of 7 days for a small satellite in an 400 km orbit inclined at 51.6°.

(b) Coverage against minimum contact time over a period of 7 days for a small satellite in an 500 km orbit inclined at 97.5°.

Figure 7.11: Overall coverage against minimum contact time needed for communications with the OneWeb (mega-)constellation for a small satellite in a 400 km inclined orbit (left) and a small satellite in a 500 km polar orbit (right) over a period of seven days

### 7.2.3. SpaceX Starlink 2019

The constellation of SpaceX in the 2019 proposal [175] is characterized by its five shells of 4409 satellites between 550 km and 1325 km. The field-of-view of the steerable and shapeable spot beams at around ±45.0° is slightly less wide than that of the Telesat constellation. The SpaceX Starlink satellites also have optical inter-satellite cross-links which means that any satellite could theoretically be used to relay data even if not in view of a gateway ground station.

#### Spatial coverage

Figure 7.12 shows the number of SpaceX Starlink satellites in view for two altitudes, 400 km and 500 km. The SpaceX constellation provides a dense global coverage even at these altitudes. The largest number of satellites in view are at ±53°, similar to the Telesat constellation, with up to 28 satellites in view at 400 km and 20 satellites in view at 500 km. The polar coverage by the SpaceX constellation is fair with several satellites at 400 km, and a few at 500 km apart from right at the poles. For the 500 km shell some gaps exist around the equator and prime meridian.

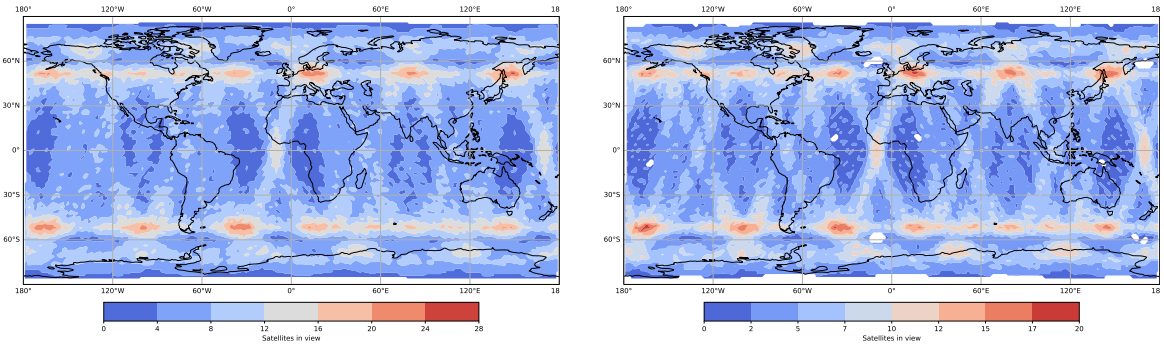


(a) Spatial coverage of at 400 km altitude

(b) Spatial coverage of at 500 km altitude

Figure 7.12: Spatial coverage (number of SpaceX Starlink satellites in view) at altitudes of 400 km and 500 km

#### Visibility

Figure 7.13 shows the number of Starlink satellites have the small satellite at 400 km / 51.5° (left) and a small satellite at 500 km / 97.5° (right) in view throughout four hours. Both small satellites are continiously in view by the Starlink satellites with a minimum of two satellites at all times. The small satellite in the 400 km inclined orbit is in view of up to 22 satellites at a time, while the small satellite in the 500 km polar orbit is in view of up to 15 satellites at a time.

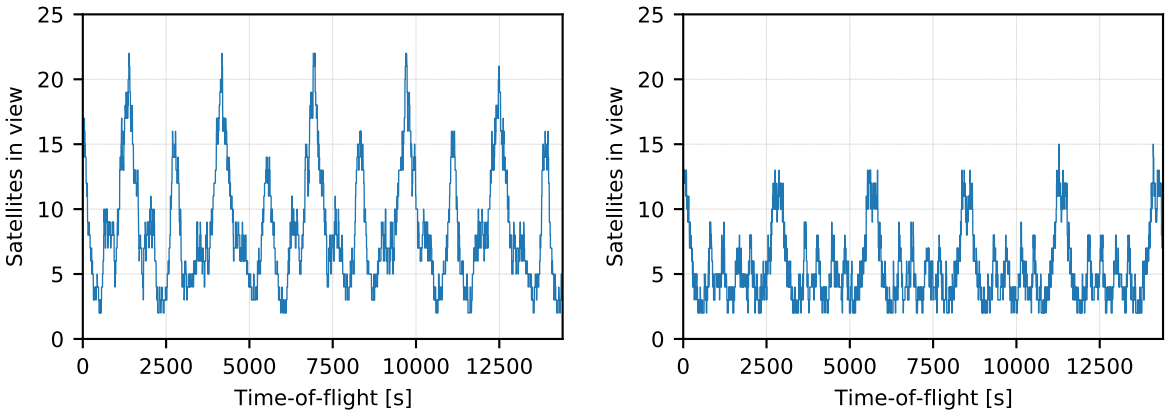


(a) Number of satellites that have the small satellite in a 400 km orbit inclined at 51.6° in view

(b) Number of satellites that have the small satellite in a 500 km orbit inclined at 97.5° in view

Figure 7.13: Number of SpaceX Starlink satellites that can view the small satellites over a period of four hours.

### Pass duration distribution

Figure 7.14 shows the distribution of the pass durations during a period of seven days for the two small satellite orbits. The majority of passes for both small satellites are with the 1110 km shell of the Starlink constellation which contains the most satellites (1600). There are less passes with the lowest shell of 550 km which has almost an equal amount of satellites (1584). Since it is at a lower altitude, the passes are also significantly shorter. Overall, most passes appear with a duration of 100 seconds. For the small satellite in the 400 km inclined orbit there are passes up to 1010 seconds with the 1110 km shell. This can be explained by their planes being almost aligned in inclination, allowing the small satellite to stay in view while following a Starlink satellite. The small satellite in the 500 km polar orbit experiences more passes around 100 seconds but does not experience passes longer than 580 seconds because it is not in plane with any of the satellites of SpaceX.

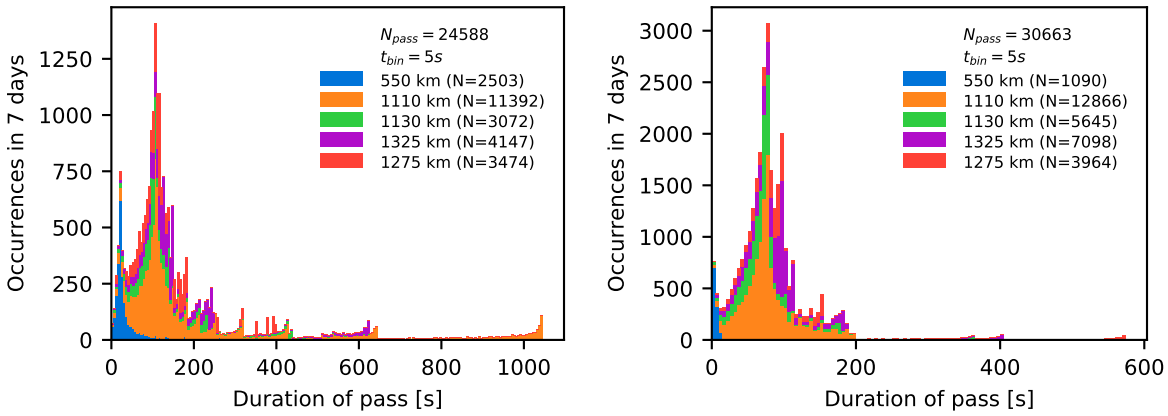


(a) Pass temporal distribution for a small satellite in an 400 km orbit inclined at 51.6°.

(b) Pass temporal distribution for a small satellite in an 500 km orbit inclined at 97.5°.

Figure 7.14: Distribution of pass durations with the SpaceX Starlink (mega-)constellation for a small satellite in a 400 km inclined orbit (left) and a small satellite in a 500 km polar orbit (right) over a period of seven days. Passes with the different orbital shells are coloured individually and stacked in the histogram.

### Gap duration distribution

As predicted by the spatial distribution and visibility timeline, there are no gaps in the coverage for the small satellites. The several gaps at 500 km identified in fig. 7.12 do not affect the coverage for the small satellite in the 500 km polar orbit due to the inclination and the movement of the satellites.

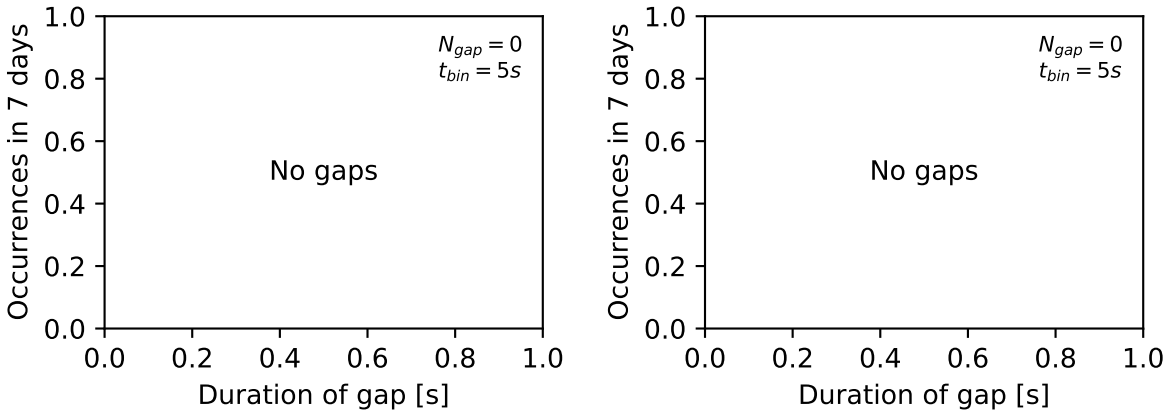


(a) Gap temporal distribution for a small satellite in an 400 km orbit inclined at 51.6°.

(b) Gap temporal distribution for a small satellite in an 500 km orbit inclined at 97.5°.

Figure 7.15: Distribution of gap durations with the SpaceX Starlink (mega-)constellation for a small satellite in a 400 km inclined orbit (left) and a small satellite in a 500 km polar orbit (right) over a period of seven days

### Overall coverage with minimum contact time

Figure 7.16 shows the overall coverage as function of the minimum contact time over a period of seven days. Both the 400 km inclined and 500 km polar small satellite orbits have a 100% coverage up to about one minute minimum contact time. For the 500 km orbit the coverage quickly drops below 20% for a minimum contact time of 200 seconds, whereas for the 400 km orbit the coverage stays above 50% until 500 seconds. The coverage drops to 0% around 600 seconds for the 500 km orbit small satellite, while for the 400 km small satellite the maximum is 1010 seconds.

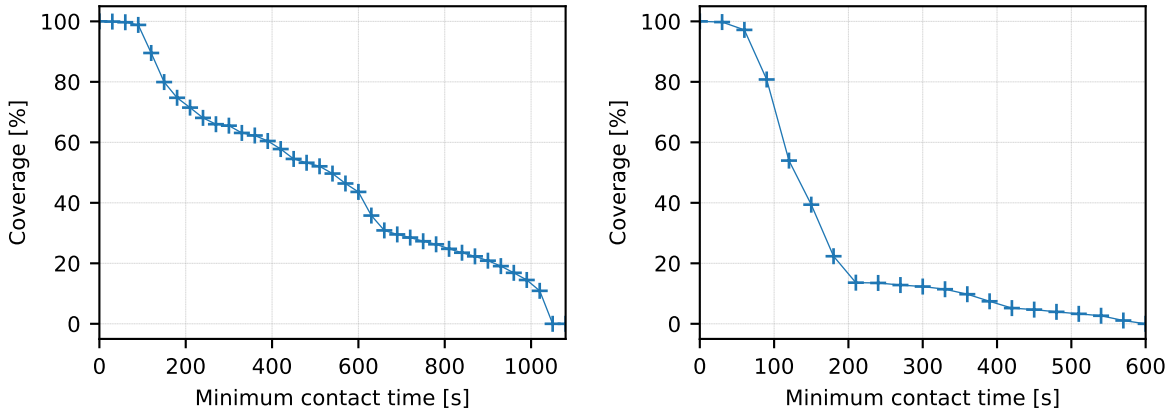


(a) Coverage against minimum contact time over a period of 7 days for a small satellite in an 400 km orbit inclined at 51.6°.

(b) Coverage against minimum contact time over a period of 7 days for a small satellite in an 500 km orbit inclined at 97.5°.

Figure 7.16: Coverage against minimum contact time needed for communications with the SpaceX Starlink (mega-)constellation for a small satellite in a 400 km inclined orbit (left) and a small satellite in a 500 km polar orbit (right) over a period of seven days

## 7.2.4. SpaceX Starlink 2020

The 2020 proposal of the SpaceX Starlink (mega-)constellation differs from the 2019 proposal by having all five shells of 4409 satellites below 600 km [163]. The operating field-of-view for each satellite is increased to ±56.50° which might compensate for the reduction in coverage by the lower altitudes.

### Spatial coverage

Figure 7.17 shows the number of SpaceX Starlink satellites in view for two altitudes, 400 km and 500 km. By lowering the shells the coverage is significantly reduced, showing a large amount of gaps at 400 km and almost no coverage at 500 km. The increase of field-of-view does not compensate for the reduction in satellite altitude.

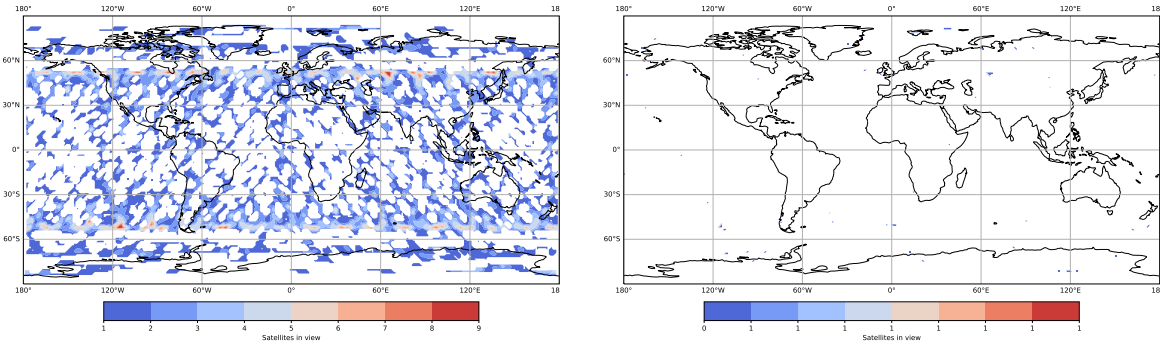

(a) Spatial coverage at 400 km altitude

(b) Spatial coverage at 500 km altitude

Figure 7.17: Spatial coverage (number of SpaceX Starlink satellites in view) at altitudes of 400 km and 500 km

### Visibility

Figure 7.18 shows the number of Starlink satellites have the small satellite at 400 km / 51.5° (left) and a small satellite at 500 km / 97.5° (right) in view throughout four hours. The small satellite in the 400 km inclined orbit is in view of up to 8 satellites at a time. The small satellite in the 500 km polar orbit is occasionally for short durations in view of at most two satellites, even though the spatial coverage at this altitude is low as was shown in fig. 7.17.

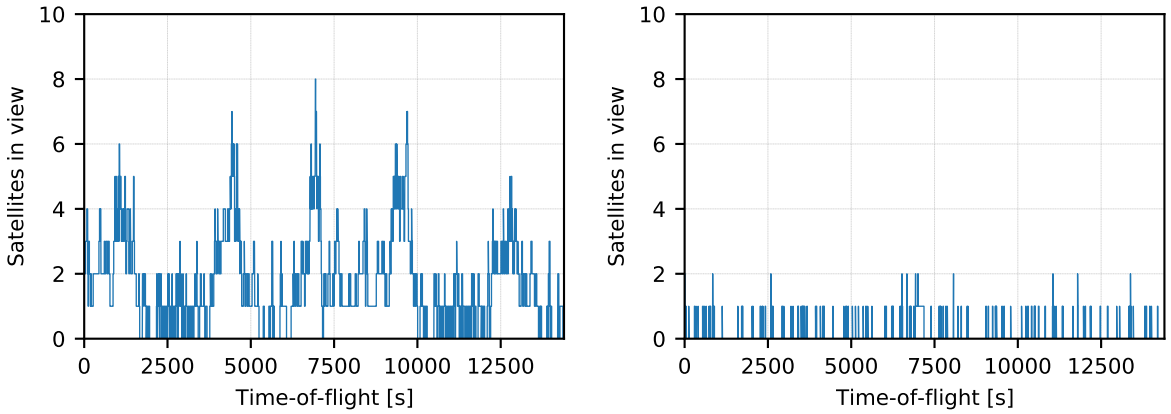


(a) Number of satellites that have the small satellite in a 400 km orbit inclined at 51.6° in view

(b) Number of satellites that have the small satellite in a 500 km orbit inclined at 97.5° in view

Figure 7.18: Number of SpaceX Starlink satellites that can view the small satellites over a period of four hours.

### Pass duration distribution

Figure 7.19 shows the distribution of the pass durations during a period of seven days for the two small satellite orbits. The majority of passes for the small satellite in the 400 km inclined orbit lie around 40 seconds, with a maximum of 600 seconds. For the small satellite in the 500 km inclined orbit the majority of the passes lie around 10 seconds with a maximum of 50 seconds.

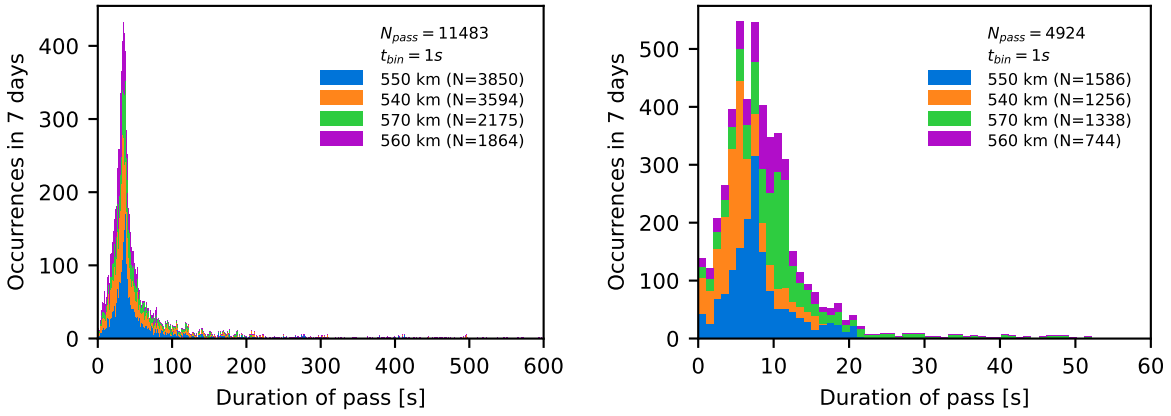


(a) Pass temporal distribution for a small satellite in an 400 km orbit inclined at 51.6°.

(b) Pass temporal distribution for a small satellite in an 500 km orbit inclined at 97.5°.

Figure 7.19: Distribution of pass durations with the SpaceX Starlink (mega-)constellation for a small satellite in a 400 km inclined orbit (left) and a small satellite in a 500 km polar orbit (right) over a period of seven days

### Gap duration distribution

Figure 7.20 shows the distribution of the gap durations during a period of seven days for the two small satellite orbits. Both the 400 km altitude and the 500 km altitude small satellites experience gaps in the coverage. For the 400 km altitude small satellite these are no longer than 300 seconds, while for the satellite at 500 km altitude the gaps can be as long as 800 seconds.

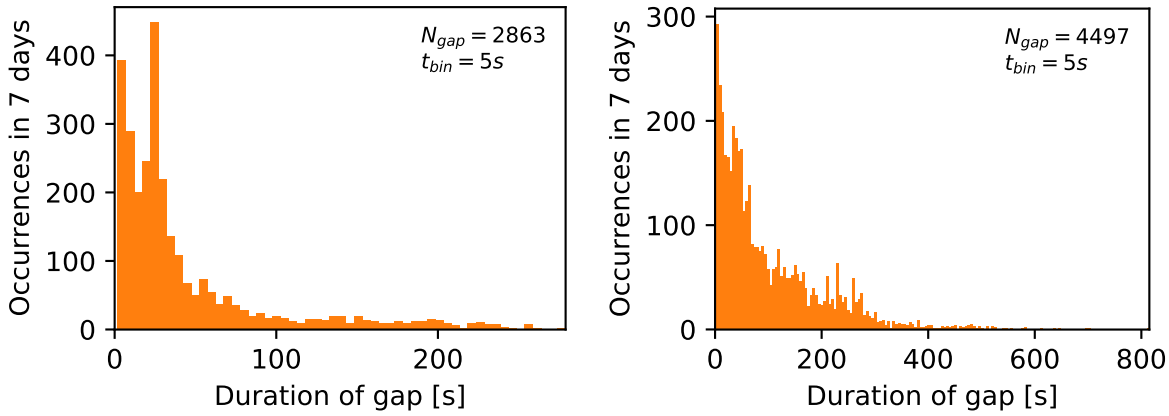


(a) Gap temporal distribution for a small satellite in an 400 km orbit inclined at 51.6°.

(b) Gap temporal distribution for a small satellite in an 500 km orbit inclined at 97.5°.

Figure 7.20: Distribution of gap durations with the SpaceX Starlink (mega-)constellation for a small satellite in a 400 km inclined orbit (left) and a small satellite in a 500 km polar orbit (right) over a period of seven days

### Overall coverage with minimum contact time

Figure 7.21 shows the overall coverage as function of the minimum contact time over a period of seven days. The small satellite in the 400 km inclined orbit starts with a coverage of about 75% which quickly drops to less than 20% for a minimum contact time of 90 seconds. For the small satellite in the 500 km polar orbit the overall coverage starts at less than 15% and drops to less than 1% for a contact time of 30 seconds.

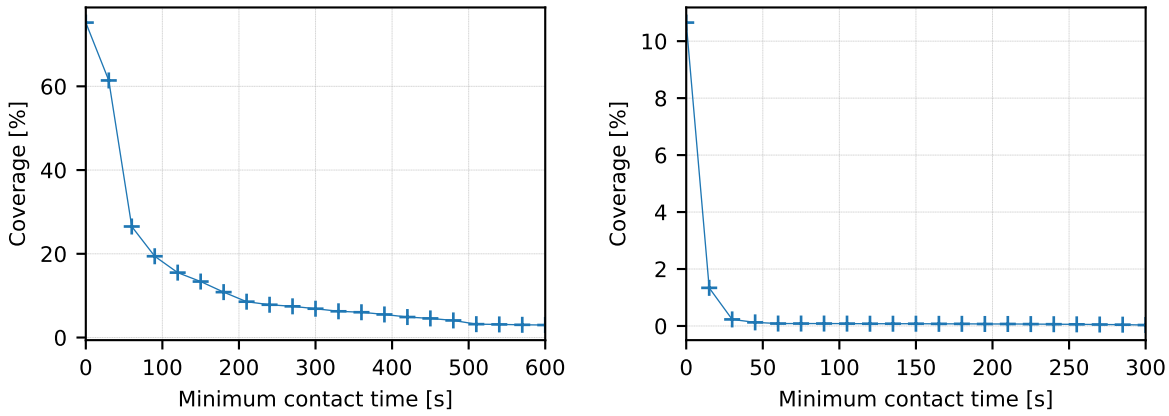


(a) Coverage against minimum contact time over a period of 7 days for a small satellite in an 400 km orbit inclined at 51.6°.

(b) Coverage against minimum contact time over a period of 7 days for a small satellite in an 500 km orbit inclined at 97.5°.

Figure 7.21: Coverage against minimum contact time needed for communications with the SpaceX Starlink (mega-)constellation for a small satellite in a 400 km inclined orbit (left) and a small satellite in a 500 km polar orbit (right) over a period of seven days

### 7.2.5. Kuiper Systems

The (mega-)constellation of Kuiper Systems is characterized by its three shells containing a total of 3236 satellites at around 600 km altitude [178]. The shells are inclined at 33.0°, 43.0°, and 51.9° therefore providing no coverage over the poles. The operating field-of-view of ±48.50 of the steerable spot beams is moderate in comparison to the other constellations. The application by Kuiper Systems does not mention the use of optical inter-satellite links between the satellites in the constellation, therefore it is unclear if the satellite can provide coverage when not in view of a gateway ground station.

#### Spatial coverage

Figure 7.22 shows the number of Kuiper System satellites in view for two altitudes, 400 km and 500 km. The low altitudes of the satellites result into a reduced coverage with large gaps at 400 km and marginal coverage at 500 km. Because of the limited inclination of the orbital shells there is no coverage at the poles beyond 52.0°.

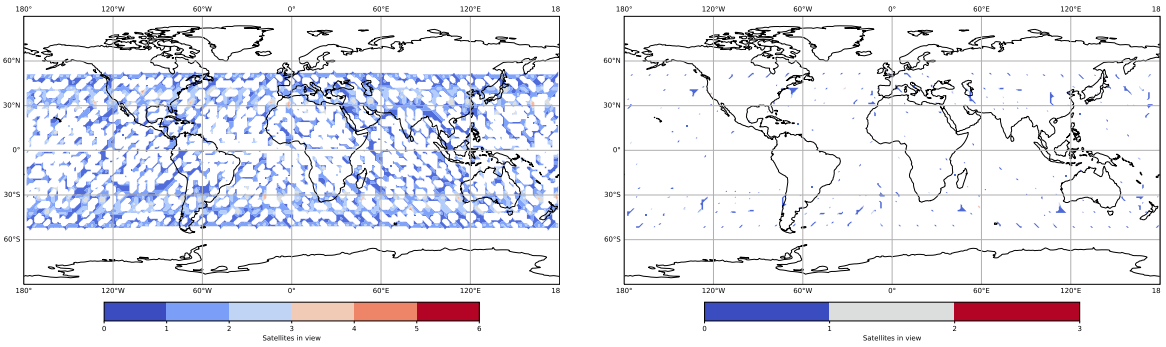

(a) Spatial coverage at 400 km altitude

(b) Spatial coverage at 500 km altitude

Figure 7.22: Spatial coverage (number of Kuiper System satellites in view) at altitudes of 400 km and 500 km

#### Visibility

Figure 7.23 shows the number of Kuiper Systems satellites have the small satellite at 400 km / 51.5° (left) and a small satellite at 500 km / 97.5° (right) in view throughout four hours. The small satellite in the 400 km inclined orbit is in view of up to 5 satellites at a time. The small satellite in the 500 km polar orbit is occasionally for short durations in view of at most three satellites.

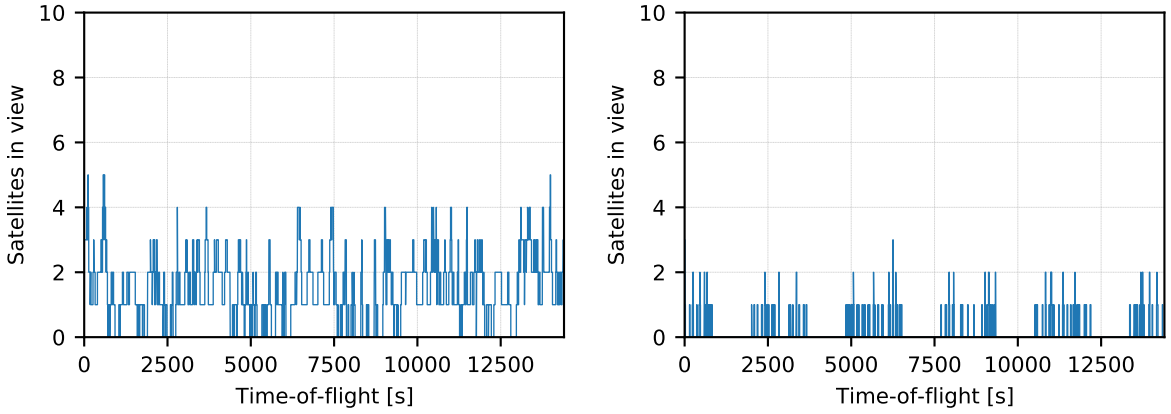


(a) Number of satellites that have the small satellite in a 400 km orbit inclined at 51.6° in view

(b) Number of satellites that have the small satellite in a 500 km orbit inclined at 97.5° in view

Figure 7.23: Number of Kuiper Systems satellites that can view the small satellites over a period of four hours.

### Pass duration distribution

Figure 7.24 shows the distribution of the pass durations during a period of seven days for the two small satellite orbits. The majority of passes for the small satellite in the 400 km inclined orbit lie around 50 seconds, with a maximum of 500 seconds. For the small satellite in the 500 km inclined orbit the majority of the passes lie around 20 seconds with a maximum of 50 seconds.

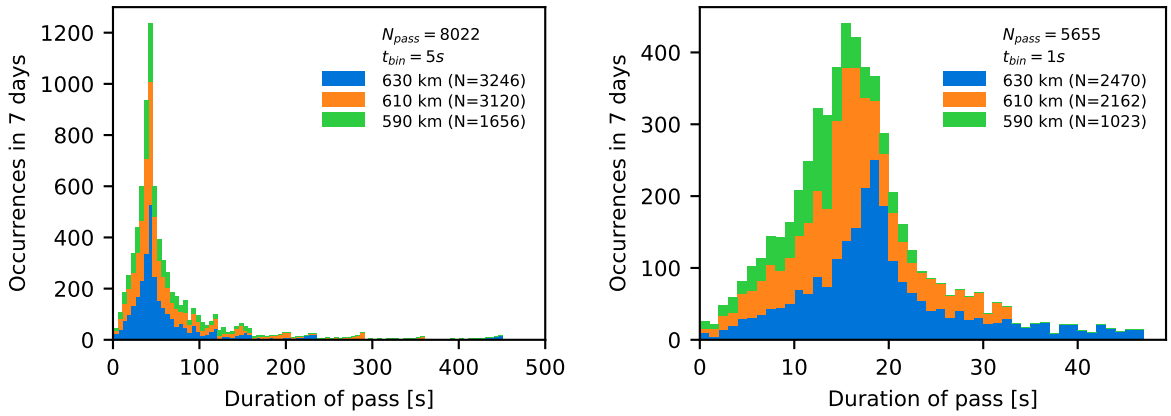


(a) Pass temporal distribution for a small satellite in an 400 km orbit inclined at 51.6°.

(b) Pass temporal distribution for a small satellite in an 500 km orbit inclined at 97.5°.

Figure 7.24: Distribution of pass durations with the Kuiper Systems (mega-)constellation for a small satellite in a 400 km inclined orbit (left) and a small satellite in a 500 km polar orbit (right) over a period of seven days

### Gap duration distribution

Figure 7.25 shows the distribution of the gap durations during a period of seven days for the two small satellite orbits. Both the 400 km altitude and the 500 km altitude small satellites experience gaps in the coverage. For the 400 km altitude small satellite these are no longer than 220 seconds, while for the satellite at 500 km altitude the gaps can be as long as 1500 seconds when passing the polar regions.

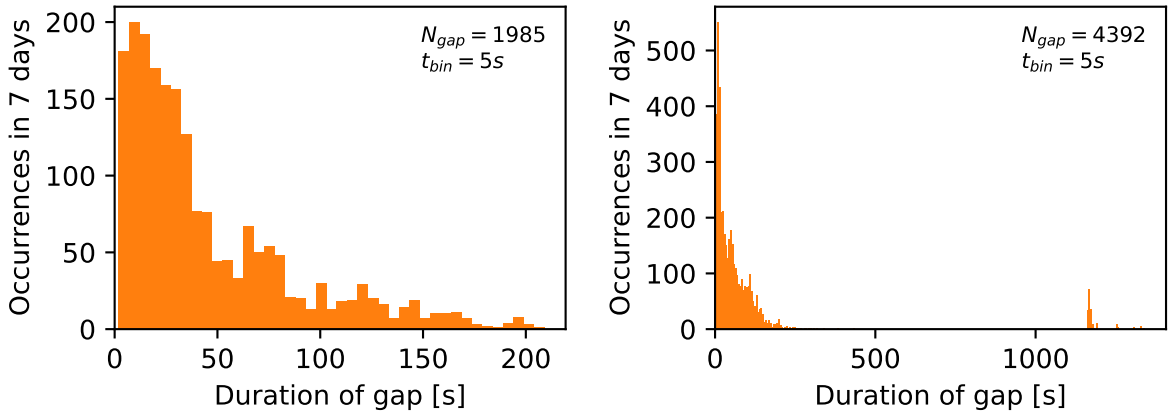


(a) Gap temporal distribution for a small satellite in an 400 km orbit inclined at 51.6°.

(b) Gap temporal distribution for a small satellite in an 500 km orbit inclined at 97.5°.

Figure 7.25: Distribution of gap durations with the Kuiper Systems (mega-)constellation for a small satellite in a 400 km inclined orbit (left) and a small satellite in a 500 km polar orbit (right) over a period of seven days

### Coverage with minimum contact time

Figure 7.26 shows the overall coverage as function of the minimum contact time over a period of seven days. The small satellite in the 400 km inclined orbit starts with a coverage of about 82% which drops to less than 20% for a minimum contact time of 150 seconds. For the small satellite in the 500 km polar orbit the overall coverage starts at about 16% and drops to less than 1% for a contact time of 50 seconds.

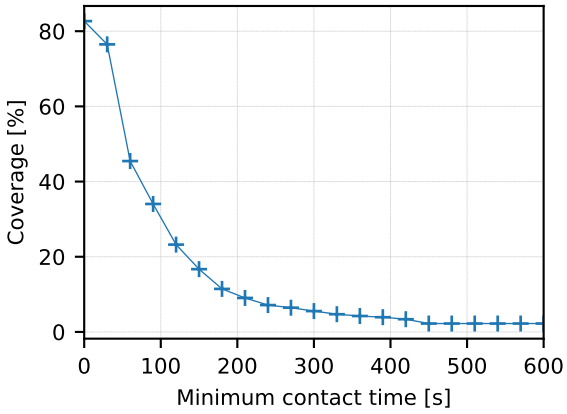


(a) Coverage against minimum contact time over a period of 7 days for a small satellite in an 400 km orbit inclined at 51.6°.

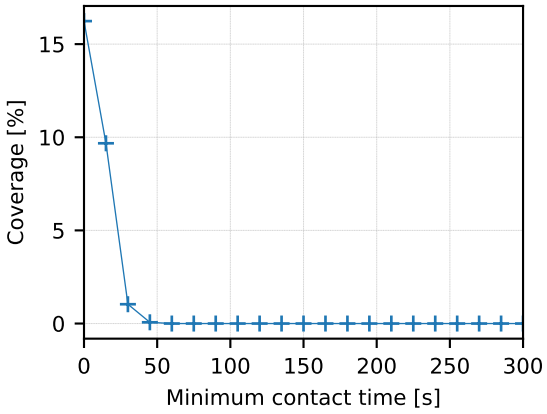


(b) Coverage against minimum contact time over a period of 7 days for a small satellite in an 500 km orbit inclined at 97.5°.

Figure 7.26: Coverage against minimum contact time needed for communications with the Kuiper Systems (mega-)constellation for a small satellite in a 400 km inclined orbit (left) and a small satellite in a 500 km polar orbit (right) over a period of seven days

## 7.2.6. Astrome SpaceNet

The (mega-)constellation of Astrome is characterized by its single shell Walker-delta configuration totalling 198 satellites at an altitude of 1530 km [179], [180]. The satellites in the 18 orbital planes are inclined at 30° and have an operating field-of-view of ±35°. Therefore, the constellation only provides coverage for the lower latitudes. The satellites in the Astrome SpaceNet constellation will have inter-satellite links.

### Spatial coverage

Figure 7.27 shows the number of Astrome SpaceNet satellites in view for two altitudes, 400 km and 500 km. Even though the Astrome satellites are at a relatively high altitude of 1530 km the limited operating field-of-view results in reduced coverage at 400 km and 500 km even within ±30° latitude.

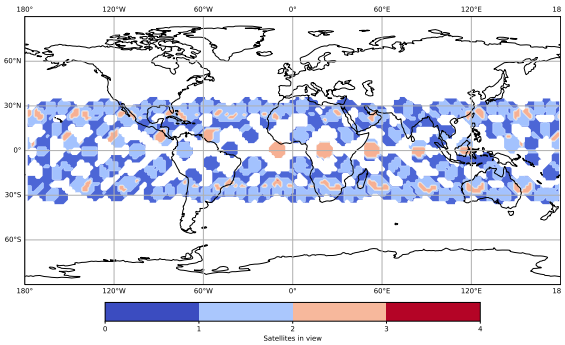


(a) Spatial coverage at 400 km altitude

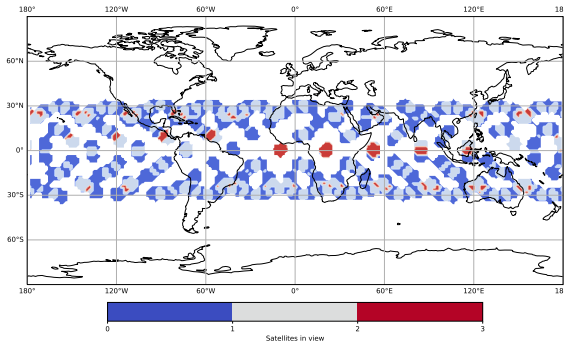


(b) Spatial coverage at 500 km altitude

Figure 7.27: Spatial coverage (number of Astrome SpaceNet satellites in view) at altitudes of 400 km and 500 km

### Visibility

Figure 7.28 shows the number of Astrome Spacenet satellites have the small satellite at 400 km / 51.5° (left) and a small satellite at 500 km / 97.5° (right) in view throughout four hours. The small satellite in the 400 km inclined orbit is in view of up to 5 satellites at a time. The small satellite in the 500 km polar orbit is in view of up to 3 satellites at a time

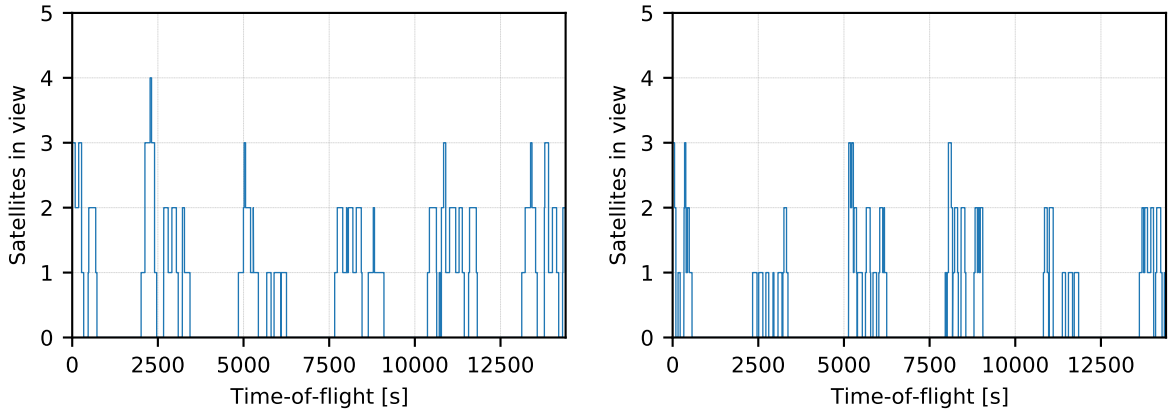


(a) Number of satellites that have the small satellite in a 400 km orbit inclined at 51.6° in view

(b) Number of satellites that have the small satellite in a 500 km orbit inclined at 97.5° in view

Figure 7.28: Number of Astrome Systems satellites that can view the small satellites over a period of four hours.

### Pass duration distribution

Figure 7.29 shows the distribution of the pass durations during a period of seven days for the two small satellite orbits with the Astrome SpaceNet constellation. The pass durations for the small satellite in the 400 km inclined orbit are spread between 15 to 550 seconds, with a total amount of 1536 passes occurring throughout the 7 days. The pass durations for the small satellite in the 500 km polar orbit are shorter of duration, up to 200 seconds. On average for both orbits most passes appear with a length of around 120 to 150 seconds.

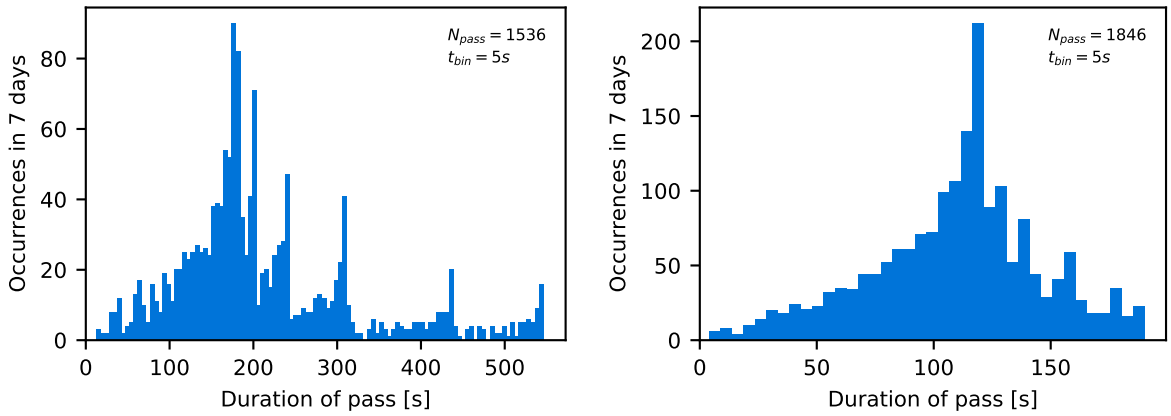


(a) Pass temporal distribution for a small satellite in an 400 km orbit inclined at 51.6°.

(b) Pass temporal distribution for a small satellite in an 500 km orbit inclined at 97.5°.

Figure 7.29: Distribution of pass durations with the Astrome SpaceNet (mega-)constellation for a small satellite in a 400 km inclined orbit (left) and a small satellite in a 500 km polar orbit (right) over a period of seven days

### Gap duration distribution

Figure 7.30 shows the distribution of the gap durations during a period of seven days for the two small satellite orbits with the Astrome SpaceNet constellation. For both the 400 km altitude and 500 km altitude orbits the gaps appear in two groups. The short duration gaps, less than 300 seconds gaps, are caused by the gaps in between the operating field-of-view of each of the Astrome satellites. The long duration gaps, around 1500 seconds at 400 km and 1800 seconds at 500 km, are caused by the satellite crossing the regions beyond ±30° latitude where the Astrome SpaceNet constellation does not provide coverage.

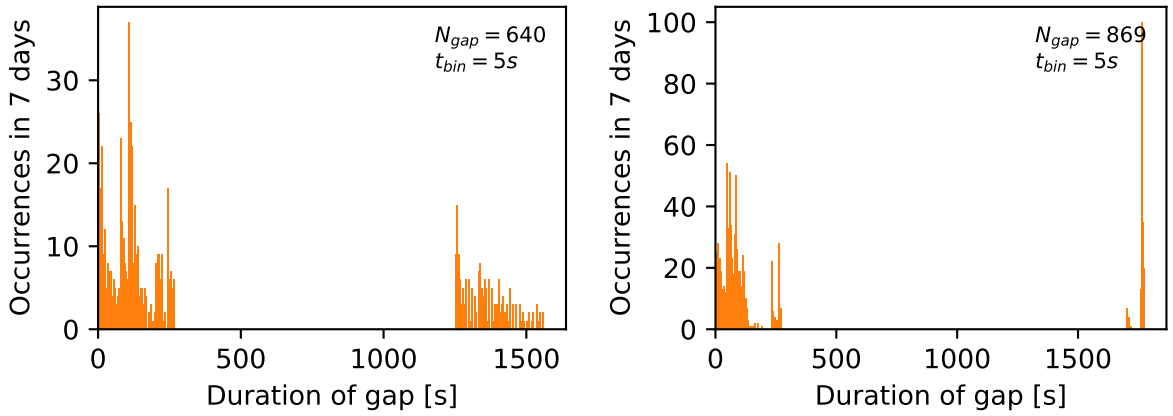


(a) Gap temporal distribution for a small satellite in an 400 km orbit inclined at 51.6°.

(b) Gap temporal distribution for a small satellite in an 500 km orbit inclined at 97.5°.

Figure 7.30: Distribution of gap durations with the Astrome SpaceNet (mega-)constellation for a small satellite in a 400 km inclined orbit (left) and a small satellite in a 500 km polar orbit (right) over a period of seven days

### Coverage with minimum contact time

Figure 7.31 shows the overall coverage as function of the minimum contact time over a period of seven days with the Astrome SpaceNet constellation. The small satellite in the 400 km inclined orbit starts with a coverage of about 42% limited by the constellation not providing coverage above ±40° latitude. The coverage by the constellation then quickly drops to less than 20% for a minimum contact time of 200 seconds but still provides some coverage up to 580 seconds. Similarly for the small satellite in the 500 km polar orbit the starting coverage of 26% is limited by there existing no coverage at higher latitudes. The coverage for this orbit quickly drops to 0% at 200 seconds.

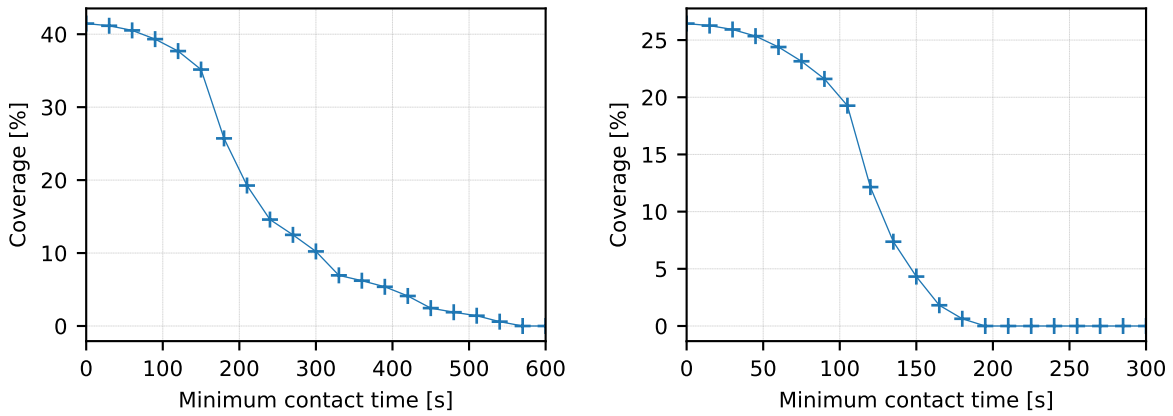


(a) Coverage against minimum contact time over a period of 7 days for a small satellite in an 400 km orbit inclined at 51.6°.

(b) Coverage against minimum contact time over a period of 7 days for a small satellite in an 500 km orbit inclined at 97.5°.

Figure 7.31: Coverage against minimum contact time needed for communications with the Astrome SpaceNet (mega-) constellation for a small satellite in a 400 km inclined orbit (left) and a small satellite in a 500 km polar orbit (right) over a period of seven days

## 7.3. MEO constellations

Two MEO constellations are considered in this work O3b and Audacy. The constellation of Audacy is designed for a satellite relay architecture and uses only three satellites at a higher MEO orbits to provide coverage in LEO. The constellation of O3b is designed for broadband connectivity and uses several satellites in lower MEO orbits with overlapping ground converage. The following two sections will the parameters of interest of section 7.1 for each constellation.

### 7.3.1. O3b mPOWER

The O3b mPOWER constellation is characterized by its 32 equatorial satellites and 10 satellites in two inclined planes [183]. The O3b satellites serve users down to 5° elevation resulting in a wide operating range for the shapeable and steerable spot beams. The satellites do not have inter-satellite links but will always be in view of a gateway ground station.

#### Spatial coverage

Figure 7.32 shows the number of O3b mPOWER satellites in view for two altitudes, 400 km and 500 km. The constellation with its equatorial and inclined satellites offer a full coverage at 400 km. At 500 km there are four spots where the low elevation angle of operation at the edges of the operating range of a satellites results into a gap at this altitude.

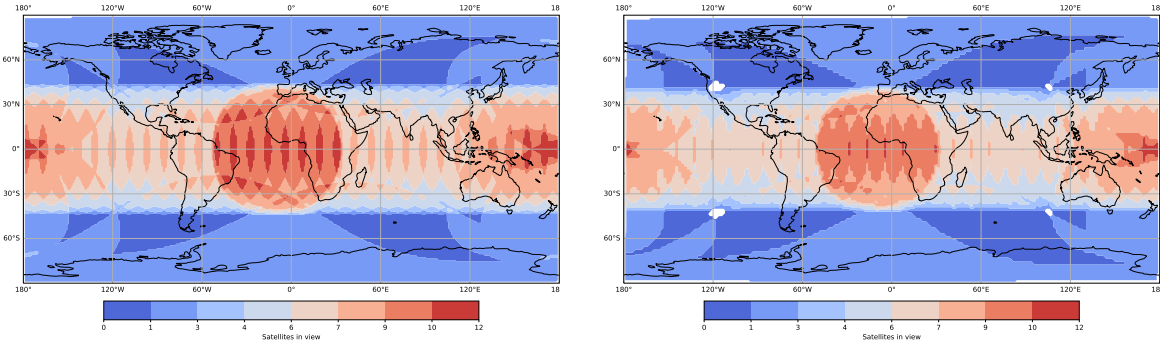

(a) Spatial coverage at 400 km altitude

(b) Spatial coverage at 500 km altitude

Figure 7.32: Spatial coverage (number of O3b mPOWER satellites in view) at altitudes of 400 km and 500 km

#### Visibility

Figure 7.33 shows the number of O3b mPOWER satellites that have the small satellite at 400 km / 51.5° (left) and a small satellite at 500 km / 97.5° (right) in view throughout four hours. The small satellite in the 400 km inclined orbit is in view of up to 12 satellites at a time with a minimum of one satellite. The small satellite in the 500 km polar orbit is in view of up to 11 satellites at a time also with a minimum of one satellite.

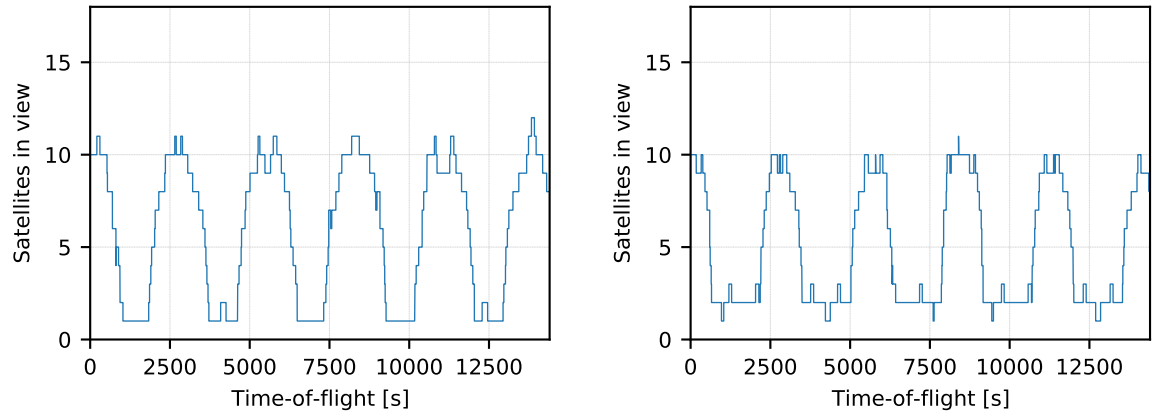


(a) Number of satellites that have the small satellite in a 400 km orbit inclined at 51.6° in view

(b) Number of satellites that have the small satellite in a 500 km orbit inclined at 97.5° in view

Figure 7.33: Number of O3b mPOWER satellites that can view the small satellites over a period of four hours.

### Pass duration distribution

Figure 7.34 shows the distribution of the pass durations during a period of seven days for the two small satellite orbits with the O3b mPOWER constellation. The wide operating field-of-view of the O3b satellites allows for long duration passes, up to 1800 seconds for both the 400 km inclined orbit and the 500 km polar orbit.

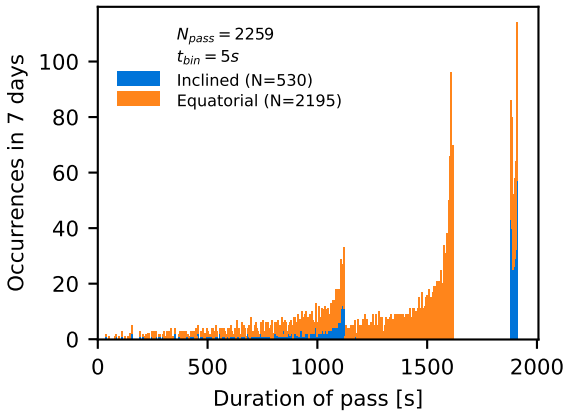


(a) Pass temporal distribution for a small satellite in an 400 km orbit inclined at 51.6°.

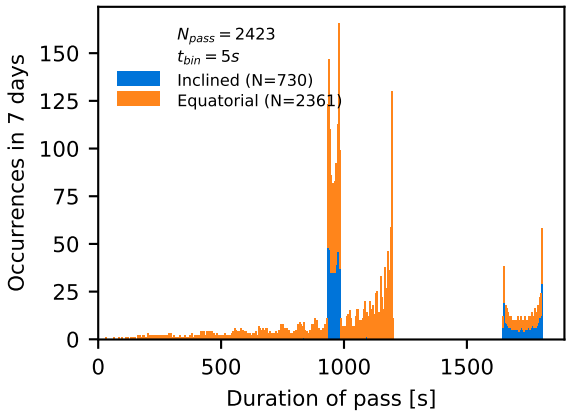


(b) Pass temporal distribution for a small satellite in an 500 km orbit inclined at 97.5°.

Figure 7.34: Distribution of pass durations with the O3b mPOWER constellation for a small satellite in a 400 km inclined orbit (left) and a small satellite in a 500 km polar orbit (right) over a period of seven days

### Gap duration distribution

The O3b mPOWER constellation provides perfect spatial coverage at 400 km and and almost perfect spatial coverage at 500 km. However, since the 500 km polar orbit is in between the two inclined planes it does not encounter the four gaps in between the coverage of the equatorial and inclined O3b satellites. Therefore, there are no gaps in the coverage for both orbits.

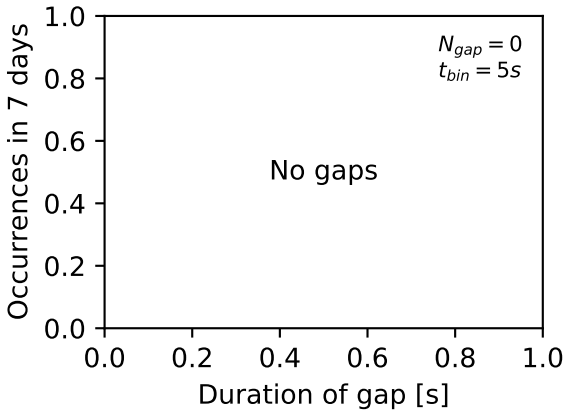


(a) Gap temporal distribution for a small satellite in an 400 km orbit inclined at 51.6°.

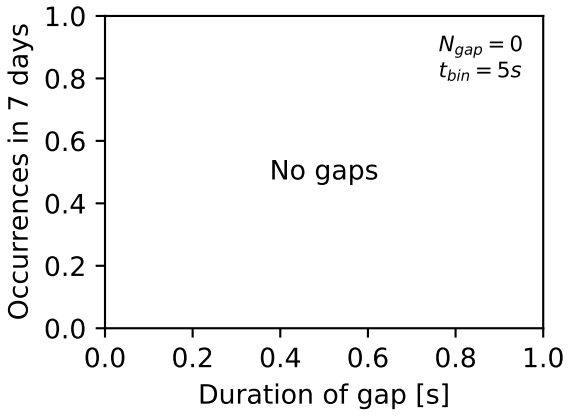


(b) Gap temporal distribution for a small satellite in an 500 km orbit inclined at 97.5°.

Figure 7.35: Distribution of gap durations with the O3b mPOWER (mega-)constellation for a small satellite in a 400 km inclined orbit (left) and a small satellite in a 500 km polar orbit (right) over a period of seven days

### Coverage with minimum contact time

Figure 7.36 shows the overall coverage as function of the minimum contact time over a period of seven days with the O3b mPOWER constellation. As shown in the previous sections the O3b constellation provides a perfect spatial coverage for 400 km orbits. This changes slightly when considering the 400 km / 51.5° inclined orbit. As can be seen in fig. 7.36, the coverage slightly reduces when considering a minimum contact time for the this orbit, while for the 500 km the coverage stays 100%. The reason for this is because the 400 km inclined orbit just passes above the coverage of the equatorial O3b satellites. Here the O3b inclined satellites can provide coverage but just at their far ends of their operating range. This results into short passes, which if excluded because of a minimum contact time become gaps in the coverage. The 500 km polar orbit does not experience this problem because it is continuously in the middel of the coverage provided by the two inclined planes of the O3b constellation.

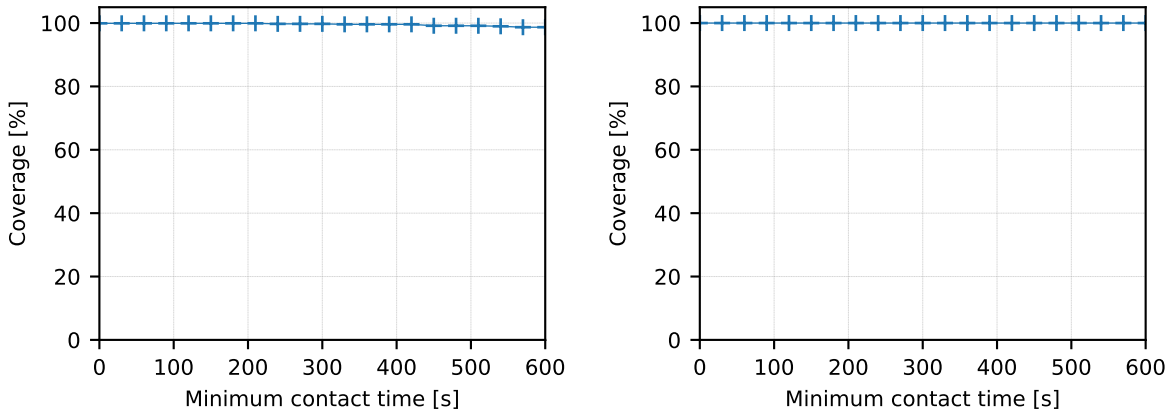


(a) Coverage against minimum contact time over a period of 7 days for a small satellite in an 400 km orbit inclined at 51.6°.

(b) Coverage against minimum contact time over a period of 7 days for a small satellite in an 500 km orbit inclined at 97.5°.

Figure 7.36: Coverage against minimum contact time needed for communications with the O3b constellation for a small satellite in a 400 km inclined orbit (left) and a small satellite in a 500 km polar orbit (right) over a period of seven days

## 7.3.2. Audacy

The Audacy constellation is characterized by its 3 equatorial satellites spaced 120° apart at a high altitude of 13900 km [76] that are specifically designed for relaying data from other satellites. The operating field-of-view for standard satellites is characteristic by having two parts, a central circle and a outer ring beyond the horizon. The Audacy constellation also features dedicated spot beams for advanced users, however in this analysis only the beams in the standard split field-of-view are considered.

### Spatial coverage

Figure 7.37 shows the number of Audacy satellites in view for two altitudes, 400 km and 500 km. As designed, the combination of a central circle of one Audacy satellite and the outer rings of the two

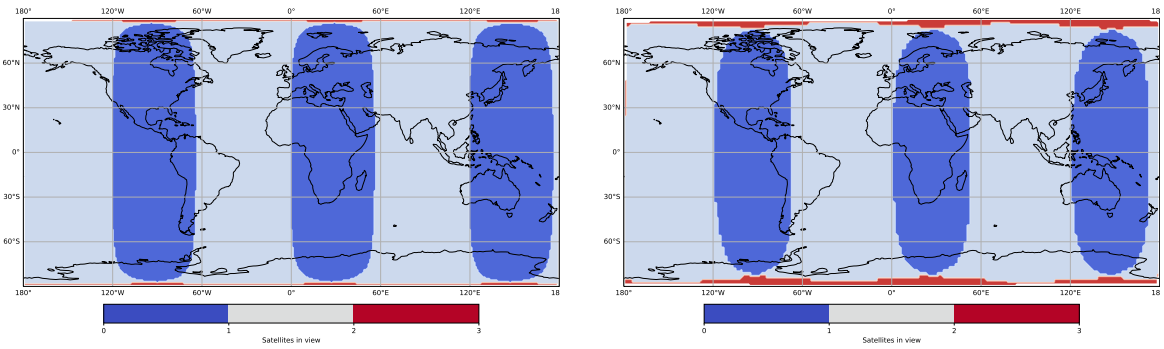


(a) Spatial coverage at 400 km altitude

(b) Spatial coverage at 500 km altitude

Figure 7.37: Spatial coverage (number of Audacy satellites in view) at altitudes of 400 km and 500 km

others provide a full spatial coverage at both altitudes. Near the far polar regions three satellites may be in view at once.

### Visibility

Figure 7.38 shows the number of Audacy satellites that have the small satellite at 400 km / 51.5° (left) and a small satellite at 500 km / 97.5° (right) in view throughout four hours. The small satellite in the 400 km inclined orbit experiences long passes with always one satellite in view and a seamless handover to the next satellite. The small satellite in the 500 km polar orbit experience similar long passes with occasionally 3 satellites in view at the polar regions.

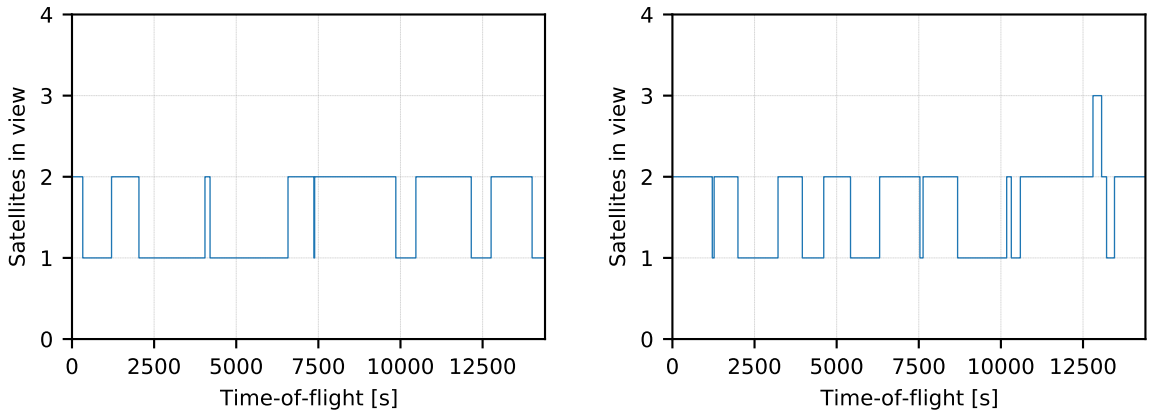


(a) Number of satellites that have the small satellite in a 400 km orbit inclined at 51.6° in view

(b) Number of satellites that have the small satellite in a 500 km orbit inclined at 97.5° in view

Figure 7.38: Number of Audacy satellites that can view the small satellites over a period of four hours.

### Pass duration distribution

Figure 7.39 shows the distribution of the pass durations during a period of seven days for the two small satellite orbits with the Audacy constellation. The constellation design allows for long duration passes around 3000 seconds or higher for the 400 km inclined orbit and 500 km polar orbit. The 500 km polar orbit also experiences some passes of 6000 seconds where it is travelling for a long duration in the outer ring of the field-of-view of a Audacity satellite that is at that moment perpendicular to its orbital plane.

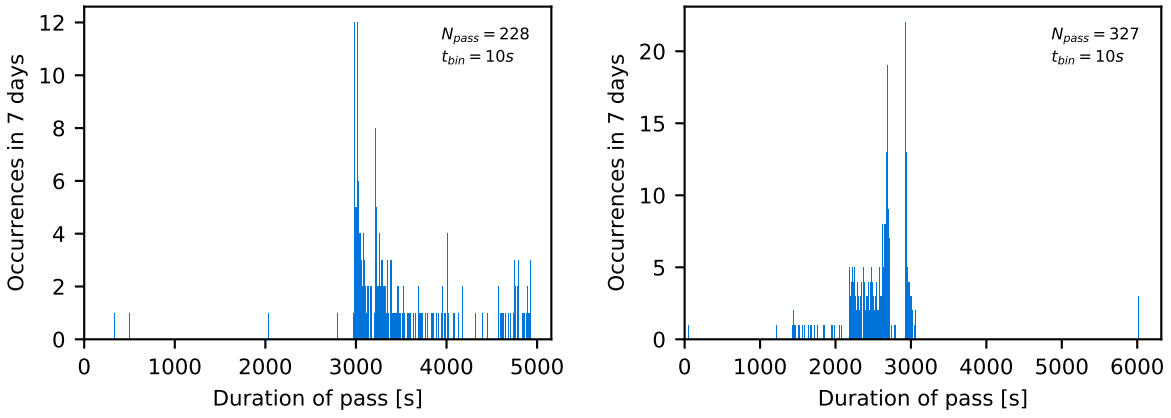


(a) Pass temporal distribution for a small satellite in an 400 km orbit inclined at 51.6°.

(b) Pass temporal distribution for a small satellite in an 500 km orbit inclined at 97.5°.

Figure 7.39: Distribution of pass durations with the Audacy constellation for a small satellite in a 400 km inclined orbit (left) and a small satellite in a 500 km polar orbit (right) over a period of seven days

### Gap duration distribution

The design of the Audacy constellation provides perfect spatial coverage at 400 km and 500 km with no gaps appearing over the simulated period of seven days.

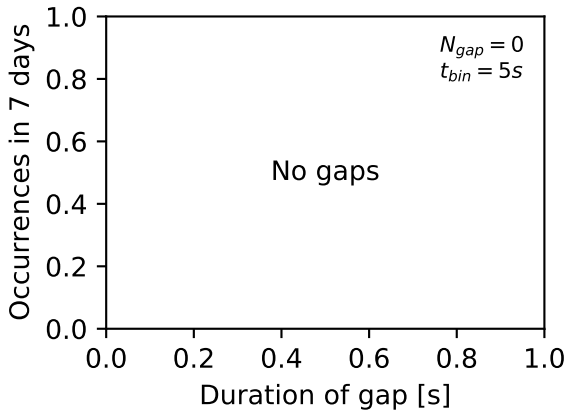


(a) Gap temporal distribution for a small satellite in an 400 km orbit inclined at 51.6°.

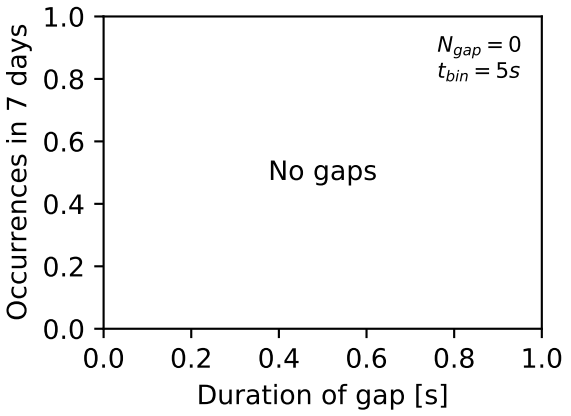


(b) Gap temporal distribution for a small satellite in an 500 km orbit inclined at 97.5°.

Figure 7.40: Distribution of gap durations with the Audacy constellation for a small satellite in a 400 km inclined orbit (left) and a small satellite in a 500 km polar orbit (right) over a period of seven days

### Coverage with minimum contact time

Figure 7.41 shows the overall coverage as function of the minimum contact time over a period of seven days with the Audacy constellation. As shown in the previous sections the Audacy constellation provides a perfect spatial coverage for 400 km and 500 km orbits with long duration contact times. Only a slight change is observed for the 500 km polar orbit, where at a minimum contact time of 600 seconds the coverage starts to decrease slightly. Short gaps appear when the small satellite passes just below the horizon for one of the Audacy satellites while coming only briefly in view of the next Audacy satellite.

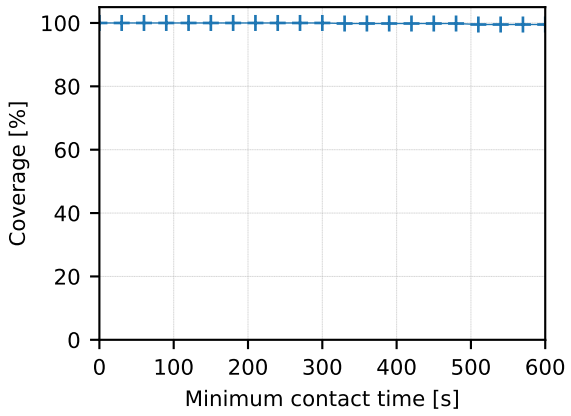


(a) Coverage against minimum contact time over a period of 7 days for a small satellite in an 400 km orbit inclined at 51.6°.

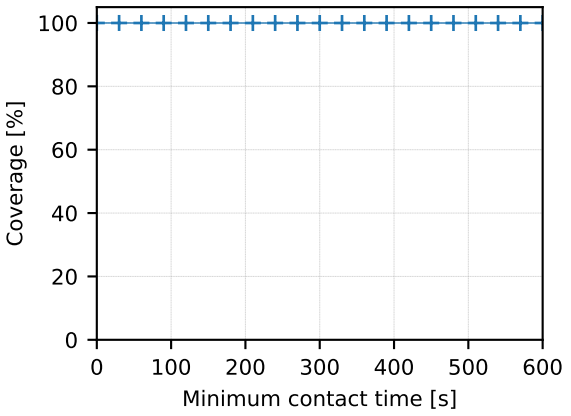


(b) Coverage against minimum contact time over a period of 7 days for a small satellite in an 500 km orbit inclined at 97.5°.

Figure 7.41: Coverage against minimum contact time needed for communications with the Audacy constellation for a small satellite in a 400 km inclined orbit (left) and a small satellite in a 500 km polar orbit (right) over a period of seven days

## 7.4. Summary

In this chapter eight different NGSO (mega-)constellations were evaluated for the data-relay downlink architecture. Six constellations in LEO and two in MEO were evaluated for two orbits, a 400 km 51.6° inclined orbit and a 500 km, 97.5° inclined Sun-synchronous. The evaluation looked at spatial coverage, visibility, pass duration, gap duration and overall coverage time taking into account a minimum contact duration. Table 7.1 and Table 7.2 shows summaries of the results for a satellite in the 400 km and 500 km orbits respectively. A qualitative rating is given based on the number of satellites in view and the coverage for minimum contact time.

The higher altitude constellations in the LEO category score the best for both altitudes, these include the Telesat constellation and the 2019 configuration of the Starlink configuration having shells of satellites around 1200 km. The lower altitude constellations including Starlink's 2020 configuration, Kuiper Systems and Astrome having shells around 550 km, score lower and are virtually un-usable for orbits above 400 km as the coverage significantly reduces for contact times over more than a minute. The OneWeb constellation uses a polar orbit configuration resulting into short contact opportunities for the 400 km satellite and therefore receives a poor rating. For the 500 km case OneWeb scores better, achieving longer passes with better coverage because the orbits are roughly in-plane with the orbit of the satellite.

Table 7.1: Summary of results for 400 km, 51.6° inclined orbit

| Constellation | Passes | Sat. in view | | Coverage for min. contact time | | | | | | Rating |
|---|---|---|---|---|---|---|---|---|---|---|
| | | min | max | 15 s | 30 s | 60 s | 150 s | 300 s | 600 s | |
| **Telesat** | 17775 | 5 | 21 | 100.0% | 100.0% | 100.0% | 99.9% | 80.3% | 69.2% | ++ |
| **OneWeb** | 4195 | 0 | 1 | 60.6% | 57.8% | 44.0% | 6.4% | 0.0% | 0.0% | - |
| **Starlink 2019** | 24588 | 2 | 22 | 100.0% | 99.9% | 99.7% | 79.9% | 65.5% | 43.6% | ++ |
| **Starlink 2020** | 11483 | 0 | 8 | 68.3% | 61.4% | 26.5% | 13.4% | 13.4% | 6.9% | - |
| **Kuiper Systems** | 8022 | 0 | 5 | 81.2% | 76.5% | 45.5% | 16.7% | 5.5% | 2.2% | +/- |
| **Astrome** | 1536 | 0 | 5 | 41.3% | 41.2% | 40.5% | 35.2% | 10.2% | 0.0% | +/- |
| **O3b** | 2259 | 1 | 12 | 99.9% | 99.9% | 99.9% | 99.9% | 99.7% | 98.7% | ++ |
| **Astrome** | 228 | 1 | 2 | 100.0% | 100.0% | 100.0% | 100.0% | 100.0% | 100.0% | ++ |

The MEO constellations perform excellent in terms of contact opportunity duration and coverage. Because of the higher altitudes of these constellations a large portion of the orbits are continuously in view of the same satellite, resulting in a high coverage that does not reduce significantly for longer pass durations. This increased coverage however comes at the cost of a significantly larger range with respect to the best rated LEO constellations. The inter-satellite distance is up to seven times longer for the O3b constellation and twelve times for the Audacy constellation. This increase in path-loss will directly impact the design of the data-relay downlink requiring higher transmission powers or larger antennas with more gain.

Table 7.2: Summary of results for 500 km, 97.5° inclined orbit

| Constellation | Passes | Sat. in view | | Coverage for min. contact time | | | | | | Rating |
|---|---|---|---|---|---|---|---|---|---|---|
| | | min | max | 15 s | 30 s | 60 s | 150 s | 300 s | 600 s | |
| **Telesat** | 19851 | 0 | 18 | 83.5% | 83.3% | 82.3% | 62.6% | 11.4% | 3.1% | ++ |
| **OneWeb** | 5854 | 0 | 4 | 56.1% | 49.5% | 24.8% | 17.6% | 11.0% | 0.0% | +/- |
| **Starlink 2019** | 30663 | 2 | 15 | 99.9% | 99.8% | 97.2% | 39.4% | 12.3% | 0.0% | ++ |
| **Starlink 2020** | 4934 | 0 | 2 | 1.3% | 0.2% | 0.1% | 0.1% | 0.0% | 0.0% | -- |
| **Kuiper Systems** | 5655 | 0 | 3 | 9.7% | 1.0% | 0.0% | 0.0% | 0.0% | 0.0% | -- |
| **Astrome** | 1846 | 0 | 3 | 26.3% | 25.9% | 24.4% | 4.3% | 0.0% | 0.0% | -- |
| **O3b** | 2423 | 1 | 10 | 100.0% | 100.0% | 100.0% | 100.0% | 100.0% | 100.0% | ++ |
| **Astrome** | 327 | 1 | 3 | 100.0% | 100.0% | 100.0% | 100.0% | 100.0% | 99.5% | ++ |

Based on these results a sub-selection can be made for the constellations that are considered in the rest of this work. The higher altitude LEO constellations are most promising as they offer the longest contact opportunities and the best coverage. Recent approval by the FCC allowed SpaceX to operate in the latest Starlink 2020 configuration [202]. In this configuration of the Starlink constellation the

proposed data-relay downlink concept becomes less promising. Similarly the future of OneWeb and its constellation is uncertain [162] [171], and its constellation is scoring worse for non-polar orbits. This leaves the Telesat constellation for consideration for further analysis, performing the best overall of the LEO constellations for both altitudes. With the recent bankruptcy of Audacy [77] it becomes obvious to only consider the O3b constellation for further analysis.

These two candidate constellations, Telesat and O3b, form a good contrast for the design optimization. The Telesat constellation has frequent contact opportunities of shorter duration with satellites that are close-by. While the O3b constellation has satellites that are further away allowing for longer passes. A future study may re-consider the other constellations, especially in the context of VLEO small satellite missions, the lower NGSO constellations might offer a solution for the downlink needs of these missions.

This page intentionally left blank.

# 8

# Communication system optimization framework

In this chapter the NGSO data-relay optimization framework is presented that was developed to optimize a data-relay communication system use of the contact opportunities with the NGSO (mega-) constellations. A multi-objective approach is used to explore the design trade-offs for the communication system in throughput, latency, energy consumption and time spend pointing the spacecraft/antenna. Additional design variables such as size, weight and power, and operational parameters such as duty cycle and contact time, are derived from these four objectives.

The data-relay optimization framework uses the `pymoo`: Multi-objective Optimization in Python framework design by J. Blank and K. Deb [203] as a framework for the multi-objective optimization. The framework runs models that are developed in this work for calculating the fitness values and constraints. These models consider the communication link budgets, variable modulation and coding schemes, energy consumption models, and parametric component models and operation models. These models are described step-by-step increasing in complexity until the complete optimization problem is formulated. Several multi-objective genetic algorithms are used to explore the complex design space of the NGSO data-relay problem.

In section 8.1 of this chapter the top-level requirements for the data-relay optimization framework are outlined and explained. Section 8.2 provides a top-level overview of the data-relay optimization framework, a description of the general operation of the optimization framework, a description of the models and a brief summary of the terminology in multi-objective genetic algorithm optimization. Section 8.3 to section 8.10 describe the different models that were developed to compute the fitness objective functions and the constraints to be used in the optimization. This chapter will conclude with a summary, recommendations and discussion for the data-relay orbital simulator in section 8.13.

## 8.1. Data-relay optimization framework requirements

This section will outline some high-level requirements that were set-up to guide the development of the data-relay optimization framework. As explained in the methodology of chapter 2, the data-relay optimization framework will generate a concept design for an NGSO data-relay downlink that makes optimal use of the contact opportunities for a given small satellite mission and NGSO (mega-)constellation. The first requirement for the data-relay optimization framework is therefore:

**DROF-1** The data-relay optimization framework shall optimize the design parameters of a data-relay downlink system on a small satellite for a given mission profile and NGSO (mega-) constellation.

Finding an optimal design is a complex task because of the amount and variation in the different contact opportunities that appear throughout the small satellite orbit. Therefore to aid in this design synthesis optimization algorithms are to be used. These optimization algorithms should consider several aspects of the data-relay downlink architecture, the first being which contact opportunity are to be used. Different combinations of contact opportunities need to be considered assuming that there is

only one data-relay downlink available on the small satellite and therefore the data can only be relayed to one NGSO satellite at a time. The contact opportunities might be (partially) overlapping and different combinations might give different results in latency and throughput. Therefore, the second requirement is to consider different combinations in contact opportunities in the optimization:

**DROF-2** The data-relay optimization framework shall evaluate using different combinations of the contact opportunities that appear throughout the small satellite orbit.

The next step is to calculate the link-budgets for the selected contact opportunities to determine the signal-to-noise ratio (SNR) at the NGSO satellite that receives the data. The link budgets should consider controllable design parameters that such as transmitter output power, antenna gain and bandwidth. In order to not generalize and come to a true optimum each contact opportunity should be considered separately. Therefore, the third requirement is:

**DROF-3** The data-relay optimization framework shall evaluate the link-budgets for each selected contact opportunity for relaying data while considering the design parameters of the components in the data-relay downlink.

After the received SNR at the NGSO satellite is determined, an optimal modulation and coding scheme can be selected[1]. The modulation and coding will influence the data-rate of the link during the contact opportunity but also the complexity of the transmitter and its power-efficiency. Because of the short duration of the contact opportunity, it is assumed that a adaptive coding and modulation (ACM) scheme, where the modulation and coding scheme is varied during the pass would not result in significantly better performance. However, a variable coding and modulation (VCM) scheme may be considered where the modulation and coding is fixed during each contact opportunity, but may be different for the different contact opportunities. Therefore the fourth requirement states:

**DROF-4** The data-relay optimization framework shall evaluate variable coding and modulation (VCM) schemes for the selected contact opportunities.

Finally, the performance of the synthesised NGSO data-relay downlink needs to be evaluated. In order to do so, the data-relay optimization framework should be able to output different performance parameters that are of interest for the use-cases discussed in chapter 5. The performance parameters included are latency, throughput and energy consumption, and size, weight and (maximum) power:

**DROF-5** The data-relay optimization framework shall determine the following performance parameters for the data-relay downlink solutions: throughput, latency and energy consumption per orbit, and size, weight and power.

## 8.2. Optimization framework overview

The data-relay optimization framework uses genetic algorithms to optimize the design of the data-relay downlink. A genetic algorithm optimizes a problem by mimicking nature's survival of the fittest using evaluation of one or multiple fitness functions and constraints [203]. Figure 8.1 shows an overview of the steps in a genetic algorithm.

The first step in a genetic algorithm is to initialize a population (0.). A population is a set of design vectors, i.e. $[\boldsymbol{x}_1, \boldsymbol{x}_2, ..., \boldsymbol{x}_{N_{pop}}]$. Each design vector can contain several variables, $\boldsymbol{x}_1 = [a_1, b_1, ..., z_1]$, that each represent a particular choice in the design space. In this work, the variables are used to for example select which contact opportunities, or transmission powers are used. A population initialization can be done by randomizing the variables in each design vector, or by using population of a previous optimization.

After a population is initialized, the design vectors in the population can be evaluated (1.) for one or multiple fitness functions, also called objective functions $f(\boldsymbol{x})$, and constraints $g(\boldsymbol{x})$. The fitness functions evaluate how well a design, specified by its design vector, is performing. The constraints are used to evaluate if the design is not violating any rules set out in the optimization problem. If it is not violating the constraints the design vector is called a solution to the problem. After evaluation, the designs can be ranked by their fitness and the highest ranking individuals are surviving (2.) and

[1] The relation between SNR and the modulation and coding scheme dependent bit-energy-to-noise-density $E_b/N_0$ or symbol-energy-to-noise-density $E_s/N_0$ is discussed in section 8.4.1

are maintained in the next population. A selection (3.) process is performed to determine which of the individuals participate in mating. Different numbers of parents can be selected depending on the algorithm that is used. The cross-over process (4.) combines the properties of several parents into new individuals. Finally, before repeating the evaluation process, several of the off-springs are mutated (5.), changing some of the variables in the design vectors to create a more diverse population. This cycle is continued until the termination criteria are met.

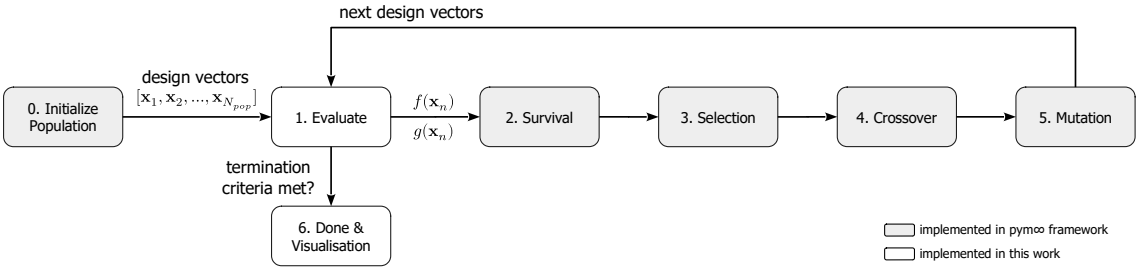


Figure 8.1: Steps in a typical genetic algorithm using the pymoo framework [203]. The models for fitness function and constraint evaluation are developed in this work.

Several optimization algorithms were evaluated and a genetic optimization algorithm was chosen because it can perform optimizations for non-linear and non-continuous problems, which makes it suitable for a practical problem such as the design of the data-relay downlink communication system. In addition, as will be shown in this chapter, the genetic algorithms can use mixed variable programming in which some design variables are binary variables (selection of a contact opportunity), some are real variables (selection of the transmitter power and antenna gain) and some are integer (selection from a set of pre-defined transmission bandwidths).

The survival, selection, cross-over and mutation processes are provided in the `pymoo` framework. This work implements the specific models for the data-relay downlink optimization that specify how the fitness functions and constraints are defined and calculated. The next section discusses the different models that were implemented.

### 8.2.1. General operation

During the optimization, the `pymoo` framework repeatedly provides the models developed in this work with a population of new individuals (specified by their design vectors) for evaluation. The models then compute, based on the selection in the design vectors, the fitness values towards the objectives and the constraints. This interface between the `pymoo` framework and the data-relay optimization framework models uses only mathematical variables including booleans, integers and floating point values. The `pymoo` framework thereby does not 'know' the optimization problem at hand is considering contact opportunities, satellites, transmission bandwidths, etc. Instead, it is programmed in such a way that the boolean, integer or floating point variables in the design vector each have a particular meaning for a choice in the data-relay downlink problem, that only the models interpret, which then provide values for each of the fitness functions, that on-itself do not have meaning for the `pymoo` framework, other than these should be minimized. This process is repeated and based on the algorithm used, new design vectors are generated, provided and evaluated until the termination criteria is met. This termination criteria could be the number of evaluations, the variation in the design or objective space, or a simple computational time limit.

### 8.2.2. Models

For the evaluation of the fitness functions and constraints, nine models were implemented. These models compute the fitness functions and constraint values given a set of contact opportunities with an NGSO (mega-)constellation (found previously using the data-relay orbital simulator chapter 6) and a design vector $\boldsymbol{x}$ that specifies how the contact opportunities are to be used. Figure 8.2 shows the models that were implemented to evaluate the fitness functions and constraints.

The visibility model takes the selection of the contact opportunity (the pass selection) and the an-

tenna gain and determines which satellites are in view. The pointing model extends on the visibility model by computing the antenna pointing angles and durations that are required to observe the inter-satellite passes with the NGSO constellation. The amount of time required for pointing the antenna is counted towards the first objective. To reduce the technical and operation complexity of the data-relay downlink the amount of time spend pointing the antenna should be minimized, allowing the satellite to perform other activities such as collecting payload data or charging batteries. Next, the link budget model computes the signal-to-noise ratios during each of the selected inter-satellite passes based on the visibility, the transmit powers and transmission bandwidth. The bandwidth model specifies the number of sub-carriers that will be used to fill the transmission bandwidth. Then the variable coding and modulation model determines the modulation and coding scheme to be used for each pass to maximize the throughput for this solution. The throughput is used as a second objective and should be maximized or reach a minimum value based on the specific mission. This throughput comes at the cost of consuming energy by the power consumption of the transmitter. This energy consumption is computed in the energy model based on the transmission power and efficiencies in the transmitter. The energy consumption of the solution is used as the third objective and is to be minimized. Next, from the actual moments for which a link is established, the maximum latency is computed in the latency model. The maximum latency is used as the fourth and final objective and is to be minimized or at least stay below a maximum value.

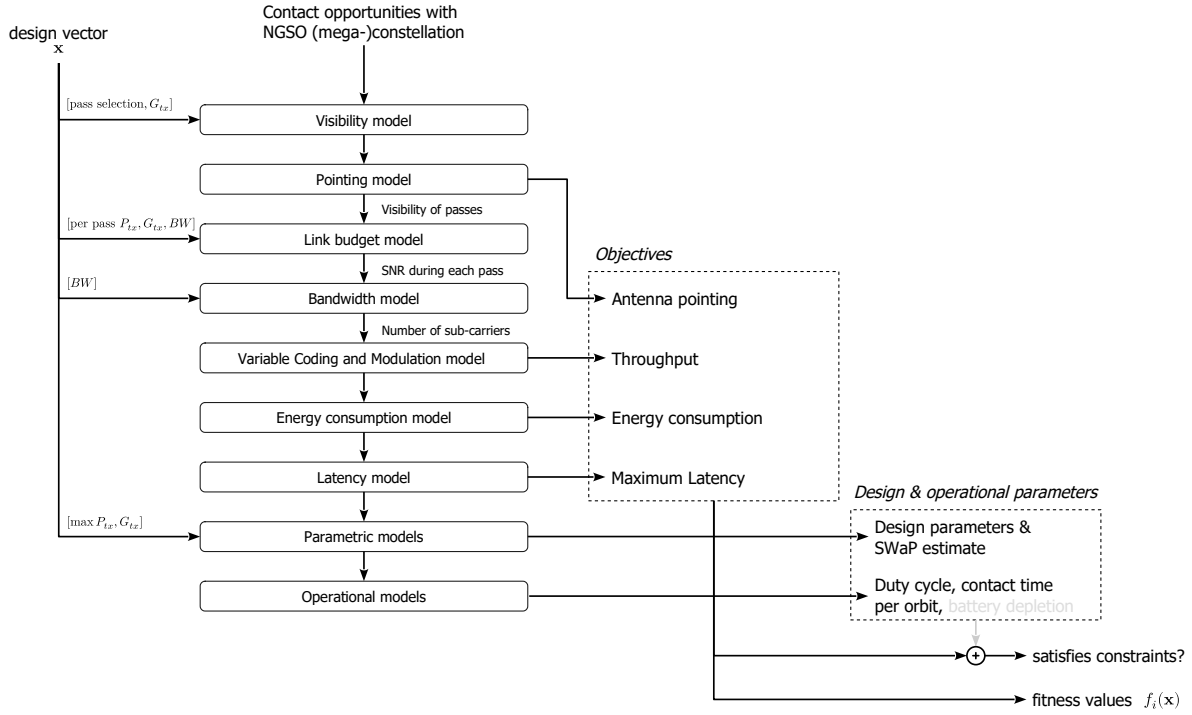


Figure 8.2: Models implemented to compute fitness functions (objectives), design and operational parameters and constraints for use in the genetic algorithm optimization of the data-relay downlink

These first six models compute the four fitness values that score the design vectors of the individuals in the populations for the four objectives; throughput, energy consumption, antenna pointing and maximum latency. The last two models use values from the design vector to compute remaining (operational) parameters of the data-relay downlink communication system. These (operational) parameters are not used as objectives, as they are the result of the selection made by the design vector or derived from the objective. However, these parameters may be used as additional constraints to the optimization, potentially invalidating a solution because it exceeds a design parameter. For example, the parametric model estimates design parameters such as size, weight and peak power consumption of the solution. The operational models include parameters such as the duty cycle at which the system is operated. The contact time per orbit that is achieved with the solution or potentially more advanced

operational parameters such as the depletion of the batteries based on the dynamic power consumption over time.

Both the fitness functions as the design and operational parameters have possible constraints associated with them that could invalidate the solution. This could be minimum and maximum requirements on the fitness values. In addition, constraints may come from an technical perspective such as the number of links that can be established at the same time. Depending on the algorithm used, the solutions with the lowest constraint violations have the higher chance of survival and selection. Leading the problem to converge to solutions that do not violate the constraints and maximize or minimize the design objectives.

The following sections (after the terminology summary) will discuss the implementation of each of the models developed. Each model is adding to the previous model and increases the optimization complexity. For each model, a description explaining what the model is supposed to provide is provided, a mathematical formulation of an optimization problem is given and the results of an example optimization are shown. This overview of models starts with the contact model, which is not directly used in the optimization framework but instead used to familiarize the reader with the approach of optimization problem formulation to implementation.

### 8.2.3. Terminology

Several terms specific to genetic optimization algorithms are used throughout this chapter. For reference their definitions are given below:

**Design vector** a vector with variables that correspond to different design choices

**Design space** the space spanned by all combinations of the variables in the design vector

**Individual** a single sample in the design space, characterized by a design vector, that survived after a generation or was created by a cross-over of other individuals in the previous generation

**Solution** an individual that does not violate any of the optimization constraints

**Population** the set of individuals that exist during a generation

**Generation** the state of the population in-between the evolution cycle

**Evaluation** the start of the evolution cycle in which the fitness of the individuals are determined

**Survival** the process of selecting the best fit individuals that survive to the next generation

**Selection** the process of selecting the individuals that are used to generate new individuals

**Cross-over** the process of mating two or more parents into new individuals for the next generation

**Mutation** a process appearing after cross-over that (slightly) alters the properties (design vector) of the individual

**Fitness function/objective function** a function that is used to evaluate the fitness of an individual, scoring for one or multiple objectives.

**Solution space** the space spanned by all possible solutions in the optimization

**Pareto set of solutions** the set of solutions for which no other solutions exists that is better towards all objectives

**Pareto front** a front of optimal solutions showing the optima towards all objectives.

## 8.3. Contact model

The contact model is setup and used in a simple optimization problem using the output data set of a simulation in the NGSO data-relay orbital simulator to get familiar with the optimization approach. The model assumes the small satellite can only establish communication with one NGSO satellite at a time and that the small satellite cannot switch satellites during a inter-satellite pass. The goal is maximizing the contact time over a given period under this constraint. In this optimization problem, there are no

constraints on the distance between the satellites or the field-of-view of the small satellite. A textual formulation of this optimization problem can be made as follows:

**Contact optimization**
Given a set of contact opportunities with a NGSO (mega-)constellation:

- Use the contact opportunities that result in the maximum contact time
- Using only one inter-satellite link at a time

The following sub-sections will discuss the mathematical formulation of the contact model and accompanied optimization problem, how it is implemented in software and results. In section 8.7 the contact model is extended to the visibility model to include field-of-view constraints of the small satellite based on the design of its antenna.

### 8.3.1. Mathematical formulation

In the textual formulation of the contact optimization problem an objective and constraint can be identified. The objective is to maximize the contact time and the constraint only to use one inter-satellite link at a time. This is a single objective optimization problem. In order to solve this problem, it first needs to be expressed in a mathematical formulation that can then be programmed into software. A mathematical representation of this problem is given below:

**Design vector**
$$\boldsymbol{x} = [x_1, x_2, ..., x_{N_{pass}}]^T \tag{8.1}$$

**Objective function**
$$\max_{\boldsymbol{x}} \sum_{i}^{N_{pass}} \int_{t_{b,i}}^{t_{e,i}} x_i \, dt \tag{8.2}$$

**Constraints**
$$x_i \cdot t_{e,i} - x_j \cdot t_{b,j} \leq 0 \qquad j > i \tag{8.3}$$

**Bounds**
$$x_i \in \{0, 1\} \qquad i \in \{1, ..., N_{pass}\} \tag{8.4}$$

The design vector (eq. (8.1)) contains the variables the optimization algorithm is can to change. In this case, it consists of a variable for each contact opportunity that can be selected to be used during the orbit. These binary variables take the value zero or one as specified in the bounds (eq. (8.4)) for the design vector. The contact time can be calculated by the summation of the durations of each selected contact opportunity, where the duration is defined by the difference between the time-of-flight at the beginning of the pass $t_b$ and the end of the pass $t_e$. The objective is to maximize this contact time by the selection of contact opportunities(eq. (8.2)). The single constraint (eq. (8.3)) says that the end time-of-flight for any selected pass $i$ should appear before the begin time-of-flight for any following selected pass $j$.

This optimization problem is a single objective binary variable problem. The optimizer can choose binary options for the design vector that state whether to use a contact opportunity for data-relaying or not. However, the mathematical formulation of the problem as specified above is not yet ready to be implemented in an optimization framework. The `pymoo` optimization framework requires the problems to be pure minimization problems [203]: multiplying the objective function by $-1$ changes the problems into a minimization problem without changing the properties (i.e. the order) of the problem itself. The same holds for the constraints, they need to be formulated as a equal or less than constraint. The constraint (eq. (8.3)) is not yet in this required mathematical formulation and can in its current form not elegantly be programmed into the optimization.

The conversion of the non-overlapping selection constraint to a equal or less than constraint can be done as follows. First a matrix is setup that indicates if passes are overlapping or not:

$$B = \begin{bmatrix} t_{b,1} & t_{b,2} & \cdots & t_{b,N} \\ t_{b,1} & t_{b,2} & \cdots & t_{b,N} \\ \vdots & \vdots & \ddots & \vdots \\ t_{b,1} & t_{b,2} & \cdots & t_{b,N} \end{bmatrix} \qquad E = \begin{bmatrix} t_{e,1} & t_{e,1} & \cdots & t_{e,1} \\ t_{e,2} & t_{e,2} & \cdots & t_{e,2} \\ \vdots & \vdots & \ddots & \vdots \\ t_{e,N} & t_{e,N} & \cdots & t_{e,N} \end{bmatrix} \tag{8.5}$$

$$O = E - B \tag{8.6}$$

where $t_{b,i}$ and $t_{e,i}$ are the beginning and end times of pass $i$. The lower triangular of matrix $O$ contains the information on if a pass appears after of during a previous pass. Each element $ij$ in $O$ contains the difference of the end time of pass $i$ and the begin time of pass $j$. If this number is positive, then the end time of pass $i$ appears after the begin time of pass $j$ and therefore the pass is overlapping. The non-overlapping passes are therefore the elements in $O$ for which:

$$O_{ij} \leq 0 \text{ where } i > 1 \text{ and } j \leq i. \tag{8.7}$$

The index specification $i > 1$ and $j \geq i$ is needed to select the entries of $O$ below the first diagonal[2]. Equation (8.7) is already in the right shape for a constraint in the *pymoo* framework. The $O$ matrix can be element-wise multiplied by the design vector, column and row wise, in order to only make the constraint active for the passes that are selected and zero for the non-selected passes:

$$O \odot \boldsymbol{x}^T \boldsymbol{x} \leq 0 \tag{8.8}$$

The optimization problem can now be formulated as required in the *pymoo* multi-objective optimization framework:

$$\begin{aligned} min \quad & f_1(\boldsymbol{x}) = -\sum \boldsymbol{x}^T (\boldsymbol{t}_e - \boldsymbol{t}_b) && \boldsymbol{t}_b = [t_{b,1}, t_{b,2}, ..., t_{b,N_{pass}}]^T \\ & && \boldsymbol{t}_e = [t_{e,1}, t_{e,2}, ..., t_{e,N_{pass}}]^T \\ s.t. \quad & g_1(\boldsymbol{x}) = O \odot \boldsymbol{x}^T \boldsymbol{x} \leq 0 \\ & x_i \in \{0, 1\} && i \in 1, ..., N \end{aligned} \tag{8.9}$$

To avoid repetitions, this report will limit the mathematical description for the optimization problems to the formulation in eqs. (8.1) to (8.4). Each optimization problem is in the Python code formulated in the shape of eq. (8.9) to be interpreted and used in the pymoo framework. The implementation of each of the models can be found in `hermes_optimization.models` and associated example optimization problems in `hermes_optimization.problems` in the GitHub repository [204].

### 8.3.2. Example evaluation

The optimization problem is solved using the *pymoo* implementation of the genetic algorithm [205]. The optimal combination of passes found by the optimization are highlighted in the range and skyplots in fig. 8.3. This simple optimization problem can be checked by hand, for example pass 7 is not chosen instead of pass 8, which makes sense because pass 8 is longer. The combination of passes result into a maximum contact time of 1900s or about 33 minutes. This already gives a rough estimate of the contact time that can be achieved per orbit, the 20 passes span about two orbits of the satellite at 500 km, which means that a contact time of about 15 minutes per orbit is achievable in this example. Which is already significantly higher than the 400s per orbit achieved with polar ground stations [2].

There are more factors to consider in order to get a precise estimate of the overall contact time with the satellite. Already from the figures in fig. 8.3 one can include addition constrains on for example the maximum range (determined by the link budgets), the visibility of the passes (determined by the beam-width of the antenna and/or steerability) and minimum pass durations for protocols (determined factors such as the time needed for negotiation with the data-relay satellite). These additional constrains will be included step-by-step to the optimization problem in the following sections.

## 8.4. Link budget model

The link budget model is the first step towards determining communication performance parameters such as data-rate and throughput per orbit. A link budget determines the signal-to-noise ratio (SNR) at the receiving system in the link based on the system level RF parameters of both the transmitter and the receiver. In its most simple form a link budget considers the transmitter power and antenna gain, the free-space path loss, the signal bandwidth, and the receiver antenna gain and noise contribution. The link budget model calculates the SNR at the receiving NGSO satellite for each time-step in each (selected) contact opportunity. If the SNR is high enough for a particular modulation, coding and data-rate, a link can be established and data can be relayed.

[2]Many programming languages have a function for the lower-triangle selection, i.e. MATLABs `tril(0, -1)` or Numpy's `numpy.tril(0, -1)`

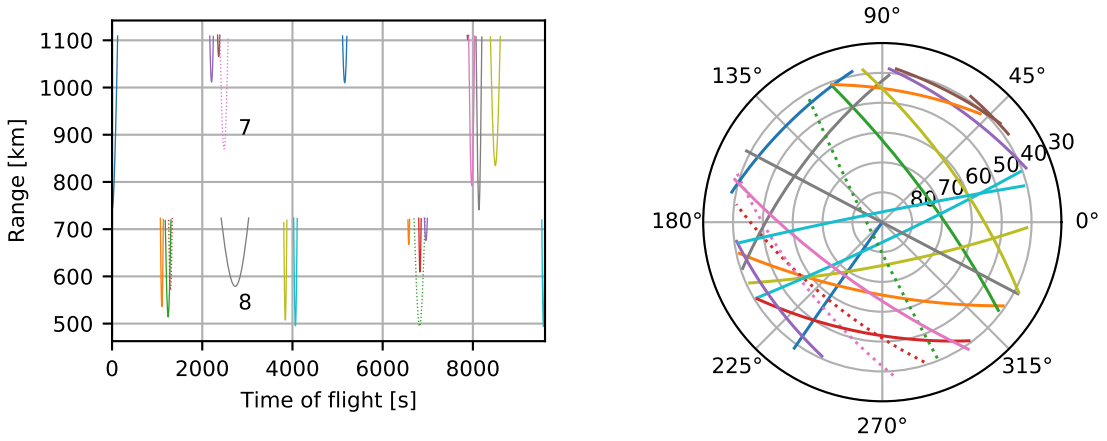


(a) Range plot showing the passes that are used (solid) to maximize contact time

(b) Skyplot showning the passes that are used (solid) to maximize contact time

Figure 8.3: Result of the contact optimization showing used (solid) and unused (dashed) passes that maximize the contact time with the satellite.

In this section a simple optimization case is considered using the link budget model where the transmitter antenna gain, signal bandwidth, receiver properties, and modulation and coding scheme are fixed for all selected passes. While the passes can be selected in the optimization as well as one transmit power for all passes. This optimization problem reads as follows:

**Throughput optimization**

Given a set of contact opportunities with a NGSO (mega-)constellation and a set of fixed link budget parameters:

- Select the contact opportunities and transmission power that result into the highest throughput
- Using the least amount of energy
- Using only one inter-satellite link at a time

The following sub-sections will discuss the mathematical formulation of the link budget model and accompanied throughput optimization problem, and results for an example problem.

### 8.4.1. Mathematical formulation

Before a mathematical formulation of the optimization problem can be made the mathematical formulation behind the link budget equations are to be established. The general model used for free space power transmission in wireless communication systems is the Friis transmission equation [206]:

$$P_R = P_{tx} G_{tx} G_R \left(\frac{\lambda}{4\pi}\right)^2 \left(\frac{1}{d}\right)^2 \quad [W] \tag{8.10}$$

where $P_R$ is the power received at the receiver in $[W]$, $P_{tx}$ the power transmitted by the transmitter in $[W]$, $G_{tx}$ and $G_R$ are the (unit less) gains of the transmit and receive antenna respectively, $\lambda$ is the wavelength of the signal in $[m]$ equal to $\lambda = c_0/f$ where $c_0$ is the speed of light in vacuum in $[m/s]$ and $f$ the frequency of the signal in $[Hz]$, and finally $d$ the distance in $[m]$ between the transmitter and receiver. The Friis equation is often expressed in decibels for convenience:

$$\begin{aligned} P_R &= P_{tx} + G_{tx} + G_{rx} + 20\log_{10}\left(\frac{\lambda}{4\pi}\right) + 20\log_{10}\left(\frac{1}{d}\right) \\ &= P_{tx} + G_{tx} + G_{rx} - 20\log_{10} d - 20\log_{10} f - 20\log_{10}\left(\frac{4\pi}{c_0}\right) \quad [dBW] \end{aligned} \tag{8.11}$$

with $P_R$ and $P_{tx}$ the received and transmitted power in $[dBm]$ respectively, $G_R$ and $G_{tx}$ the gains of the receive and transmit antenna in $[dBi]$ respectively, $f$ the frequency in $[Hz]$ and $d$ the distance in $[m]$.

The constant $-20\log_{10}\left(\frac{4\pi}{c_0}\right)$ in this equation is roughly equal to $-147.55\ dB$ allowing for a convenient representation of the received power is the summation of all the link parameters expressed in decibels.

The noise power, assuming no interferers, at the demodulator of the receiver is given by the following equation:

$$P_N = kT_{sys}B \quad [W] \tag{8.12}$$

or in decibel scale:

$$P_N = 10\log_{10} k + 10\log_{10} T_{sys} + 10\log_{10} B \quad [dBW] \tag{8.13}$$

where $k$ is the Boltzmann constant in $[JK^{-1}]$, $T_{sys}$ is the system noise temperature of the receiver in $[K]$, and $B$ the transmission bandwidth in $[Hz]$. Often a system level RF parameter that is used is the antenna gain-to-noise temperature $G/T = G_{rx}/T_{sys}$ in $dB/K$. This allows combining the receiver performance in one parameter when considering the received SNR:

$$SNR = \frac{P_R}{P_N} \quad [.] \tag{8.14}$$

which in decibel using eq. (8.11) and eq. (8.13), and combining the receiver parameters in antenna gain-to-noise temperature gives:

$$SNR = P_{tx} + G_{tx} - 20\log_{10} d - 20\log_{10} f + G/T - 10\log_{10} k - 10\log_{10} B - 147.55 \quad [dB]. \tag{8.15}$$

In eq. (8.15) the receiver antenna gain $G_{rx}$ and system noise temperature are $T_{sys}$ collected in the $G/T$ figure. A similar figure exists for the transmitter, the effective isotropic radiated power (EIRP) $EIRP = P_{tx}G_{tx}$. In eq. (8.15) these terms are not combined however because the gain of the antenna and transmit power are two interesting design variables that can be individually explored in a multi-objective optimization approach. On a satellite system level these two variables relate to different aspects, the antenna gain relates to antenna size, mass and (stowed) volume, while the transmit power (when combined with transmitter efficiency) relates to the power budget and generated heat. Therefore these variables are kept separate during the optimization.

The final step to make the bridge to the modulation and coding scheme and achievable data rates comes from the relation between SNR, bandwidth data rate, and the modulation and coding scheme specified symbol-energy-to-noise-density ratio:

$$SNR = \frac{E_s}{N_0}\frac{R_s}{B} \quad [.] \tag{8.16}$$

where $E_s/N_0$ is the symbol-energy-to-noise-density in $[dB]$ and $R_s$ the symbol rate in $[sym/s]$. For a given modulation and coding scheme symbol-energy-to-noise density is given specified in tables like those in the DVB-S2 standards [87], [88], [102]. The symbol rate and bandwidth are directly related by the roll-off factor $\alpha$ of the pulse-shaping filter that is used:

$$R_s = B/(1+\alpha) \quad [sym/s] \tag{8.17}$$

where when $\alpha = 1$ an ideal brick-wall filter is used resulting into a symbol rate equal to the bandwidth. Figure 8.4 shows an example of the effect of pulse shaping, also called Nyquist filtering, on a pulse amplitude modulated (PAM) optical signal. For an explanation on Nyquist filtering the reader is referred to the paper by Chi et. al. [207]

Finally, the symbol rate is related to the effective data-rate after encoding specified by the spectral efficiency $\eta$:

$$\eta = \frac{R_b}{R_s} \quad [bits/symbol]. \tag{8.18}$$

The spectral efficiency is given by the specification of the modulation and coding scheme (see [87], [88], [102]). For an uncoded transmission the spectral efficiency is equal to the modulation order of the modulation scheme (see chapter 3). When error correction is introduced the spectral efficiency reduces as some bits are used for the error correction coding.

Now given the roll-off factor, transmission bandwidth and required $E_s/N_0$ the required SNR for a given modulation and coding scheme can be calculated using eq. (8.16) and eq. (8.17). From the link

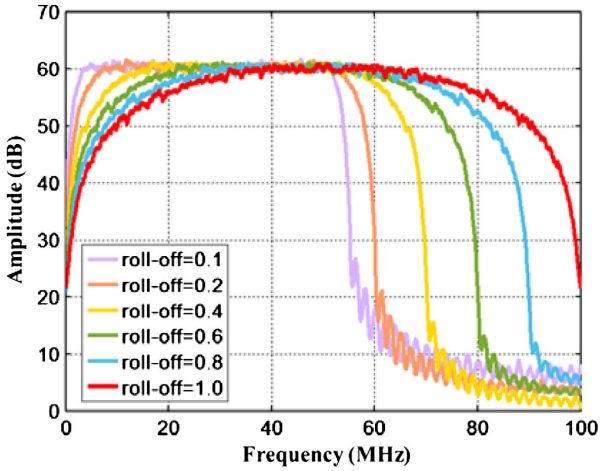


Figure 8.4: Spectral shape of an optical pulse amplitude modulated (PAM) signal after pulse shaping/Nyquist filtering with different roll-off factors to reduce signal bandwidth. From [207]

budget model follows the SNR during each of the selected contact opportunities. If the SNR is higher than the required SNR for the modulation and coding scheme, a link is achieved and the corresponding (useful) data rate can be calculated from the spectral efficiency using eq. (8.18). The throughput for a single pass can therefore be calculated as followed:

$$T_{hroughput} = \int_{t_b}^{t_e} R_b(t)\, dt \qquad [bits] \tag{8.19}$$

$$\text{where } R_b(t) = \begin{cases} R_s \cdot \eta & \text{if } SNR(t) \geq SNR_{req} \\ 0 & \text{otherwise} \end{cases} \qquad [bit/s] \tag{8.20}$$

where $t_b$ and $t_e$ are the beginning and end time-of-flight of the pass in $[s]$, $R_b(t)$ the bitrate during the pass per eq. (8.18), $SNR(t)$ the SNR in $[dB]$ during the pass and $SNR_{req}$ the required SNR for the modulation scheme and bit-rate that is used per eq. (8.16).

For the example optimization problem a second metric is used, the energy consumption of the transmitter. A simplified model is used that assumes the energy consumption is the product of the transmit power and transmit duration:

$$E_{nergy,\, simplified} = \int_{t_b}^{t_e} 10^{\frac{P_{tx}-30}{10}}\, dt \quad [J] \tag{8.21}$$

where $P_{tx}$ is the transmit power in $[dBm]$. This simplified model is later extended in the energy model of section 8.5 to include a modulation and technology depended model.

## 8.4.2. Throughput optimization problem

The textual formulation of the link budget optimization problem can now be described in a mathematical formulation using the above link budget equations. Two objectives can be identified from the textual formulation, maximize the throughput and minimize the energy consumption. The constraint of using only one inter-satellite link at a time remains. This optimization problem can be considered a multi-objective optimization problem.

The link budget optimization problem again considers picking a combination of contact opportunities, but this time also the transmit power $P_{tx}$ is included in the design vector (eq. (8.22)). The objective function is changed into two objective functions; one for the throughput (eq. (8.23)) and one for the total energy consumed during transmission (eq. (8.24)). The mathematical representation of this optimization problem is shown below:

**Design vector** $$\boldsymbol{x} = [x_1, x_2, \ldots, x_N, P_{tx}]^T \tag{8.22}$$

**Objective functions** $$f_{throughput} = \max_{\boldsymbol{x}} \sum_{i}^{N_{pass}} x_i \cdot \int_{t_{b,i}}^{t_{e,i}} R_{b,i}(t)\, dt \qquad [bits] \tag{8.23}$$

$$f_{energy} = \min_{\boldsymbol{x}} \sum_{i}^{N_{pass}} x_i \cdot \int_{t_{b,i}}^{t_{e,i}} 10^{\frac{P_{tx}-30}{10}}\, dt \qquad [J] \tag{8.24}$$

**Constraints**
$$t_{e,i} - t_{b,j} \geq 0 \qquad j > i \tag{8.25}$$

**Bounds**
$$x_i \in \{0, 1\} \qquad i \in \{1, ..., N\} \tag{8.26}$$
$$P_{tx} \in \mathbb{R} : P_{tx,min} \leq P_{tx} \leq P_{tx,max} \qquad [dBm] \tag{8.27}$$

**Equations**
$$SNR(t) = P_{tx} + G_{tx} - 20\log_{10} d(t) - 20\log_{10} f + G/T \tag{8.28}$$
$$- 10\log_{10} k - 10\log_{10} B - 147.55 \qquad [dB] \tag{8.29}$$
$$R_s = B/(1+\alpha) \qquad [syms/s] \tag{8.30}$$
$$R_{b,i}(t) = \begin{cases} R_s \cdot \eta & \text{if } SNR_i(t) \geq SNR_{req} \\ 0 & \text{otherwise} \end{cases} \qquad [bit/s] \tag{8.31}$$

The throughput objective function $f_{throughput}$ is defined as the sum of the throughput during the passes of the selected contact opportunities. The SNR requirement is deliberately not written as a constraint. If it were, then if at any moment during the pass the SNR drops below the required SNR then the whole solution is considered invalid. However, in practice packet drops during satellite downlinks are expected, especially at the beginning and end of a pass where the slant range is the highest. Specific transmission protocols and strategies (i.e. retransmissions or transmitting the least important information at the beginning or end of the pass) are used to deal with this issue. The second objective function $f_{energy}$ considers the total power consumption during the passes of the selected contact opportunities. The problem has now changed to a mixed variable multi-objective problem.

### 8.4.3. Example evaluation

An example optimization problem is run to test the link budget model. Table 8.1 shows the (constant) parameters that are used in this optimization. This example assumes that the targetted satellites are similar to those of the Telesat NGSO constellation, operating at an uplink frequency of 20.0 GHz, with a transmission bandwidth of 20.0 MHz, using a DVB-S2 8PSK with 8/9 FEC. The small satellite is assumed to have an antenna gain of 20 dBi and the receiving satellite system a antenna-gain-to-noise-temperature of 13.2 dBK. The same contact opportunities that were used in the contact optimization example of section 8.3 are used in this example.

Table 8.1: Parameters for the example link budget optimization

| | Symbol | Value(s) | Unit |
|---|---|---|---|
| *Spectral* | | | |
| Carrier frequency | $f_c$ | 20.0 | GHz |
| Bandwidth | $B$ | 20.0 | MHz |
| *Waveform* | | | |
| Modulation | | DVB-S2 8PSK-8/9 | |
| Roll-off factor | $\alpha$ | 0.35 | |
| Required symbol energy-to-noise ratio | $E_s/N_{0_{req}}$ | 10.69 | dB |
| Spectral efficiency | $\eta$ | 2.6460120 | bit/symbol |
| *Communication system* | | | |
| Transmit power (for all passes | $P_{tx,min}$ | 10 | dBm |
| | $P_{tx,max}$ | 40 | dBm |
| Antenna gain | $G_{tx}$ | 20 | dBi |
| *Receiving satellite system* | | | |
| Constellation | Example constellation | | |
| Antenna gain-to-temperature ratio | $G/T$ | 13.2 | dBK |

#### Convergence

The optimization problem is solved using the NSGA-II multi-objective genetic algorithm [208]. The settings of the algorithm and termination criteria were tuned in order for the algorithm to perform a good

exploration of the design space. fig. 8.5 shows an example between a not converged and converged Pareto-optimal set for this problem. The Pareto-optimal set is the set of solutions for which no better solution exists that is optimal (minimizes both objectives) [208]. In this example there would be no solutions achieving a lower energy usage for the same throughput than the ones in the Pareto-optimal set. When fully converged the Pareto-optimal set can show the Pareto-front. In this example, the Pareto-front is not know beforehand, and the optimization is used as a means for exploration of the design space, showing all optimal solutions and thereby the trade-off between throughput and energy usage.

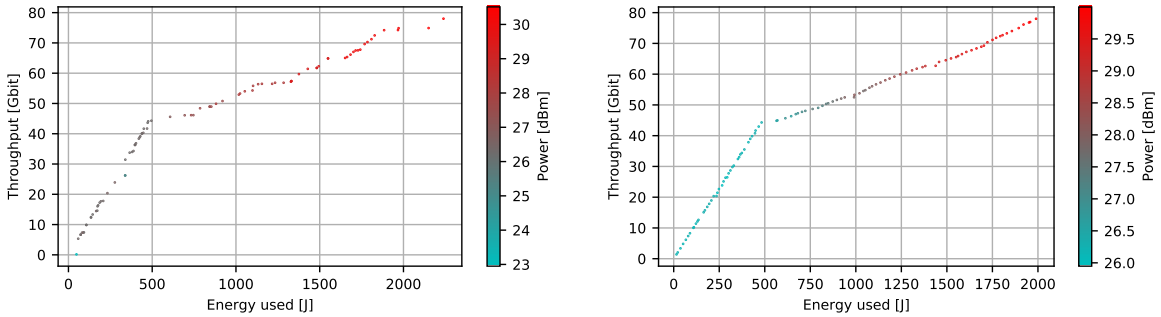


(a) Not converged

(b) Converged

Figure 8.5: Pareto fronts for the multi-objective link budget problem

In this example the Pareto front consists of two linear sets, one with a high slope up to a throughput of 45 Gbit, and one with a lower slope up to 78 Gbit. Each point in fig. 8.5 shows an optimal solution for the problem, i.e. the solution achieves the throughput for the least amount of energy. To highlight the design choices, the solutions are coloured by their power selection. Up to 45 Gbit throughput, a power level of 25.0 dBm is sufficient and the throughput can be increased by simply using more contact opportunities. After this point, the power needs to be increased to achieve sufficient SNR with the higher altitude satellites. From fig. 8.3a it can be seen that the passes with these higher altitude satellites are shorter of duration. Therefore there are diminishing returns, it requires more power to close the link with these satellites, but it does not result into a much longer contact time. This makes the slope of the set from 45 Gbit to 78 Gbit lower. Figure 8.5b is useful in design exploration as it can quickly answer the question of how much more throughput can be achieved when more energy is spend.

There are several ways to determine whether or not the results of the optimization are converged. Visually from the Pareto front in fig. 8.5a the two linear sets can already be identified but the result is visibly not converged yet. In fig. 8.5b the result is converged and two sharp lines are visible. Table 8.2 shows the algorithm settings and termination criteria that were used in this example. To obtain the better convergence, the number of off-springs per generation were increased to help exploring adjacent points on the Pareto front. In addition, the maximum evaluations and generations were increased to allow for more sampling of the design space.

Table 8.2: Algorithm settings for link budget optimization example

| | Not converged | Converged |
|---|---|---|
| *Algorithm settings* | | |
| Population size | 100 | 100 |
| Number of off-springs | 20 | 40 |
| *Termination criteria* | | |
| Objective function tolerance | 0.005 | 0.0005 |
| Maximum generations | 100 | 1000 |
| Maximum evaluations | 2000 | 10000 |

Alternatively, an indicator that may be used to evaluate the performance of the multi-objective optimization is the Hypervolume [209]. This performance indicator is useful in this case because it does not require prior knowledge of the optimum of the problem, i.e. does not require the Pareto front to be

know a-priori, and only requires a reference point. The Hypervolume calculates the area (two-objective functions) or volume (three or more objective functions) from a reference point $r$ to the Pareto front. The desire is to maximize the performance metric, showing how far the Pareto front has moved away from the reference point. In this optimization problem, the reference point can be chosen as $r = (0, \infty)$ corresponding to case where zero throughput is achieved but an infinite amount of energy is spend, an obviously bad solution. Since the expected the Pareto front for this problem follows; more energy consumed relates to more throughput, possibly with diminishing returns for the higher ranges and a minimum energy to be spent on the lower ranges, this is a good reference point to take.

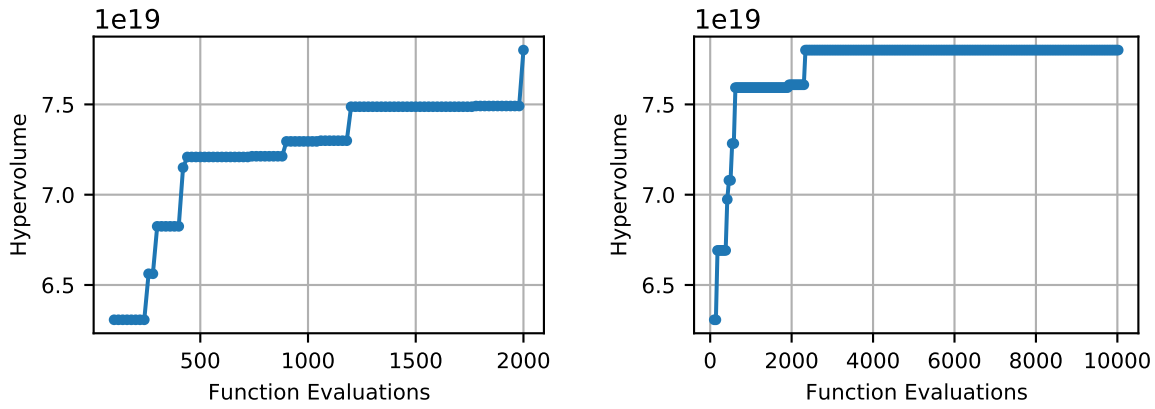


(a) Not converged case

(b) Converged case

Figure 8.6: Hypersurfaces as a performance indicator in the link budget optimization problem.

Figure 8.6 shows the sizes of the hypersurfaces for the not converged and converged cases. The absolute value of the hypersurface is proportional to the reference point taken here $r = (0, 1 \cdot 10^9)$. The strategy that is used to determine convergence is as follows: first the optimization is ran with some initial termination settings that does not terminate on the maximum generations or evaluations. Then the objective function tolerance is halved and number of off-springs are doubled until the hypervolume stops increasing after a double amount of evaluations. During this process, the Pareto front is observed for its convergence and, if needed, the reference point for the hyper surface is adjusted.

### Verification

After confirming convergence in the optimization, a closer look can be taken into the results of fig. 8.5b and verify the link budget model used. First, given the parameters in table 8.1 the maximum data rate that can be achieved is 39.2 Mbit/s. From section 8.3 the maximum contact time that could be achieved from the set of contact opportunities is 1990 seconds. Therefore the maximum throughput that can be achieved is 78.01 Gbit over these contact opportunities, which matches the performance of top right solution in fig. 8.5b.

The link budget equations can be verified by hand calculations. Taking the two maximum ranges from fig. 8.3a, 1100 km and 700 km, two link budgets can be calculated. This is done in table 8.3 showing that a transmit power of 26 dBm is sufficient for the lower altitude satellites, and 30 dBm is sufficient for the higher altitude satellites. These values correspond to the power at the transition point and maximum respectively in fig. 8.5b.

With these power levels the minimum energy consumption for the maximum throughput can be calculated as a final verification check. The maximum transmit power of 30 dBm corresponds to 1 W. With the maximum contact time of 1990 seconds, the simplified energy consumption model gives eq. (8.21) gives a energy consumption of 1990 J. This corresponds to what is found for the maximum throughput in fig. 8.5b.

This example assumes that it is possible to perfectly control the transmitting power to exactly what is necessary. In practice this might not be possible and fluctuations in the output power of the transmitter and pointing accuracy still require a margin to be taken on the link budget. In addition, since the power required for the lower altitude satellites and higher altitude satellites is more than 4 dB (more than twice the power) therefore it would make sense to select a transmit power for each pass individually.

Table 8.3: Hand calculated link budgets for the two altitudes 700 km and 1100 km

| | Symbol | 700 km | 1100 km | Unit |
|---|---|---|---|---|
| Carrier frequency | $f_c$ | 20.0 | 20.0 | GHz |
| Transmit power | $P_{tx}$ | 26.0 | 30.0 | dBm |
| Antenna gain | $G_{tx}$ | 20.0 | 20.0 | dBi |
| Isotopically radiated power (*) | $EIRP$ | 19.0 | 23.0 | dBWi |
| Range | $d$ | 700 | 1100 | km |
| Free space path loss (*) | $FSPL$ | 175.37 | 179.30 | dB |
| Received power (*) | $P_S$ | -159.37 | -156.93 | dBW |
| Bandwidth | $B$ | 20.0 | 20.0 | MHz |
| kB (*) | $kB$ | -155.59 | -155.59 | dBJHz/K |
| Antenna-gain-to-noise-temperature | $G/T$ | 13.2 | 13.2 | dBK |
| Received signal-to-noise-ratio (*) | $SNR$ | 9.42 | 9.49 | dB |
| Roll-off factor | $\alpha$ | 0.35 | 0.35 | |
| Symbol-energy-to-noise-ratio requirement | $E_b/N_{0_{req}}$ | 10.96 | 10.96 | dB |
| Required signal-to-noise-ratio (*) | $SNR_{req}$ | 9.39 | 9.39 | dB |
| Signal-to-noise-ratio margin (*) | | 0.03 | 0.11 | dB |

*Rows with a (*) are calculated from other rows. The other values are constants.*

This simplified example does however already show how optimization algorithms can aid in the system trade-offs for a satellite (data relay) communication system. For example it answers the question how much more throughput can be achieved for a (slightly) higher energy/power consumption. Several improvements for the model were mentioned in this section: making the transmit power specific for each pass, including an (technology and modulation dependent) transmitter efficiency in the energy consumption model and including a model for the antenna gain. The next section will make the first two of these improvements by extending the link budget model with different modulation schemes.

## 8.5. VCM and energy consumption models

This section will extend the link budget model of the previous section with a model in which different modulation schemes can be used. In addition, an energy model is formulated that includes the efficiency of the transmitter by considering the power amplifier technologies and the impact of the modulation scheme. As explained in chapter 3 variable coding and modulation (VCM) and adaptive coding and modulation (ACM) are methods to make more efficient use of the available spectrum and link margin to maximize the data rate through the channel. This work assumes only a single direction link (from the small satellite to the data-relay satellite), therefore only variable coding and modulation (VCM) is considered. In addition, because of the short duration contact opportunities it is assumed that changing the modulation and coding during a pass would not significantly increase the performance and does not justify the increase in complexity required. The VCM optimization implemented in this work can optimize the modulation and coding for each pass but does not change it during the pass.

The digital modulation protocols specified by Consultative Committee for Space Data Systems (CCSDS) and European Telecommunications Standards Institute (ETSI) (see chapter 3) implement different MODCODs to maximize spectral efficiency. Each MODCOD has a different required symbol-energy-to-noise ratio ($E_s/N_0$) and spectral efficiency ($\eta$). In general, a higher spectral efficiency requires a higher symbol-energy-to-noise ratio. Therefore more power is required for more throughput in the same bandwidth. However, an additional consideration needs to be made as the higher order MODCODs have waveforms with symbols having several power levels, i.e. two for 16-APSK or three for 32-APSK. The use of multiple power levels gives a non-constant amplitude waveform that requires the power amplifier in the transmitter to operate linearly and reduced power efficiency [116].

The following sub-sections will discuss the mathematical formulation of the VCM and energy consumption models and accompanied optimization problem, and results for an example problem.

### 8.5.1. Mathematical formulation

As explained in the introduction of this section, higher order modulation schemes require more power to achieve higher throughputs. However, as will be shown, the selected modulation scheme influences the maximum energy efficiency that can be achieved. The sub-section will first focus on this impact of the modulation scheme on the energy efficiency.

Modulation schemes such as 16-APSK are by definition non-constant envelope waveforms, as multiple amplitude levels are used to increase the number of symbols. However, constant envelope modulation schemes such as QPSK and 8-APSK will also turn out to be non-constant envelope as pulse-shaping (i.e. raised-cosine or root-raised cosine filter) is applied to limit the out-of-band emissions. A non-constant envelope waveform has variation in the signal peak power and its overall root mean square (RMS) power. This variation is described in the Peak to Average Power Ratio (PAPR). The power efficiency reduction of a linear power amplifier is reduced when amplifying a non-constant envelope modulated signal. The minimum theoretical impact on the power amplifier efficiency due to signal PAPR can be described as [116]:

$$\eta_{PA} = \eta_0 10^{-\left(\frac{PAPR}{20}\right)}, \tag{8.32}$$

with the PAPR expressed in dB and $\eta_0$ is a transistor technology-dependent term below 0.5. The actual energy efficiency of the power amplifier during the transmission however depends on the distribution of the envelope of the modulated signal over time and the power dissipation of the power amplifier across this distribution.

To capture this effect the modulation-available energy efficiency (MAEE) metric for modulations is introduced in [210] that relates: 1) the normalized signal envelope voltage probability density function (PDF), and 2) the power dissipation of a linear amplifier transistor. The MAEE metric can be used as an upper bound to the energy efficiency and can be made transistor technology dependent. The metric is compared in [211] with measured PA performance and is shown to provides a good upper bound to the efficiency.

The first step in the MAEE model is obtaining the (normalized) envelope voltage PDF $P_{Env}(u)$ which can be calculated for each modulation scheme using (double sided) distribution analysis. Figure 8.7 shows the complex samples and envelope voltage PDF for two modulation schemes in the DVB-S2 standard, 8-PSK and 32-APSK, using a root-raised-cosine (RRC) filter with a roll-off factor of $\alpha = 0.35$. Both waveforms spend a non-zero amount of time crossing between symbols, thereby making the envelope non-constant even for the 8-PSK scheme.

The transistors in the power amplifier dissipate power while transitioning between the off and on-states. The transistor power dissipation profile across the amplitude $A$ is more accurately described by the transistors load line. This dissipation can be determined by the transistor power dissipation profile [210][3]:

$$P_D(\gamma, a) = K_{PA}\left(\gamma(1-\gamma) - \frac{a^2}{2}\right) \quad [W]; 0 \leq a \leq 1-\gamma \tag{8.33}$$

with (normalized) bias point $\gamma = \frac{1}{2}\left(\frac{V_k}{V_s}\right)$. The proportional constant $K_{PA}$ is set by the specific load line and supply voltage, and cancels out in the MAEE calculation because both the dissipated power in eq. (8.33) and the RF output power of the amplifier $P_{tx}$ are proportional to this constant. The knee voltage to supply voltage ratio $V_k/V_s$ is a transistor technology dependent property and can be found in Table 1 of [210] for several transistor technologies. The power dissipation profile for a knee voltage ratio of $V_k/V_s = 0.12$ is shown in red in the distributions of fig. 8.7.

The expected value of the power dissipation is the integral across the product of the modulated signal envelope PDF and the power dissipation profile (after normalizing to $a_{max} = 1$):

$$E[P_D] = \int_0^1 P_{Env}(u) \cdot P_D(\gamma, u)\, du \quad [W]. \tag{8.34}$$

The MAEE metric is defined as the efficiency ratio:

$$\eta_{MAEE}(V_k, P_{Env}) = \frac{P_{Tx}}{P_{Tx} + E[P_D]} \quad [.] \tag{8.35}$$

[3]For a derivation of this equation see appendix A

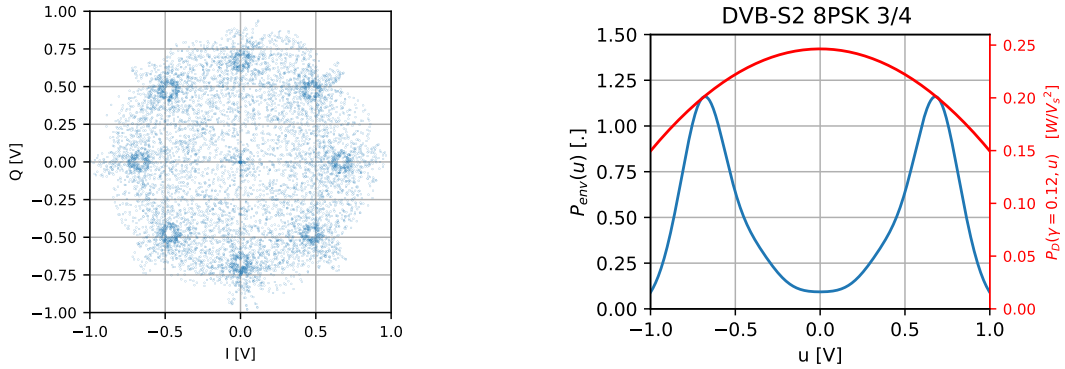


(a) 8-PSK

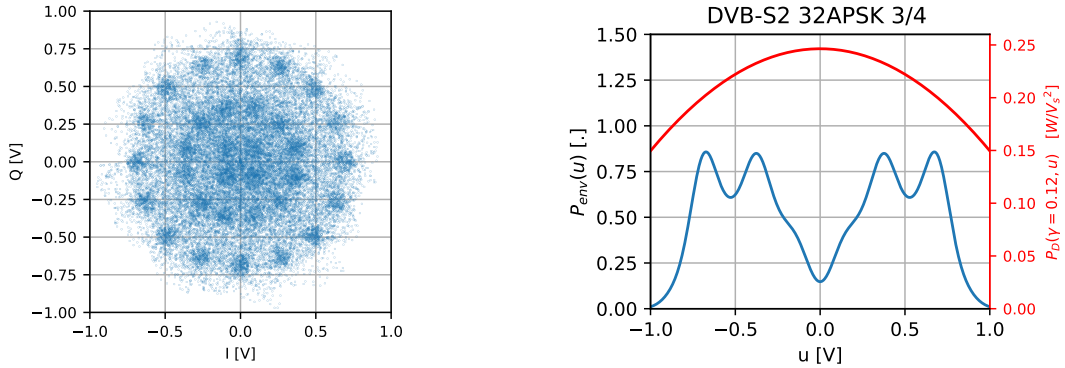


(b) 32-PSK

Figure 8.7: Complex samples (left) and voltage envelope pdf (right) of two RRC filtered waveforms in the DVB-S2 protocol

with $V_k$ the transistor technology dependent knee voltage ($V_k/V_s = 0.0$ in the theoretical case and $V_k/V_s = 0.12$ for a practical case, see [211] for values for different transistor technologies.) and $P_{tx}$ the output power of the PA in [W].

Figure 8.8 shows the MAEE metric values for the DVB-S2 modulations for four different knee-voltages; a theoretical case, a more practical case and typical values for Gallium Arsenide (GaAs) and Silicon (Si-CMOS) transistors. The MAEE power dissipation profile of eq. (8.33) assumes a class-A amplifier type dissipation, that has a theoretical maximum efficiency of 50% when amplifying an unmodulated wave with a zero knee-voltage. However, because of the non-constant envelope of the modulated signals even the quadrature phase-shift keying (QPSK) modulation does not reach this efficiency, only reaching a maximum of 38% efficiency. This efficiency reduces to below 20% when considering typical knee-voltage values of transistor technologies.

From fig. 8.8 it can be seen that, in general, an increase in spectral efficiency reduces the power efficiency. For the DVB-S2 modulations, this reduction is minimal (up to a few percent) as the radii of the symbols in the higher order schemes are optimized to compensate for this fact (see [102, p. 28-30]).

The MAEE metric is used to improve the energy consumption objective function of section 8.4 o allow for a more accurate trade-off between spectral efficiency and power efficiency. Rewriting eq. (8.35) into a form where the (direct current) power dissipation for a given output power and modulation can be found:

$$P_{DC} = P_{tx} + E\left[P_D\right] = P_{tx} \cdot \frac{1}{\eta_{MAEE}} \quad [W] \tag{8.36}$$

where $P_{DC}$ is the DC power dissipation of the PA in [W] and $P_{tx}$ the PA output power in [W] that is also used in eq. (8.16). For each modulation standard in the communication protocol the $\eta_{MAEE}$ is be calculated and used for a modulation dependent power energy model to be used in the multi-objective optimization.

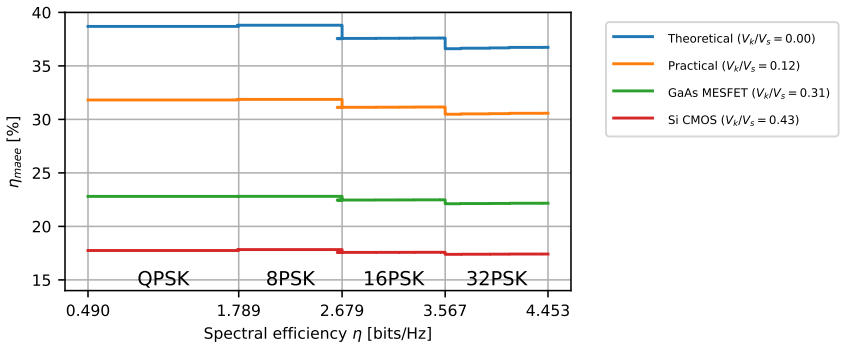


Figure 8.8: MAEE values against spectral efficiencies of the DVB-S2 modulation schemes for several knee voltages from [211]

The throughput metric is changed to include the (tabulated) spectral performance of the MODCODs in a standard, i.e. DVB-S2 or CSSDS. The MODCOD dependent throughput for a single pass can therefore be calculated as followed:

$$T_{hroughput} = \int_{t_b}^{t_e} R_b(t)\, dt \qquad [bits] \tag{8.37}$$

$$\text{where } R_b(t) = \begin{cases} R_s \cdot \eta(m) & \text{if } SNR(t) \geq SNR_{req}(m) \\ 0 & \text{otherwise} \end{cases} \qquad [bit/s] \tag{8.38}$$

The variable $m$ selects the MODCOD that is used, i.e. 0 to 27 for the MODCODs in the DVB-S2 standard. The MODCOD selection influences the spectral efficiency $\eta(m)$ and the required signal-to-noise ratio $SNR_{req}(m)$, both tabulated values in [87], [88], [102] for the DVB-S2 standard.

The energy model is changed to include a modulation and transistor technology dependent efficiency for the power amplifier in the transmitter using the MAEE model. These efficiency values are calculated beforehand (see `hermes-optimization.dvbs2_analysis.ipynb`). The new energy consumption per pass with the MAEE efficiency depending on the MODCOD is calculated as followed:

$$E_{nergy} = \int_{t_b}^{t_e} (R_b(t) > 0) \cdot \frac{10^{\frac{P_{tx}-30}{10}}}{\eta_{MAEE}(m)}\, dt \quad [J] \tag{8.39}$$

The MAEE efficiency is selected by the MODCOD variable $\eta_{MAEE}(m)$. The inclusion of the $R_b(t) > 0$ statement makes sure energy is only consumed when the link margin is positive. This allows solutions in which only part of the pass is used for transmission. This also assumes that the transmission starts and stops can be perfectly timed.

## 8.5.2. VCM optimization problem

The link budget problem of section 8.4 is now extended to include different selectable modulation and coding schemes for each of the passes. There are multiple ways to include a modulation and coding scheme selection into the optimization. The MODCOD per pass can be directly included into the design vector, while the transmit power is derived for a positive margin. This however results into a slow-converging optimization problem for the maximum throughput solution. As there is a $(1/N_{MODCOD})^{N_{passes}}$ probability (assuming only random sampling) for choosing the optimum design vector, having the highest MODCOD for each pass. Alternatively, a transmit power per pass can be included in the design vector, while choosing the maximum MODCOD for the resulting margin. This has the advantage that initially too-high transmit powers can be selected, thereby using the highest MODCODs and finding the highest throughput option quickly. Then following generations can converge to a lower energy solution by reducing the power setting each generation.

The new design vector therefore contains a power selection for each pass ($P_{tx,i}$ in eq. (8.40)). The design-vector keeps a variable for each pass to be use for a faster convergence for selecting which contact opportunity to use. The MODCOD is derived based on the highest MODCOD that results in

the lowest signal-to-noise ratio margin (eq. (8.47)). There is no additional margin taken on the link. The energy objective function (eq. (8.42)) is changed to include the modulation and coding dependent MAEE efficiency. And similarly, the spectral efficiency is made dependent on the selected modulation and coding (eq. (8.48)).
The new optimization problem and equations are shown below:

**Design vector**
$$\boldsymbol{x} = [x_1, x_2, ..., x_N, P_{tx,1}, P_{tx,2}, ..., P_{tx,N}]^T \tag{8.40}$$

**Objective functions**
$$f_{throughput} = \max_{\boldsymbol{x}} \sum_{i}^{N_{pass}} x_i \cdot \int_{t_{b,i}}^{t_{e,i}} R_{b,i}(t)\, dt \tag{8.41}$$

$$f_{energy} = \min_{\boldsymbol{x}} \sum_{i}^{N_{pass}} x_i \cdot \int_{t_{b,i}}^{t_{e,i}} (R_{b,i}(t) > 0) \cdot \frac{10^{\frac{P_{tx,i}-30}{10}}}{\eta_{MAEE}(m_i)}\, dt \tag{8.42}$$

**Constraints**
$$t_{e,i} - t_{b,j} \geq 0 \qquad j > i \tag{8.43}$$

**Bounds**
$$x_i \in \{0, 1\} \qquad i \in \{1, ..., N\} \tag{8.44}$$
$$P_{tx,i} \in \mathbb{R} : P_{tx,min} \leq P_{tx} \leq P_{tx,max} \qquad [dBm] \tag{8.45}$$

**Equations**
$$SNR(t) = P_{tx} + G_{tx} - 20\log_{10} d(t) - 20\log_{10} f + G/T - 10\log_{10} k - 10\log_{10} B - 147.55 \qquad [dB] \tag{8.46}$$
$$m_i = \text{highest MODCOD within } SNR_i(t)$$
$$R_s = B/(1+\alpha) \qquad [syms/s] \tag{8.47}$$
$$R_{b,i}(t) = \begin{cases} R_s \cdot \eta(m_i) & \text{if } SNR_i(t) \geq SNR_{req}(m_i) \\ 0 & \text{otherwise} \end{cases} \qquad [bit/s] \tag{8.48}$$

### 8.5.3. Example evaluation

An example optimization problem is run to test the VCM and energy model. Table 8.4 shows the (constant) parameters that are used in this optimization. For this example, the DVB-S2 MODCODs are used with a constant bandwidth of 20.0 MHz and roll-off factor of 0.35. The same contact opportunities that were used in the contact optimization example of section 8.3 are used in this example. To limit the design space, a minimum throughput of 50 Gbit is required as a design constraint.

Table 8.4: Parameters for the example VCM optimization

| | Symbol | Value(s) | Unit |
|---|---|---|---|
| *Spectral* | | | |
| Carrier frequency | $f_c$ | 20.0 | GHz |
| Bandwidth | $B$ | 20.0 | MHz |
| *Waveform* | | | |
| VCM protocol | | DVB-S2 | (see [87], [88], [102]) |
| Roll-off factor | $\alpha$ | 0.35 | |
| *Communication system* | | | |
| PA knee-voltage ratio | $V_k/V_s$ | 0.12 | |
| Transmit power (per pass) | $P_{tx,min}$ | 10 | dBm |
| | $P_{tx,max}$ | 60 | dBm |
| Antenna gain | $G_{tx}$ | 20 | dBi |
| *Receiving satellite system* | | | |
| Constellation | Example constellation | | |
| Antenna gain-to-temperature ratio | $G/T$ | 13.2 | dBK |
| *QoS requirements* | | | |
| Minimum throughput | | 50 | Gbit |

**Results**

Figure 8.9 shows the Pareto-set of optimal solutions for the VCM optimization problem using the NSGA-II algorithm. The throughput and energy are now dependent on two variables; pass selection and power selection per pass. Therefore the problem is no longer linear as was seen in fig. 8.5b. Instead now the converged Pareto-front of optimal solutions shows a gradual curve.

Comparing with the previous results in fig. 8.5b the higher spectral efficiency of the higher order modulation and coding schemes allow for an increase in throughput, now up to 131 Gbit over all the contact opportunities. At the previous maximum throughput of 72 Gbit, the energy consumption is increased by three times from 2 kJ to 6 kJ. This increase corresponds to an decrease by the MAEE efficiency 30% in fig. 8.8.

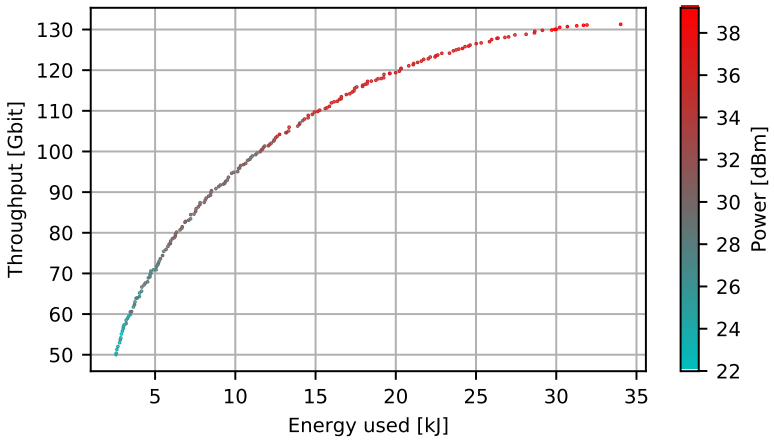


Figure 8.9: Pareto-set of optimal solutions for the example multi-objective VCM problem

## 8.6. Bandwidth model

In this section, the optimization framework is extended with a model for the transmission bandwidth. Section 8.4 showed that the symbol rate is related to the transmission bandwidth of the link by the roll-off factor. A higher transmission bandwidth would therefore directly result into a higher throughput. As shown in chapter 4, the NGSO constellations provide user uplink bandwidths up to 500 MHz. The state-of-the art Dove satellites are capable of transmitting at bandwidths up to 300 MHz using aggregation [2] of up to three sub-carriers with 100 MHz baseband-bandwidth.

Several considerations come into play when considering high bandwidth carrier-aggregated links, such as reduced sub-channel bandwidth and reduced energy efficiency. The following sub-sections will discuss the mathematical formulation of the bandwidth model and accompanied bandwidth optimization problem and results for an example problem.

### 8.6.1. Mathematical formulation

The use of carrier-aggregation is required to keep the baseband bandwidth and baseband processing manageable while still fully utilizing wide transmission bandwidths. Higher baseband bandwidths requires a higher processing speed (clock speed) of the baseband processor. The state-of-the-art Dove and Corvus satellites have modulators capable of reaching base-band bandwidths of around 96 MHz [2] [1]. The Dove satellite is capable of aggregating three sub-carriers for each polarization in 300 MHz. These state-of-the-art performance figures are used to formulate the bandwidth/carrier-aggregation model for the optimization framework.

In the bandwidth model it is assumed that for bandwidths lower than 100 MHz there are no sub-carriers and the spectrum is fully utilized by the modulator, resulting in a symbol rate of $R_s = 100MHz/(1+\alpha)$ as per eq. (8.17). Two higher bandwidths are assumed, 200 MHz and 300 MHz, to stay within the lowest maximum uplink bandwidth of the NGSO constellations of chapter 4. For 200 MHz and 300 MHz, the number of sub-carriers are two and three respectively. Figure 8.10 shows how the spectra at these bandwidths might look like. As shown by the Dove and Corvus satellites, the effective sub-channel bandwidth is slightly less than the overall bandwidth divided by the number sub-carriers (i.e.

96 MHz instead of 100 MHz). This is likely to avoid symbol interference between the channels as the pulse shape filtering does not provide a perfect brick wall filtering for each of the channels. Therefore, additional bandwidth spacing in between the channels is required. This is illustrated in fig. 8.10, here the individual channels have a roll-off factor of $\alpha = 0.35$ and symbol rates of $R_s = 96MHz/(1 + 0.35)$. The overall data rate is therefore reduced by a factor of $(N_{carrier} \cdot B_{channel})/B$:

$$\begin{aligned} R_b &= \frac{N_{carrier} \cdot B_{channel}}{B} \cdot \eta \cdot \frac{B}{1+\alpha} \\ &= \eta \cdot \frac{N_{carrier} \cdot B_{channel}}{1+\alpha} \quad [bit/s]. \end{aligned} \tag{8.49}$$

where $N_{carrier}$ is the number of carriers, $B_{channel}$ is the channel bandwidth for each sub-carrier in Hz, $\eta$ the spectral efficiency of the modulation scheme used in the channel in bits/Hz, and $\alpha$ the roll-off factor. For this optimization, the multi-carrier situation assumes a channel bandwidth equal to that of the

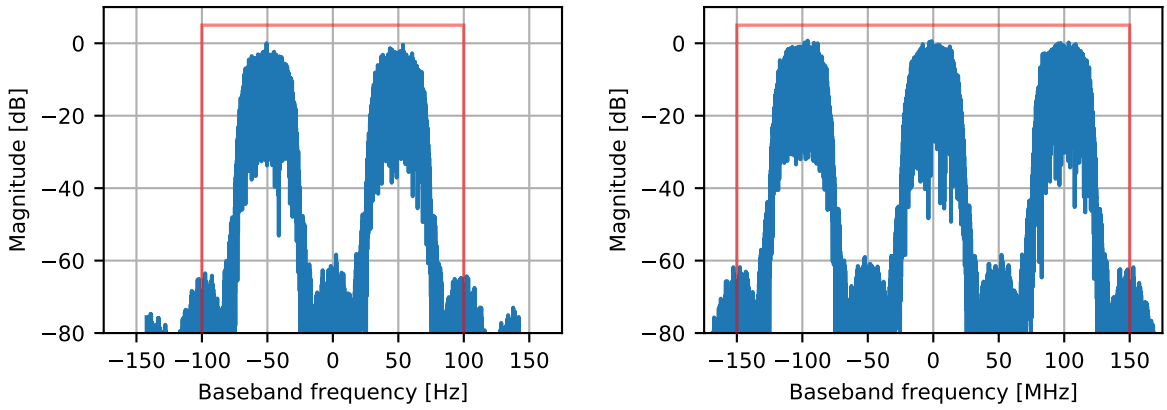


(a) Spectrum of two sub-carriers in a 200 MHz bandwidth

(b) Spectrum of three sub-carriers in a 300 MHz bandwidth

Figure 8.10: In carrier aggregation, multiple sub-carriers are used with different modulation streams to fill a wider bandwidth.

state-of-the-art $B_{channel} = 96\ MHz$, with a fixed roll-off factor of $\alpha = 0.35$, using the same modulation and coding. For 200 MHz there are two sub-carriers, at $f_c$ - 50 MHz and $f_c$ + 50 MHz, and for 300 MHz there are three sub-carriers at $f_c$ - 100 MHz, $f_c$ and $f_c$ + 100 MHz, as shown in fig. 8.10, where $f_c$ is the carrier frequency of the RF signal.

In addition to a reduction in channel bandwidth, a multi-carrier situation also reduces the energy efficiency of the waveform. As can be seen in fig. 8.11a, the voltage envelope PDF of a three sub-carrier 32-APSK signal has a higher distribution closer to $u = 0$ where the dissipation of the transistor (red line) is the highest.

This negatively impacts the efficiency following from the MAEE definition in [210]. Figure 8.11b shows the reduction in efficiency for the modulation schemes in the DVB-S2 standard when using two carriers in 200 MHz or three carriers in 300 MHz.

For the bandwidth, the model number of carriers is assumed to be one below 100 MHz, two for 200 MHz and three for 300 MHz. The resulting symbol rate calculation is as follows:

$$N_{carrier} = \begin{cases} 1 & \text{if } B \leq 100\ MHz \\ 2 & \text{if } 100\ MHz \leq B \leq 200\ MHz \\ 3 & \text{if } 200\ MHz \leq B \leq 300\ MHz \end{cases} \quad [.] \tag{8.50}$$

$$R_s = \begin{cases} B/(1+\alpha) & \text{if } N_{carrier} = 1 \\ (N_{carrier} \cdot B_{channel})/(1+\alpha) & \text{if } N_{carrier} = 2,3 \end{cases} \quad [syms/s] \tag{8.51}$$

The channel bandwidth $B_{channel}$ in-case of carrier-aggregation is assumed to be equal to that of the current state-of-the-art at 96 MHz.

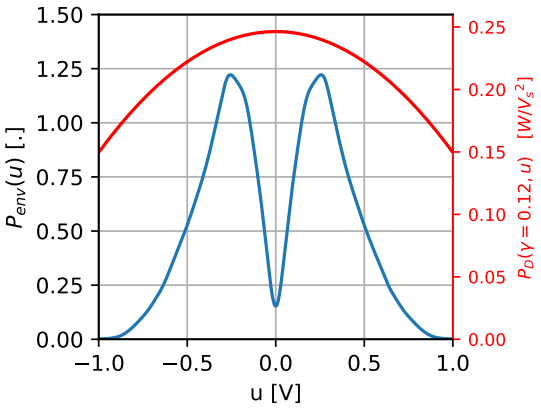


(a) Voltage envelope pdf of three sub-carrier 32-APSK signal in 300 MHz bandwidth

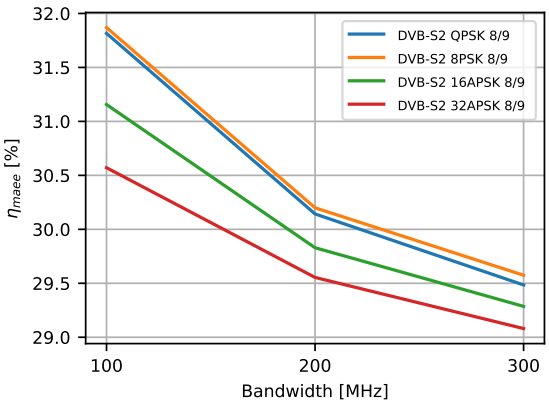


(b) The energy efficiency of high bandwidth waveforms decreases with addition sub-carriers.

Figure 8.11: A multi-carrier modulation, i.e. two sub-carriers for 200 MHz and three for 300 MHz, negatively impacts the efficiency of the power amplifier.

## 8.6.2. Bandwidth optimization problem

The VCM optimization problem of section 8.5 is now extended to include a selectable bandwidth to be used for all passes. The new design vector now contains a bandwidth selection $B$ (eq. (8.52)) that is selected from a list of bandwidths (eq. (8.58)). The bitrate for each pass is made dependent on the number of carriers in the bandwidth and the maximum channel bandwidth $B_{channel}$ (eq. (8.62)). The energy objective function also includes the MAEE efficiencies for each modulation scheme and number of carriers (eq. (8.54)). The new design problem and equations are shown below:

**Design vector**
$$\boldsymbol{x} = [x_1, x_2, ..., x_N, P_{tx,1}, P_{tx,2}, ..., P_{tx,N}, B]^T \tag{8.52}$$

**Objective functions**
$$f_{throughput} = \max_{\boldsymbol{x}} \sum_i^N x_i \cdot \int_{t_{b,i}}^{t_{e,i}} R_{b,i}(t)\, dt \tag{8.53}$$

$$f_{energy} = \min_{\boldsymbol{x}} \sum_i^N x_i \cdot \int_{t_{b,i}}^{t_{e,i}} (R_{b,i}(t) > 0) \cdot \frac{10^{\frac{P_{tx,i}-30}{10}}}{\eta_{MAEE}(m_i, B)}\, dt \tag{8.54}$$

**Constraints**
$$t_{e,i} - t_{b,j} \geq 0 \qquad j > i \tag{8.55}$$

**Bounds**
$$x_i \in \{0, 1\} \qquad i \in \{1, ..., N\} \tag{8.56}$$
$$P_{tx,i} \in \mathbb{R} : P_{tx,min} \leq P_{tx} \leq P_{tx,max} \qquad [dBm] \tag{8.57}$$
$$B \in \{B_1, B_2, ...\} \qquad [Hz] \tag{8.58}$$

**Equations**
$$SNR(t) = P_{tx} + G_{tx} - 20\log_{10} d(t) - 20\log_{10} f + G/T - 10\log_{10} k - 10\log_{10} B - 147.55 \qquad [dB] \tag{8.59}$$
$$m_i = \text{maximum MODCOD within } SNR_i(t) \tag{8.60}$$
$$N_{carrier} = \begin{cases} 1 & \text{if } B \leq 100\ MHz \\ 2 & \text{if } 100\ MHz \leq B \leq 200\ MHz \\ 3 & \text{if } 200\ MHz \leq B \leq 300\ MHz \end{cases} \tag{8.61}$$
$$R_s = \begin{cases} B/(1+\alpha) & \text{if } N_{carrier} = 1 \\ (N_{carrier} \cdot B_{channel})/(1+\alpha) & \text{if } N_{carrier} = 2, 3 \end{cases} \qquad [syms/s] \tag{8.62}$$
$$R_{b,i}(t) = \begin{cases} R_s \cdot \eta(m_i) & \text{if } SNR_i(t) \geq SNR_{req}(m_i) + 3 \\ 0 & \text{otherwise} \end{cases} \qquad [bit/s] \tag{8.63}$$

## 8.6.3. Example evaluation

An example optimization problem is run to test the addition of the bandwidth variable to the optimization problem. Table 8.5 shows the (constant) parameters that are used in this optimization. The

bandwidth can be set from 100 kHz to 300 MHz, with a maximum channel bandwidth of 96 MHz in case of the 200 MHz and 300 MHz with sub-carriers.

Table 8.5: Parameters for the example bandwidth optimization problem

| | Symbol | Value(s) | Unit |
|---|---|---|---|
| *Spectral* | | | |
| Carrier frequency | $f_c$ | 20.0 | GHz |
| Bandwidth settings | $B$ | [0.1, 0.5, 1, 5, 10, 50, 100, 200, 300] | MHz |
| *Waveform* | | | |
| VCM protocol | | DVB-S2 | (see [87], [88], [102]) |
| Roll-off factor | $\alpha$ | 0.35 | |
| *Communication system* | | | |
| PA knee-voltage ratio | $V_k/V_s$ | 0.12 | |
| Transmit power (per pass) | $P_{tx,min}$ | 10 | dBm |
| | $P_{tx,max}$ | 43 | dBm |
| Antenna gain | $G_{tx}$ | 20 | dBi |
| Maximum channel bandwidth | $B_{channel}$ | 96 | MHz |
| *Receiving satellite system* | | | |
| Constellation | Example constellation | | |
| Antenna gain-to-temperature ratio | $G/T$ | 13.2 | dBK |

## Results

Figure 8.12 shows the Pareto-set of optimal solutions for the bandwidth optimization problem. The increase in maximum bandwidth now allows up to 1200 Gbit (or 150 GByte) to be transferred during the 20 contact opportunities with the example constellation. Achieving such high rates comes at cost of increased energy consumption. The bandwidth increase reduces the SNR and therefore require a higher transmission power, but also the reduced efficiency of the multi-carrier modulation increases the overall power consumption.

The used energy of the solutions at the lower end of the Pareto-front is reduces in comparison to the previous result in section 8.5. The previous best of 131 Gbit at 35 kJ is now obtained for less than 5 kJ. In this optimization the lower throughputs are achieved by using only a few passes, with the highest bandwidth/symbol-rate and using the transmit power/MODCOD to fine tune the energy consumption.

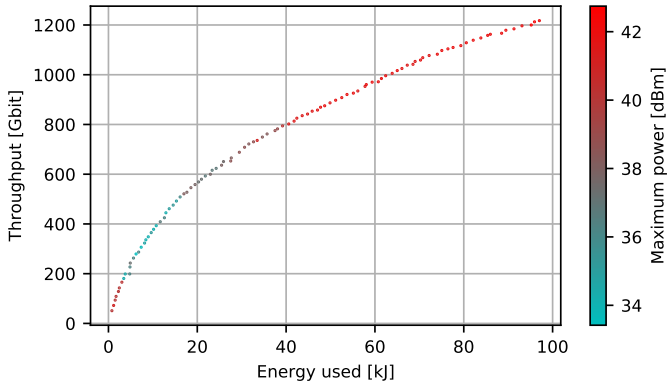


Figure 8.12: Pareto optimal set of solutions for the bandwidth optimization problem

In its current form, the bandwidth model strongly favours the maximum bandwidth settings, with the only negative feedback coming from a slight decrease in power efficiency for carrier aggregated operation. When the throughput is to be maximized, it is more effective to increase the bandwidth than to increase the signal-to-noise ratio and use a higher order modulation scheme. This relation is

captured in the Shannon-Hartley theorem [27][p. 19]:

$$C = B \log_2 \left(1 + \frac{S}{N}\right) \tag{8.64}$$

where $C$ is maximum theoretical upper bound for the channel capacity in bits per second, $B$ the bandwidth in hertz, and $S/N$ the linear signal-to-noise ratio. From eq. (8.64) it can be seen that the channel capacity linearly increases with the bandwidth. While the signal-to-noise ratio has a logarithmic relation with the channel capacity. In section 8.9.1 the energy model is refined by relating higher bitrate with a higher modulator power consumption further increasing the feedback to minimize bandwidth in the optimization.

## 8.7. Visibility and pointing model

The next parameter that is added to the optimization framework is the antenna gain, $G_{tx}$ in eq. (8.15). Apart from influencing the link budget, the antenna gain also influences the field-of-view of the small satellite. As shown in fig. 8.13 an antenna with a large gain (red, $\approx 15\ dBi$) will have a small field-of-view of $\approx \pm 20°$, and therefore might not see all passes. Whereas an antenna with a small gain (green, $\approx 7.5\ dBi$) will have a larger field-of-view of $\approx \pm 45°$ and can see most of the passes, however now a higher transmitter power is required to close the link budget.

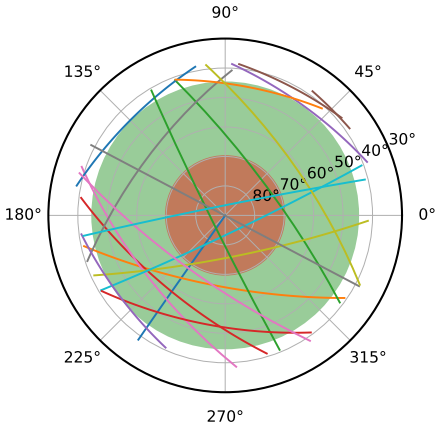


Figure 8.13: A limited field-of-view for two antennas (red, $\approx 15\ dBi$) and (green, $\approx 7\ dBi$) reduces the amount of passes that can be observed without antenna/body-pointing.

The visibility model captures this trade-off between antenna gain and visibility, and adds the antenna gain as a design variable in the optimization. The pointing model adds to the visibility model by considering how far the antenna needs to be steered in order to be able to observer the selected contact opportunities. A higher gain antenna with a narrower beam-width needs to be pointed towards the data-relay satellite. This pointing comes at a cost by either using an antenna steering mechanism as discussed in section 3.2.3, or by body-pointing satellite. In the latter case this reduces the time for which the satellite can point its payload to the required target and therefore possibly reducing mission return. In this work no particular pointing/steering techniques are considered, instead a pointing penalty is introduced as a third design objective that captures the need for antenna pointing to obtain the solution with the selected antenna. The following sub-sections will discuss the mathematical formulation of the visibility and pointing models, accompanied optimization problem and results for an example problem.

### 8.7.1. Mathematical formulation

For directive antennas a the half-power beam-width may be used to determine the field-of-view. The half-power beamwidth is the angle between the half-power points where the power of the antenna pattern is half (-3 dB) that of the maximum power of the front-lobe as illustrated in fig. 8.14a. Outside the half-power beamwidth the gain of the antenna reduces significantly.

The relation between the maximum gain of the antenna $G_{tx}$ and the half-power beamwidth depends on the particular type and design of the antenna. However, several approximate relationships exist

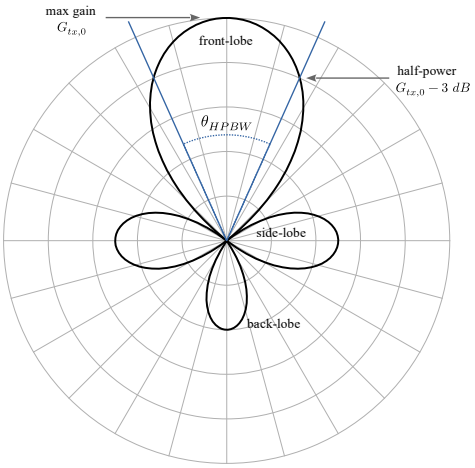


(a) Example of the antenna gain pattern of a directive antenna in the elevation plane.

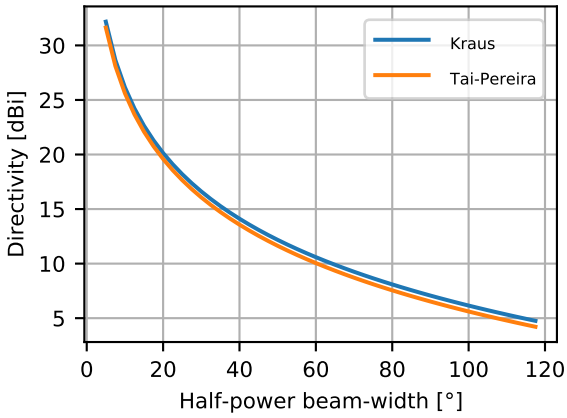


(b) Approximations for the relation ship between antenna-gain and half-power beamwidth

Figure 8.14: For directive antennas the maximum antenna gain is related to the half-power beamwidth.

for directive antennas such as the Kraus formula [212, p. 25] or the formula by Tai-Pereira [213]. Figure 8.14b shows these two approximations. According to Balanis, the Kraus formula leads to a smaller error for a half-power beamwidth greater than 39.77° [189, p. 49] for symmetrically rotational directive antennas having $\cos^n \theta$ patterns. In this work the Kraus formula is uses as wider beam-widths are needed to capture low elevation passes, i.e. as in fig. 8.13. The directivity and beam-width relation by Kraus' formula is given by [212, p. 25]:

$$D_{0,dB} = 10 \log_{10} \left( \frac{4\pi}{\theta_1 \theta_2} \right) \quad [dB] \tag{8.65}$$

where $D_0$ is the directivity, and $\theta_1$ and $\theta_2$ in $[rad]$, the half-power beam-widths in two orthogonal planes (i.e. elevation and azimuth). For the rotationally symmetric antenna patterns that are assumed in this work these half-power beamwidths are equal, $\theta_1 = \theta_2$. The antenna directivity and antenna gain is related by the antenna efficiency $e$ by $G(\theta, \phi) = e \cdot D(\theta, \phi)$ [189, p. 77]. In this work ideal lossless antennas are assumed and therefore $G_{tx} = D_0$.

For a given bore-sight antenna gain, the half-power beamwidth can be estimated by the inverse of the Krauss formula of eq. (8.65), assuming the antenna is rotationally symmetric:

$$\theta_{HPBW} = \sqrt{\frac{4\pi}{10^{G_{tx,0}/10}}} \quad [rad] \tag{8.66}$$

where $G_{tx,0}$ is the antenna bore-sight gain in [dB]. In this work it is assumed that the antenna gain is equal to the boresight gain inside the half-power beamwidth and zero outside the half-power beamwidth:

$$G_{tx}(\theta) = \begin{cases} G_{tx,0} & \text{if } \theta \leq \theta_{HPBW}/2 \\ 0 & \text{otherwise} \end{cases} \quad [dBi]. \tag{8.67}$$

In reality the gain will reduce gradually when moving away from the bore-sight direction towards the half-power beamwidth in a $\cos^n(\theta)$ relation. However, since a 3 dB (half-power) margin is taken in the link budget the link would still close at the half-power points making this a reasonable assumption for the antenna gain pattern.

The antenna must be pointed towards the data-relay satellite if the pass of a contact opportunity lies outside the half-power beam-width. An antenna with a higher gain has a lower half-power beamwidth and therefore needs to be pointed across a greater angle for a longer duration. The time spent pointing therefore depends on the half-power beamwidth as followed:

$$P_{ointing} = \int_{t_b}^{t_e} (\theta(t) - \theta_{HPBW}/2 > 0)\ dt \quad [s] \tag{8.68}$$

where $t_b$ and $t_e$ are the beginning and end time-of-flight in [s] of the pass and $\theta(t)$ the elevation angle to the date-relay satellite in [deg] as function of the time-of-flight.

## 8.7.2. Antenna gain optimization problem

The link budget optimization problem of section 8.4 is now extended to include the antenna gain as a variable in the design vector (eq. (8.69)) taking real values between a minimum and maximum value eq. (8.78). The antenna gain is assumed to be zero outside of the half-power beam-width (eq. (8.80)). A 3 dB margin is taken to account for the antenna gain reducing for elevation angles towards half-power beamwidth (eq. (8.85)).

For the pointing penalty, a third optimization objective is added (eq. (8.72)) that integrates the total time spend pointing the antenna in order to observe the passes of the selected contact opportunities. Two constraints are added (eq. (8.74) and eq. (8.75)) to limit the elevation and azimuth rates of the pointing, i.e. to the maximum pointing rate of the attitude control system. It is assumed that the pointing accuracy is not limiting and is accounted for in the 3 dB margin. The new design problem and equations are shown below:

**Design vector**

$$\boldsymbol{x} = [x_1, x_2, ..., x_N, P_{tx,1}, P_{tx,2}, ..., P_{tx,N}, B, G_{T,0}]^T \tag{8.69}$$

**Objective functions**

$$f_{throughput} = \max_{\boldsymbol{x}} \quad \sum_i^N x_i \cdot \int_{t_{b,i}}^{t_{e,i}} R_{b,i}(t)\, dt \qquad [bits] \tag{8.70}$$

$$f_{energy} = \min_{\boldsymbol{x}} \quad \sum_i^N x_i \cdot \int_{t_{b,i}}^{t_{e,i}} (R_{b,i}(t) > 0) \cdot \frac{10^{\frac{P_{tx,i}-30}{10}}}{\eta_{MAEE}(m_i, B)}\, dt \qquad [J] \tag{8.71}$$

$$f_{pointing} = \min_{\boldsymbol{x}} \quad \sum_i^N x_i \cdot \int_{t_{b,i}}^{t_{e,i}} (\theta_i(t) - \theta_{HPBW}/2 > 0)\, dt \qquad [s] \tag{8.72}$$

**Constraints**

$$t_{e,i} - t_{b,j} \geq 0 \qquad j > i \tag{8.73}$$

$$\dot{\theta}(t) \leq \dot{\theta}_{max} \tag{8.74}$$

$$\dot{\phi}(t) \leq \dot{\phi}_{max} \tag{8.75}$$

**Bounds**

$$x_i \in \{0, 1\} \qquad i \in \{1, ..., N\} \tag{8.76}$$

$$P_{tx} \in \mathbb{R} : P_{tx,min} \leq P_{tx} \leq P_{tx,max} \qquad [dBm] \tag{8.77}$$

$$G_{tx,0} \in \mathbb{R} : G_{tx,min} \leq G_{tx,0} \leq G_{tx,max} \qquad [dBi] \tag{8.78}$$

**Equations**

$$\theta_{HPBW} = \sqrt{\frac{4\pi}{10^{G_{tx,0}/10}}} \qquad [rad] \tag{8.79}$$

$$G_{tx}(\theta) = \begin{cases} G_{tx,0} & \text{if } \theta \leq \theta_{HPBW}/2 \\ 0 & \text{otherwise} \end{cases} \qquad [dBi] \tag{8.80}$$

$$SNR(t) = P_{tx} + G_{tx} - 20\log_{10} d(t) - 20\log_{10} f + G/T - 10\log_{10} k - 10\log_{10} B - 147.55 \qquad [dB] \tag{8.81}$$

$$m_i = \text{maximum MODCOD within } SNR_i(t) \tag{8.82}$$

$$N_{carrier} = \begin{cases} 1 & \text{if } B \leq 100\ MHz \\ 2 & \text{if } 100\ MHz \leq B \leq 200\ MHz \\ 3 & \text{if } 200\ MHz \leq B \leq 300\ MHz \end{cases} \tag{8.83}$$

$$R_s = \begin{cases} B/(1+\alpha) & \text{if } N_{carrier} = 1 \\ (N_{carrier} B_{channel})/(1+\alpha) & \text{if } N_{carrier} = 2, 3 \end{cases} \qquad [syms/s] \tag{8.84}$$

$$R_{b,i}(t) = \begin{cases} R_s \cdot \eta(m_i, B) & \text{if } SNR_i(t) \geq SNR_{req}(m_i) + 3 \\ 0 & \text{otherwise} \end{cases} \qquad [bit/s] \tag{8.85}$$

## 8.7.3. Example evaluation

The antenna optimization problem is ran with the parameters shown in table 8.6. The bore-sight antenna gain can take values between 3 dBi and 30 dBi, corresponding to a half-power beamwidth between 145° and 5° respectively according to eq. (8.65). The transmit power, bandwidth and modulation

settings remain identical to the example in section 8.6.2.

Table 8.6: Parameters for the example antenna optimization problem

| | Symbol | Value(s) | Unit |
|---|---|---|---|
| *Spectral* | | | |
| Carrier frequency | $f_c$ | 20.0 | GHz |
| Bandwidth settings | $B$ | [0.1, 0.5, 1, 5, 10, 50, 100, 200, 300] | MHz |
| *Waveform* | | | |
| VCM protocol | | DVB-S2 | (see [87], [88], [102]) |
| Roll-off factor | $\alpha$ | 0.35 | |
| *Communication system* | | | |
| PA knee-voltage ratio | $V_k/V_s$ | 0.12 | |
| Transmit power (per pass) | $P_{tx,min}$ | 10 | dBm |
| | $P_{tx,max}$ | 43 | dBm |
| Antenna bore sight gain | $G_{tx0,min}$ | 3 | dBi |
| | $G_{tx0,max}$ | 30 | dBi |
| Maximum channel bandwidth | $B_{channel}$ | 96 | MHz |
| *Receiving satellite system* | | | |
| Constellation | Example constellation | | |
| Antenna gain-to-temperature ratio | $G/T$ | 13.2 | dBK |

## Results and algorithm comparison

Three algorithms are evaluated for solving the optimization problem, the NSGA-II algorithm [208], used in the previous problems, and two extensions to this algorithm the NSGA-III algorithm [214], [215] and the R-NSGA-II algorithm [216]. The three algorithms are ran with the same maximum iterations (5000) and population (400) for the example problem and their results are compared.

The R-NSGA-II algorithm adds reference points that are used in the selection step of the genetic algorithm to select solutions closest to these points [216]. This way the algorithm can split the Pareto front and create a tighter set of solutions that converges to the reference points. An example pair of (normalized) reference points is shown in Figure 8.15a, the green reference point converges to the maximum throughput for zero-energy solution, while the red reference point converges to the zero-pointing solution. If fully converged, this would lead to the same result as running the optimization with only two of the objectives. The NSGA-III algorithm adds reference directions that in the selection step

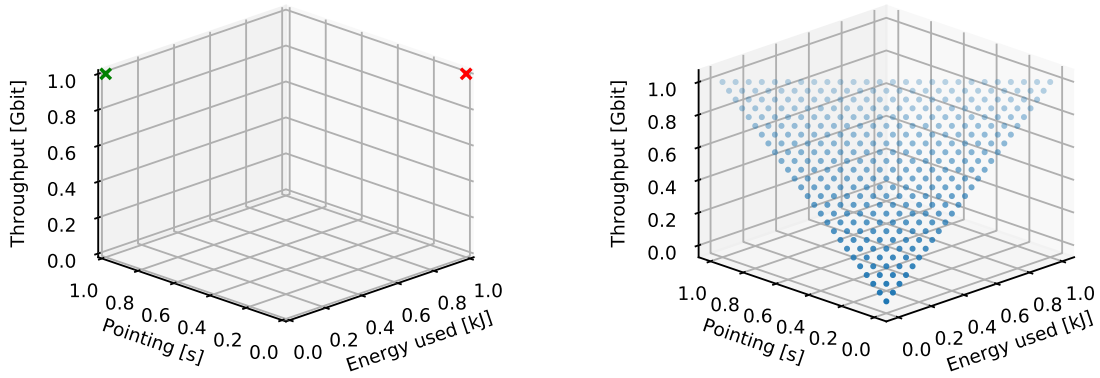


(a) Example of reference points in the R-NSGA-II algorithm

(b) Reference directions used in the NSGA-III algorithm

Figure 8.15: The R-NSGA-II and NSGA-III algorithms extend on the NSGA-II algorithm by adding reference points, and reference directions respectively

of the genetic algorithm selects solutions that have the smallest distance to the reference plane [214], [215]. This way the algorithm converges to non-dominating solutions, solutions that are 'in-between' the extremes in maximum throughput, minimum energy or minimum pointing. Figure 8.15b shows the

reference directions created by the Das-Dennis method [217]. The solutions on Pareto front using NSGA-III will naturally converge to these points if possible.

Figure 8.16a shows the solutions in Pareto optimal set in three dimensions found by using the NSGA-II algorithm. The figures in fig. 8.16b show the same solutions in two-dimensions. The solution set shows two fronts, a main diagonal where throughput is increasing for more energy used and more pointing. The second front can be seen at the bottom of the first and third graph of fig. 8.16b. This front includes the solutions that primarily minimize pointing, i.e. solutions that have a low antenna gain with a wide visibility, and use more energy to close the link. Three solutions are highlighted in the graphs of fig. 8.16, in red the maximum throughput solution, in green the maximum throughput on the minimum pointing front and in blue the solution that lies in the middle of the solution space. The NSGA-II algorithm has no particular selection of the solutions on the Pareto optimal front and therefore is not giving a good sampling of the whole solution space.

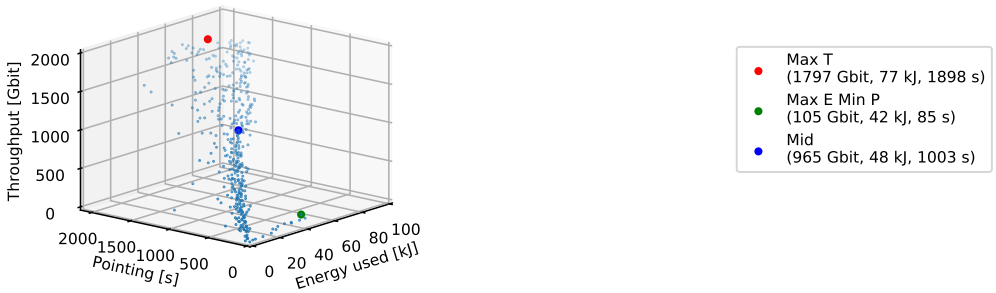


(a) Three dimensional Pareto optimal solutions using NSGA-II

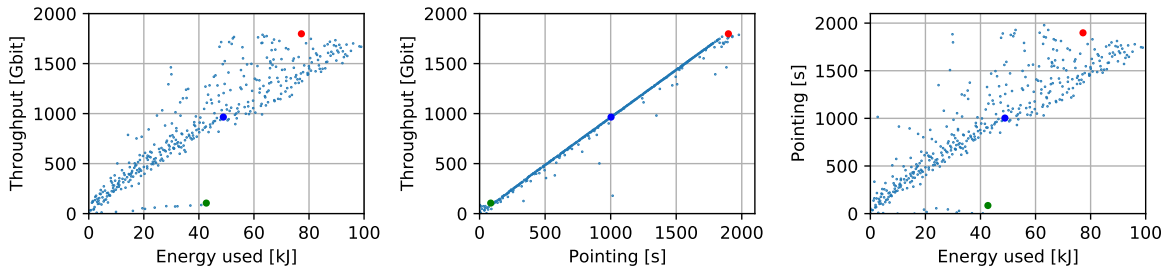


(b) Pareto optimal set

Figure 8.16: Visibility optimization using the NSGA-II algorithm

Figure 8.17 shows the same graphs, now using the NSGA-III algorithm that uses the reference directions to obtain a better sampling of the design space. The graphs in fig. 8.17b show that the objective space is more spread out, where-as with the NSGA-II algorithm, the solutions were primarily confined on the main diagonal. By using the reference directions for selection, NSGA-III algorithm therefore gives a better sampling of the whole Pareto front. This however comes at the cost of not finding the extremes, for example the maximum throughput solution (red) found by the NSGA-III algorithm only achieves a throughput of 1623 Gbit, whereas the NSGA-II algorithm found this extreme at 1797 Gbit. The NSGA-III algorithm gives a better sampling at the cost of not fully exploring towards the extremes.

For the R-NSGA-II algorithm, the reference points are chosen to explore the extremes towards the red and green solutions, at (1800 GBit, 45 kJ, 2000s) and (250 GBit, 60 kJ, 100 s) respectively, slightly beyond the extremes found using the NSGA-II algorithm. As can seen in fig. 8.18 this gives a selective sampling around these reference points points. The maximum throughput is now found at 1877 GBit, beyond what was found using the NSGA-II algorithm for less energy. Similarly, the green minimum pointing solution is now found to can reach a throughput of 151 GBit, 50% higher than what was found with the other two algorithms. The R-NSGA-II algorithm is therefore particularly useful to explore a particular location in the objective space, or to explore all solutions close to a desired solution.

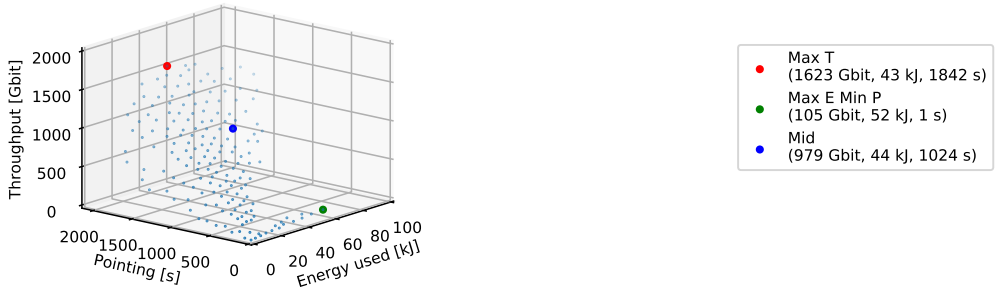


(a) Three dimensional Pareto optimal solutions using NSGA-III

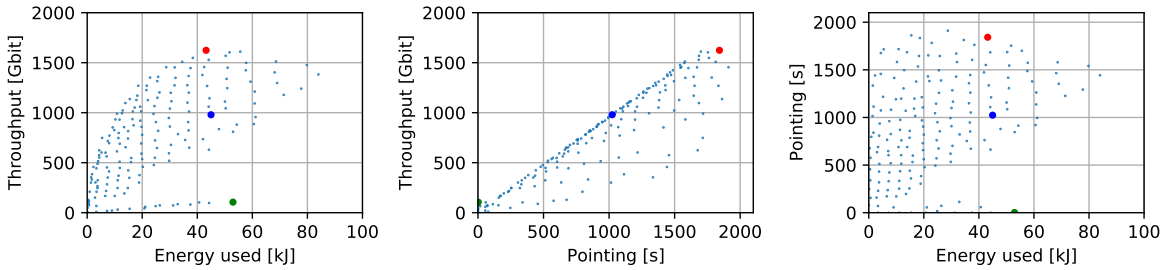


(b) Pareto optimal set

Figure 8.17: Visibility optimization using the NSGA-III algorithm

In general, the NSGA-III and R-NSGA-II can be used in different scenarios. The NSGA-III algorithm is particularly useful when the shape of the Pareto front(s) is unknown and evenly sampling the objective space.This gives a quick insight into, for example, how a low-antenna gain solution would trade-off against throughput and energy consumption. The R-NSGA-II algorithm is useful when the objective space is to be explored, i.e. when a particular set of requirements is to be met for the communication system.

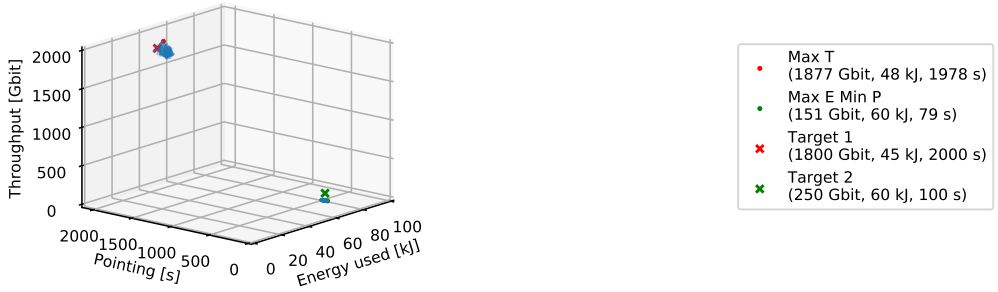


(a) Three dimensional Pareto optimal solutions using R-NSGA-II

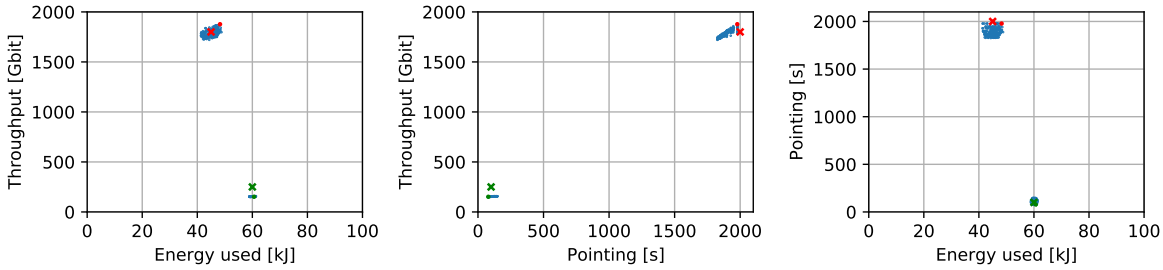


(b) Pareto optimal set

Figure 8.18: Visibility optimization using the R-NSGA-II algorithm ($\epsilon = 0.001$)

## 8.8. Latency model

In this section, a fourth objective is added to the optimization framework that is used to score the solutions on the maximum latency for data generated on-board the satellite. As explained in chapter 5, the latency is defined as the time from data generation by the payloads on-board the satellite until the data is delivered to a internet connected ground station. The main contributor to this latency is the time the satellite is waiting in a gap between two contact opportunities. This can be in the order of minutes, while the latency introduced by the NGSO (mega-)constellations will be in the order of milliseconds.

The following sub-sections will discuss the mathematical formulation of the latency model, accompanied optimization problem and results for an example problem.

### 8.8.1. Mathematical formulation

A gap between the end of a contact opportunity and the beginning of the following contact opportunity causes a delay in the delivery of data that is acquired on the satellite during this period of no communication. The actual start of a contact opportunity depends on the moment when the link margin becomes positive, and the actual end depends on when the link margin drops below zero. These actual begin and end times are denoted as $t'_b$ and $t'_e$. A gap between pass $i$ and following pass $j$ therefore causes a maximum latency for data delivery of:

$$L_{atency} = \max t'_{b,j} - t'_{e,i} \quad [s] \quad \text{for all } i, j = i + 1. \tag{8.86}$$

This metric accounts the maximum latency that can occur across the gap. For example, given two passes with $t'_{e,i} = 120s$ and $t'_{b,j} = 212s$, data that is ready for transmission at the end of the first pass would have a latency of 92 seconds while the satellite waits for the following contact opportunity. Data that is ready for transmission during a pass has no additional latency.

A maximum latency metric is used in the optimization because it guarantees a quality-of-service, i.e. all data will be transmitted within the maximum latency. In section 8.10.4 an average latency is defined taking into account the average latency data experiences throughout the simulated orbit. This average latency can be substituted as a design objective for the maximum latency if desired.

In general, the latency models assume that there is no data accumulating in the on-board storage waiting for transmission and, therefore, also assumes that whatever data is ready for transmission can be fully transmitted in the next pass. This means that, for example, the IoT/M2M packets that are collected during a gap are of small enough size that all can be transmitted in the next pass. Future research could extend on this model by adding a demand/data-generation model that relates for example the data that is generated on-board the satellite is dependent on the location of the satellite such as is done in [218] and [3]. For example, more data IoT/M2M is generated over populated areas or less EO data is collected over uninteresting areas such as the oceans and polar regions.

### 8.8.2. Latency optimization

The latency metric of eq. (8.86) is used as a fourth objective in the design optimization (eq. (8.89)) and only the passes that are selected are considered in the latency. The new design problem and equations are shown below:

**Design vector**

$$\boldsymbol{x} = [x_1, x_2, ..., x_N, P_{tx,1}, P_{tx,2}, ..., P_{tx,N}, B, G_{T,0}]^T \tag{8.87}$$

**Objective functions**

$$f_{throughput} = \max_{\boldsymbol{x}} \sum_{i}^{N} x_i \cdot \int_{t_{b,i}}^{t_{e,i}} R_{b,i}(t)\, dt \quad [bits] \tag{8.88}$$

$$f_{latency} = \min_{\boldsymbol{x}} \max_{i} x_i \cdot (t'_{b,j} - t'_{e,i}) \quad j = i + 1 \quad [s] \tag{8.89}$$

$$f_{energy} = \min_{\boldsymbol{x}} \sum_{i}^{N} x_i \cdot \int_{t_{b,i}}^{t_{e,i}} (R_{b,i}(t) > 0) \cdot \frac{10^{\frac{P_{tx,i}-30}{10}}}{\eta_{MAEE}(m_i, B)}\, dt \quad [J] \tag{8.90}$$

$$f_{pointing} = \min_{\boldsymbol{x}} \sum_{i}^{N} x_i \cdot \int_{t_{b,i}}^{t_{e,i}} (\theta_i(t) - \theta_{HPBW}/2 > 0)\, dt \quad [s] \tag{8.91}$$

**Constraints**

$$t_{e,i} - t_{b,j} \geq 0 \quad j > i \tag{8.92}$$

$$\dot{\theta}(t) \leq \dot{\theta}_{max} \tag{8.93}$$

**Bounds**

$$\dot{\phi}(t) \leq \dot{\phi}_{max} \tag{8.94}$$

$$x_i \in \{0,1\} \quad i \in \{1,...,N\} \tag{8.95}$$

$$P_{tx} \in \mathbb{R} : P_{tx,min} \leq P_{tx} \leq P_{tx,max} \quad [dBm] \tag{8.96}$$

$$G_{tx,0} \in \mathbb{R} : G_{tx,min} \leq G_{tx,0} \leq G_{tx,max} \quad [dBi] \tag{8.97}$$

**Equations**

$$\theta_{HPBW} = \sqrt{\frac{4\pi}{10^{G_{tx,0}/10}}} \quad [rad] \tag{8.98}$$

$$G_{tx}(\theta) = \begin{cases} G_{tx,0} & \text{if } \theta \leq \theta_{HPBW}/2 \\ 0 & \text{otherwise} \end{cases} \quad [dBi] \tag{8.99}$$

$$SNR(t) = P_{tx} + G_{tx} - 20\log_{10} d(t) - 20\log_{10} f + G/T - 10\log_{10} k - 10\log_{10} B - 147.55 \quad [dB] \tag{8.100}$$

$$m_i = \text{maximum MODCOD within } SNR_i(t)$$

$$N_{carrier} = \begin{cases} 1 & \text{if } B \leq 100\ MHz \\ 2 & \text{if } 100\ MHz \leq B \leq 200\ MHz \\ 3 & \text{if } 200\ MHz \leq B \leq 300\ MHz \end{cases} \tag{8.101}$$

$$R_s = \begin{cases} B/(1+\alpha) & \text{if } N_{carrier} = 1 \\ (N_{carrier} B_{channel})/(1+\alpha) & \text{if } N_{carrier} = 2,3 \end{cases} \quad [syms/s] \tag{8.102}$$

$$R_{b,i}(t) = \begin{cases} R_s \cdot \eta(m_i, B) & \text{if } SNR_i(t) \geq SNR_{req}(m_i) + 3 \\ 0 & \text{otherwise} \end{cases} \quad [bit/s] \tag{8.103}$$

$$t'_{b,i} = \text{first } t \text{ for which } R_{b,i}(t) > 0 \quad [s] \tag{8.104}$$

$$t'_{e,i} = \text{last } t \text{ for which } R_{b,i}(t) > 0 \quad [s] \tag{8.105}$$

### 8.8.3. Example evaluation

The latency optimization problem is ran with the same parameters as the previous example (see table 8.6). The difference with the previous example is that the optimization problem now includes four objectives; throughput, latency, energy consumption and antenna pointing. The problem is solved using the NSGA-III algorithm with 13 reference directions (population size of 600) and a maximum of 5000 generations. A constraint is added that limits the maximum latency to 5700s, approximately one orbit.

#### Results

Figure 8.19 shows the Pareto-optimal set of solutions plotted against two objectives in each graph. Several solutions are again highlighted: in red the maximum throughput solution, and in green the maximum throughput on the minimum pointing front. For these points, similar values are found as in the previous example using the NSGA-III algorithm in fig. 8.17. The solutions marked in blue achieve a throughput of around 1000 Gbit using the minimum energy (blue dot •), minimum latency (blue plus +) or minimum pointing (blue cross x).

The three solutions marked in blue illustrate the trade-off's to be made when targeting a throughput of 1000 Gbit. The minimum energy solution for this throughput (•), has a relatively high latency of 3000 seconds. This latency can be more than halved when slightly more energy is spend to include intermitted passes, obtaining the minimum latency solution for this throughput (+). In this particular case it could therefore be desirable to spend slightly more energy. Similarly, the minimum pointing solution for this throughput (x) would require almost as much energy as the maximum throughput solution (•) to compensate for a low antenna gain, and would have a much worse latency of 5000 seconds as only the most optimal (overhead) passes are used.

In general however, the minimum through maximum throughput can always be obtained for the minimum latency (see the •, + and • in the throughput-latency plot in the top right of fig. 8.19). This indicates that given enough energy is spent, throughput and latency are directly related. This makes sense as both objectives are proportional to the contact time with the satellite. If the use-case requires either high throughput, or low latency (as is with the EO or IoT/M2M use-cases formulated in chapter 5)

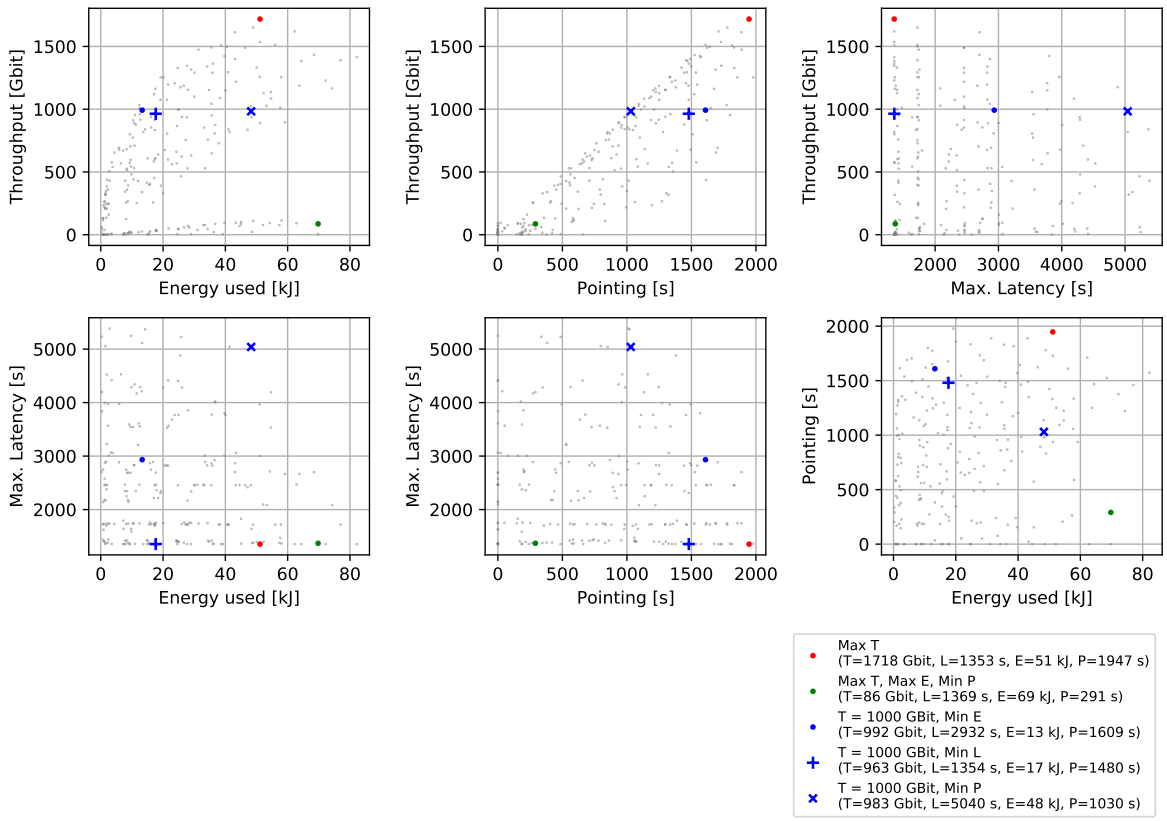


Figure 8.19: Pareto optimal solutions for the four-objective latency optimization

it is computationally beneficial to remove one of the objectives and put a minimum/maximum constraint on the other, limiting the multi-objective problem to a three-objective problem.

## 8.9. Parametric models

The following sub-sections provide the equations that are used to model power, size and mass of the data-relay downlink. These models are based on performance data reported in literature presented in chapter 3 of small satellite antennas and transmitters. As the number of available data-points from literature is limited, these models lack the fidelity needed to accurately estimate the volume and mass, especially for the miniaturization of small satellite hardware.. Future research may develop these models further. In this work these models are used to provide a first order method of limiting the optimization design space by putting constraints on size, weight and power.

### 8.9.1. Power

So far the power consumption/energy model only considered the consumption of the power amplifier. When transmission bandwidths and data-rates increases the power consumed by the digital baseband modulation becomes significant as higher clock speeds are required to perform the processing. Using performance figures from literature provided in section 3.2.2 an estimation of the contribution of the modulator is made. The modulator power consumption is assumed to be the remaining part of the DC power consumption, assuming a power amplifier efficiency of 30%[4]. Figure 8.20a shows the resulting modulator power consumption as function of the data rate for the transmitters in section 3.2.2. The new resulting power consumption of the transmitter is calculated as followed:

$$P_{DC} = P_{MOD} + P_{PA} \quad [W] \tag{8.106}$$

where

$$P_{MOD} = 0.015 \cdot \frac{R_s}{1Mbps} + 14.967 \quad [W] \tag{8.107}$$

[4] $P_{mod} = P_{dc} - P_{rf}/\eta$ where $\eta = 30\%$ based on the efficiencies for DVB-S2

and

$$P_{PA} = \frac{1}{\eta_{MAEE}(m,B)} \cdot 10^{\frac{P_{tx}-30}{10}} \quad [W] \tag{8.108}$$

The energy objective function for the optimization is adjusted accordingly:

$$E_{nergy} = \int_{t_b}^{t_e} (R_b(t) > 0) \cdot P_{DC}\, dt \quad [J] \tag{8.109}$$

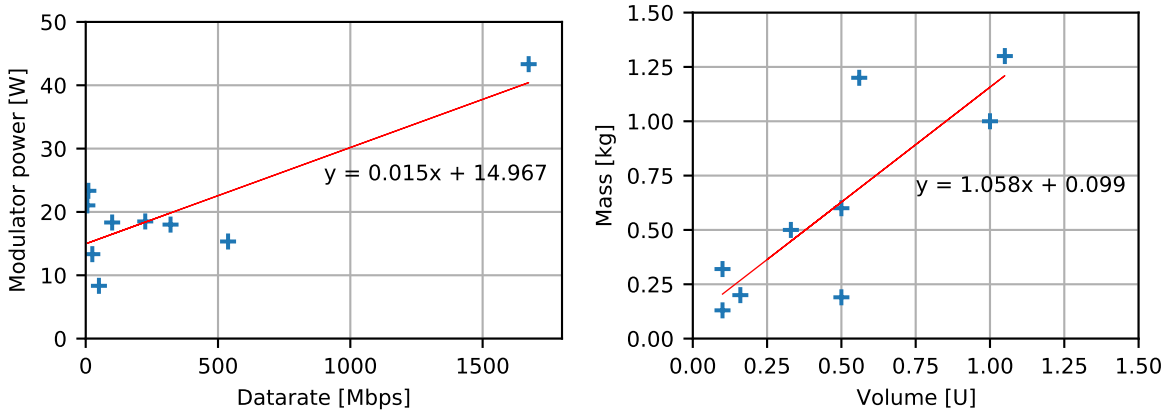


(a) Estimate of modulator power dissipation based on reported values in literature

(b) Estimate of transmitter mass based on reported values in literature

Figure 8.20: Estimate of modulator power consumption and transmitter mass

### 8.9.2. Size

The size of the data-relay downlink is estimated from two parts, a part for the transmitter and part for the (stowed) antenna, based on the literature presented in chapter 3. The average volume to RF transmit power ratio is taken from table 3.7 (inverse of column 6) to estimate the volume of the transmitter. The inverse of the linear trend found in fig. 3.11 is taken to estimate antenna (stowed) volume. The resulting volume is calculated in standardized 10 x 10 x 10 cm units [U]:

$$V = V_{tx} + V_{ant} \quad [U] \tag{8.110}$$

where

$$V_{tx} = 0.123 \cdot P_{tx,W} \quad [U] \tag{8.111}$$

$$V_{ant} = 0.239 \cdot G_{tx,dBi} - 5.990 \quad [U] \tag{8.112}$$

### 8.9.3. Mass

The mass of the data-relay downlink is estimated from two parts, a part for the transmitter and part for the (stowed) antenna, based on the literature presented in chapter 3. The volume of the transmitter found from eq. (8.112) is used to estimate the transmitter mass based on the linear trend in fig. 8.20b. The inverse of the linear trend found in fig. 3.11 is taken to estimate antenna mass. The resulting equations for mass estimation are:

$$m = m_{tx} + m_{ant} \quad [kg] \tag{8.113}$$

where

$$m_{tx} = 1.058 \cdot V_{tx} + 0.099 \quad [kg] \tag{8.114}$$

$$m_{ant} = 0.646 \cdot G_{tx,dBi} - 18.658 \quad [kg] \tag{8.115}$$

# 8.10. Operational models

The following sub-sections provide equations that are used to model operational performance of the design solutions. These models can be used to assess the impact on the mission operations of using a NGSO data-relay downlink.

## 8.10.1. Contact time

The contact time is defined as the overall time per orbit the small satellite is downlinking its data. Contact time in combination with throughput is an indicator of how the satellite operates its downlink. If a high contact time used to achieve a low throughput, this indicates that the satellite is spreading out the downlinking of its data, using a low rate link and several contact opportunities. Vice-versa if a high throughput is achieved with low contact time that means the satellite concentrates its downlinking in only a few (good) contact opportunities. The average contact time per orbit can be calculated as:

$$T_{contact} = \frac{T_{orbit}}{T_{sim}} \sum_{i}^{N} x_i \cdot \int_{t'_{b,i}}^{t'_{e,i}} (R_{b,i}(t) > 0)\, dt \quad [s] \tag{8.116}$$

where $T_{orbit}$ is the orbital period of the satellite and $T_{sim}$ the simulation time.

## 8.10.2. Transmitting duty cycle

The transmitting duty cycle indicates the percentage of the orbit in which the transmitter is active and consuming power. The transmitter can be one of the highest power consumers on the satellite. While peaks in power consumption might be allowable, a continuous transmission might drain the batteries on the satellite too much. The transmitting duty cycle can be calculated from the contact time as:

$$d_{tx} = \frac{T_{contact}}{T_{orbit}} \cdot 100\% \quad [\%] \tag{8.117}$$

## 8.10.3. Pointing duty cycle

Similar to the transmitting duty cycle, the pointing duty cycle indicates the percentage of the orbit in which the antenna is to be pointed towards a target. If the satellite does not have an antenna steering mechanism, either mechanical or electrical, body-pointing must be used to steer the antenna. If body-pointing is used this might mean that no payload data can be collected while relaying-data, potentially reducing mission return. The pointing duty cycle can be calculated from the pointing objective as:

$$d_{ant} = \frac{P_{ointing}}{T_{sim}} \cdot 100\% \quad [\%] \tag{8.118}$$

## 8.10.4. Average latency

Alternatively to the maximum latency the average latency can be used as a metric. A gap between pass $i$ and following pass $j$ causes an average latency over these two passes of:

$$\begin{aligned} L_{atency} &= \frac{1}{t'_{e,j} - t'_{b,i}} \int_{t'_{e,i}}^{t'_{b,j}} t'_{b,j} - (t'_{b,j} - t)\, dt \\ &= \frac{1}{t'_{e,j} - t'_{b,i}} \int_{0}^{t'_{b,j} - t'_{e,i}} t\, dt \quad [s] \qquad j = i + 1. \end{aligned} \tag{8.119}$$

This metric accounts average latency across the gap instead of just taking the gap duration as the latency metric. For example, given two passes with $t'_{e,i} = 5s$ and $t'_{b,j} = 13s$, data that is ready for transmission at $t = 6s$ has a latency of $t'_{b,j} - t = 13 - 6 = 7\ s$, data ready at $t = 10s$ has a latency of $t'_{b,j} - t = 13 - 10 = 3\ s$. Data that is ready for transmission during the first pass has a latency of 0 and does not count towards the latency average.

## 8.11. Optimization for many overlapping passes

So far the selection of which contact opportunities are used for relaying data has been based on the method described in section 8.3. Here each contact opportunity is assigned a binary variable that indicates if the contact opportunity is used or not. A constraint is used to invalidate any selection of contact opportunities that overlaps. This method works well when considering scenarios in which only one or two passes are overlapping at a time (like the example in fig. 8.3a). When one longer pass is overlapping many shorter passes this method becomes problematic and results into only local optima being found.

This problem is illustrated in fig. 8.21, showing the range over time for seven contact opportunities. An overall longer pass 1. is overlapping with four shorter passes 2. to 5.. The current optimization has a high likelihood to converge to the local optimum, where the shorter passes are used as it would require all five binary variables to be in the correct state to not result into a constraint violation that invalidates the whole solution. Once the solution is towards using some of the shorter passes, it is unlikely to converge using the overlapping pass as each single bit-flip using pass 1. would result into a violation. There would only be a small chance that all five variables flip to the global optimum and this chance decreases with increasing number of overlapping passes.

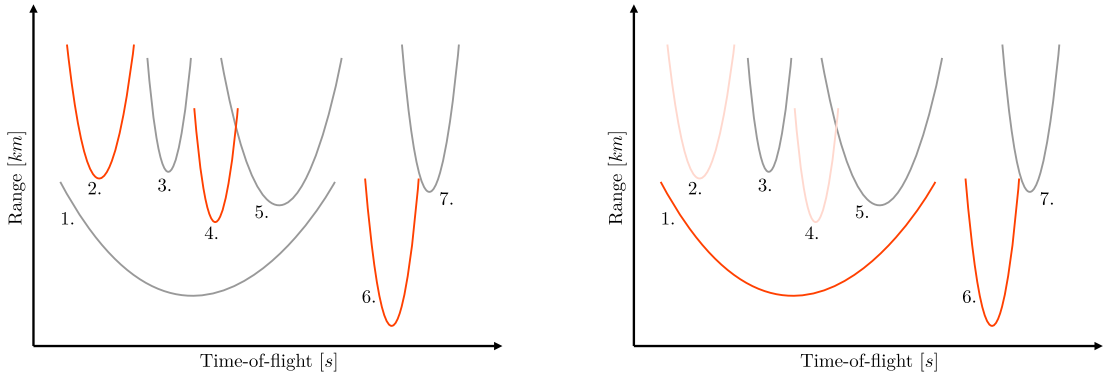


(a) Without downselection there is a small likelihood that the optimization will use the longer pass, as it requires five variables to be in the correct state to not result into a constraint violation. ($x_{local} = [0,1,0,1,0,1,0] \rightarrow x_{global} = [1,0,0,0,0,1,0]$)

(b) When using downselection a single bit-flip would result into the global optimal solution as following overlapping passes are ignored instead of resulting into a constraint violation. ($x_{local} = [0,1,0,1,0,1,0] \rightarrow x_{global} = [1,1,0,1,0,1,0]$)

Figure 8.21: Pass downselection helps with converging to the global optimum by removing the overlapping constraint and only selecting the contact opportunity that were not overlapping with previous selected contact opportunities

### Pass downselection

Instead, a downselection algorithm is used in which there is no longer a constraint that would invalidate any overlapping solution. The downselection algorithm starts by the first occurring selected contact opportunity and ignores any following selected contact opportunity if it was overlapping with the previous selected contact opportunity. In this case, as shown in fig. 8.21b, only one bit-flip is required to converge to the global optimum, regardless of how many shorter passes were selected. Using downselection, the optimization no longer prefers multiple shorter passes over a longer pass causing initial constraint violation. Simultaneously, shorter overlapping passes are not fully excluded from the optimization.

This downselection can be implemented using the information in the original overlap matrix $O$ defined in eq. (8.6). Values in the $O$-matrix greater than zero indicate overlapping passes. The first column of the $O$-matrix shows which passes are overlapping with the first pass, the second column those overlapping with the second pass, the third column with the third pass, and so forth. Each column can therefore be converted into a binary mask that can be used to ignore selected contact opportunity if they are overlapping with a previously selected contact opportunity. For example, in fig. 8.21b, the mask for the first pass is $mask_1 = [0,1,1,1,0,0]$, for the sixth pass it is $mask_6 = [0,1,1,1,0,0]$. Using binary logic the mask can be applied iteratively to the original pass selection vector until only the non-overlapping passes remain. The algorithm for this downselection is shown in algorithm 4.

**Algorithm 4:** Downselection of contact opportunities

**Input:** $x_{pass} = [x_1, x_2, ..., x_{N_{pass}}]$, $O$

**Output:** $x_{pass}$

**for** $i = 1; i \leq N_{pass}; i = i + 1$ **do**
  **if** $x_{pass}[i] == 1$ **then**
    $mask = O[:, i] > 0$
    $x_{pass} = x_{pass}\ \&\ \sim mask$
  **end**
**end**
**return** $x_{pass}$

Figure 8.22 shows the difference for the maximum throughput solution in a scenario with many overlapping passes in the Telesat case see chapter 9. As can be seen from fig. 8.22b, simply increas-

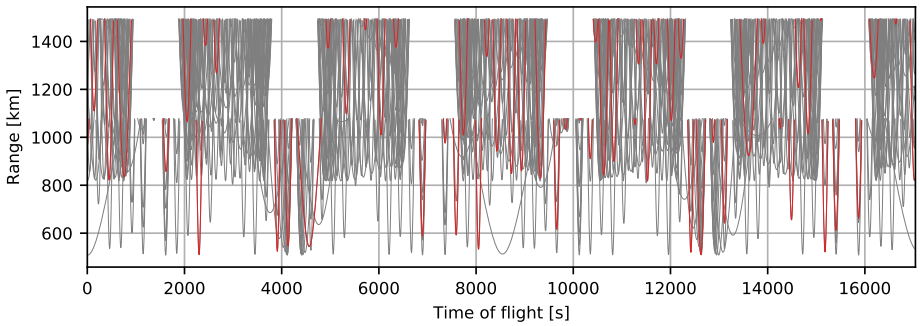


(a) population size = 100, number of generations = 1600, no-downselection

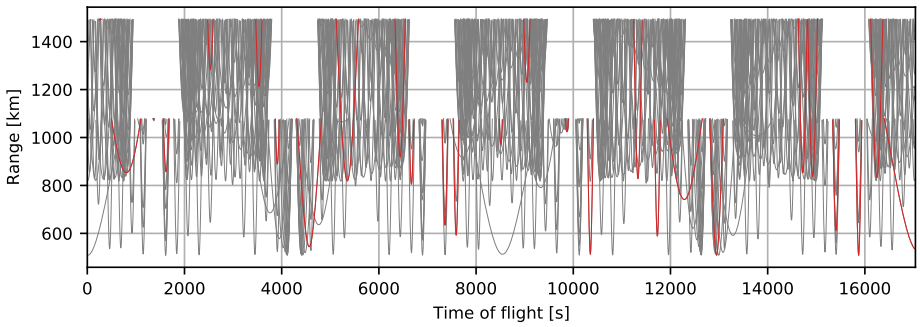


(b) population size = 400, number of generations = 1600, downselection

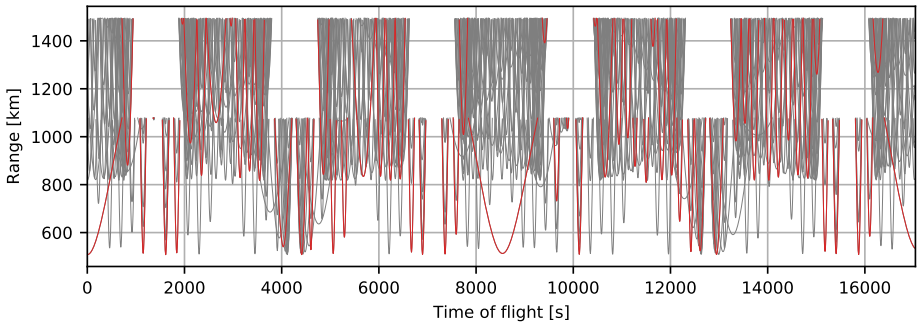


(c) population size = 400, number of generations = 1600, downselection

Figure 8.22: Pass downselection helps with converging to the global optimum by removing the overlapping constraint and only selecting the contact opportunity that were not overlapping with previous selected contact opportunities

ing the population size does not yield a better result. Similarly, when the number of generations are increased the solution does not improve as only a local maxima is reached, requiring violation of the overlapping constraint to improve. When down selection is used instead the solution converges to the global maxima for contact time as shown in fig. 8.22c.

### Biased initialization

Even with downselection, the optimization takes a significant amount of time (i.e. tens of minutes) to converge to the optimal contact opportunity selection for the given use-case. To improve this, biased initialization can be used. The biased initialization implemented in this work uses the contact optimization from section 8.3 to find several initial contact opportunity selections. Prior to the data-relay downlink optimization, a contact time optimization is ran using the NSGA-III algorithm. This pre-optimization finds the maximum contact time for the minimum contact opportunities used. Figure 8.23 shows the result of this pre-optimization on the Telesat case. The NSGA-III finds the selections that offer the most potential for both use-cases. In the extremes it finds the single contact opportunity that results in the maximum contact time, and the minimum combination of contact opportunities that results into the maximum contact time, and all optimal choices in between. This initial set of selections is used as the initial population with all other variables (power, bandwidth, antenna gain, etc.) maximized. The optimization hereby spends more time finding i.e. right power levels than just running permutations of contact opportunity selections.

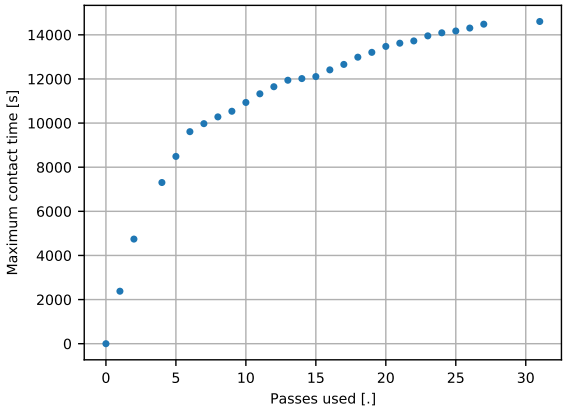


Figure 8.23: Pre-optimization for contact time. Each solution is used as an individual in the initial optimization for the data-relay downlink optimization.

### Selection, cross-over and mutation

So far the cross-over, mutation and selection processes (see fig. 8.1) were not discussed in this chapter. For an optimization with many overlapping passes these become important to achieve a fast convergence and global optima. A custom cross-over and tournament selection is used to achieve satisfactory results when considering many overlapping passes.

The custom cross-over function is used to address the dependence between the pass selection variables ($\boldsymbol{x_{pass}} = [x_1, x_2, ..., x_{N_{pass}}]^T$) and the pass power setting variables ($\boldsymbol{P_{tx,pass}} = [P_{tx,1}, P_{tx,2}, ..., P_{tx,N_{pass}}]^T$). A standard cross-over function would consider these variables from two selected parents and apply the cross-over to create the children for the next generation. For the pass selection a half-uniform cross-over (HUX) function is used. This cross-over will first determine what indices are different in the first and the second parent. Then, it will take half of the difference to be selected from the other parent [203]. This cross-over works as intended when downselection is used. However, a cross-over on the power selections should only consider the power settings of the parents for the passes that are used as only these contributed to the fitness (throughput, latency, etc.) of the parent. To do so, the cross-over for the pass selection and pass power selections are combined. First, a HUX is performed on the parents to find the new pass selection for the children. Then for each selected pass in the children it is determined whether parent 1, parent 2 or both parents used the pass in their solutions. If only one of the parents used the pass, its power selection is used. If both parents used the pass, the average of the two power selections are used. The mutation function then slightly alters the variables to create a better variation in the new individuals. By only considering the variables in the design vector of the parents that

contributed to the fitness value, a better convergence is obtained and the power variables converge with the pass selection variables. Table 8.7 shows the different functions used for the variables in the design vector. The antenna gain and bandwidth variables use simulated-binary cross-over (SBX) functions and polynomial mutations both described in [219]. A one percent probability for mutations on all variables was used.

Table 8.7: Cross-over and mutation operators

| | | cross-over | mutation |
|---|---|---|---|
| **pass selection** | $x_i$ | custom | binary bit-flip ($p = 0.1\%,\ \eta = 3$) |
| **pass power** | $P_{tx,i}$ | HUX | polynomial mutation ($p = 10\%,\ \eta = 3$) |
| **antenna gain** | $G_{tx}$ | real SBX | polynomial mutation ($p = 1\%,\ \eta = 3$) |
| **bandwidth** | $B$ | real SBX | polynomial mutation ($p = 1\%,\ \eta = 3$) |

To further improve convergence, the U-NSGA-III algorithm may be used. This algorithm is identical to NSGA-III but instead of randomly selecting parents for mating, it adds tournament pressure by comparing parents by fitness and constraint violation [220]. This tournament pressure works well in combination with the biased initialization described in the previous section. The initial population will consist of individuals having increasing numbers of selected passes and all other variables maximized. At the start of the optimization when optimizing for throughput, all individuals will obtain the maximum throughput and energy consumption as all variables are maximized. All solutions will therefore likely exceed the maximum energy constraint, however those individuals with less passes will consume less energy and therefore be selected for mating, resulting the solution to converge to only using the minimal 'best' passes, while further optimizing the power, bandwidth and gain. Similarly, when optimizing for latency, the individuals having a lot of passes selected will have the lowest latency and will in that case be selected for mating, resulting the solution to converge to using a lot of passes to minimize the latency.

## 8.12. Verification

Several steps were taking in order to verify the models developed in this chapter. The step-wise approach was used that gradually increases the complexity of the optimization. After each additional model an example optimization was used to proper test each models contribution individually. Where possible, hand calculations were performed to verify the computations of the model, i.e. in section 8.4 for the link-budget calculations and section 8.5 for throughput and energy. More complex models such as the MAEE model were taken from literature in which the predictions were compared with measurements. The verification of the end results of the optimization will be performed in the next chapter, where the output of the optimization is compared with state-of-the-art small satellite communication technology.

## 8.13. Summary, discussion and recommendations

This chapter described the NGSO data-relay optimization framework that was developed to optimize a data-relay communication system for using the contact opportunities with the NGSO (mega-) constellations. The data-relay optimization framework takes a set of contact opportunities between a satellite and a NGSO (mega-)constellation and optimizes which contact opportunities are used and the design parameters of the data-relay downlink. These design parameters include the antenna gain and transmission bandwidth. The optimization considers the link-budget for each inter-satellite pass of the contact opportunity and adjusts the transmission power, modulation and coding for each inter-satellite pass to obtain optimal performance for the data-relay downlink. The performance can be optimized towards multiple objectives including throughput per orbit, latency, energy consumption per orbit and time spent pointing the antenna.

The data-relay optimization framework uses the `pymoo` genetic algorithm multi-objective optimization framework by J. Blank and K. Deb [203]. This work developed the models for evaluation of the fitness functions. These models include inter-satellite visibility, link-budgets, multi-carrier aggregation,

variable coding and modulation, modulation dependent energy consumption and maximum latency as well as parametric models for size, weight and power, and operational models for transmission and pointing duty cycles. Any combination of the four objectives, throughput, latency, energy and pointing, may be used in the optimization. Using different optimization algorithms, the trade-offs between these four objectives can be visualized. The four objectives can be translated to data-relay downlink size, weight and power consumption by the use of the parametric models derived from the state-of-the-art performance in literature.

The data-relay optimization framework is designed to handle scenarios considering over 900 contact opportunities which can be expected in a LEO-to-LEO mega-constellation case. It includes biased initialization to speed-up convergence by using a two objective pre-optimization for contact time and number of contact opportunities used.

### Discussion and recommendations

In its current state, the data-relay optimization framework provides an end-to-end framework to optimize the (top-level) design parameters of a data-relay downlink downlink. The framework captures with good accuracy the important trade-offs for the components in the payload downlink system including the modulator, power amplifier and antenna. Some of these models however may be improved in further work. The power consumption estimate of the modulator based on the maximum data rate from fig. 8.20a is based on a limited set of data and therefore is likely to be less accurate for different bit-rates and data. Future work may extend upon the available data from literature to estimate modulator power consumption, or increase the fidelity of this model by considering a lower-level model that takes into account the clock-speeds required for the waveform[5] and the performance of state-of-the-art processors and field-programmable-gate arrays.

The next improvement that can be made is to include the power consumption of the up-converter. For this component, the trade-off for linearity becomes of importance especially when considering multi-carrier aggregated waveforms. The power amplifier efficiency model currently only considers the power consumption in the final stage of the amplifier. Although it is able to capture different transistor technologies, this model is somewhat limited when considering Ka-band frequencies because of the reduced gain of the transistor, multiple stages are required to create gain and boost the signal level from the modulator, further reducing efficiency [221].

The antenna models can be made more accurate by including the frequency in estimating the size, weight and gain of the antenna. As the wave-length decreases with increasing frequency, the size of the antenna reduces for the same gain. The models currently used in this work ignore these physics and effectively assume all antennas from the literature study are operating at the same frequency. This assumption does not cover this benefit of moving towards Ka-band frequencies, and does not capture, for instance, that a reflect array antenna on Ka-band would have higher gain than an identical sized reflect array antenna on X-band.

[5] The clock-speed should be equal or greater than the complex baseband bandwidth following Nyquist theorem [27]

# 9

# Data-relay downlink optimization

In this chapter the optimizations for the design of an NGSO data-relay downlink for several baseline small satellite missions are performed. Chapter 5 defined two use-cases that could benefit from a NGSO data-relay downlink: an IoT/M2M small satellite mission and an EO small satellite mission. Chapter 7 identified two promising target NGSO constellations for relaying the data from the small satellites, the Telesat LEO mega-constellation and the O3b MEO constellation. All four combinations of use-cases and targets are simulated and optimized in this chapter.

In section section 9.1 of this chapter the parameters and targets for the NGSO data-relay downlink are defined based on the selected small satellite use-cases and NGSO targets. In section 9.2 and section 9.3 the results are discussed for the Telesat constellation for the EO and IoT/M2M missions respectively. In section 9.4 and section 9.5 the results are discussed for the O3b constellation for the EO and IoT/M2M missions respectively. Section 9.6 briefly summarizes the verification approach for the use-cases. This chapter will end with a summary and recommendations for future analysis in section 9.7.

## 9.1. Optimization parameters and targets overview

In this section the definitions and requirements from the two use-cases defined in chapter 5 are translated into parameters and targets for the data-relay downlink optimization. The optimization parameters define what configurations are considered during the optimization. Similar to the examples in chapter 8, these parameters include the limits of the variables in the design vector. The optimization targets are a translation of the requirements of the use-case to optimization objectives.

Table 9.1 shows the optimization parameters used for the two use-cases and two data-relay targets. The carrier frequencies for the optimizations are chosen in the center of the user uplink bands of the constellations, 20 GHz (Ku-band) for the Telesat constellation and 28.4 GHz (Ka-band) for the O3b constellation. Transmission bandwidths from 100 kHz to 300 MHz may be used, where the 200 MHz and 300 MHz are double and triple carrier-aggregated signals with channel bandwidths of 96 MHz. The VCM protocol is assumed to be DVB-S2, similar to the current state-of-the art used by the Dove and Corvus satellites with a roll-off factor of 0.35. For the power amplifier model a knee-voltage ratio of 0.12 is used for a practical lower bound. For both constellations the transmit power setting up to 43 dBm (20 W) may be used. For the Telesat optimization an antenna gain of up to 43 dBi is allowed (up to the lower range of parabolic mesh antennas). For the O3b constellation an antenna gain of up to 50 dBi is allowed (current state-of-the art with parabolic mesh antennas) to overcome the higher path loss by the increase in distance to MEO. For the Telesat constellation the May 2020 configuration is assumed, having 1671 satellites with an antenna gain-to-noise temperature of 13.2 dBK [166]. For the O3b constellation the 2017 configuration is assumed, having 42 satellites with a antenna gain-to-noise temperature of 7.0 dBK [183].

Each optimization considers a simulation period of three orbits of a single satellite. The data-relay orbital simulator is used prior to the optimization to find the contact opportunities in each orbit with the targetted NGSO constellations. The considered satellite orbits were discussed in chapter 5 with the tabulated orbital parameters in table 5.1.

Table 9.1: Parameters for the data-relay downlink optimizations

| | Symbol | Value(s) | | Unit |
|---|---|---|---|---|
| *Spectral* | | | | |
| Carrier frequency | $f_c$ | 20.0 | 28.4 | GHz |
| Bandwidth settings | $B$ | [0.1, 0.5, 1, 2.5, 5, 10, 50, 100, 200, 300] | | MHz |
| *Waveform* | | | | |
| VCM protocol | | DVB-S2 | | see: [102] |
| Roll-off factor | $\alpha$ | 0.35 | | [87], [88] |
| *Communication system* | | | | |
| PA knee-voltage ratio | $V_k/V_s$ | 0.12 | | |
| Transmit power (per pass) | $P_{tx,min}$ | 0 | 0 | dBm |
| | $P_{tx,max}$ | 43 | 43 | dBm |
| Antenna bore sight gain | $G_{tx0,min}$ | 3 | 3 | dBi |
| | $G_{tx0,max}$ | 43 | 50 | dBi |
| Maximum channel bandwidth | $B_{channel}$ | 96 | | MHz |
| *Receiving satellite system* | | | | |
| Constellation | | Telesat (LEO) May 2020 | O3b (MEO) 2017 | |
| Antenna gain-to-temperature ratio | $G/T$ | 13.2 | 7.0 | dBK |

## Earth Observation mission

Table 9.2 shows the optimization targets and limits for the the data-relay downlink optimization for the Earth Observation mission. The primary goal for the data-relay downlink for the Earth Observation satellites is to maximize the throughput for the minimal energy usage, to downlink as much payload data and maximize mission return. If possible it should also minimize the time spend pointing the antenna system to the data-relay satellite to minimize the need of a antenna steering mechanism or body-pointing of the satellite. The Earth Observation mission optimization has three objectives: maximizing throughput, minimizing energy consumption and minimizing the amount of time pointing the antenna. From the baseline mission definition in chapter 5 a throughput requirement of 120 GB was determined, which is used directly as a target for the optimization. For the energy target an equivalent energy consumption to the reference Dove satellite for a single pass with a polar ground station is assumed (i.e. a duty cycle of 14.5% on the mission duration dissipating 50 W in the transmitter) which equates to a energy consumption of 41.16 kJ per orbit. The pointing target is normalized to the percentage of the orbit in which the satellite is pointing the antenna, for this optimization it is set to 0.0%.

Table 9.2: Optimization targets and limits for the data-relay downlink optimization for the Earth Observation mission

| | Symbol | Value(s) | Unit |
|---|---|---|---|
| *Targets* | | | |
| Throughput per orbit | $T_{target}$ | 120.0 | GB/orbit |
| Energy consumption per orbit | $E_{target}$ | 41.16 | kJ/orbit |
| Pointing target | $P_{target}$ | 0.0% | |
| *Optimization limits* | | | |
| Throughput limits | $T_{min}$ | 78.0 | GB/orbit |
| | $T_{max}$ | 162.0 | GB/orbit |
| Latency limit | $L_{max}$ | 1.5 | hours |
| Energy limit | $E_{max}$ | $\infty$ | kJ/orbit |
| Pointing limit | $P_{max}$ | 100% | |

Limits are put on the throughput, latency and energy consumption to reduce the objective space of the optimization. The limit for throughput are chosen to be ±35% that of the target values, this gives a lower bound that matches the current highest performing throughput satellite system on the Dove satellite of roughly 80 GB per orbit, while keeping a wide higher limit to show the potential of the data-relay downlink. The latency has an upper limit of 1.5 hours as defined as the requirement in chapter 5. For now, no limits on energy, pointing, size, weight and power are assumed to keep the optimization under constrained allowing for better convergence.

### IoT/M2M mission

Table 9.3 shows the optimization targets and limits for the the data-relay downlink optimization for the IoT/M2M mission. This mission benefits from a lower latency allowing for a better quality of service for the users of the service. The maximum latency experienced is therefore to be minimized using minimal energy and pointing. The IoT/M2M mission has therefore three objectives, minimizing the maximum latency experienced, minimizing energy consumption and minimizing the amount of time pointing the antenna. From the baseline mission definition in chapter 5, a maximum latency of 60 seconds was determined as the requirement, used directly as a target for the optimization. For the energy target an equivalent energy consumption to the reference Hiber satellite for a single pass with a polar ground station is assumed (i.e. a duty cycle of 14.5% on the mission duration dissipating 20 W in the transmitter) which equates to a energy consumption of 16.82 kJ per orbit. The pointing target is normalized to the percentage of the orbit in which the satellite is pointing the antenna, for this optimization it is set to 0.0%. Only a minimum requirement is set on the throughput, of 2.5 GB/orbit as defined in the chapter 5. The rest of the objectives, and size, weight and power are un constraint to keep the optimization under constrained allowing for better convergence.

Table 9.3: Optimization targets and limits for the data-relay downlink optimization for the IoT/M2M mission

| | **Symbol** | **Value(s)** | **Unit** |
|---|---|---|---|
| *Targets* | | | |
| Maximum latency experienced | $L_{target}$ | 120.0 | GB/orbit |
| Energy consumption per orbit | $E_{target}$ | 41.16 | kJ/orbit |
| Pointing target | $P_{target}$ | 0.0% | |
| *Optimization limits* | | | |
| Throughput limits | $T_{min}$ | 2.5 | GB/orbit |
| | $T_{max}$ | ∞ | GB/orbit |
| Latency limit | $L_{max}$ | 10 | minutes |
| Energy limit | $E_{max}$ | ∞ | kJ/orbit |
| Pointing limit | $P_{max}$ | 100% | |

## 9.2. Telesat - Earth Observation mission

The optimization for the data-relay downlink on the EO mission using the Telesat constellation was first run using the NSGA-III algorithm ($n_{dirs} = 300$, $n_{pop} = 300$, $n_{offspring} = 75$, $n_{gen} = 9000$) across three orbits. The grey points in Figure 9.1 show the solutions obtained against the three objectives (latency, energy and pointing) using this algorithm. The targetted performance is marked as a red cross (x), being a throughput of greater or equal to 120 GByte/orbit, an energy consumption of less than 41 kJ/orbit and zero pointing. All solutions shown in fig. 9.5 have a maximum latency of 1.5 hours or less.

The NSGA-III algorithm shows a wide spread in the optimal solutions on the energy-throughput graph (fig. 9.1-a) all with a pointing duty cycle of around 20% (fig. 9.1-b). Up to 150 GB/orbit may be achieved using the targetted 41 kJ/orbit. The solutions shown in fig. 9.1 almost all use the highest antenna gain setting of 43 dBi. Although this is achievable with a parabolic mesh reflector, it is desirable to instead find a solution with a lower antenna gain that can be achieved with a reflect array or horn antenna. The reason for the optimization to strongly favour high antenna gains is that the pointing objective only provides limited means of pushing towards lower antenna gain solutions when only a small number of contact opportunities that are used. In that case, the pointing duty cycle can easily be lowered by using less and shorter passes and is less influenced by the number of passes used. In this case it would make sense to change the pointing objective to a different objective, like size or mass to force the optimization to consider lower antenna gain solutions.

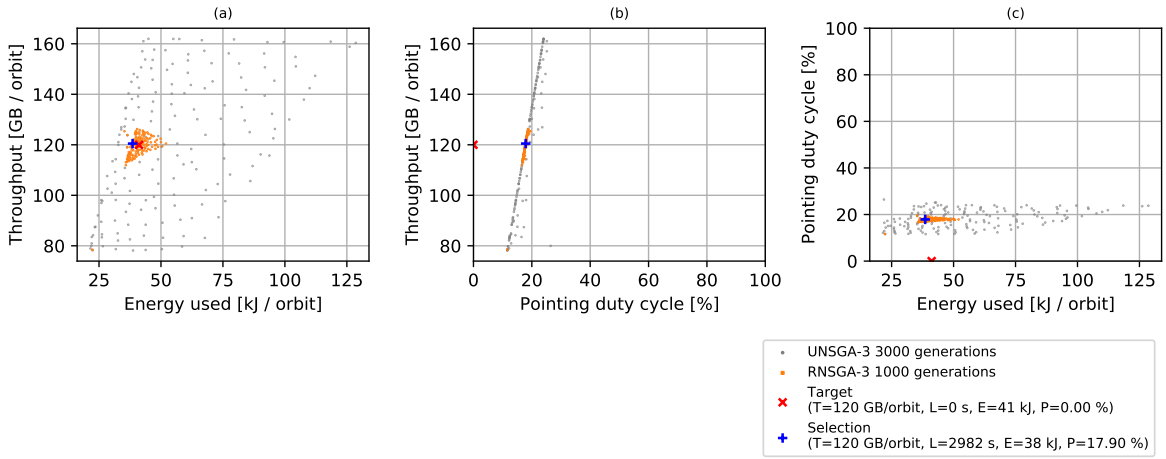


Figure 9.1: Optimization result for the EO use-case with the Telesat constellation

Instead, a second optimization is ran using the R-NSGA-III algorithm[1], using the results of the first optimization as the initial population. The optimization was run with a lower bound on the maximum antenna gain of 36 dBi, within the capabilities of reflect array antennas. The orange solutions in fig. 9.1 show the results obtained with the R-NSGA-III algorithm ($n_{pop/ref} = 210$, $n_{offspring} = 210$, $n_{gen} = 1000$, $\mu = 0.15$). The energy-throughput optimal front has now moved slightly to the right, as more energy needs to be spend for a higher transmitter power. However, the new set of optimal solutions still encompasses the target solution. A solution that meets the requirements was manually chosen from the new set of solutions and is indicated with a blue plus (+).

Figure 9.2 shows the range graph, power and energy usage, and pointing angles during the three orbits for this solution. Figure 9.2c shows that the selected solution uses an antenna gain of 36.0 dBi, which is approximately that of the Ka-band reflect array antenna of the ISARA mission [133]. As this solution lies close to the new energy-throughput Pareto front, it is unlikely that a solution with a horn or lens antenna (up to 25 dBi) will achieve the required throughput within the energy requirement. The range plot of fig. 9.2a shows that only contact opportunities with the lower constellation satellites are used to minimize the required transmission power. An interesting set of passes is used. In the first and second orbit two short passes of about 200 seconds are used to ensure the maximum latency of 1.5 hours is met, while in the third orbit a long duration pass of 40 minutes is used to transmit the bulk of the data. Although short contact opportunities are used, the contact time obtained with the satellite in the first two orbits is still similar to what can be obtained with a single ground station. However only about 8 GB is transmitted in each 200 second pass. The way the throughput objective is set up results into the average throughput per the simulation time to be 120 GB/orbit. It however does not guarantee a 120 GB/orbit for each orbit in the simulated time. Depending on how and when data is generated on the satellite, this could result into operational problems and some data to have a higher latency. This could however be changed in a future update of the orbital simulator.

[1] The R-NSGA-III algorithm combines reference points from the R-NSGA-II algorithm with reference directions from the NSGA-3 algorithm [216]. It was found that for three objectives this algorithm gave better results by equally spreading points around a reference point.

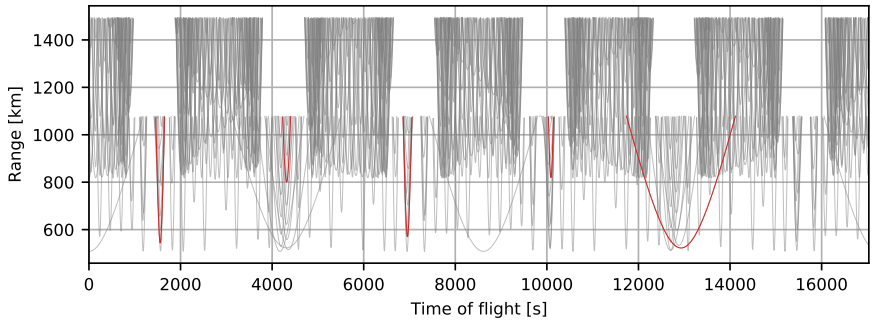


(a) Range and selected contact opportunities

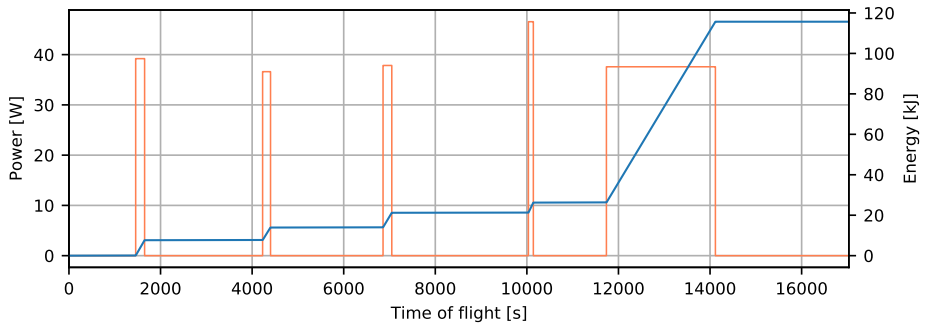


(b) Power and energy consumption

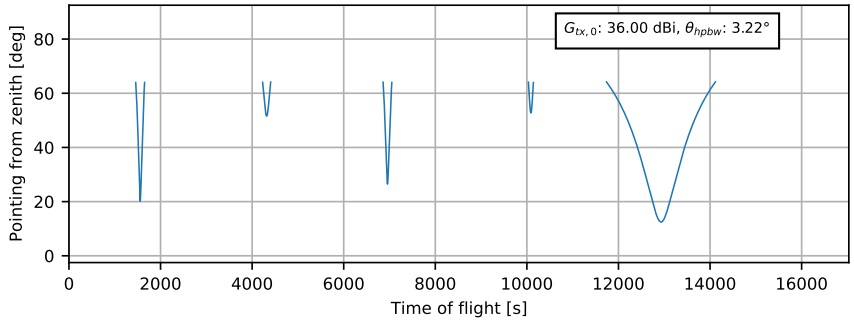


(c) Pointing angle from zenith

Figure 9.2: Range plot with the selected passes highlighted (top), power and energy (middle) and pointing angles (bottom) for the selected solution in the EO case with the Telesat constellation.

The power and energy consumption graph of fig. 9.2b shows a peak transmitter power consumption of 46.55 W, at this point the transmitter is providing a RF power of 37 dBm (5.01 W). A low transmission duty cycle is used which is beneficial for charging the batteries before a transmission period. The bandwidth used in the solution is 300.0 MHz with a maximum MODCOD of 32-APSK 9/10 FEC, giving a maximum data-rate of 950.4 Mbit/s. The pointing angles in fig. 9.6c show that the antenna is pointed up to 65 degrees from the zenith direction. Using the parametric models the estimated transmitter size and mass is 0.62 U and 0.75 kg. As the antenna for the ISARA satellite would be the ideal candidate for this mission, its volume of 0.72 U is assumed as the antenna stowed size. No mass numbers for the ISARA antenna are available therefore a conservative estimate assumes the rest of the 2 kg in the mass budget is used for the antenna, which is assumed to be adequate as the antenna is made from fibre glass material and its mounting is shared with the solar panels [133]. This results in a overall volume and mass of 1.34 U and 2 kg, slightly exceeding the volume budget, however this volume is potentially dual used with the solar panels.

## 9.3. Telesat - IoT/M2M mission

The optimization for the data-relay downlink on the IoT/M2M mission using the Telesat constellation was run using the NSGA-III algorithm ($n_{dirs} = 300$, $n_{pop} = 300$, $n_{offspring} = 75$, $n_{gen} = 9000$). Figure 9.3 shows the solutions obtained against the three objectives (latency, energy and pointing) of this optimization. The targetted performance is marked as a red cross (x), being a maximum latency less or equal to 60 seconds, an energy consumption of less than 16.82 kJ/orbit and zero pointing. All solutions shown in fig. 9.3 achieve a throughput of 2.5 GByte/orbit or more. A R-NSGA-II optimization was also run which did not show significantly different results from the NSGA-III obtained solutions

The set of optimal solutions shows a minimum maximum latency of around 250 seconds (fig. 9.3-a,b). This lower bound is due to non-continuous coverage in this orbit and this duration is equal to the longest gap experienced. This minimum latency can be achieved from energy consumption of about 80 kJ/orbit and higher. Below that point the latency increases significantly as less contact opportunities are used and more gaps appear in the coverage.

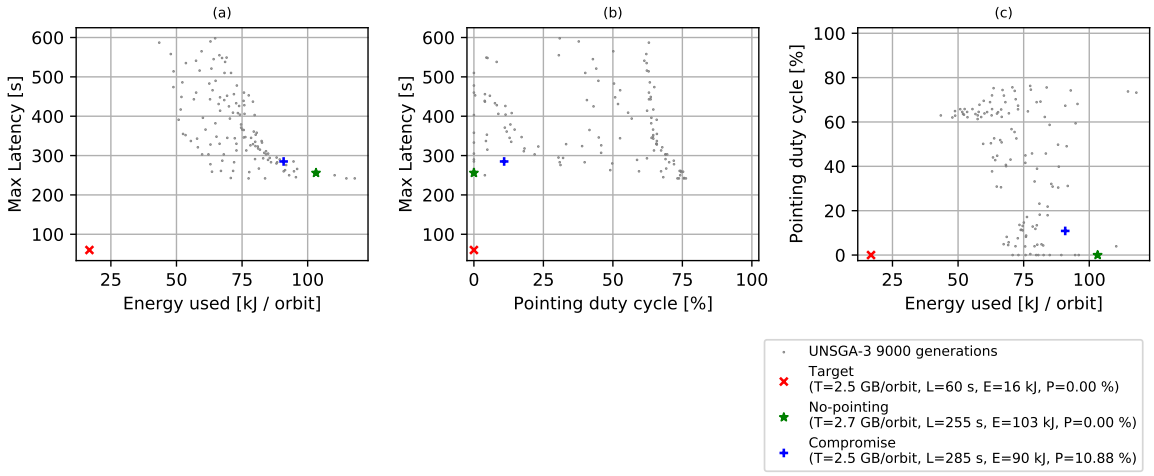


Figure 9.3: Optimization result for the IoT/M2M use-case with the Telesat constellation

The minimum latency can be achieved with a zero-pointing solution, marked by the green star (⋆). This solution uses a low antenna gain of 3 dBi, which could be achieved with a single patch antenna providing a hemispherical zenith coverage. This low antenna gain however means that a higher transmit power is required and therefore the solution uses 103 kJ/orbit to obtain the required throughput. A compromise would be the solution marked by the blue plus sign (+) using a 4.58 dBi antenna. This solution achieves a similar latency with a pointing duty-cycle of 10.88% similar to a reference mission with a single ground station, however using 90 kJ/orbit to obtain the required throughput.

Figure 9.4 shows the range graph, power and energy usage, and pointing angles during the three orbits for this solution. The range graph fig. 9.4a shows that the longer passes are used where-ever possible and the gaps in between are filled with shorter passes. The power and energy usage fig. 9.4b shows a peak transmitter power consumption of 27.58 W, at this peak the transmitter is providing a RF power of 36 dBm (4.00 W). On average, the power consumption is close to 20 W, which results in an almost constant energy draw over time with a transmission duty cycle of 72.6%. The bandwidth used in the solution is 5.0 MHz with a maximum MODCOD of 8-phase-shift keying (PSK) 8/10 FEC, giving a maximum data-rate of 9.88 Mbit/s, similar to the Hiber satellite (achieving 8 Mbps [185]). The pointing angles (bottom in fig. 9.4) show that the antenna is pointed up to 5 degrees from the zenith direction at the beginning and ends of some passes.

The antenna gain of 4.81 dBi can be achieved with a patch antenna (array) similar to the design on the Dove satellites (achieving 15 dBi on X-band [2]). The parametric models developed from literature in chapter 8 and chapter 3 do not extend to these low antenna gains. Therefore an antenna volume of 0.1 U and mass of 100 grams is assumed which is assumed to be representative considering the Dove example. The mass and volume of the solution is dominated by that of the transmitter, which the parametric models estimated at 0.98 U and 1.13 kg for this solution.

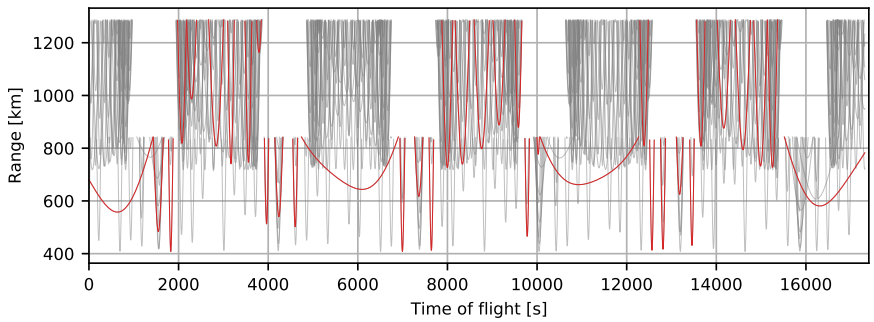


(a) Range and selected contact opportunities

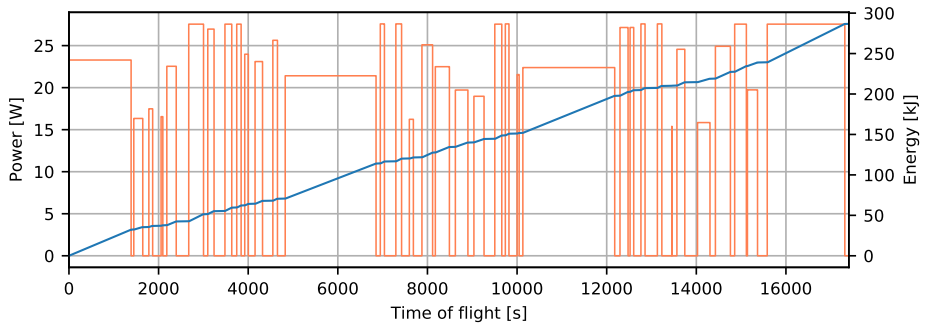


(b) Power and energy consumption

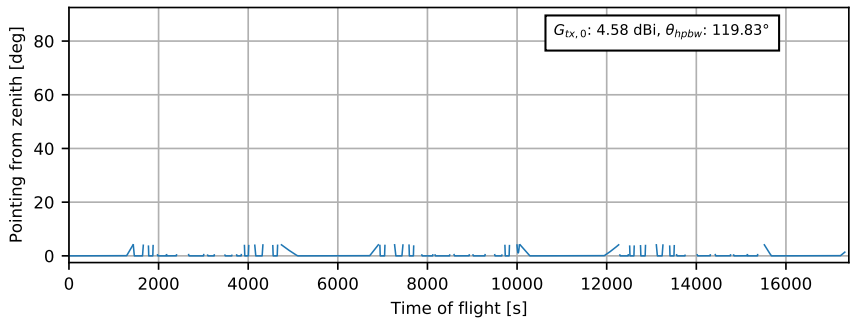


(c) Pointing angle from zenith

Figure 9.4: Range plot with the selected passes highlighted (top), power and energy (middle) and pointing angles (bottom) for the selected solution in the IoT/M2M case with the Telesat constellation.

The solution from this design optimization meets the throughput, volume and mass requirements for the IoT/M2M mission. Its latency is bound by the coverage of the constellation to a maximum of about four minutes. The selected solution uses a low antenna gain to minimize pointing, resulting into a pointing duty cycle similar to that of a single ground-station direct link. The solution however uses a high transmission duty cycle to minimize latency and while achieving the targetted 2.5 GByte per orbit it does so with almost six times the targetted energy consumption. A data-relay downlink with the Telesat constellation therefore cannot provide a reduced latency while also providing an increase in overall throughput. There is however potential to achieve the reduced latency if the throughput is not increased. A first order estimate would predict a throughput in the same order of magnitude as the reference mission, i.e. reducing the throughput by a factor of six to meet the energy requirement. This could either be done by reducing the bandwidth or by reducing the power and using the lower order MODCODs or a combination of both. This option should be evaluated with a new design optimization using lower target values.

## 9.4. O3b - Earth Observation mission

The optimization for the data-relay downlink on the EO mission using the O3b constellation was run using the NSGA-III algorithm ($n_{dirs} = 300$, $n_{pop} = 300$, $n_{offspring} = 75$, $n_{gen} = 3000$). Figure 9.5 shows the solutions obtained against the three objectives (throughput, energy and pointing) of this optimization. The targetted performance is marked as a red cross (x), being a throughput of greater or equal to 120 GByte/orbit, an energy consumption of less than 41 kJ/orbit and zero pointing. All solutions shown in fig. 9.5 have a maximum latency of 1.5 hours or less.

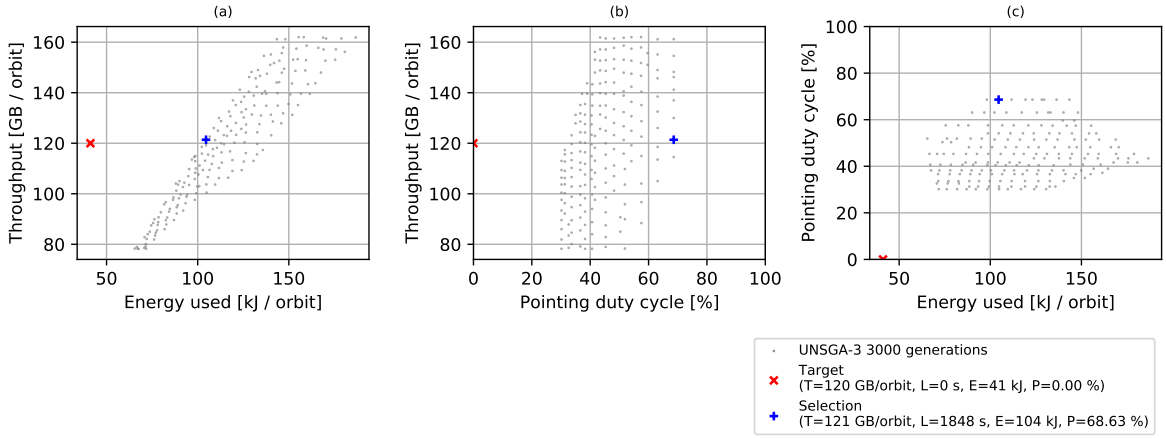


Figure 9.5: Optimization result for the IoT/M2M use-case with the Telesat constellation

The set of optimal solutions for throughput-energy (fig. 9.5-a) show that the targetted 120 GB/orbit cannot be achieved for the allowable energy per orbit. The closest solution, marked with a blue plus (+), achieves the targetted throughput using 104 kJ/orbit. The longer distances in this LEO-to-MEO data-relay determines the throughput-energy Pareto front. A higher transmit power may be used, resulting into a higher throughput but also higher energy consumption (moving up the Pareto front in fig. 9.5-a). However, the throughput-energy front will not move further to the left unless the bandwidth is increased (beyond 300 MHz) or a higher antenna gain is used (beyond 50 dBi). A 50 dBi antenna gain can be achieved with the current state-of-the-art deployable parabolic mesh reflectors (see section 3.2.3). Achieving a higher gain would require a larger area reflector which becomes increasingly difficult to stow in a small volume and deploy. Therefore the better option would be to increase the transmission bandwidth. As the theoretical maximum uplink bandwidth of the O3b constellation is limited to 300 MHz (see section 4.3), the only option for doing so would be to utilize a dual polarization solution like in the Dove satellite [2]. This effectively doubles the bandwidth and data-rate from what is achieved in fig. 9.5 but will at most half the energy consumption. It is therefore unlikely that the 120 GB/orbit will be met within the energy requirement, but a throughput of 100 GB/orbit for the targetted energy consumption would be possible.

The pointing duty cycle for the selected solution is 68.63%. This can be reduced to roughly 30% (moving left in fig. 9.5-b) while maintaining the the same throughput at the cost of increased energy (moving right in fig. 9.5-a and bottom-right in fig. 9.5-c). As shown in fig. 9.6c the satellite is pointing its 50.0 dBi antenna throughout the passes, resulting in an equal transmission duty cycle. The maximum pointing angles are relatively high at 65° from zenith due to the large operating field-of-view of the O3b mPOWER satellites. For this case reducing the pointing duty cycle does not result in a lower required antenna gain. Instead, for the lower pointing solutions in fig. 9.5, different contact opportunities are used that are shorter and require less pointing, but the high gain antenna is still required to close the link.

As shown in fig. 9.6b, the peak power consumption of the transmitter is 41.41 W, at this peak the transmitter is providing a RF power of 38 dBm (6.31 W). The used bandwidth is 300.0 MHz using a maximum MODCOD of QPSK-8/9 FEC. From the parametric models the expected volume and mass of the transmitter are 0.78 U and 0.92 kg. The parabolic mesh antennas outperform the trend that was used to setup the volume and mass equations in the parametric models (see fig. 3.11). Therefore the volume and mass of the KaTENna are used as a reference at 3 U and 2.5 kg. Resulting in an overall volume and mass of 3.78 U and 3.42 kg, thereby not meeting the volume and mass requirements for

this mission.

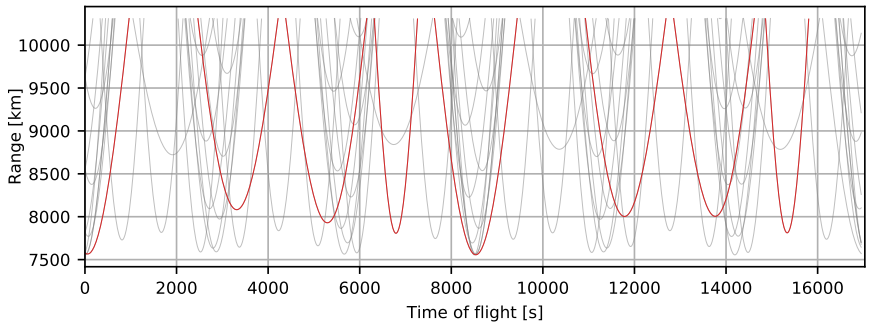


(a) Range and selected contact opportunities

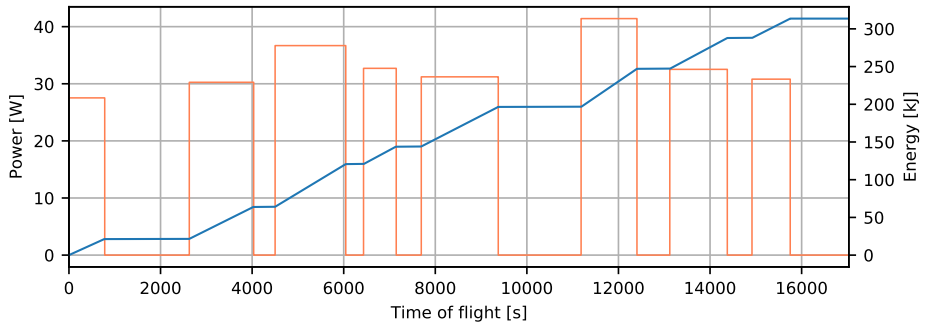


(b) Power and energy consumption

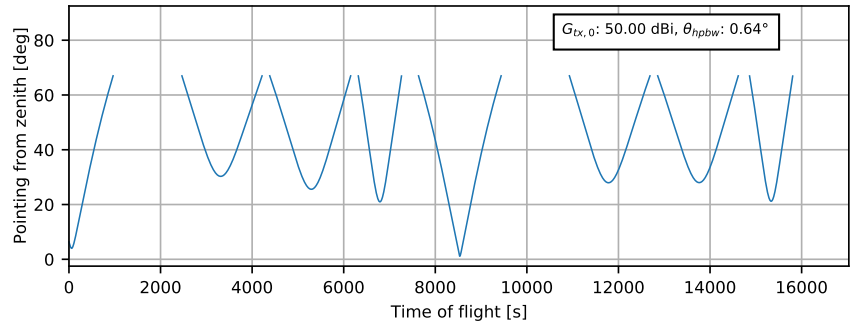


(c) Pointing angle from zenith

Figure 9.6: Range plot with the selected passes highlighted (top), power and energy (middle) and pointing angles (bottom) for the selected solution in the EO case with the O3b constellation.

## 9.5. O3b - IoT/M2M mission

The optimization for the data-relay downlink on the IoT/M2M mission using the O3b constellation was run using the NSGA-III algorithm ($n_{dirs} = 300$, $n_{pop} = 300$, $n_{offspring} = 75$, $n_{gen} = 4500$). Figure 9.5 shows the solutions obtained against the three objectives (throughput, energy and pointing) of this optimization. The targetted performance is marked as a red cross (x), being a maximum latency less or equal to 60 seconds, an energy consumption of less than 16.82 kJ/orbit and zero pointing. All solutions shown in fig. 9.7 achieve a throughput of 2.5 GByte/orbit or more. The set of optimal solutions shows a lower bound on the maximum latency of around 540 seconds, or 9 minutes (fig. 9.7-a,b). This lower bound is due to non-continuous coverage in the orbit and is equal to the longest gap experienced. This minimum latency can be achieved from an energy consumption of about 70 kJ/orbit and higher.

The minimum energy minimum latency solution is highlighted in fig. 9.7 with a blue plus (+). This solution uses a 50 dBi antenna, and like in the previous section, this would require a parabolic mesh

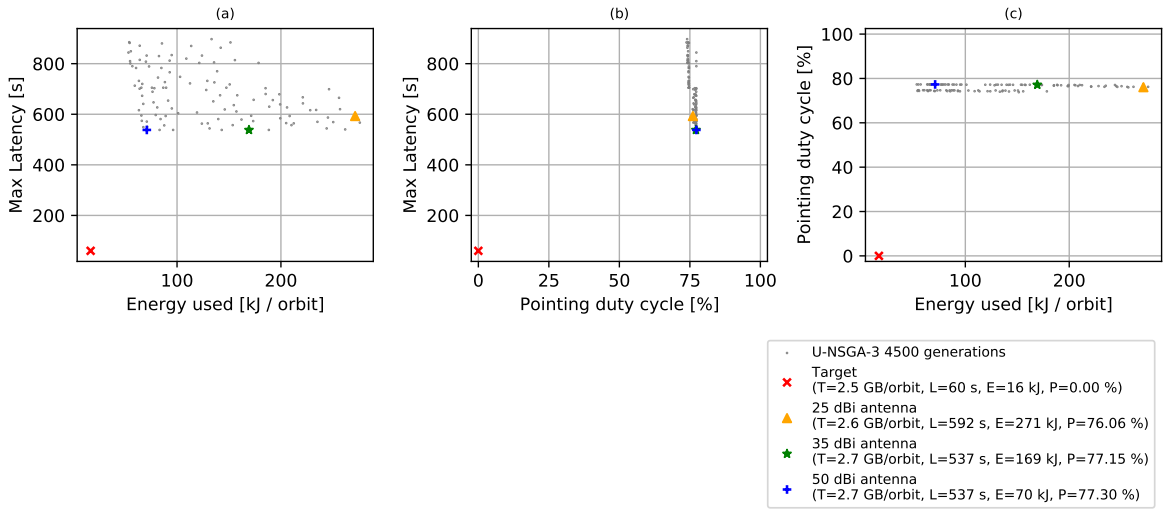


Figure 9.7: Optimization result for the IoT/M2M use-case with the O3b mPOWER constellation

reflector antenna having a large volume and mass footprint. Two additional solutions are highlighted. A solution with a 35 dBi antenna marked with an green star (★) that is achievable with reflect-array antennas, and a solution with a 25 dBi antenna marked with an orange triangle (▲) that is achievable with horn antennas. Reducing the antenna gain results into a higher energy consumption and a higher peak transmitter power dissipation of 65 W. The pointing duty cycle does not decrease with a lower gain antenna with a wider beamwidth because to the large range from LEO-to-MEO.

Figure 9.8 shows the range graph, power and energy usage, and pointing angles during the three orbits for this solution. There are two combinations of contact opportunities selections that result into a low latency, this can be seen by the solutions lying on two discrete lines in fig. 9.7-b and fig. 9.7-c. Figure 9.8a shows the selection using 11 passes for the minimum energy minimum latency solution. If the contact opportunities could be used partially, the optimization would be able to achieve a zero latency solution as the coverage by the O3b constellation is continuous, however with overlapping passes. Figure 9.8b shows the power dissipation and energy consumption over time for the solution. The maximum power dissipation is 18.39 W while providing a RF power of 30 dBm (1.00 W). The minimum dissipation however is determined by the minimum dissipation in the modulator parametric model from fig. 8.20a of 14.97 W. This shows that the solution is using all passes with a low-data rate to minimize the transmission power required to close the link. The bandwidth used in the solution is 2.0 MHz, however it uses the maximum MODCOD in the DVB-S2 protocol of 32-APSK 9/10 FEC to achieve the targetted throughput, giving a maximum data-rate of 6.59 Mbit/s. The resulting data-rates and power consumptions are similar to that of the Hiber satellite (achieving 8 Mbps [185] at 20 W).

This example shows the importance of a low modulator power dissipation for IoT/M2M missions using the data-relay downlink concept. As a high transmission duty cycle is used, to spread out the throughput over the orbit the power consumption of the modulator becomes the driving parameter in the energy consumption of the downlink. This results into the minimum energy minimum latency Pareto front visible in fig. 9.7-a, that only can be reduced with a lower modulator power consumption. Similar to the previous section the volume and mass of the KaTENna are used as a reference at 3 U and 2.5 kg. From the parametric models the expected volume and mass of the transmitter are 0.123 U and 0.23 kg. Resulting in an overall volume and mass of 3.12 U and 2.8 kg, thereby not meeting the volume and mass requirements for this mission.

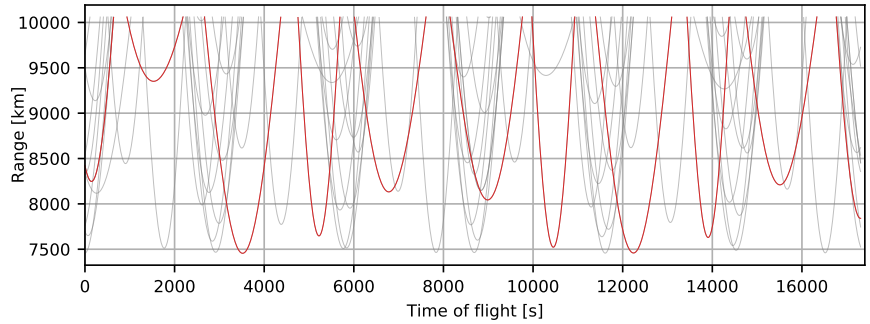


(a) Range and selected contact opportunities

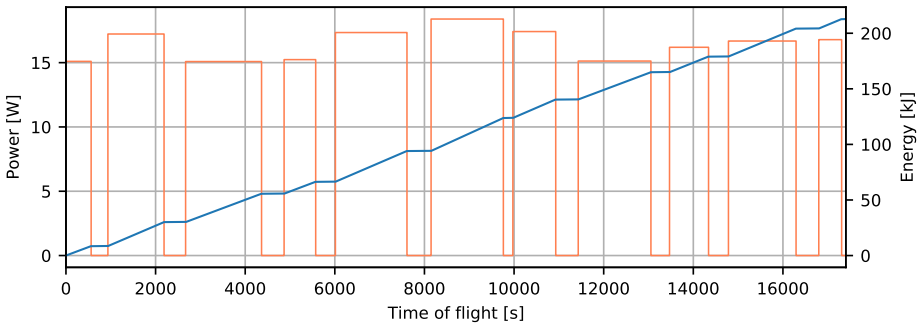


(b) Power and energy consumption

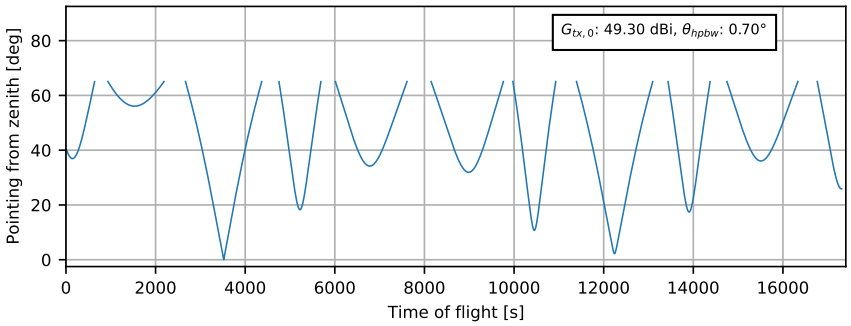


(c) Pointing angle from zenith

Figure 9.8: Range plot with the selected passes highlighted (top), power and energy (middle) and pointing angles (bottom) for the selected solution in the IoT/M2M case with the O3b constellation.

## 9.6. Verification

Verification of the results presented in this chapter was done by comparing the performances predicted by the optimization and the resulting architectures with the current state-of-the-art in small satellite communication technologies. The optimization targets and design limits were set to be representative to reference nano satellite missions, by doing all optimization results remain within the bounds of what is currently possible while still showing the improvement that can be made with the data-relay downlink. In addition, for each of the four cases evaluated in section 9.2 to section 9.5, the components of the optimized design were compared with existing technologies from COTS components or described in literature in terms of transmitter output power, data rate and antenna gain. It was found that designs were either already existing, i.e. for the antennas, or already exist with close matching performance, i.e. for the transmitters. This shows that the designs obtained with the data-relay optimization framework are within the current capabilities of small satellites.

## 9.7. Overview and recommendations

In this chapter four scenarios were analysed using the data-relay optimization framework, a EO use-case and a IoT/M2M use case for two target constellations, the Telesat LEO constellation and the O3b mPOWER MEO constellation. Each scenario was considered individually over a mission period of three orbits. Table 9.4 shows a summary of the optimization results obtained for the EO use-case. In this use-case the obtained throughput per orbit is of importance as with the increase in payload performances comes a higher data generation. The mission return can be increased if more data can be downlinked. The state-of-the-art reference mission for this use-case is the 3U Dove EO satellite by Planet that currently has the highest performing downlink system on a small satellite [2]. This system achieves 80 GB per orbit, consuming roughly 41 kJ during a single pass with a polar ground station while dissipating a peak of 50 W in the transmitter. The data-relay optimization showed that the target throughput of 120 GB/orbit is achievable with both constellations. For the Telesat constellation this throughput can be achieved using the same energy consumption per orbit as the Dove satellites. The optimization showed that higher throughputs up to 160 GB/orbit are obtainable within the current state-of-the-art technologies. Because multiple contact opportunities per orbit may be used, the overall latency may be reduced, achieving contact with the satellites every 50 minutes. The Telesat design can use an antenna gain of 36 dBi and a total power dissipation 40 W to obtain the 120 GB/orbit. A reflect array antenna like the Ka-band one of the ISARA mission [133] would be a perfect fit for this mission. This Integrated Solar Array Reflect Array combines the surface area of the deployable solar array with that of the reflect antenna array, allowing for a high gain antenna on a 3U nano-satellite. By combining the structural design for both the occupied volume shared between the two, and if done effectively the obtained design would meet all requirements that were set up to meet future needs of EO small satellite constellations.

Table 9.4: EO use-case data-relay downlink design optimization summary

| | Requirement | Telesat | O3b | Reference mission |
|---|---|---|---|---|
| *Requirements/Compliance* | | | | |
| Throughput per orbit | ≥ 120 GB | 120.0 GB | 121.0 GB | 80 GB |
| Maximum latency | ≤ 1.5 h | 50 m | 30 m | 1.39 h |
| Energy consumption per orbit | ≤ 41 kJ | 41 kJ | 104 kJ | 41 kJ |
| *data-relay downlink specifications* | | | | |
| Power | ≤ 50 W | 39.79 W | 41.41 W | 50 W |
| Volume | fits 1U | 1.34 U | 3.78 U | 1 U |
| Mass | ≤ 2 kg | 2 kg | 3.42 kg | 2 kg |
| Bandwidth | | 300 MHz | 300 MHz | 2x300 MHz (dual pol) |
| Highest DVB-S2 MODCOD | | 32-APSK 8/9 FEC | QPSK 8/9 FEC | 32-APSK 8/9 FEC |
| Antenna boresight gain | | 36 dBi | 50 dBi | 15 dBi |
| Transmit duty cycle | | 17.90% | 68.63% | 14.5% |
| Pointing limit | | 17.90% | 68.63% | 14.5% |

The same use-case with the O3b mPOWER MEO constellation can achieve the required throughput only for 2.5 times the energy consumption per orbit. It also requires a high gain antenna of 50 dBi, which is achievable with state-of-the-art mesh parabolic reflect antenna however it significantly impacts the volume (3.78 U) and mass (3.42 kg). This would not fit a 3U nano-satellite and would take up a significant part of the volume and mass of a 6U nano-satellite. The LEO-to-MEO data-relay concept is therefore unlikely to be beneficial for the EO use-case.

Table 9.5 shows a summary of the optimization results obtained for the IoT/M2M use-case. In this use-case the maximum latency experienced for data collected from sensors on the ground is of importance. The biggest contributor in this latency for the LEO-to-NGSO use-case is the time spend waiting for the small satellite to come in view of a NGSO constellation satellite. This time can be reduced by careful selection of the contact opportunities and the target maximum latency was set to 60 seconds. At the same time a higher throughput per orbit to the current state-of-the-art is desired as the needs for IoT/M2M connectivity will grow. The reference satellite for this use-case is the Hiber

satellite [54] achieving 400 MB/orbit and achieving contact every 1.4 hours. A throughput requirement of 2.5 GB/orbit is set for the IoT/M2M use-case.

The Telesat constellation can achieve an upper limit on the maximum latency of 5 minutes. This upper latency is determined by the gaps in the coverage of the Telesat constellation. The design leverages a low-gain antenna to minimize the pointing required to less than 11% of the orbit, this however comes at the cost of a slightly higher than targetted power dissipation and energy consumption. The antenna used in the design has a gain of 4.81 dBi, which can be achieved with a patch antenna design well fitting the volume and mass budget of the satellite. The design uses a low bandwidth of 5 MHz with a moderate modulation and coding scheme to spread out the data transmission across the contact opportunities, thereby using a high transmission duty cycle.

The design with the O3b constellation achieves a latency of an upper limit on the maximum latency of 9 minutes. The O3b constellation provides a continuous coverage of the orbit, if the optimization framework allowed for partial passes to be used the latency could be zero. The design with the O3b constellation uses a high gain antenna of 47.35 dBi which increases the size (3.12 U) and mass footprint (2.80 kg) of the solution, making it only applicable for 6U satellites or bigger. The design uses a low transmission power and bandwidth to spread out the data transmission across the contact opportunities however with the high-gain antenna the pointing duty cycle is 77.50% of the orbit.

Table 9.5: IoT/M2M use-case data-relay downlink design optimization summary

| | Requirement | Telesat | O3b | Reference mission |
|---|---|---|---|---|
| *Requirements/Compliance* | | | | |
| Throughput per orbit | ≥ 2.5 GB | 2.5 GB | 2.7 GB | 400 MB |
| Maximum latency | ≤ 60 s | 285 s | 537 s | 1.39 h |
| Energy consumption per orbit | ≤ 16 kJ | 90 kJ | 70 kJ | 16.8 kJ |
| *data-relay downlink specifications* | | | | |
| Power | ≤ 20 W | 27.58 W | 18.39 W | 20 W |
| Volume | fits 1U | 0.98 U | 3.12 U | fits 1U |
| Mass | ≤ 2 kg | 1.13 kg | 2.80 kg | unknown |
| Bandwidth | | 5 MHz | 2.0 MHz | 8 MHz |
| Highest DVB-S2 MODCOD | | 8-PSK 9/10 FEC | 32-APSK 9/10 FEC | OQPSK |
| Antenna boresight gain | | 4.81 dBi | 47.35 dBi | unkown |
| Transmit duty cycle | | 72.6% | 77.30% | 14.5% |
| Pointing limit | | 10.88% | 77.30% | 14.5% |

## Recommendations

The data-relay optimization framework showed to produce useful system level designs for the data-relay downlink for the four scenarios discussed. Besides providing an estimate for the communication system performance, size, mass and power, the framework can also estimate the constraints on the small satellite platform to support such a data-relay downlink. The power and energy graphs of figs. 9.2b, 9.4b, 9.6b and 9.8b can be used to size the power system of the satellite and similarly figs. 9.2c, 9.4c, 9.6c and 9.8c provides the requirements on the attitude control system or antenna steering mechanism if used. Vice-versa models for energy generation and consumption, or satellite attitude control can be used to refine the results of the design optimization. As some of the designs generated require a high transmission duty cycle, where the transmitter is on for most of the orbit. This should be well matched with the power generated on the satellite. An energy model that determines the energy generation and storage over time can be combined with the optimization to include an operational constraint to not deplete the batteries. If taken a step further the sizing of the solar panels and batteries can be included in the optimization to create a satellite covering optimization model. Refinements including satellite level design considerations are suggested for future work.

Several model improvements to underlying models of the data-relay optimization framework can be made. First, a data generation over time model can be implemented. Such a model could for example depend on the user demand, i.e. more over land/populated areas for the IoT/M2M missions, as is done in the paper by Del Portillo et. al. [218]. Similarly for the EO missions some ground locations could be more interesting than others, creating a varying amount of data from the payload over time. Including such a model would allow for the sizing of the storage on board the satellite and provide a

more accurate representation of latency in the system if all collected data cannot be downlinked in the next contact opportunity. Defining such demand models is recommended for future work.

Another aspect that can be improved is the models used for the power dissipation of the modulator. As seen by the IoT/M2M use-case with the O3b constellation, in a low-throughput scenario the energy consumption is dominated by the modulator power consumption which currently has a 15 W consumption minimum and therefore will never meet the target energy consumption per orbit when the data transmission is spread out over the orbit. Refined power consumption models should be considered as well as low signal-to-noise-ratio modulation schemes such as those in the DVB-S2X standards, especially to make the LEO-to-MEO concept feasible.

Several modifications are suggested for the operation of the optimization algorithm. The current framework cannot make good use of the contact opportunities with long overlapping passes, causing a non-continuous operation in for example the IoT/M2M use-case with the O3b constellation. Different algorithms should be considered to allow for partial pass usage. In addition, it was found that the pointing objective in some cases was not sufficient to show the trade-off for different antenna gain solutions, often favouring the highest allowable antenna gain solution. This can be avoided by adding an alternative objective that considers antenna mass or size. This would however require improvement of those models with more data from literature or using an physics related model. A first option that could be tried is the antenna aperture gain relation, i.e. described in Balanis [189, eq. 4-76].

Finally, a note should be made to bandwidth usage of the solutions. For NGSO operators, user bandwidth is the primary billable resource and therefore using bandwidth would cost money. The return link for the NGSO operator would only be used by ground users to upload data which is used to a lesser extend than downloading through the forward link. However, small satellites using a full uplink user bandwidth of several hundreds of megahertz will likely impact the mission costs.

# 10

# Conclusions and recommendations

Technological advancements and miniaturization of space hardware now allows small satellites, having a mass below 500 kg, to perform missions that used to only suite larger class satellites. However, low downlink data rates are limiting the scientific and commercial return for small satellite missions. As the payload capabilities and mission complexity of the small satellites increases, higher payload downlink capability is required [1], [2] creating the need for higher performing downlink architectures.

This thesis investigated a novel downlink communication architecture for Earth orbiting small satellites in which data is relayed through NGSO (mega-)constellations. Companies such as Telesat, SpaceX, OneWeb and O3b are building constellations aimed to provide broadband connectivity from space [3]. Some of their constellation proposals are called mega-constellations by the large number of satellites used to provide global coverage. The satellites in these NGSO (mega-) constellations have their orbits, field-of-views, spot beams and frequency re-use schemes optimized for ground coverage. This leaves gaps in LEO where a small satellite is not in view of the constellation satellite. This results in interesting challenges for the proposed LEO-to-NGSO data-relay downlink system, requiring consideration of the orbital dynamics between the satellites as well as the the design trade-offs for the communication system in order to evaluate the concept and estimate its performance. This work was performed in this thesis, assessing the feasibility of the communication architecture. Two concept small satellite missions were defined and a design optimization was performed on two target NGSO (mega-)constellations.

The source code of the data-relay orbital simulator and data-relay optimization framework that were developed in this work are available on Github [26], [204]. Part of the work performed during this thesis was presented at the 2019 International Astronautical Congress [222]. This paper is added to this report in appendix A.

## 10.1. Thesis outcomes

**Constellations of small satellites for Earth Observation (EO) and Internet-of-Things (IoT)/Machine-to-Machine (M2M) communication will drive the need for high performance downlink solutions from LEO**

The first research question of this thesis was set-up to identify which small satellite missions would benefit from the proposed NGSO data-relay downlink. A literature study into the small satellite market showed a rapid increase in missions using constellations of small satellites for EO, RS and IoT/M2M. In these categories, the EO missions are producing a significant amount of data in LEO up to 80 GByte per orbit per satellite [2] with constellations growing beyond 100 satellites. Recent publications show that the payload downlink systems on these small satellites are outperforming those on larger class satellites by size, mass and throughput. It is expected that the need will grow for higher payload downlink performance for EO and IoT/M2M satellites. The NGSO data-relay downlink investigated in this work provides a solution to this need by offering a high contact time with the satellites allowing higher throughput and lower latency.

**Higher altitude LEO mega-constellations or MEO constellations offer the best opportunities for relaying data from small satellites in LEO.**

The second research question of this thesis aimed to answer which NGSO (mega-)constellations would be suitable for relaying data from small satellites in LEO. The satellites in NGSO (mega-) constellations operate in LEO region (around 500 to 1500 km altitude) or MEO region (around 8000 to 14000 km). A visibility and contact time analysis was performed for two typical small satellite orbits, a satellite in a 400 km, 51.6° inclined orbit and a satellite in a 500 km, 97.5° inclined orbit, for six LEO mega-constellations and two MEO constellations. It was found that the higher altitude LEO mega-constellations, those with orbital shells at 1500 km altitude, offered coverage with long duration inter-satellite passes. The LEO mega-constellations with only lower orbital shells around 500 km altitude, offered some coverage at the 400 km altitude orbit, however with contact opportunities of only short durations making the data-relay link impractical. The MEO constellations offered the longest contact opportunities reaching up to 50 minutes of continuous coverage.

From the eight analysed constellations, two were selected for further investigation. The Telesat constellation in LEO was chosen because its satellites in 1015 km and 1325 km shells offer a good coverage with long duration contact opportunities to relay data. The O3b mPOWER constellation was chosen as the best MEO constellation. It provides an interesting trade-off for the data-relay system. The constellation provides excellent coverage for small satellites in LEO, however its satellites being at an altitude of 8062 km has consequences on the link budgets for communications.

**Vectorized orbital simulation and multi-objective genetic algorithms allow for a design optimization of a complex data-relay communication system through mega-constellations while considering all important parameters.**

The third research question was related to designing a framework that could analyse data-relay communication links in a complex dynamic system and use optimization algorithms to optimize the design of a data-relay downlink for a small satellite mission. This work showed that a vectorized and just-in-time approach to orbital simulation of (mega-)constellations can be used to analyse the positions of the satellites for a small time step, i.e. one second, over a long simulation period, i.e. 7 days. This approach allows for an effective method of finding the line-of-sight satellite pairs for which an inter-satellite link (or data-relay link) could be established. This capability on-itself allows for the ability to perform quantitative analysis on the contact opportunities in a LEO-to-NGSO data-relay architecture using metrics such as spatial coverage, visible satellites over time or contact and gap distributions.

However, to estimate the actual performance of a data-relay downlink additional aspects need to be considered including communication link budgets and communication component models. Because of the complex dynamics between the orbit of a LEO satellite and those of NGSO satellites, resulting in a many contact opportunities to design the system around this becomes a excessive task to perform manually. This tasks becomes even more excessive if the aim is to show different design trade-offs. This work showed how a multi-objective genetic algorithm optimization can be used up to perform a design optimization of a communications system for a small satellite. The optimization framework build in this work considers all components of the small satellite payload downlink system including the modulator, modulation and coding scheme, power amplifier and the antenna. The optimization framework is also able to show the requirements on other satellite subsystems to support a data-relay downlink such as those on the power system and the attitude determination and control system.

**A LEO-to-LEO data-relay downlink with mega-constellations can offer EO small satellite missions increased throughput per orbit with an equal size, weight and power performance to the current state-of-the-art.**

The fourth research question was set up to find the performances and design characteristics of a NGSO data-relay downlink for a small satellites. For the EO use-case it was found that an LEO-to-LEO data-relay downlink with the Telesat constellation would offer a higher throughput per orbit. The current state-of-the-art small satellite missions can achieve throughputs of roughly 80 GB per orbit using one polar ground station [2]. The design optimization showed that with the Telesat constellation a throughput of 120 GB per orbit can be achieved while using the amount of energy per orbit as the state-of-the-art.

The design for this mission would use a DVB-S2 modulator with three carriers each of 96 MHz bandwidth aggregated to an overall transmission bandwidth of 300 MHz. Using a 32-APSK modulation with 9/10 FEC this would result into a maximum data-rate of 950.4 Mbit/s. The power amplifier of the transmitter would provide a peak output power of 37 dB (5.01 W) resulting into an overall estimated power dissipation for the transmitter of 46.55 W. The design uses a reflect array antenna providing a gain of 36 dBi similar to the ISARA mission [133]. This reflect array can be combined with the (back of) the deployable solar array. The overall solution would use a volume of roughly 1.34 U and have a mass below 2 kg.

**A LEO-to-LEO data-relay downlink with mega-constellations can offer IoT/M2M small satellite missions increased in throughput per orbit and sub-5 minute latency with an similar size, weight and power performance to the current state-of-the-art.**

For the IoT/M2M use-case it was found that an LEO-to-LEO data-relay downlink with the Telesat constellation would offer a lower latency and a six times higher throughput per orbit. Current IoT/M2M small satellite missions use a store-and-forward scheme where the latency, defined as the moment from which by sensors on the ground to the moment at which this data is available to the user, is primarily determined by the revisit time and the number of ground stations. With one ground station the upper bound on the latency would be one orbit, roughly 1.5 hours for a typical orbit of such a mission. The design optimization showed that this latency can be reduced to 5 minutes with the proposed data-relay downlink architecture. The optimization was also set up to reach a higher throughput than the current state-of-the-art missions to allow for future growth in IoT/M2M connectivity. A throughput of 2.5 GB per orbit can be achieved however at the costs of a higher energy consumption per orbit.

The design for this mission would also use a DVB-S2 modulator using a transmission bandwidth of 5 MHz. Using a 8-PSK modulation with 9/10 FEC this would result into a maximum data-rate of 9.88 Mbit/s. The power amplifier of the transmitter would provide a peak output power of 36 dB (4.00 W) resulting into an overall estimated power dissipation for the transmitter of 27.85. This power consumption is similar to the transmitter used on the Hiber nano satellite [54], [185]. The increase in energy consumption results from the higher transmission duty cycle of 72.6% to achieve a higher contact time with the satellite and reduce the latency. The solution uses a low gain antenna of 4.58 dBi to minimize the need for pointing to the data-relay satellites, achieving a pointing duty cycle of only 10.88 %, whereas a single ground station per orbit would result into 14.5 %.

## 10.2. Recommendations

### Incorporate recent work on mega-constellation propagation

Simulating the orbital dynamics of large constellations is an active topic of research. During this project work by Juan Luis Cano Rodríguez under the OpenSatCom initiative [201] benchmarked several implementations of the Simplified General Perturbations 4 (SGP4) propagator for cases like many-satellites-many-dates using parallel multi-core processing. The SGP4 model allows for the use of two-line element sets and these implementations would be an interesting alternative to the vectorized implementation of this work. Using these implementations is recommended for future work potentially as a replacement for the vectorized orbital propagator as an SGP4 propagator would allow for a more accurate representation of the satellite orbits.

### Investigate into on demand models and constraints

In its current state the data-relay optimization framework does not make any assumptions on how and when data is generated on-board of the small satellite. Depending on the mission the payloads may generate more data over land or highly populated area resulting into a non-constant rate of generation. Specific data downlink demand models should be investigated to create a model that predicts payload data generation over time. Such a model could for example depend on the user demand, i.e. more over land/populated areas for the IoT/M2M missions, as is done in the paper by Del Portillo et. al. [218] and incorporating them into a design optimization as is done in the works of C. Jilla [70], [223], [224]. Similarly for the EO missions some ground locations could be more interesting than others. Including such a model would allow for the sizing of the storage on board the satellite and provide a more accurate representation of latency in the system if all collected data cannot be downlinked in the

next contact opportunity. Expanding the data-relay optimization framework with such demand models is recommended for future work.

### Expand on operational models and constraints

Besides providing an estimate for the communication system performance, size, mass and power, the data-relay optimization framework can also estimate the constraints on the small satellite platform to support a data-relay downlink in terms of power generation and attitude control. Future work can expand this further and effectively step out of the communications (sub-)system boundary and include the design considerations of the power sub-system and attitude control and determination sub-system into the optimization. This would for example allow for determination of the required energy generation and storage over time depending on the satellite orbit and provide a means to solar panel and battery sizing on the small satellite. Similarly, together with the refined demand models of the previous paragraph, the satellite operations can be optimized to maximize mission return.

### Refine component parametric models

In its current state the data-relay optimization framework provides an end-to-end framework to optimize the (top-level) design parameters of a data-relay downlink downlink. However, some of these models may be improved in further work. The model used to estimate the power consumption of the modulator based on performance from literature should be revised as in its current state it dominates the power consumption for low data-rate high contact time optimization. Similarly the model used to estimate the size of the antenna, also based on performance from literature, does not well capture particularly low or high gain designs. It does also not capture advantages in size reduction when moving to higher frequencies. For both components, a physics related model should be sought allowing for a better estimate on size, weight and power consumptions over a broader range allowing for better capturing of trade-offs in the optimization.

### Further analyse in low-rate/low-SNR modulation schemes

An area that can currently not be well explored with the data-relay optimization framework is using low data-rate communication links however with a high contact time, i.e. continuous throughout the orbit. Several limitations in the current framework made this difficult. As mentioned in the previous paragraph, the model used for modulator power consumption becomes dominating for low rate solutions. Therefore creating a high contact time using a high number of contact opportunities and spreading out the transmission will not meet a low enough energy consumption. In addition to this change, different modulation schemes should be considered, such as the very low signal-to-noise schemes in the DVB-S2X standard. As well as using partial contact opportunity to utilize the continuous coverage provided by MEO constellations. Doing so might show that a LEO-to-MEO data-relay would be feasible without spending a lot of energy to close the link for the larger distance. Refining the models to show the trade-offs in such a solution and re-analysing the LEO-to-MEO data-relay is therefore recommended for future work.

### VLEO orbits, bi-directional links and spectrum costs

Finally there are several details and use-cases that could be explored in future work. It was shown that the LEO mega-constellations having only shells around 500 km would not provide sufficient coverage for typical small satellites in LEO. However, with the gaining interest in VLEO missions the concept with these constellations would become possible as it was shown that there would be some coverage from these constellations around 400 km altitude.

This work only considered the communication system as a uni-directional data-relay downlink. It is likely that some bi-directionality is required to perform the link negotiation with the NGSO satellites. Future work could explore how such a link would look like while remaining compatible with the NGSO constellations.

Lastly, this work did not consider and spectral or bandwidth costs, rights and/or interference from other users. Future work should consider these aspects in collaboration with one of the current NGSO operators to explore the economical feasibility of the concept.

# Glossary

**apsis line** The line between the periapsis and the apoapsis. 160

**argument of perigee** One of the classical orbital elements describing the angle between the ascending node and the perigee of the orbit 58, 163

**classical orbital element** The classical orbital elements are six parameters ($a$, $e$, $i$, $\Omega$, $\omega$, $\theta$) that describe the position of an object in a Keplarian orbit. 55, 58, 159, 160

**contact opportunity** A period of time in which two communication capable objects (i.e. a ground-station and a satellite, or a pair of satellites) are in each others field-of-view and have a line-of-sight. v, 4, 7, 9, 45, 47, 48, 51–55, 71–74, 78, 100, 101, 103–105, 108–110, 112–116, 119–121, 125–127, 131, 135–141, 144–154, 156, 158

**coverage** The percentage of time or per orbit in which communication is available with a ground station or satellite. 9

**cross-over** The process of mating two or more parents into new individuals for the next generation 107

**data-relay downlink** A transmitting comunication system that is used to downlink satellite data by relaying it first to another satellite. v, vi, 4, 5, 7, 9–11, 13, 14, 19, 43–49, 51, 77, 78, 100, 101, 103–106, 133–135, 138–143, 146–153, 155–158

**data-relay optimization framework** The optimization framework for optimizing data-relay links to NGSO (mega-)constellations v, 74, 103–105, 139, 140, 151–153, 155, 157, 158

**data-relay orbital simulator** The purpose build orbital simulator for simulation of data-relay opportunities to NGSO (mega-)constellations 51–58, 60, 64, 66–68, 71, 72, 74, 75, 77, 103, 105, 107, 141, 155

**design space** The space spanned by all combinations of the variables in the design vector 107

**design vector** A vector with variables that correspond to different design choices 107

**eccentric anomaly** An auxiallary angle relating to the true anomaly that aids in the computation of the true anomaly as function of the time-of-flight. 60, 61, 163

**eccentricity** One of the classical orbital elements describing how much an eliptical orbit varies from a circle. 58

**evaluation** The start of the evolution cycle in which the fitness of the individuals are determined 107

**fitness function** A function that is used to evaluate the fitness of an individual's scoring against one or multiple objectives. 107

**generation** The state of the population in-between the evolution cycle 107

**inclination** One of the classical orbital elements describing the angle of the orbit with respect to the (equatorial) plane. 58, 163

**individual** A sample in the design or objective space, characterized by a design vector, that survived after a generation or was created by a cross-over of other individuals in the previous generation 107

**Keplerian orbit** Two-body orbits that follow elliptical paths around the sun. The path of these orbits are described by the orbit equation eq. (6.9). 58, 59

**link parameter** The system level parameters such as range, location and velocity during an (inter-)satellite pass. 7

**mean anomaly** An auxillary angle that is monotonically increasing to the time-of-fligth and proportional to the orbital period. 59, 60, 163

**mean motion** The average angular speed of a body in orbit. 60

**mutation** A process appearing after cross-over that (slightly) alters the properties (design vector) of the individual 107

**objective function** A function that is used to evaluate the fitness of an individual's scoring against one or multiple objectives. 107

**Pareto front** A front of optimal solutions showing the optima towards all objectives. 107

**Pareto set** The set of solutions for which no other solutions exists that is better towards all objectives. 107

**perifocal frame** A coordinate system centered in the focal point of the orbit with $\hat{p}$ pointing in the direction of the periapsis, $\hat{q}$ parallel to the semilatus rectum and $\hat{w} = \hat{p} \times \hat{q}$. As $\hat{\vec{p}}$ and $\hat{q}$ span the orbital plane the $\hat{w}$ component in this frame is alway zero. 58–60, 62, 160

**population** The set of individuals that exist during a generation 107

**right ascension of the ascending node** One of the classical orbital elements describing the angle between the equinox and the ascending node of the orbit 58, 163

**selection** The process of selecting the individuals that are used to generate new individuals 107

**semi-major axis** One of the classical orbital elements equal to half the length of the longest axis of an elliptica orbit. 58, 163

**solution** An individual that does not violate any of the optimization constraints 107

**solution space** The space spanned by all possible solutions in the optimization. 107

**survival** The process of selecting the best fit individuals that survive to the next generation 107

**true anomaly** One of the classical orbital elements describing the angle between the orbital position in the perifocal frame and the apsis line. This quantity is key in describing the orbital position (and velocity) as function of time. 58–60, 62, 64, 159, 163

# Acronyms

**ACM** adaptive coding and modulation 24, 104, 116

**ADCS** attitude determination and control system 44

**APSK** amplitude and phase-shift keying vi, 116, 117, 122, 123, 145, 150, 157

**BEC** backwards error correction 22

**BER** bit-error rate 22

**BPSK** binary phase-shift keying 22

**CCSDS** Consultative Committee for Space Data Systems 116

**COTS** Commercially Of The Shelf 13, 14, 23, 24, 151

**CPU** central processing unit 20, 21

**ECI** Earth centred inertial 52

**ECIF** Earth centred inertial frame 52, 54, 62, 63, 68, 72, 73

**EDRS** European Data Relay Satellite System 31

**EIRP** effective isotropic radiated power 111

**EO** Earth Observation v, 2, 15, 16, 18, 19, 43, 47–50, 77, 131, 132, 141, 143–145, 148, 149, 152, 153, 155–157

**EPS** Electric Power System 44

**ETSI** European Telecommunications Standards Institute 116

**FCC** Federal Communications Commission 8, 33

**FEC** forwards error correction vi, 22, 113, 145, 146, 148, 150, 157

**FoV** field of view 9, 40, 52–54, 57, 68

**GEO** geostationary Earth orbit 3, 16, 18, 23, 31, 33, 38

**HUX** half-uniform cross-over 138, 139

**IF** intermediate frequency 21

**IoT** Internet-of-Things v, vi, 1, 2, 16–20, 43, 45–50, 77, 82, 131, 132, 141, 143, 146–155, 157

**ISL** intersatellite link 31

**LEO** low Earth orbit v, vi, 1–4, 14, 16, 18, 19, 27, 31–37, 39, 40, 54, 77–79, 82, 95, 100, 101, 140, 141, 148, 150, 152, 154–158

**LO** local oscillator 21

**M2M** Machine-to-Machine v, vi, 1, 2, 16–20, 43, 45–50, 77, 82, 131, 132, 141, 143, 146–155, 157

**MAEE** modulation-available energy efficiency 117–123

**MEO** medium Earth orbit v, vi, 2, 18, 23, 32, 33, 38–40, 78, 95, 100, 141, 148, 150, 152, 154, 156, 158

**MODCOD** modulation and coding 22, 23, 116, 119, 120, 124, 145–148, 150

**NGSO** non-geostationary orbit v, 2–5, 7–11, 13, 14, 16, 18, 19, 21, 27, 32, 33, 39–41, 43–54, 65, 67–69, 71–75, 77, 78, 100, 101, 103–110, 113, 121, 131, 135, 139, 141, 152, 154–156, 158, 159

**OBDH** On-board Data Handling 44

**PA** power amplifier 21, 117, 118, 120, 124, 128, 165

**PAPR** Peak to Average Power Ratio 117

**PDF** probability density function 117, 122

**PSK** phase-shift keying 117, 146, 157

**QPSK** quadrature phase-shift keying 117, 118, 148

**RF** radio frequency 1–3, 21, 52, 109, 111, 117, 122, 145, 146, 148, 150

**RMS** root mean square 117

**RRC** root-raised-cosine 117, 118

**RS** Remote Sensing v, 155

**SBX** simulated-binary cross-over 139

**SDR** software defined radio 21

**SF** satellite fixed 52, 72

**SFF** satellite fixed frame 52, 68, 72, 73

**SNR** signal-to-noise ratio 104, 109, 111–114, 124

**TDRSS** Tracking and Data Relay Satellite System 31

**TRL** technology readiness level 21, 25, 27

**TT&C** Tracking Telemetry and Command 20, 31, 43, 44

**VCM** variable coding and modulation 24, 104, 116, 120, 121, 123, 141

**VLEO** very low Earth orbit 1, 16, 35, 101, 158

# List of Symbols

| Sign | Description | Unit | Ref. |
|---|---|---|---|
| $B$ | bandwidth | Hz | |
| $E$ | eccentric anomaly | $rad$ | [192, p. 159] |
| $G/T$ | gain-to-noise temperature | dBK | |
| $M_e$ | mean anomaly | $rad$ | [192, p. 157-158] |
| $T_{orbit}$ | Orbital period | $s$ | |
| $T_{sim}$ | Simulation period | $s$ | |
| $T_{sys}$ | system temperature | K | |
| $\Omega$ | right ascension of the ascending node | $rad$ | [192, p. 209] |
| $\mu$ | gravitational parameter | $m^3 s^{-2}$ | [192, p. 93] |
| $\omega$ | argument of perigee | $rad$ | [192, p. 209] |
| $\theta$ | true anomaly | $rad$ | [192, p. 79] |
| $a$ | semi-major axis | $rad$ | [192, eq. 271] |
| $e$ | eccentricity of the orbit | | [195, p. 84] |
| $h$ | angular momentum | $kg/m^2/s^{-1}$ | [192, p. 93] |
| $i$ | inclination | $rad$ | [192, p. 209] |
| $p$ | Parameter of the orbit/semi-latus rectum | $rad$ | [192, eq. 2.53] |
| GHz | Gigahertz | | |
| MHz | Megahertz | | |

This page intentionally left blank.

# A

# Dissipation of a power amplifier

Given a PA output stage looking like fig. A.1 The power dissipated in the transistor is the product of

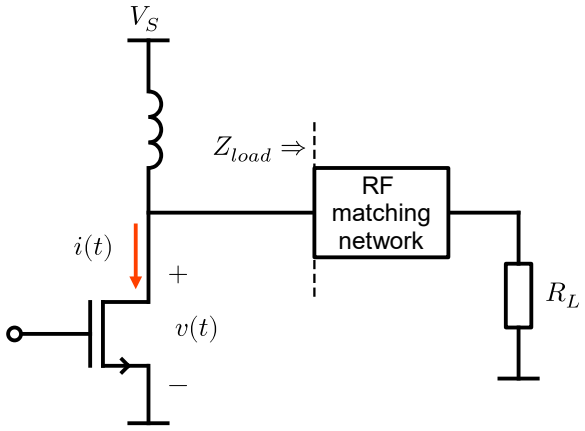


Figure A.1: Simplified output stage of a power amplifier

the current through the transistor $i(t)$ and the voltage across the transistor $v(t)$:

$$P_D(t) = i(t) \cdot v(t) \tag{A.1}$$

$$= \frac{1}{Z_{load}} \left(V_s - v(t)\right) v(t) \tag{A.2}$$

Now assuming $v(t)$ is a modulated sinusoidal with slow[1] time-varying amplitude $A$ and phase $\phi$, biased around point $\beta$:

$$v(t) = A \sin(2\pi f_c t + \phi) + \beta \tag{A.3}$$

$$P_D(t) = \frac{1}{Z_{load}} \left(A \sin(2\pi f_c t + \phi) + \beta\right) \left(V_s - \left(A \sin(2\pi f_c t + \phi) + \beta\right)\right. \tag{A.4}$$

$$= \frac{1}{Z_{load}} \left(V_s \left(A \sin(2\pi f_c t + \phi) + \beta\right) - \left(A \sin(2\pi f_c t + \phi) + \beta\right)^2\right) \tag{A.5}$$

[1] Slow with respect to the period of the carrier frequency.

Then over a single period, the power dissipation is only dependent on the amplitude $A$ and the bias point $\beta$:

$$P_D(A,\beta) = \frac{1}{Z_{load}}\frac{1}{2\pi}\int_0^{2\pi} V_s\left(A\sin(x+\phi)+\beta\right) - \left(A\sin(x+\phi)+\beta\right)^2 \, dx \tag{A.6}$$

$$= \frac{1}{Z_{load}}\frac{1}{2\pi}\left(\pi(2\beta(V_s-\beta)-A^2)\right) \tag{A.7}$$

$$= \frac{1}{Z_{load}}\frac{1}{2\pi}\left(2\pi(\beta(V_s-\beta)-\frac{A^2}{2})\right) \tag{A.8}$$

$$= \frac{1}{Z_{load}}\left(\beta(V_s-\beta)-\frac{A^2}{2}\right) \tag{A.9}$$

Now taking the bias-point to be half-way between the transistors knee voltage and supply voltage and defining $\gamma = \beta/V_s$:

$$\beta = V_k + \frac{1}{2}(V_s - V_k) = \frac{1}{2}(V_s + V_k) \tag{A.10}$$

$$\gamma = \frac{\beta}{V_s} = \frac{1}{2}\left(1+\frac{V_k}{V_s}\right) \tag{A.11}$$

$$P_D(A,\gamma) = \frac{1}{Z_{load}}\left(\gamma\cdot V_s\left(\gamma\cdot V_s - V_s\right) - \frac{A^2}{2}\right) \tag{A.12}$$

$$= \frac{1}{Z_{load}}\left(\gamma\cdot V_s^2(\gamma-1) - \frac{A^2}{2}\right) \tag{A.13}$$

$$= \frac{V_s^2}{Z_{load}}\left(\gamma(\gamma-1) - \frac{A^2}{2V_s^2}\right) \tag{A.14}$$

To avoid clipping the amplitude should stay below $A \leq 0.5(V_s - Vk)$. Defining a normalized instantaneous amplitude $a = A/V_s$ gives the power dissipation profile:

$$a = \frac{A}{V_s} \quad a_{max} = \frac{1}{2}(V_s - V_k) = 1-\gamma \tag{A.15}$$

$$P_D(a,\gamma) = \frac{V_s^2}{Z_{load}}\left(\gamma(\gamma-1) - \frac{a^2}{2}\right) \quad 0 \leq a \leq 1-\gamma \tag{A.16}$$

Finally, the proportionality constant $K_{PA}$ is defined by the specific load line and supply voltage used to obtain the result in [210, eq. 3] and eq. (8.33):

$$K_{PA} = \frac{V_s^2}{Z_{load}} \tag{A.17}$$

$$P_D(a,\gamma) = K_{PA}\left(\gamma(\gamma-1) - \frac{a^2}{2}\right) \quad 0 \leq a \leq 1-\gamma \tag{A.18}$$

# B

# International Astronautical Congress 2019 paper

The following pages include a paper that was written, accepted and presented at the 2019 International Astronautical Congress on part of the work performed during this thesis [222].

70th International Astronautical Congress (IAC), Washington D.C., United States, 21-25 October 2019.


IAC-19-B4.7.12

# Low Latency IoT/M2M Using Nano-Satellites

**Jos van 't Hof[a]*, Visweswaran Karunanithi[b], Stefano Speretta[c], Dr. Chris Verhoeven[d], Prof. Earl W. McCune[e]**

[a] *Department of Microelectronics/Department of Space Engineering, Delft University of Technology (TU Delft), Mekelweg 5, 2628 CD Delft, The Netherlands, J.J.VantHof@student.tudelft.nl*
[b] *Department of Microelectronics/Innovative Solutions in Space. BV, Delft University of Technology (TU Delft), Mekelweg 5, 2628 CD Delft, The Netherlands, V.Karunanithi-1@tudelft.nl*
[c] *Department of Space Engineering, Delft University of Technology (TU Delft), Mekelweg 5, 2628 CD Delft, The Netherlands, S.Speretta@tudelft.nl*
[d] *Department of Microelectronics, Delft University of Technology (TU Delft), Mekelweg 5, 2628 CD Delft, The Netherlands, C.J.M.Verhoeven@tudelft.nl*
[e] *Department of Microelectronics, Delft University of Technology (TU Delft), Mekelweg 5, 2628 CD Delft, The Netherlands E.w.McCunejr-1@tudelft.nl*
* Corresponding Author

## Abstract

Nano-satellite IoT/M2M missions are gaining popularity in recent time. Various companies have launched their pilot missions last year in 2018 and all these companies intend to place a constellation in (V)LEO that can communicate with low power sensors on the ground (sometimes remote locations) and relay it back to the end-user who is monitoring these sensors. This paper discusses two possible architectures of using nano-satellites for low latency IoT/M2M, by presenting information such as, number of satellites needed, number of orbital planes needed and communication strategy. The first proposed architecture will comprise of a self-sustaining network of nano-satellites that communicate with low power, low data-rate sensors on the ground and relay the data to rest of the nano-satellites in the network using inter-satellite links, which is downlinked by a nano-satellite that is in the view of a ground station that is connected to IMT. The second proposed architecture will use nano-satellites to communicate with low power, low data-rate sensors on the ground and relay it to satellites that intend to provide internet from space (Mega-constellation). The internet constellations considered in this study for the second architecture are: Telesat's constellation, SpaceX's Starlink, OneWeb's constellation, Astrome's SpaceNet constellation and Audacy's constellation. Using both these architectures, it can be seen that the latency can be reduced considerably.
**Keywords:** IoT, latency, nano-satellite, inter-satellite link, (mega-)constellation

**Acronyms/Abbreviations**

| | |
|---|---|
| DSA | Delay Sensitive Application |
| DTA | Delay Tolerant Application |
| FoV | Field of View |
| GEO | Geostationary Orbit |
| IMT | International Mobile Telecommunication |
| IOMT | Internet of Military Things |
| IoRT | Internet of Remote Things |
| IoT | Internet of Things |
| ISL | Inter-Satellite Link |
| LEO | Low Earth Orbit |
| M2M | Machine to Machine |
| MEO | Medium Earth Orbit |
| NGSO | Non Geo Stationary Orbit |
| RF | Radio Frequency |
| SSO | Sun Synchronous Orbits |
| UTCG | Universal Time Coordinated in Gregorian format |
| VLEO | Very Low Earth Orbit |

## 1. Introduction

### *1.1 Motivation*

Nano-satellite missions aimed at providing connectivity for Internet of Things (IoT)/Machine-to-Machine (M2M) applications are gaining popularity. Companies such as Hiber, Fleet, Lacuna Space and Kepler are planning to put constellations of nano-satellites into Low Earth Orbit (LEO) or Very Low Earth Orbit (VLEO) that can connect with sensors world-wide [1-4]. The nano-satellites in these missions collect data from remote locations on Earth that do not have other means of connectivity and forward it to ground stations connected to the internet.

With the capabilities of nano-satellites increasing the communication architectures for these satellites also increases in complexity. Nano-satellite technology exist that allows the nano-satellites to downlink their data at gigabit speeds at high frequencies where more bandwidth is available [5]. Some of the nano-satellite constellations

are planning to use Inter-Satellite Links (ISLs) to create a network in between the satellites of the constellation. For example the nano-satellites in the constellation of Kepler will be using Radio Frequency (RF) ISLs at Ka-band frequencies [4]. Also hardware for optical communication is being developed at this moment [6].

At the same time another revolution in satellite-based connectivity is going on with the rise of the Non-Geostationary Orbit (NGSO) satellite constellations that aim to provide global broadband connectivity from space. The networks created by the constellations of Telesat, SpaceX and OneWeb (also called "mega-constellations" because of their number of satellites) could achieve a high total system throughput [7]. This throughput is an order of magnitude higher than what can currently be achieved with the highest data rate communication systems for nano-satellites.

However, these constellations are focussed on providing broadband connectivity involving high data rates at high frequencies and require the user to have parabolic dishes of around half a meter or some equivalently phased array antenna system [8, 9]. These requirements are less appropriate for IoT/M2M applications. Where there is a focus on low power, low data rate and low frequency. An option could be to let the nano-satellites communicate with the IoT/M2M applications and relay the data through large NGSO satellite constellations.

This paper discusses two communication architectures for IoT/M2M nano-satellite missions. The first architecture considers a self-sustaining network of nano-satellites that communicate with low power, low data-rate sensors on the ground. After receiving the data, the nano-satellites will relay the data to rest of the nano-satellites in the constellation using ISLs. The data will be eventually downlinked by a nano-satellite that is in view of an International Mobile Telecommunication (IMT) connected ground station. In the second architecture the nano-satellites instead relay their data to a higher NGSO constellation that intends to provide global broadband connectivity from space.

### *1.2 Paper objectives*

The main objective of this paper is to perform a first order comparison between two communication architectures for nano-satellites in IoT/M2M mission from a latency perspective; one architecture using a self-sustaining network of nano-satellites, the other using higher NGSO satellites to relay data. Later studies, for which this study forms the basis, will investigate the requirements for the RF communication systems in each of the architectures and estimate their total throughput. This paper will also introduce a purpose build NGSO data relay simulator that is used to find a first order estimation of the availability of a data relay between a nano-satellite and a higher orbit NGSO constellation.

### *1.3 Paper structure*

This paper is structured as followed: Section 2 will give a description of the two IoT/M2M communication architectures, IoT/M2M use-cases and protocols and will discuss the NGSO satellite constellations that are considered to use as a data relay; Section 3 describes the models used to compute and compare the latency of the two communication architectures; Section 4 will present the results of the latency analysis of the two architectures. Section 5 will compare the two architectures; and Section 6 will present the conclusions.

## 2. IoT/M2M mission architecture overview

This section gives a description of the two proposed architectures, it will present some IoT/M2M applications and communication protocols and it will give a description of the NGSO constellations that were considered for the data relay architecture.

### *2.1 Description of architectures*

In this work two architectures for nano-satellite IoT/M2M mission are considered; a self-sustaining constellation of nano-satellites and a constellation of nano-satellites that uses higher NGSO constellations to relay data.

Fig. 1 shows an illustration of the self-sustaining nano-satellite constellation architecture. In this architecture the nano-satellites in (V)LEO communicate with the low data-rate IoT/M2M users on the ground using common IoT/M2M communication standards. The constellation is self-sustaining because of the network the satellites create using ISLs. This self-sustaining network allows the satellites to relay the received data to the rest of the nano-satellites in the network. The data is eventually downlinked by a nano-satellite that is in view of a ground station connected to IMT.

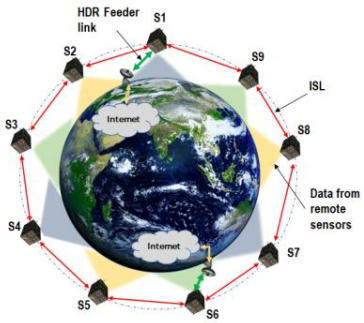


Fig. 1. Illustration of a self-sustaining nano-satellite IoT/M2M constellation [10].

Fig. 2 shows an illustration of the nano-satellites constellation that uses higher NGSO data relays. Like the first architecture the nano-satellites in (V)LEO also communicate with the IoT/M2M users on the ground. However, instead of having a network with ISLs the nano-satellites can individually relay the data through

NGSO constellations. In this architecture the nano-satellite constellation can take advantage of the large throughput that NGSO constellations offer. After relaying the data routing and downlinking the data is taken care of by the NGSO constellation.

The Velox-II satellite has already demonstrated this type of relay to a geostationary orbit (GEO) data relay satellite [11, 12]. In addition, the Commcube 1 satellite will attempt to communicate with the GlobalStar constellation [13].

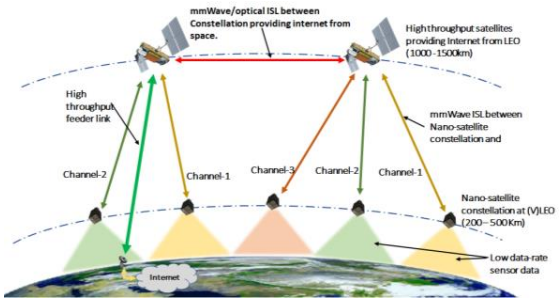


Fig. 2. Illustration of a nano-satellite IoT/M2M constellation using NGSO constellations to relay data [10].

### *2.2 Use cases and latency requirements*

This section provides an overview of IoT/M2M use-cases based on literature in [14-18] and their latency requirements. The IoT applications can be broadly classified into delay tolerant applications (DTA) and delay sensitive applications (DSA). The DSA use-cases typically have a latency requirement in the order of few milliseconds to seconds [16]. These applications include smart homes applications, Internet of Military Things (IOMT), Internet of Remote Things (IORT) in smart grids. The DTA use-cases tolerate larger latency and can be categorized as high and moderately high latency applications which are in the order of few minutes to hours.

The energy/smart grid use case is described in [16] with a detailed analysis on the latency requirements. With the advancements in automation of the power grids aspects such as timely communication of monitoring information, controlling and transmission of emergency alarms becomes crucial. The data traffic types for this use-case are; network monitoring (packets of 32 bytes), network alarms (packets of 60 bytes), control commands (packets of 60 bytes) and coordination traffic (packets of 1000 bytes). Among these types the network alarm packets have the lowest latency requirements, in the order of less than 1 second. Coordination traffic is less stringent with a latency requirement of 90 seconds. For use-cases such as geological disaster monitoring and weather forecasting, the latency requirement is moderate in the order of seconds and considered “Moderately low latency”. IoT through satellites can play a very crucial role in e-health care and elderly assistance especially in remote locations. The latency requirement for this use-case can be low when emergency alerts need to be sent from user terminal to an emergency room but may still be larger than 1 second. IoMT is another use-case where secure and reliable near real-time communication could be an significant advantage [18].

The DTA use-cases do not have a very stringent requirement on latency. One such use-case is logistics, transportation and asset tracking. The frequency of data collection from the user terminals for this use-case can be in the order of hours. The main advantage of using satellite based IoT for such an application is the larger coverage and access to remote locations for example oceans when tracking ships. Another use-case where satellites can play a key role is smart agriculture/farming.

Table 1 Overview of IoT/M2M use cases and their latency requirements.

| | Service sector | Location | Devices | Requirement | Ref. |
|---|---|---|---|---|---|
| DSA | Energy/Smart grid | Power generation (distributed over large geographical areas), sub-stations, smart metering. | Solar panels, windmills, Distribution centers and substations, power meters | Near real-time | [16] |
| DSA | Geologic disaster forecasting and weather monitoring | Disaster prone areas (earthquake, volcano), coastal areas, river beds, large forest covers. | Distributed electro-mechanical, Temperature monitoring. | Moderately low latency | [15] |
| DSA | Healthcare and elderly assistance | Homes located in urban and remote locations, Hospitals, Elderly homes. | Electro-medical sensors | Moderately low latency | [14, 17] |
| DSA | Internet of Military Things (IOMT) | Logistics, weapon support, environment monitoring, ISR and C2. | Radars, imaging sensors, Sonars, RFID | Near real-time | [18] |
| DTA | Logistics and transportation | Maritime, Aeronautical, Airports, harbors. | Vessels, cargo and passenger aircrafts, terrestrial communication infrastructure. | Moderately high latency | [14] |
| DTA | Smart farming/agriculture | Large cattle farming areas spread into remote locations, Large agricultural areas | Cattle tracking and health monitoring, soil moisture monitoring. | High latency | |
| DTA | Environment monitoring | Large forest areas, Mountains | Tracking wild animals and endangered species | High latency | [14] |

In the case of agriculture, various types of sensors could be deployed over a large land area to monitor the health of the crop and moisture content to improve the yield. Similarly, in the case of farming, cattle tracking, and monitoring could be challenging when spread over very large area, in such cases satellite based IoT can help with the advantage of large coverage. Since this type "monitoring and tracking" type of data is not expected to change with-in a short period of time, the latency requirement for this application is assumed to be in the order of thrice to four times a day (6 to 8 hours). A similar use-case with a similar latency requirement is tracking wild and endangered species in large forest areas.

Table 2 summarizes the latency requirement classifications and their corresponding data type that is communicated through the user terminal. It can be inferred that emergency and protection related service information need low latency/near-real time requirements, controlling and monitoring needs moderately low latency, monitoring information from fast moving objects need moderately high latency and tracking information from slow moving objects can have high latency.

Table 2. Overview IoT/M2M communication protocols

| | Data delivery duration | | Data types |
|---|---|---|---|
| DSA | Near real time | < 1 s | - Emergency services<br>- Protection |
| | Moderately low latency | 1 to 90 s | - Controlling<br>- Monitoring |
| DTA | Moderately high latency | < 1 h | - Monitoring & tracking (fast moving objects) |
| | High latency | 6 to 8 h | - Monitoring & tracking (slow moving objects) |

### *2.3 IoT/M2M communication standards*

Looking at existing IoT standards is fundamental to better define the final constellation performances, both in terms of latency and throughput. First it is important to define which current IoT standard would lead to the best performances on a ground to space link. It is important to note that implementing an IoT network in space aims mainly at a global coverage and this could be complex given that most services operate on country-specific bands and sometimes protocols (mainly driven by pre-existing spectrum allocations).

As shown in Table 3, five main IoT standard have been analysed [19]: the most important characteristics for our analysis are the communication band, the data throughput, transmission latency (seen as the time required to transmit the smallest information unit) and eventual characteristics that would make the standard difficult to implement in a space-based receiver.

LoRa is a very popular standard for IoT devices employing a chirp spread spectrum modulation: this makes the signal quite insensitive to narrow-band interferers and provides high de-spreading gains, allowing a low-power implementation. LoRa is based on an open network definition, allowing independent suppliers to implement it. This also allowed the successful demonstration of space reception of ground nodes [20], making it one of the prominent choices for the constellation described in this paper.

SigFox [21], on the contrary, is based on a closed network infrastructure and, so far, saw no in-space demonstration. SigFox also shows a very narrow-band implementation that could suffer from interference when received from space (due to the much wider number of nodes that can be received from space).

NB-IoT and LTE-M [22] have been implemented to coexist with 4th generation cellular networks, making them very suited for high bandwidth applications (still with respect to small sensors) but hard to implement on a space receiver (mainly due to the modulation selection and the round-trip-time constraints, typical in cellular phones.

Iridium Edge requires a special mention as it is the only protocol designed for space applications but, being used already in a LEO constellation, would not fit the constellation being targeted in this article.

### *2.4 Overview of NSGO constellations*

For the second architecture the NGSO constellations considered in this work are: Telesat's LEO constellation, SpaceX's Starlink LEO constellation, OneWeb's LEO constellation, Astrome's SpaceNet constellation and Audacy's MEO relay constellation. Some of these NGSO constellations are considered "mega-constellations" due to their large number of satellites. Table 4 shows an overview of these NGSO constellations.

Table 3. Overview IoT/M2M communication protocols

| Protocol | Frequency | Bandwidth | Protocol Latency | Mode | Bitrate | Notes |
|---|---|---|---|---|---|---|
| LoRa(WAN) | 433 MHz,<br>868 MHz,<br>915 MHz | 125 kHz,<br>250 kHz,<br>500 kHz | 0.1 – 3 s | Half-duplex | 0.25 - 11 kbps | Demonstrated Ground to LEO with 125 kHz bandwidth |
| NB-IOT | 617 – 2200 MHz | 180 kHz | 10 ms | Half-duplex | 62 kbps | |
| Sigfox | 868 MHz<br>902 MHz | 600 Hz | 330 ms | Half-duplex | 600 bps | Closed standard, low power and narrow band |
| LTE-M | | 1.4 MHz | 100 ms | Half-duplex | < 1 Mbps | LTE compatible, designed for cellular networks |
| Iridium Edge | 1621 MHz | - | - | Half-duplex | 2400 bps | Designed for space applications |

For analysing the latency of the data relay architecture of interest are the number of satellites, their orbital parameters and their fields of view (FoVs). In a later study that will focus on the design of the RF system on the nano-satellite the user frequency bands, user bandwidth and user beam types are of interest.

The next sections will shortly describe the properties of each of the NGSO constellations based on their FCC filings and published materials. An extensive discussion of the orbital configurations and beam patterns of Telesat's, OneWeb's and SpaceX's constellations can also be found in [7]**.**

### *2.4.1 Telesat LEO constellation*

In November 2016 Telesat Canada filed its first application for a LEO constellation of 117 satellites operating in Ku/Ka-band [23]. In March 2017 Telesat has requested approval for a seperate LEO constellation operating in V-band [24].

This study considers Telesat's initial LEO constellation as defined in [23]. The 117 satellites in this constellation are placed in 11 orbital planes. Of these orbital planes six are circuit polar orbits at 1000 km, 99.5° inclination with each 12 satellites per plane and five are circular inclined orbits at 1200 km, 37.4° inclination with each 9 satellites per plane. Fig. 3 shows Telesats LEO constellation inside the NGSO relay simulator. The figure also shows a nano-satellite in a 500 km polar orbit with an ISL to one of the Telesat satellites as reference.

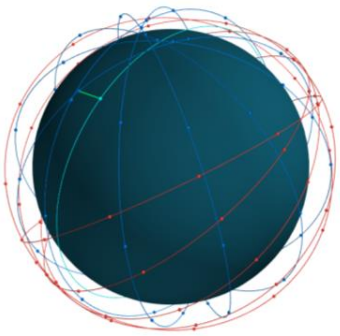

Fig. 3. Telesat LEO constellation inside the NGSO relay simulator together with a nano-satellite. The figure shows Telesat's polar orbits (blue) and inclined orbits (red), and the nano-satellite orbit (cyan) around Earth

Each of Telesat's satellites will serve users that can see the satellite down to an elevation angle of 10° [23]. This gives a FoV of ±58.34° for the 1000 km orbits and ±55.43° for the 1248 km orbits. Users will initiate communication with the satellite through the satellites fixed wide-area beam. After the initiation the satellite will provide the communication with the user with its shapeable and steerable user-beams of which there are at least 16 available on each satellite.

The user uplink band is 17.8 – 20.2 GHz (Ka-band) with a theoretical maximum bandwidth of 500 MHz. The user downlink band is 27.5 – 30 GHz with a theoretical maximum bandwidth of 850 MHz. The constellation uses optical ISLs that allows any two adjacent satellites to communicate regardless of their orbital planes. This allows a satellite to forward its data to a satellite that is in view of an internet connected ground station.

### *2.4.2 SpaceX Starlink LEO constellation*

In November 2016 SpaceX filed its first application for a LEO constellation of 4425 satellites [25]. In March 2017 SpaceX has requested approval for a VLEO extension to this constellation with an additional 7518 satellites [26]. In November 2018 SpaceX requested to modify the altitude of the satellites in the lowest shell of satellites in the original constellation of 4425 satellites to 550 km [27] and change the number of planes and satellites per plane in this lower shell in later in August 2019 [28].

This study considers the LEO part of the constellation of SpaceX as defined in [28]. The 4409 satellites in this constellation are placed in five (spherical) orbital shells. The first shell at 550 km altitude has 72 planes at 53.0° inclination with each 22 satellites per plane.
The second shell at 1110 km altitude has 32 planes at 53.8° inclination with each 50 satellites per plane. The third shell at 1130 km has 8 planes at 74.0° inclination with each 50 satellites per plane. The fourth shell at 1275 km has 5 planes at 81.0° inclination with each 75 satellites per plane. The fifth and final shell in the LEO constellation at 1325 km altitude has 6 planes at 70.0° inclination with each 75 satellites per plane. Fig. 4 shows SpaceX's LEO constellation inside the NGSO relay simulator. The figure also shows a nano-satellite in a 500 km polar orbit with an ISL to one of the SpaceX's satellites as reference.

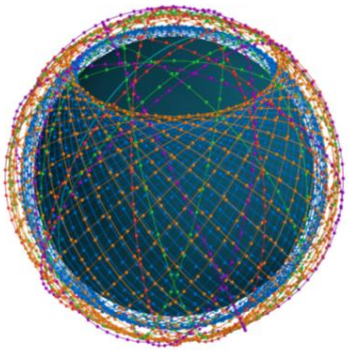

Fig. 4. SpaceX Starlink LEO constellation inside the NGSO relay simulator together with a nano-satellite. The figure shows Starlink's 550 km orbits (blue), 1100 km orbits (orange), 1130 km orbits (green) and 1325 km orbits (red), and the nano-satellite orbit (cyan) around Earth

After full deployment of the constellation each satellite will serve users that can see the satellite down to an elevation angle of 40° [25]. This gives an FoV of ±44.85° for the 550 km altitude satellites (also specified in [27]), ±44.85° for the 550 km altitude satellites, ±40.72° for the 1110 km altitude satellites, ±40.59° for the 1130 km altitude satellites, ±39.67° for the 1275 km altitude satellites and ±39.67° for the 1325 km altitude satellites. The SpaceX satellites use steerable and shapeable user beams of which there are at least 8 available on each satellite [25].

The user uplink band is 12.75 – 14.5 GHz with a theoretical maximum bandwidth of 500 MHz. The user downlink band is 27.5 – 30 GHz with a theoretical maximum bandwidth of 1 GHz. The SpaceX satellites will use optical inter-satellite links between the satellites in the constellation [25].

### *2.4.3 OneWeb LEO constellation*

In April 2016 OneWeb filed its first application for a LEO constellation of 720 satellites [8]. In March 2017 OneWeb filed an application for a V-band extension to the constellation with 1280 satellites in MEO when fully deployed [29]. In March 2018 OneWeb requested to double the number of planes in the initial LEO constellation to 36 and the number of satellites per plane to 55 increasing the total amount of satellites to 1980 [30]. However in an December 2018 interview OneWeb's founder said the company is scaling back the LEO constellation to around 600 satellites [31].

This study considers OneWeb's initial LEO constellation of 720 satellites as defined in [8] because of the intent of the company to scale back the constellation. This constellation would have 18 polar orbital planes at an altitude of 1200 km and an inclination of 87.9° with 40 satellites per plane [28]. Fig. 5 shows OneWeb's initial LEO constellation inside the NGSO relay simulator. The figure also shows a nano-satellite in a 500 km polar orbit with an ISL to one of the OneWeb's satellites as reference.

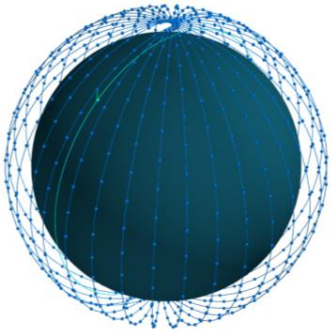

Fig. 5. OneWeb's initial LEO constellation inside the NGSO relay simulator together with a nano-satellite. The figure shows OneWeb's orbits (blue), and a nano-satellite orbit (cyan) around Earth.

Each of OneWeb's satellites will serve users that can see the satellite down to an elevation angle of 55° [28]. This gives the 1200 km altitude satellites an FoV of ± 40.14°. The 16 user beams of OneWeb's satellites are however fixed and elliptical, therefore a circular FoV is a simple approximation of the actual FoV.

The user uplink band is 14.0 – 14.5 GHz with a bandwidth of 125 MHz. The user downlink band is 10.7 – 12.7 GHz with a bandwidth of 250 MHz. The OneWeb satellites do not have an inter-satellite link and should therefore always be in line of sight of a ground station.

### *2.4.4 Astrome SpaceNet*

Astrome's has not filed FCC filings for its constellations yet. However they released two papers related to their constellation design in June 2019 [9] and July 2019 [32].

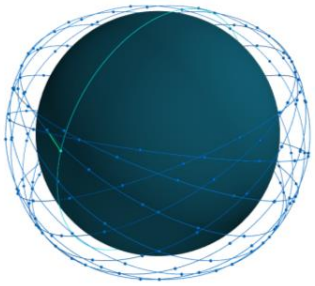

Fig. 6. Astrome SpaceNet constellation inside the NGSO relay simulator together with a nano-satellite. The figure shows SpaceNet's orbits (blue), and a nano-satellite orbit (cyan) around Earth.

Astrome's SpaceNet constellation is designed to provide coverage between ±38° latitude with 198 satellites from LEO [32]. The constellation has 11 orbital planes at an altitude of 1530 km and an inclination of 30° with each 18 satellites per plane [9]. Fig. 5 shows Astrome's LEO constellation inside the NGSO relay simulator. The figure also shows a nano-satellite in a 500 km polar orbit with an ISL to one of the Astrome's satellites as reference.

Each of Astrome's satellites has a FoV of ±37° and uses digital beam forming to create multiple steerable spot beams [9].

The user uplink band is 81.0 – 86.0 GHz and the user downlink band is 71.0 – 76.0 GHz. Each satellite will have six RF inter-satellite links at 66.0 – 71.0 GHz to communicate with all neighbouring satellites [9].

### *2.4.5 Audacy MEO constellation*

In December 2016 Audacy filed its application for a MEO constellation of 3 satellites [33]. Audacy's constellation is the only one considered in this work that is not aimed at providing connectivity on earth from

space. Instead their MEO constellation is specifically designed as a data relay constellation for spacecraft in LEO.

The constellation consist of three satellites with at 13900 km at 25° inclination spaced 120° apart [33]. Fig. 7 shows Audacy's MEO constellation inside the NGSO relay simulator. The figure also shows a nano-satellite in a 500 km polar orbit with an ISL to one of the Audacy's satellites as reference.

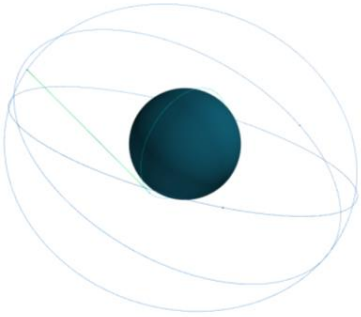

Fig. 7. Audacy's data relay MEO constellation inside the NGSO relay simulator together with a nano-satellite. The figure shows Audacy's orbits (blue), and a nano-satellite orbit (cyan) around Earth.

The relay satellites have a split FoV with an inner ring and an outer ring that are filled with spot beams. The inner ring is nadir pointing while the outer ring surrounds the earth up to 1500 km. The gaps in between the two beams of one relay satellite is filled with that of the other two [33]. Estimated from the figures in the FCC filing the FoV of the inner ring is approximately ±16.55° and the outer ring is from approximately 18.29° to 21.22°.

The relay satellites operate in K-band and V-band, the user uplink and downlink bands are 22.95 – 33.00 GHz with a maximal bandwidth of 600 MHz. The relay satellites also have dedicated spot beams for advanced users in a 10000 km field of view. The uplink and downlink bands are 22.55 – 32.8 GHz with a maximal bandwidth of 500 MHz for a single user. The relay satellites have RF inter-satellite links in the V-Band to forward data if one of the satellites cannot establish a connection to a ground station [33].

#### *2.4.6 NGSO constellation discussion*

The constellations of Telesat, SpaceX, OneWeb and Astrome all aim to provide broadband connectivity on the surface of the earth from space. The constellations of Telesat SpaceX and OneWeb aim to do so globally but with a vastly different number of satellites, orbital configurations and beam types as can be seen in Table 4. SpaceX having the largest number of satellites also has the overall highest number of satellites in line of sight from earth as was shown by [7].

These first four constellations are however optimized to provide ground coverage. Of the considered constellations for this work all except Audacy's aims to provide broadband connectivity on the surface of the earth from space. Fig. 8 shows a comparison of the FoVs of the satellites in each of the constellations projected on earth. Because of the limited FoVs of the satellites this means that at higher altitudes gaps in the coverage may exist.

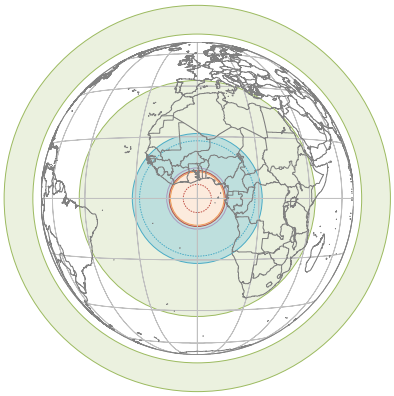

Fig. 8. Overlay of FoVs of NGSO satellites of Telesat LEO (blue), SpaceX Starlink (red), OneWeb LEO (orange), Astrome SpaceNet (purple) and Audacy (green). Dashed lines are the FoVs of the lowest altitude satellites in the constellation.

## 3. Methodology and model description

This section describes the methodology that was used to estimate the latency performance of IoT/M2M missions of the two communication architecture concepts. Fig. 9 and Fig. 10 show the models developed (grey-shaded rounded boxes) and the inputs (white boxes) and outputs (text) for the self-sustaining nano-satellite constellation architecture and the NGSO constellation relay architecture respectively. The dashed models are planned for future research.

Several elements contribute to the overall latency of the communication architecture. The latency considered in this paper is defined as the time between an IoT/M2M application having generated data and the time it took for the nano-satellite constellation to have forwarded this data to an IMT connected ground station.

The analysis of this paper is starts with a basic model for the nano-satellite constellation design that uses polar orbits. The number of satellites and number of planes in this constellation is chosen in such a way that the revisit time $t_{revisit}$, the time it takes for a location on earth to come in the FoV of the constellation is zero. In other words, it is optimized that every location on earth has can see at least one nano-satellite within a minimum elevation.

Table 4. Information of considered NGSO constellations for data relay

| Constellation | Altitude | $i$ | Number of: Planes | Sats/Plane | Sats | User bands & (User bandwidth) Uplink | Downlink | User beam Type | FoV |
|---|---|---|---|---|---|---|---|---|---|
| Telesat LEO | 1000 km<br>1248 km | 99.5°<br>37.4° | 6<br>5 | 12<br>9 | 117 | 17.8 – 20.2 GHz<br>(≤ 500 MHz) | 27.5 – 30 GHz<br>(≤ 850 MHz) | Steerable & shapeable spot beams | ± 58.34°<br>± 55.43° |
| SpaceX Starlink LEO | 550 km<br>1110 km<br>1130 km<br>1275 km<br>1325 km | 53.0°<br>53.8°<br>74.0°<br>81.0°<br>70.0° | 72<br>32<br>8<br>5<br>6 | 22<br>50<br>50<br>75<br>75 | 4409 | 12.75 – 14.5 GHz<br>(≤ 500 MHz) | 10.7 – 12.7 GHz<br>(≤ 1 GHz) | Steerable & shapeable spot beams | ± 44.85°<br>± 40.72°<br>± 40.59°<br>± 39.67°<br>± 39.36° |
| OneWeb LEO (2016) | 1200 km | 87.9° | 18 | 40 | 720 | 10.7 – 12.7 GHz<br>(250 MHz) | 14.0 – 14.5 GHz<br>(250 MHz) | Fixed elliptical beams | ± 40.14° |
| Astrome Spacenet | 1530 km | 30.0° | 11 | 18 | 198 | 81.0 – 86.0 GHz<br>(< 500 MHz) | 71.0 – 76.0 GHz<br>(< 500 MHz) | Digital beam-forming spot beams | ± 37.00° |
| Audacy | 13900 km | 25.0° | 3 | 1 | 3 | 22.95 – 33.0 GHz<br>(<= 600 MHz) | 22.95 – 33.0 GHz<br>(<= 600 MHz) | Spot beams | [1)]±21.22° |

*1) There is a gap in the FoV of the relay satellites of Audacy between 16.55° and 18.29°*

The user uplink model considers the time it takes to uplink the data, $t_{uplink}$, from the IoT/M2M application to the nano-satellite. This paper provides some examples for this latency using the protocols presented in section 2.3

For the first architecture, using the self-sustaining network between the nano-satellites, the rest of the latency is determined by the routing through the network, $t_{routing}$. This number is determined by the routing strategy in the network, the propagation and processing time from satellite to satellite and the time it takes to downlink the data $t_{prop,dl}$.

For the second architecture, using higher NGSO constellations for data relay, there is an additional element that causes latency. Namely the time it takes for the nano-satellite to come within FoV of the NGSO satellite. To find this delay time $t_{delay}$, the orbital dynamics between the nano-satellite and the higher NGSO constellation are simulated. From this simulation the availability of a data relay between the nano-satellite and an NGSO satellite is extracted. The final delay for this architecture is determined by the routing speed of the NGSO constellation. For this latency advertised numbers of the NGSO constellations are taken.

The following sections describe each of the models in detail. Section 3.1 describes the orbit design of the nano-satellite constellations to provide the connectivity for the IoT/M2M applications. Section 3.2 describes the model used for the user uplink. For the first architecture, section 3.3 describes the routing strategy. For the second architecture, section 3.4 describes the orbital mechanics simulator, section 3.5 the relay availability model and section 3.6 the relay routing model. A summary of how the contributing delays add to the overall latency of the two architectures is provided in section 3.6.

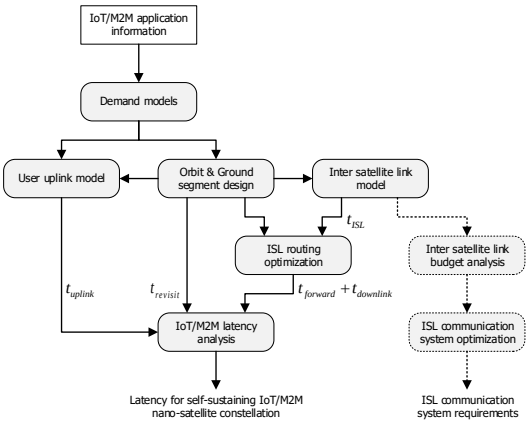


Fig. 9. Block diagram of the methodology employed to estimate IoT/M2M missions using the self-sustaining constellation of nano-satellites communication architecture

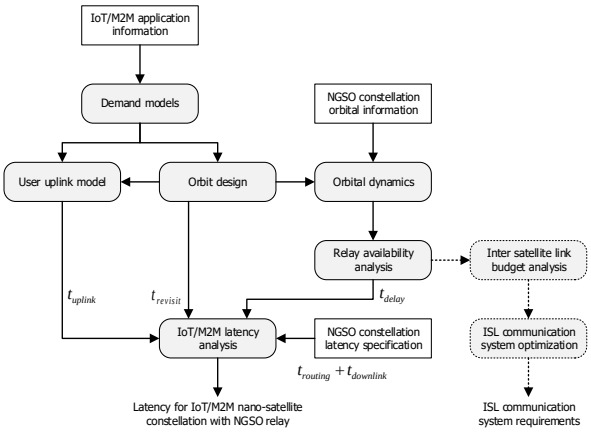


Fig. 10. Block diagram of the methodology employed to estimate IoT/M2M missions using a NGSO constellation relay concept.

*3.1 Constellation design*

The purpose of this paper is not to design the most optimal constellation for a specific use-case or cater to a specific region on Earth. Therefore, a simple constellation that can provide continuous global coverage using satellites in polar orbits is considered.

The purpose of this calculation is to find out the various possibilities in number of satellites needed per orbital plane and number of orbital planes for various combination of minimum elevation angle El and constellation altitude. All the calculations are done for single satellite coverage, when for a given El there is at-least one satellite always visible.

The total number of satellites N needed for continuous global coverage in a polar orbit depends on the altitude of the constellation H and the coverage angle of the payload on the satellite. The half power beam-width of payload coverage is given by α. The corresponding half power earth centred cone is given by ψ. The total number of satellites is given by N = n*m, where n is the number of orbital planes and m is the number of satellites per orbital plane. To calculate the total number of satellites the needed for continuous global coverage with at-least one satellite in coverage, N must satisfy the following relation [34]:

$$N \cong \frac{4 * \cos(\lambda)}{1 - \cos(\psi)} \tag{1}$$

where:

$$\psi = \arccos\left(\frac{Re}{Re + H} * cos(El)\right) - El \tag{2}$$

where λ is the coverage latitude. For global coverage λ is 0 degrees. In order to determine the number of satellites needed per orbital plane (m) and the number of orbital planes (n), based on [34] the relation between m and n must satisfy:

$$1.3n \ < m * \cos(\lambda) < 2.2n \tag{3}$$

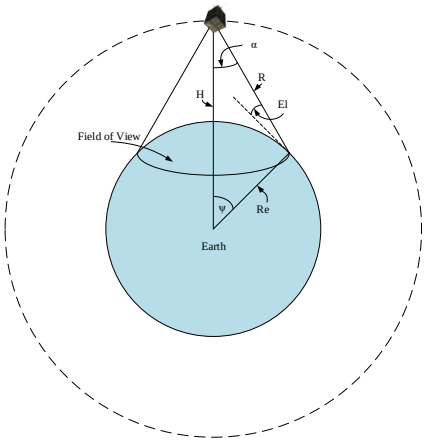


Fig. 11. Diagram of parameter definitions.

Based on the above equations, a plot of the number of satellites needed to form a constellation that can provide continuous global coverage is shown in the left graph of Fig. 12. In order to determine m and n using Equ. (3), m is chosen as 2n and the different combinations are shown in the middle graph of Fig. 12. Another parameter that is important with respect to the payload design is the half beam-width angle of the FoV α. The right graph of Fig. 12 shows the relation between α, H and El.

All these calculations correspond to a single satellite coverage, for three satellites coverage (at-least three satellites are within the coverage of a user terminal) the total number of satellites is given by:

$$N \cong \frac{11 * \cos(\lambda)}{1 - \cos(\psi)} \tag{4}$$

which must satisfy:

$$1.4n \ < m * \cos(\lambda) < 2.4n \tag{5}$$

In applications such as IoMT where reliability of a link between user-terminal and satellite is important multi-satellite coverage is preferred, which would result into a larger number of satellites.

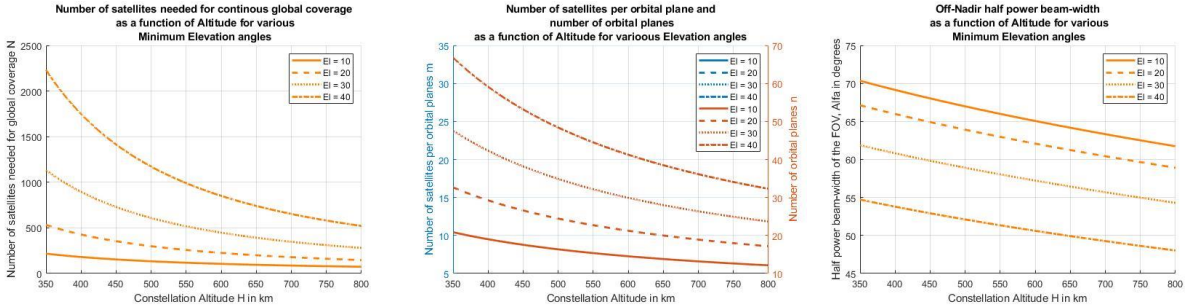


Fig. 12. Graphs showing properties of nano-satellite constellation for different altitudes

### *3.2 User uplink model*

For this paper the user uplink model is kept simple. Three elements contribute to the $t_{uplink}$ time; the time it takes to transfer a packet $t_{transfer}$, the set-up and overhead latency added by the protocol $t_{protocol}$ and the propagation delay from the ground to the nano-satellite $t_{prop,ul}$. This gives the following equation:

$$t_{uplink} = t_{protocol} + t_{transfer} + t_{prop,ul} \quad (6)$$

The protocol and transfer speeds for several packet sizes are shown in Fig. 13. For the propagation delay the slant range is calculated for different minimum elevation angles. The propagation delay is therefore:

$$t_{prop,ul} = \frac{d_{slant}}{c} \quad (7)$$

Fig. 14 shows the slant ranges at several elevation angles for different nano-satellite altitudes. Also plotted is the propagation delay assuming propagation with the speed of light. As can be seen the propagation delay is in the order of a few milliseconds. Comparing this to Fig. 13 the propagation delay quickly gets two orders of magnitude smaller than the protocol and transfer time. It is therefore expected that the larger contributors to the latency will be the protocol latency and the latency of the nano-satellite network, either self-sustaining or using NGSO relays.

### *3.3 Self-sustaining network routing*

For the self-sustaining network of nano-satellites the $t_{routing}$ duration is defined as:

$$t_{routing} = \gamma \frac{N_s}{N_G}\left(t_{ISL} + t_{processing}\right) + t_{prop,dl} \quad (8)$$

In Equ. (8) the $t_{ISL}$ duration is the time it takes for a single nano-satellite to forward its data to a neighbouring satellite in the same plane over the ISL. The $t_{processing}$ duration is the time required for on board processing on the nano-satellite for each ISL transmission and is based on [16] to be 3 ms. The total routing time depends on the number of nano-satellites in the chain $N_S$ and the number of ground stations that have line of sight with the chain of nano-satellites $N_G$. It is assumed that at-least one satellite in any orbital plane can be seen by a ground station, this is possible if the ground stations are located near the poles and $N_G = 1$. The influence of the routing strategy is defined by the factor γ. For a bi-directional routing γ=½, for uni-directional routing γ=1. This work only considers ISL within an orbital plane and not between orbital planes. The $t_{downlink}$ for a self-sustaining architecture is considered for a worst-case sc scenario i.e, when the satellite is at its lowest elevation limit of 10 degrees, this corresponds to the longest propagation delay.

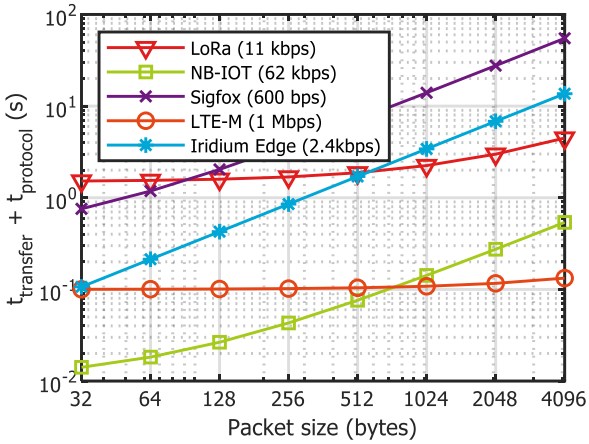


Fig. 13. Transfer speeds for different IoT protocols

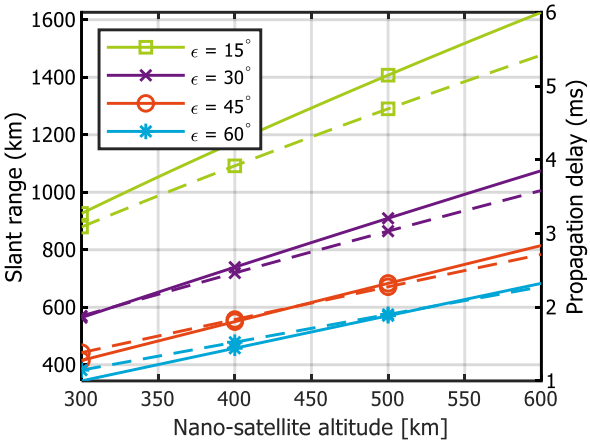


Fig. 14. Slat range (solid, left axis) and propagation delay (dashed, right axis)

### *3.4 Relay orbital dynamics*

A purpose build tool was made to simulate the availability of the NGSO constellation data relay. The NGSO relay simulator is made in Python using the Poliastro Python package [35] for astrodynamics computation and the Mayavi library [36] for visualisation. The simulator is optimized for simulating a large amount of satellites simultaneously to find the lines of sight and pass durations while maintaining a reasonable accuracy. It uses two-body propagation and the Markley algorithm of solving Keplers equation [37].

The orbital mechanics of the simulator was validated by comparing a simple scenario in the free version of Analytical Graphics Incorporated Systems Toolkit® 11 using its two body propagator. Fig. 15 shows a side by side comparison of the simple scenario inside the two simulators. This scenario contains two satellites in circular orbits around Earth having orbital elements as defined in Table 5.

To compare the two simulators the (inter-satellite) pass duration (the time in which there was a line of sight between the two satellites) between the two satellites are analysed. The higher orbit satellite has a constrained

nadir pointing field of view that is varied in each of the cases. The lower orbit satellite has an unconstrained field of view. The analysis period is two hours starting at 1 September 2019 10:00:00.000 UTCG and the step size was set to 1 second.

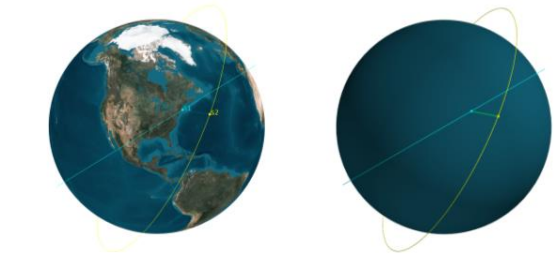

Fig. 15. Side by side comparison of a simple scenario with AGI's Systems Toolkit® 11 (left) and the purpose build simulator (right)

Table 6 shows the pass durations of the first pass encountered in the scenario. The pass duration found in the NGSO relay simulator corresponds to that in STK for all the cases. However, the adaptive step size computation in STK results to a much greater accuracy than is achieved with the fixed 1 second step size of the NGSO relay simulator.

Table 5. Orbital elements of the two satellites in the validation scenario

| | Satellite 1 | Satellite 2 |
|---|---|---|
| $h_a$ | 500 | 1500 |
| $e$ | 1 | 1 |
| $i$ | 45° | 60° |
| Ω | 0° | 45° |
| ν | 15° | 0° |
| Epoch | J2000 | J2000 |

Table 6. Contact durations of the first pass of the two satellites in the validation scenario

| FOV | STK Simulator | NGSO relay simulator |
|---|---|---|
| ± 60° | 1218.986 s | 1218 s |
| ± 45° | 463.702 s | 462 s |
| ± 30° | 246.317 s | 246 s |
| ± 15° | 100.317 s | 99 s |

For this paper a step size of 1 second is considered acceptable and accurate enough. With this step size the NGSO relay simulator can find the pass durations with an accuracy of ±2s. The minimum duration for a usable inter-satellite pass will be determined by the overhead in setup and connection time of the communication protocol used by the NGSO constellations. This number is unknown for the considered NGSO constellations however it is assumed that it will be in the order of seconds and not milliseconds. Without knowing the exact duration of the setup times, simulating with a smaller step sizes is not considered useful at this time.

### *3.5 Relay availability model*

After the nano-satellite received the data from the IoT/M2M user it needs to wait until it gets in FoV of the higher orbit NGSO satellite to be able to forward this data. This duration is a contributor to the latency of the architecture that depends on the relative motion of the nano-satellite and the NGSO satellites. The Telesat, SpaceX, OneWeb and Astrome constellations are optimized for coverage on ground in their orbits, FoVs and (steerable) user beams. Therefore, the coverage in (V)LEO could be significantly lower for these constellations.

The NGSO relay simulator extracts the (inter-satellite) pass information while simulating the orbital dynamics. This information contains the positions of the two nodes during the pass, the start and stop time of the pass and its total duration. Based on this information the gap duration, the time in between two passes, can also be calculated. This gap duration, or more specifically its distribution, will contribute as a delay to the overall latency of this architecture.

The inter-satellite passes are simulated between a nano-satellite in a 500 km polar orbit and each of the NGSO constellations. Table 5 shows the orbital elements of this nano-satellite. It is assumed that the distributions of the passes are similar among the rest of the nano-satellites inside the IoT/M2M constellation. It is assumed that once the nano-satellite enters the FoV of the NGSO constellation satellite it can relay its data. The exact location of the spotbeams are therefore not considered. It could however be that not the entire FoV of the NGSO constellation satellite is covered by the spotbeams especially when the satellite uses shape able and or steerable spot beams.

Table 7. Orbital parameters of the single nano-satellite in polar orbit that is used as a reference for the IoT/M2M nano-satellite constellation.

| | Nano-satellite orbital parameters |
|---|---|
| $h_a$ | 500 km |
| e | 1 |
| i | 90° |
| Ω | 0°, 45°, 90° or 135° |
| ν | 0° |
| T | 5677 s |
| Epoch | J2000 |

The NGSO relay simulator does not take any perturbations into account. Therefore, the effect of a perturbation such as the J2 perturbation that causes the right ascension Ω to over time at a constant rate is not modelled. This effect is also used to create Sun Synchronous Orbits (SSO) such as the ones used for the Kepler IoT constellation [4]. To compensate for this inaccuracy of the simulator the cases are repeated for varying values of the right ascension Ω.

### *3.6 Relay routing model*

Round trip time numbers reported by the NGSO constellation companies or other studies are used to estimate the latency caused by routing through their satellite networks and downlinking the data to a ground station. Table 8 shows an overview of the latencies of the satellite networks. The analysis in [38] is by far the most realistic in as it takes into account the routing between the satellites when connecting two different places on earth. Whereas the other numbers only take the round-trip time from earth to the satellite and back.

Table 8. Round trip time numbers for the considered NGSO constellations

| Constellation | Round trip time | Ref. |
|---|---|---|
| Telesat LEO | 18 - 40 ms | [39] |
| SpaceX Starlink | 50 - 75 ms | [38] |
| OneWeb LEO | 32 ms | [40] |
| Astrome SpaceNet | 10 ms | [32] |
| Audacy | < 1000 ms | [33] |

### *3.7 Overall architecture latency*

The overall latency of the architectures can be defined as followed:

$$t_{overall} = t_{revisit} + t_{uplink} + t_{delay} + t_{routing} \qquad (1)$$

In Equ. (1) the $t_{revisit}$ duration is defined as the time it takes for an IoT/M2M constellation nano-satellite to come within view of the IoT/M2M user. As shown in section 3.1 this number can be reduced to zero if the nano-satellite constellation uses enough satellites in polar orbits. The $t_{uplink}$ duration is defined as the total time it takes for an IoT/M2M user to uplink its data to the nano-satellite. Section 3.2 showed that this number is mainly dependent on the data rate of the link and the protocol latency and not on the propagation delay. The $t_{delay}$ duration is the time it takes before the nano-satellite can forward the data through the network. For the self-sustaining network this number is zero if the ISLs are always on. For the NGSO constellation data relay this duration is the time it takes for the nano-satellite to come is the time it takes for the nano-satellite to come within the field of a NGSO satellite. Finally, the $t_{routing}$ is the rest of the time it takes for the data to travel through the network to an internet connected ground station. For the self-sustaining network of nano-satellites this number depends on the altitude of the constellation and the number of satellites as explained in section 3.3. For the NGSO constellation data relay the latency reported by the constellations were taken as explained in section 3.6.

## 4. Results

This section will present the results for the latency analysis of the architecture using the self-staining network of nano-satellites and the architecture that uses higher NGSO constellations to relay data.

### *4.1 Self-sustaining network*

Based on the formulas discussed in section 3.1 to 3.3 the routing time $t_{routing}$ is calculated for the self-sustaining network of nano-satellites. This data is tabulated in Table 9.

Table 9. Routing delay for self-sustaining network of nano-satellites

| El | H [km] | $t_{prop,ul}$ [ms] | N | m | n | $t_{ISL}$ [ms] | $\gamma N_s N_G^{-1} t_{hop}$ [ms] | $t_{prop,dl}$ [ms] | $t_{route}$ [ms] |
|---|---|---|---|---|---|---|---|---|---|
| 10° | 350 | 4.35 | 210 | 21 | 10 | 6.73 | 101.49 | 4.35 | 105.83 |
| | 400 | 4.80 | 190 | 19 | 10 | 7.43 | 99.18 | 4.80 | 103.98 |
| | 450 | 5.23 | 162 | 18 | 9 | 8.11 | 97.45 | 5.23 | 102.68 |
| | 500 | 5.65 | 128 | 16 | 8 | 8.75 | 96.12 | 5.65 | 101.77 |
| | 550 | 6.05 | 120 | 15 | 8 | 9.38 | 95.10 | 6.05 | 101.15 |
| 20° | 350 | 2.92 | 528 | 33 | 16 | 4.31 | 119.31 | 4.35 | 123.66 |
| | 400 | 3.28 | 433 | 29 | 15 | 4.84 | 114.71 | 4.80 | 119.51 |
| | 450 | 3.63 | 351 | 27 | 13 | 5.37 | 111.23 | 5.23 | 116.46 |
| | 500 | 3.98 | 288 | 24 | 12 | 5.87 | 108.52 | 5.65 | 114.17 |
| | 550 | 4.31 | 253 | 23 | 11 | 6.37 | 106.38 | 6.05 | 112.43 |
| 30° | 350 | 2.17 | 1152 | 48 | 24 | 2.96 | 141.78 | 4.35 | 146.13 |
| | 400 | 2.46 | 882 | 42 | 21 | 3.35 | 134.36 | 4.80 | 139.15 |
| | 450 | 2.75 | 722 | 38 | 19 | 3.74 | 128.68 | 5.23 | 133.92 |
| | 500 | 3.03 | 595 | 35 | 17 | 4.13 | 124.24 | 5.65 | 129.89 |
| | 550 | 3.31 | 512 | 32 | 16 | 4.50 | 120.68 | 6.05 | 126.74 |

The switching/processing delay considered in the calculations is 3 mS, this is based on the assumption made in [16], this delay is protocol and data rate dependent and can vary for a different application. The calculations show that $t_{routing}$ delay can vary between 100 mS to 150 mS for different altitudes H and El considered. In the table, the lower elevation limit for user-terminal to the nanosatellite is considered for 10, 20 and 30 degrees El, with the increase of lower Elevation limit, it can be seen that larger number of satellites are needed to provide continuous global coverage. In the table, various altitudes are considered between 350 to 550 km which also has an influence on the total number of satellites needed for continuous global coverage. The $t_{ISL}$ is calculated based on the line-of-sight distance between the nanosatellites in the same orbital plane. $t_{forward,ring}$ depends on the worst-case number of hops needed before data propagates to the satellite closest to the ground station and $t_{downlink}$ is calculated based on the line-of-sight distance between the nanosatellite at an elevation angle of 10 degrees (minimum elevation limit for nanosatellite to ground station) and the ground station. $t_{routing}$ is the sum of $t_{forward,ring}$ and $t_{downlink}$.

### *4.2 NGSO data relay*

Using the NGSO relay simulator the relay availability for a nano-satellite in a 500 km polar orbit to each of the NGSO constellations was analysed. For each of the

constellations four different cases are simulated varying the right ascension Ω of the nano-satellite to compensate for perturbation effects not being taken into account in the simulator. All cases were simulated over 7 days starting at 1 September 2019 10:00:00.000 UTCG.

Fig. 16 and Fig. 17 show histograms of the pass and gap durations respectively for each of the five constellations. The histograms for the pass durations show each individual pass with a NGSO satellite. It is possible that at a particular moment the nano-satellite is able to communicate with multiple satellites in the NGSO constellation. The histograms for the gap durations are created by computing the time in which the nano-satellite was not in the FoV of any of the NGSO satellites in the constellation.

All histograms are fitted with a normal distribution to indicate the mean and variation of the pass and gap durations. As can be seen in Table 10 these do not vary significantly between the different cases for the right ascension Ω of the nano-satellite, except for the scenario of a relay to OneWeb's LEO constellation. The polar orbits of OneWeb make the pass and gap durations strongly dependent on whether or not the orbital plane of the nano-satellite lines up with one of the polar orbits in the constellation. In the right ascension Ω = 0° case the plane lined up and more than double the number of passes are registered and the average gap duration decreased. However, the additional passes are of short duration and therefore lower the mean of the overall distribution.

Table 10. Tabulated results of NGSO relay availability analysis

| Ω | $N_{passes}$ | $\mu_{pass}$ | $\sigma_{pass}$ | $N_{gaps}$ | $\mu_{gap}$ | $\sigma_{gap}$ |
|---|---|---|---|---|---|---|
| *Telesat LEO* | | | | | | |
| 0° | 1155 | 132 s | 132 s | 902 | 526 s | 492 s |
| 45° | 837 | 162 s | 98 s | 710 | 668 s | 480 s |
| 90° | 801 | 180 s | 129 s | 627 | 770 s | 530 s |
| 135° | 948 | 148 s | 112 s | 770 | 612 s | 527 s |
| *SpaceX Starlink LEO* | | | | | | |
| 0° | 36574 | 132 s | 145 s | 1649 | 26 s | 32 s |
| 45° | 38692 | 116 s | 85 s | 1133 | 24 s | 28 s |
| 90° | 36343 | 119 s | 91 s | 1351 | 29 s | 40 s |
| 135° | 36020 | 125 s | 116 s | 1238 | 25 s | 31 s |
| OneWeb LEO | | | | | | |
| 0° | 14996 | 158 s | 272 s | 2087 | 72 s | 169 s |
| 45° | 6826 | 345 s | 359 s | 226 | 266 s | 196 s |
| 90° | 6046 | 381 s | 382 s | 235 | 345 s | 316 s |
| 135° | 7007 | 331 s | 372 s | 238 | 259 s | 214 s |
| Astrome SpaceNet | | | | | | |
| 0° | 2915 | 187 s | 66 s | 725 | 518 s | 736 s |
| 45° | 2930 | 185 s | 64 s | 741 | 504 s | 735 s |
| 90° | 2961 | 182 s | 62 s | 611 | 605 s | 778 s |
| 135° | 3027 | 179 s | 63 s | 702 | 532 s | 753 s |
| Audacy | | | | | | |
| 0° | 331 | 1251 s | 981 s | 331 | 215 s | 176 s |
| 45° | 757 | 1180 s | 643 s | 325 | 225 s | 186 s |
| 90° | 705 | 1280 s | 997 s | 356 | 184 s | 112 s |
| 135° | 676 | 1326 s | 1096 s | 328 | 206 s | 138 s |

The pass duration with the constellation of Astrome has the lowest variation. This is because the constellation has only set of orbits providing coverage between ±38° latitude. This also results into the gap distribution having two peaks.

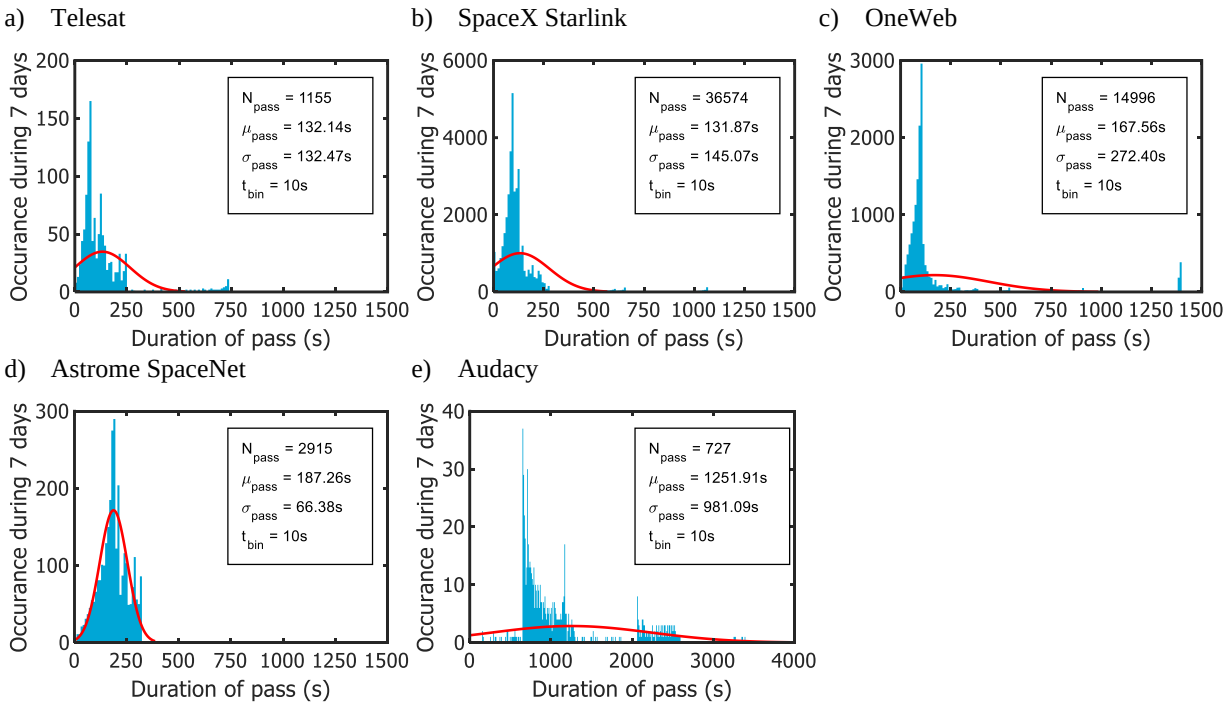


Fig. 16. Distributions of pass durations for a relay with a) Telesat LEO constellation, b) SpaceX Starlink constellation, c) OneWeb LEO constellation, d) Astrome SpaceNet constellation and e) Audacy constellation. *Note: the duration range for Audacy's histogram is larger than the other*

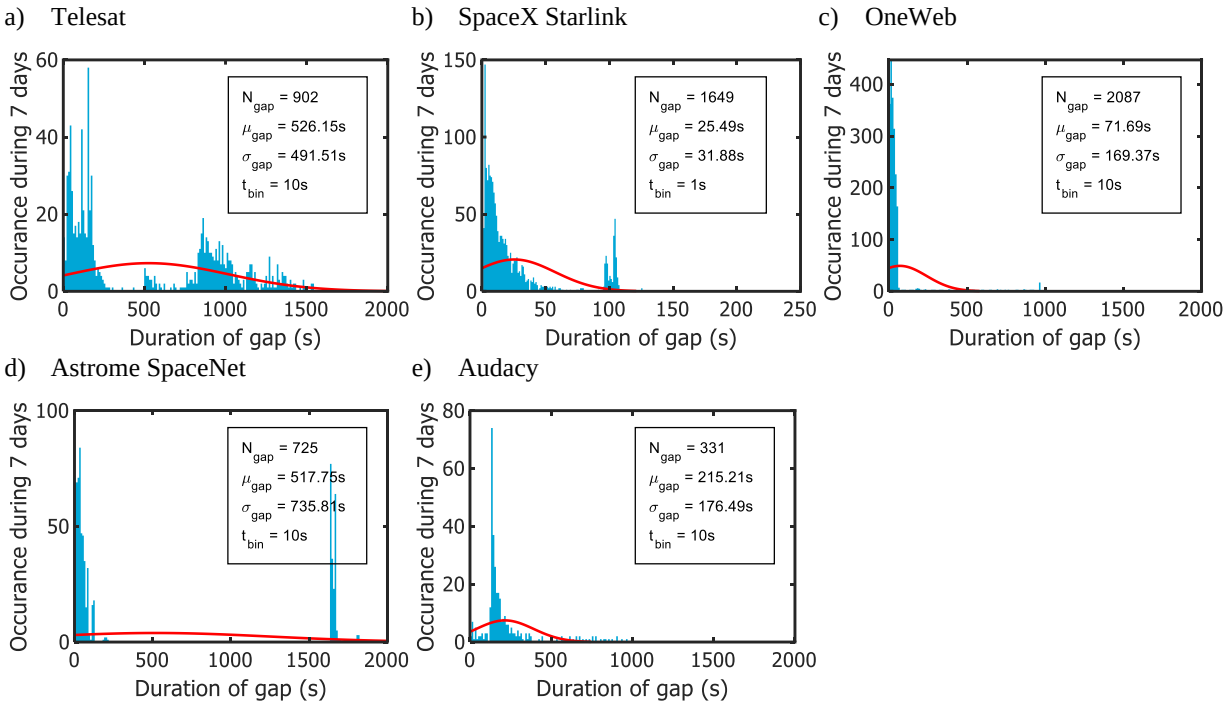


Fig. 17. Distributions of gap durations for a relay with a) Telesat LEO constellation, b) SpaceX Starlink constellation, c) OneWeb LEO constellation, d) Astrome SpaceNet constellation and e) Audacy constellation. *Note: the duration range for SpaceX's historgram is smaller than the others.*

One with a long duration for the part in which the nano-satellite is traveling beyond ±38° latitude and one with a short for the part in which the nano-satellite is traveling within the ±38° latitude and passing between the satellites.

Even though the Audacy MEO constellation is designed for coverage in LEO the simulations show that the coverage is not continuous. These gaps are caused due to the line of sight intersecting the surface of the earth. At higher orbits it is possible that the coverage is continuously provided by the three satellites.

Fig. 18 shows just the normalized distributions of the pass durations respectively. A relay with the Audacy constellation provides the longest pass durations, on average about 20 minutes.

The disadvantage is however the longer inter-satellite distance which requires a higher transmission power. The other constellations all provide a pass duration on average of about 2 to 4 minutes with SpaceX and Astrome having the lowest variance. It should be noted that the OneWeb constellation provides on average in this configuration 3 minutes of contact time, however as can be seen Fig. 16-c there are also significantly longer pass durations of about 20 minutes when the planes align and the nano-satellite can catch up with a satellite of OneWeb.

Fig. 19 shows just the normalized distributions of the gap durations. A relay with SpaceX would provide the lowest gap durations and therefore also the lowest average latency caused by the nano-satellite having to wait to come in view of the higher orbit NGSO satellite. OneWeb provides the second lowest gap duration on average and Audacy the third, caused by the line of sight intersecting the surface of the earth. Telesat and Astrome provide the longest gap duration on average due to the orbits being spaced out, in the case of Telesat, or concentrated around one region of the earth, in the case of Astrome.

A different metric to evaluate the latency of the NGSO data relay concept is to look at the total gap time over the whole simulation period.

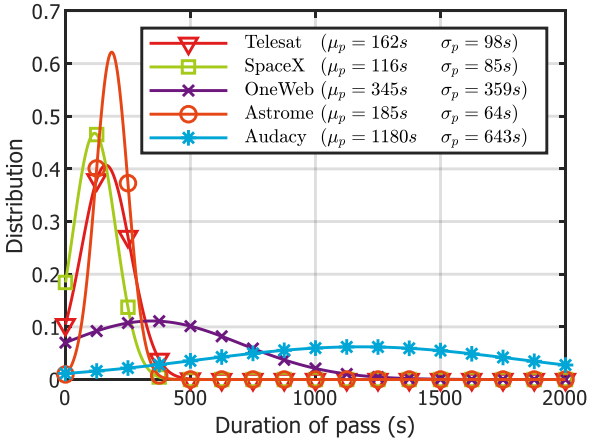


Fig. 18. Normalize pass distributions for a nano-satellite (500 km, i = 90°, Ω = 45°) to higher orbit NGSO constellations.

Fig. 20 shows the total time the satellite is in darkness; the time where there is no relay available. Similar conclusions can be taken as to when just looking at the gap distributions. SpaceX and Audacy provide the most coverage, and Telesat and Astrome the least.

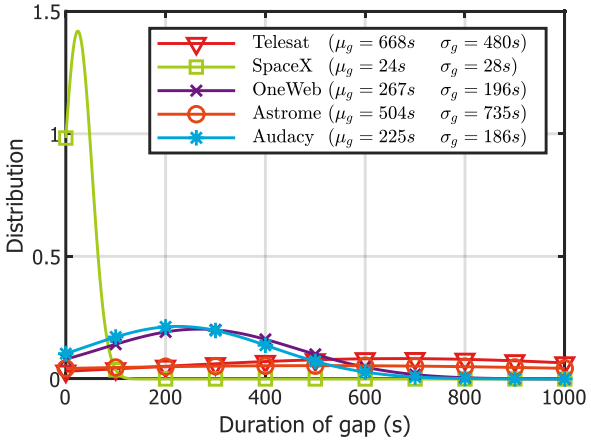


Fig. 19. Normalize gap distributions for a nano-satellite (500 km, i = 90°, Ω = 45°) to higher orbit NGSO constellations.

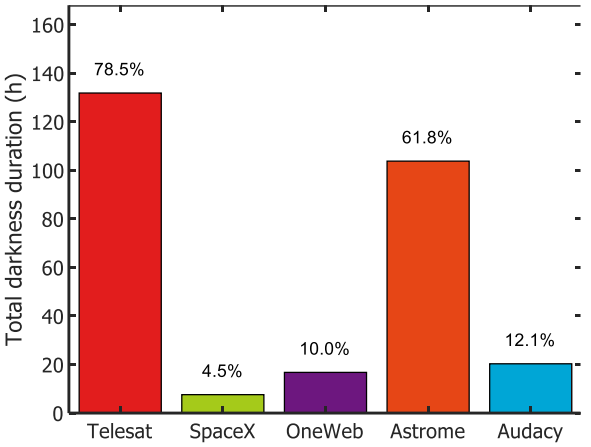


Fig. 20. Total darkness duration for a nano-satellite (500 km, i = 90°, Ω = 45°) relay to higher orbit NGSO constellations during a 7-day period.

## 5. Discussion

Fig. 21 shows how each of the durations add up to the overall architecture latency in an example worse-case scenario. In this scenario a packet of 1024 bytes is uplinked to the nano-satellite using the LoRa protocol with a 3 second protocol latency. This results into an uplink latency of about 4 seconds. For the self-sustaining network of nano-satellites the constellation is selected to be at 500 km altitude with a user minimum elevation angle of 10°. This results into a routing latency of about 102 ms. For the architecture using the NGSO data relays the average gap duration and average routing delay is taken as the worse-case number.

For the self-sustaining network of nano-satellites the biggest contributor is the time to uplink the data to the satellite. Because the network from ISLs is always on the data can be immediately routed further. There is a disadvantage however with having a network of ISL that is always turned on. In this case the duty cycle of the communication system is much higher than what is common for a nano-satellite. This requires a higher power budget on the satellite to be dedicated to maintaining these ISLs.

For the NGSO constellation data relay architecture the biggest contributor is the gap duration. Depending on when the data arrives at the nano-satellite there is a chance it can immediately relay this data, with a probability varying by the used relay constellation as seen in Fig. 20, or it has to wait up till several minutes before the relay becomes available, as shown in Fig. 19.

In the NGSO constellation data relay architecture the actual latency will therefore depend on at which point in the orbit of the nano-satellite the IoT/M2M data is received. Then at that moment the position of the nano-satellite with respect to the NGSO constellation should be considered. A possible analysis could be done on the average latency for an IoT/M2M application using this architecture depending on the latitude of its position.

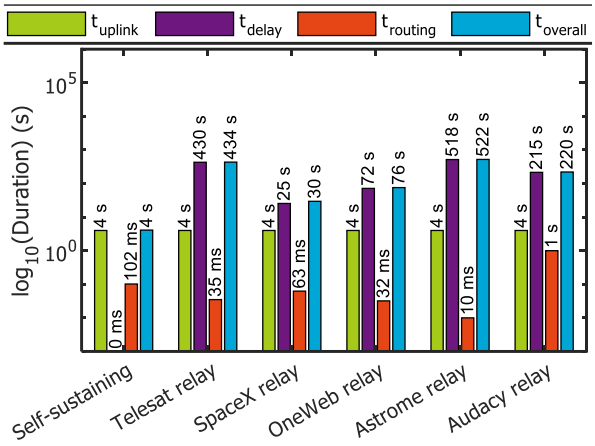


Fig. 21. Main contributing elements to overall latency in the architectures. For the relay architectures the mean gap duration and mean routing latencies are shown.

Some additional assumptions were taken for this architecture that might influence actual latency. First, the setup time required to setup the nano-satellite to NGSO constellation date relay could be in the order of seconds. Therefore, some of the inter-satellite passes can be immediately discarded because there is too little time to setup the link and start communicating. Second, the whole FoV of the NGSO constellation satellites might not be continuously filled with spotbeams and the spotbeams might be moving around. This could further reduce the effective communication time. In addition, frequency reuse schemes are used from spotbeam to

spotbeam which depending on the protocol used might introduce some overhead in handovers. Finally, there were no limitations put on the communication system of the nano-satellite. The performance of this architecture will eventually come down to the capabilities of the communication hardware on the nano-satellite. If the hardware on the nano-satellite can work in a wide FoV and can handle fast switching between spotbeams it can utilize most of the inter-satellite passes. Exploring the technical capabilities of the nano-satellite hardware is part of the roadmap of the authors of this paper.

## 6. Conclusions

In this paper two communication architectures for IoT/M2M nano-satellite missions are presented. The first architecture uses a self-sustaining network of nano-satellites. In this architecture the achievable latency can be in the order of seconds depending on the data rate of the IoT/M2M protocol. The latency through the network alone is always in the order of hundred milliseconds if the ISLs are kept turned on. For the communication system of this architecture this means a high duty cycle is required for a low latency. The second architecture uses planned NGSO constellations for data relay. A first order analysis showed that this architecture could achieve a latency down to several minutes which would be low enough for some IoT/M2M applications. The capabilities of the communication system of the nano-satellite to communicate in short inter-satellite pass durations will primarily determine the performance of this architecture.

## Acknowledgements

The authors of this paper would like to thank Analytical Graphics Incorporated for providing a license for STK Free.

## References

[1] *Hiber. "www.hiber.global." https://hiber.global (accessed.*

[2] *Fleet. "Fleet." https://www.fleet.space/ (accessed.*

[3] *Lacuna Space. "Lacuna Space." https://www.lacuna.space/ (accessed.*

[4] *Kepler Communications Inc. "Application for Fixed Satellite Service by Kepler Communications Inc. [SAT-PDR-20161115-00114]." https://fcc.report/IBFS/SAT-PDR-20161115-00114 (accessed.*

[5] *K. Devaraj et al., "Planet High Speed Radio: Crossing Gbps from a 3U CubeSat," 2019.*

[6] *R. Welle et al., "A CubeSat-Based Optical Communication Network for Low Earth Orbit," 2017.*

[7] *I. del Portillo, B. G. Cameron, and E. F. Crawley, "A technical comparison of three low earth orbit satellite constellation systems to provide global broadband," Acta Astronaut, vol. 159, pp. 123-135, 2019/06/01/ 2019, doi: 10.1016/j.actaastro.2019.03.040.*

[8] *OneWeb. "Application for Fixed Satellite Service by WorldVu Satellites Limited [SAT-LOI-20160428-00041]." https://fcc.report/IBFS/SAT-LOI-20160428-00041 (accessed.*

[9] *Astrome Space Technologies SARL, "Astrome: SpaceNet Constellation Design Yellow Paper," 2019-06-23, 2019.*

[10] *I. V. Karunanithi, C. J. M. Verhoeven, and E. W. McCune, "Solutions to Data Congestion in Space; mmWave Communication for Nano-Satellites," in 2019 IEEE Aerospace Conference, 2-9 March 2019 2019, pp. 1-12, doi: 10.1109/AERO.2019.8742131. [Online]. Available: https://ieeexplore.ieee.org/ielx7/8727865/8741395/08742131.pdf?tp=&arnumber=8742131&isnumber=8741395&ref=*

[11] *K. S. Low, M. S. C. Tissera, and J. W. Chia, In-orbit Results of VELOX-II Nanosatellite (Proceedings of the 2016 IEEE Region 10 Conference). 2016, pp. 3658-3663.*

[12] *A. T. Ltd, "Addvalue's Inter-Satellite Data Relay Terminal completes one year of in-orbit testing," ed, 2016.*

[13] *A. Babuscia et al., "CommCube 1 and 2: A CubeSat Series of Missions to Enhance Communication Capabilities for CubeSat," in 2013 IEEE Aerospace Conference, (IEEE Aerospace Conference Proceedings, 2013.*

[14] *Z. QU, G. ZHANG, H. CAO, and A. J. XIE, "LEO Satellite Constellation for Internet of Things," IEEE Access, 2017.*

[15] *M. D. Sanctis, E. Cianca, G. Araniti, I. Bisio, and R. Prasad, "Satellite Communications Supporting Internet of Remote Things," IEEE INTERNET OF THINGS JOURNAL, pp. VOL 3, NO. 1, FEBRUARY 2016.*

[16] *Q. Yang, D. I. Laurenson, and a. J. A. Barria, "On the Use of LEO Satellite Constellation for Active Network Management in Power Distribution Networks," IEEE TRANSACTIONS ON SMART GRID, pp. VOL. 3, NO. 3, SEPTEMBER 2012.*

[17] *M. Corici et al., "Assessing satellite-terrestrial integration opportunities in the 5G environment," September 2016.*

[18] *L. Yushi, J. Fei, and Y. Hui, "Study on Application Modes of Military Internet of Things (MIOT)," 2012 IEEE International Conference on Computer Science and Automation Engineering (CSAE), 2012.*

[19] IoT Academy. "IoT Connectiviteit LPWAN update 2019: Wat is er beschikbaar in Nederland en daarbuiten?" https://premium.nl/wp-content/uploads/2019/01/20190124-IoT-whitepaper-LPWAN.pdf (accessed.

[20] Lacuna Space. "Lacuna Space Achieves Major Milestone for LoRa® in Space." http://www.parabolicarc.com/2019/08/15/lacuna-space-achieves-major-milestone-for-lora-in-space (accessed.

[21] Sigfox. "Sigfox Radio Configurations." https://build.sigfox.com/sigfox-radio-configurations-rc (accessed.

[22] Accent Systems. "Differences between Nb-IoT and LTE-M." https://accent-systems.com/blog/differences-nb-iot-lte-m/ (accessed.

[23] Telesat Canada. "Application for Fixed Satellite Service by Telesat Canada [SAT-PDR-20161115-00108]." https://fcc.report/IBFS/SAT-PDR-20161115-00108 (accessed.

[24] Telesat Canada. "Application for Fixed Satellite Service by Telesat Canada [SAT-PDR-20170301-00023]." https://fcc.report/IBFS/SAT-PDR-20170301-00023 (accessed.

[25] Space Exploration Holdings. "Application for Fixed Satellite Service by Space Exploration Holdings, LLC [SAT-LOA-20161115-00118]." https://fcc.report/IBFS/SAT-LOA-20161115-00118 (accessed.

[26] Space Exploration Holdings. "Application for Fixed Satellite Service by Space Exploration Holdings, LLC [SAT-LOA-20170301-00027]." https://fcc.report/IBFS/SAT-LOA-20170301-00027 (accessed.

[27] Space Exploration Holdings. "Application for Fixed Satellite Service by Space Exploration Holdings, LLC [SAT-MOD-20181108-00083]." https://fcc.report/IBFS/SAT-MOD-20181108-00083 (accessed.

[28] Space Exploration Holdings. "Application for Fixed Satellite Service by Space Exploration Holdings, LLC [SAT-MOD-20190830-00087]." https://fcc.report/IBFS/SAT-MOD-20190830-00087 (accessed.

[29] OneWeb. "Application for Fixed Satellite Service by WorldVu Satellites Limited [SAT-LOI-20170301-00031]." https://fcc.report/IBFS/SAT-LOI-20170301-00031 (accessed.

[30] OneWeb. "Application for Fixed Satellite Service by WorldVu Satellites Limited [SAT-MOD-20180319-00022]." https://fcc.report/IBFS/SAT-MOD-20180319-00022 (accessed.

[31] SpaceNews_Inc. "OneWeb scales back baseline constellation by 300 satellites - SpaceNews.com." https://spacenews.com/oneweb-scales-back-constellation-by-300-satellites/ (accessed.

[32] Astrome Space Technologies SARL, "Astrome's SpaceNet: Ubiquitous Internet For Real," 2019-07-08 2019. [Online]. Available: https://astrome.co/publications/white-paper.pdf.

[33] Audacy Corporation. "Application for Fixed Satellite Service Other by Audacy Corporation [SAT-LOA-20161115-00117]." https://fcc.report/IBFS/SAT-LOA-20161115-00117 (accessed.

[34] D. C. BESTE and M. IEEE, "Design of Satellite Constellation for Optimal Continous Coverage," IEEE TRANSACTIONS ON AEROSPACE AND ELECTRONIC SYSTEMS, pp. AES-14, NO. 3, MAY 1978.

[35] A. H. Juan Luis Cano Rodríguez, Shreyas Bapat, Nikita Astrakhantsev, Jorge Martinez, Chatziargyriou Eleftheria, Daniel Lubián, et al., "poliastro/poliastro: poliastro 0.13.0 (late PyAstro '19 edition)," 2019, doi: 10.5281/zenodo.3360886

[36] P. a. V. Ramachandran, G., "Mayavi: 3D Visualization of Scientific Data," Computing in Science & Engineering, vol. 13, 2, pp. 40--51, 2011.

[37] F. L. Markley, "Kepler Equation solver," Celestial Mechanics & Dynamical Astronomy, journal article vol. 63, no. 1, pp. 101-111, March 01 1995, doi: 10.1007/bf00691917.

[38] M. Handley, "Delay is Not an Option," presented at the Proceedings of the 17th ACM Workshop on Hot Topics in Networks - HotNets '18, 2018. [Online]. Available: http://delivery.acm.org/10.1145/3290000/3286075/p85-Handley.pdf?ip=145.94.9.203&id=3286075&acc=ACTIVE%20SERVICE&key=0C390721DC3021FF%2E512956D6C5F075DE%2E4D4702B0C3E38B35%2E4D4702B0C3E38B35&acm=1563434987_db0a1051c1be0136bb125fc6564e008a.

[39] Telesat Canada. "World's First 5G Backhaul Demo over LEO Satellite | Telesat." https://www.telesat.com/news-events/worlds-first-5g-backhaul-demo-over-leo-satellite (accessed.

[40] OneWeb. "OneWeb's Satellites Deliver Real-Time HD Streaming from Space | OneWeb." https://www.oneweb.world/media-

*center/onewebs-satellites-deliver-real-time-hd-streaming-from-space (accessed.*

This page intentionally left blank.

# Bibliography


[1] K. Leveque, Z. Cuseo, L. Carleton, J. King, and R. Babb, “Unlocking the Next Generation of Nano-Satellite Missions with 320 Mbps Ka-Band Downlink: On-Orbit Results,” *33rd Annual AIAA/USU Conference on Small Satellites*, 2019.

[2] K. Devaraj, M. Ligon, E. Blossom, *et al.*, “Planet High Speed Radio: Crossing Gbps from a 3U CubeSat,” *33rd Annual AIAA/USU Conference on Small Satellites*, 2019.

[3] I. del Portillo, B. G. Cameron, and E. F. Crawley, “A technical comparison of three low earth orbit satellite constellation systems to provide global broadband,” *Acta Astronautica*, vol. 159, pp. 123–135, 2019, ISSN: 0094-5765. DOI: https://doi.org/10.1016/j.actaastro.2019.03.040.

[4] I. V. Karunanithi, C. J. M. Verhoeven, and E. W. McCune, “Solutions to Data Congestion in Space; mmWave Communication for Nano-Satellites,” *2019 IEEE Aerospace Conference*, pp. 1–12, 2019, ISSN: 1095-323X. DOI: 10.1109/AERO.2019.8742131. [Online]. Available: https://ieeexplore.ieee.org/ielx7/8727865/8741395/08742131.pdf?tp=&arnumber=8742131&isnumber=8741395&ref=.

[5] E. Kulu, “Database | nanosats.eu | Erik Kulu,” *Airtable*, 2020. [Online]. Available: https://airtable.com.

[6] Web Page, 2019. [Online]. Available: https://hiber.global.

[7] Web Page, 2019. [Online]. Available: https://www.fleet.space.

[8] Web Page, 2019. [Online]. Available: https://www.lacuna.space/.

[9] FierceWireless, “Kepler delivers 120 Mbps uplink to Arctic via satellite broadband,” 2019. [Online]. Available: https://www.fiercewireless.com/tech/kepler-delivers-120-mbps-uplink-to-arctic-via-satellite-broadband.

[10] C. Peebles, The CORONA project: America’s first spy satellites. Naval Inst Press, 1997, ISBN: 1557506884.

[11] F. E. Tubbal, R. Raad, and K. Chin, “A Survey and Study of Planar Antennas for Pico-Satellites,” *IEEE Access*, vol. 3, pp. 2590–2612, 2015, ISSN: 2169-3536. DOI: 10.1109/ACCESS.2015.2506577.

[12] E. Mabrouk, “What are SmallSats and CubeSats?” *NASA*, 2015. [Online]. Available: http://www.nasa.gov/content/what-are-smallsats-and-cubesats.

[13] “3D SpaceX Starlink Satellite | CGTrader,” [Online]. Available: https://www.cgtrader.com/3d-models/space/spaceship/spacex-starlink-satellite.

[14] K. P. Tan and E. Trachtman, “Inter-Satellite Data Relay System (IDRS) for LEO Satellites Using a Commercially Available GEO Satellite System,” 2019.

[15] K. S. Low, M. S. C. Tissera, and J. W. Chia, In-orbit Results of VELOX-II Nanosatellite, ser. Proceedings of the 2016 IEEE Region 10 Conference. 2016, pp. 3658–3663, ISBN: 978-1-5090-2597-8. [Online]. Available: %3CGo%20to%20ISI%3E://WOS:000400378903168.

[16] Addvalue Technologies Ltd, “Addvalue’s Inter-Satellite Data Relay Terminal completes one year of in-orbit testing,” 2016.

[17] NanoAvionics, “EU’s Horizon 2020 And ESA Are Part Of €10 Million Grant For NanoAvionics’ Global IoT Constellation-as-a-Service Aimed at IoT/M2M Communications Providers,” 2019. [Online]. Available: https://n-avionics.com/eus-horizon-2020-and-esa-are-part-of-e10-million-grant-for-nanoavionics-global-iot-constellation-as-a-service-aimed-at-iot-m2m-communications-providers/.

[18] B. Li, X. Peng, H. Yang, and G. Liu, “Modeling and performance analysis of multi-layer satellite networks based on STK,” in *Lecture Notes of the Institute for Computer Sciences, Social-Informatics and Telecommunications Engineering, LNICST*, vol. 226 LNICST, 2018, pp. 382–393. DOI: 10.1007/978-3-319-73564-1_38. [Online]. Available: https://www.scopus.com/inward/record.uri?eid=2-s2.0-85045218569&doi=10.1007%2f978-3-319-73564-1_38&partnerID=40&md5=a103dc9e2e06f59e8c5efada380c8d3c%20https://link.springer.com/content/pdf/10.1007%2F978-3-319-73564-1_38.pdf.

[19] M. Handley, “Delay is Not an Option,” *Proceedings of the 17th ACM Workshop on Hot Topics in Networks - HotNets ’18*, pp. 85–91, 2018. DOI: 10.1145/3286062.3286075.

[20] P. K. Chowdhury, M. Atiquzzaman, and W. Ivancic, “Handover schemes in space networks: Classification and performance comparison,” *Smc-It 2006: 2nd IEEE International Conference on Space Mission Challenges for Information Technology, Proceedings*, pp. 101–+, 2006.

[21] J.-H. Hu, K. L. Yeung, and T. Li, “Routing and re-routing in a LEO/MEO two-tier mobile satellite communications system with inter-satellite links,” in *IEEE International Conference on Communications*, vol. 1, pp. 134–138. [Online]. Available: https://www.scopus.com/inward/record.uri?eid=2-s2.0-0033697775&partnerID=40&md5=9c1b7a593b63ed15138f5589849cb

[22] Y. Liu, W. Xu, F. Tang, L. Kuang, and Y. Yang, “An improved multi-path routing algorithm for hybrid LEO-MEO satellite networks,” in *Proceedings - 15th IEEE International Conference on Trust, Security and Privacy in Computing and Communications, 10th IEEE International Conference on Big Data Science and Engineering and 14th IEEE International Symposium on Parallel and Distributed Processing with Applications, IEEE TrustCom/BigDataSE/ISPA 2016*, pp. 1101–1105. DOI: 10.1109/TrustCom.2016.0181. [Online]. Available: https://www.scopus.com/inward/record.uri?eid=2-s2.0-85015174769&doi=10.1109%2fTrustCom.2016.0181&partnerID=40&md5=97f41081885eea47f803aea9c3d5ceaa%20https://ieeexplore.ieee.org/ielx7/7845250/7846883/07847064.pdf?tp=&arnumber=7847064&isnumber=7846883&ref=.

[23] International Astronautical Federation, “IAF : International Astronautical Congress (IAC),” [Online]. Available: https://www.iafastro.org/events/iac/.

[24] Small Satellite Conference, “SmallSat - Home,” [Online]. Available: https://smallsat.org/.

[25] J. van ’t Hof, “AE4020 Literature Study - Small satellite state-of-the-art communication technologies,” 2020.

[26] Computer Program, 2020. [Online]. Available: https://github.com/Josvth/hermes-simulator.

[27] L. Couch, “Digital and Analog Communication Systems, LW Couch, II,”

[28] Planet, “Planet imagery product specifications,” *Planet Team: San Francisco, CA, USA*, 2019.

[29] “Lemur-2 - eoPortal Directory - Satellite Missions,” [Online]. Available: https://directory.eoportal.org/web/eoportal/satellite-missions/l/lemur.

[30] S. Global, “Spire Global, Inc. FCC International Bureau Filings [IBFS],” 2020. [Online]. Available: https://fcc.report/IBFS/Company/Spire-Global-Inc.

[31] “BlackSky Constellation - eoPortal Directory - Satellite missions,” [Online]. Available: https://directory.eoportal.org/web/eoportal/satellite-missions/b/blacksky-constellation.

[32] G. D. Krebs, “BlackSky Global 1, ..., 60,” [Online]. Available: https://space.skyrocket.de/doc_sdat/blacksky-global.htm.

[33] “BlackSky | Be the first to know,” [Online]. Available: https://blacksky.com/.

[34] G. Denis, A. Claverie, X. Pasco, *et al.*, “Towards disruptions in Earth observation? New Earth Observation systems and markets evolution: Possible scenarios and impacts,” *Acta Astronautica*, vol. 137, pp. 415–433, 2017, ISSN: 0094-5765. DOI: https://doi.org/10.1016/j.actaastro.2017.04.034.

[35] Web Page. [Online]. Available: https://www.newspace.im/constellations/astro-digital.html.

[36] "CICERO - eoPortal Directory - Satellite Missions," [Online]. Available: https://directory.eoportal.org/web/eoportal/satellite-missions/content/-/article/cicero.

[37] H. Saito, J. Hirokawa, T. Tomura, *et al.*, "Development of Compact SAR Systems for Small Satellite," in *IGARSS 2019 - 2019 IEEE International Geoscience and Remote Sensing Symposium*, pp. 8440–8443, ISBN: 2153-7003. DOI: 10.1109/IGARSS.2019.8898663.

[38] "QuickBird-2 - eoPortal Directory - Satellite Missions," [Online]. Available: https://directory.eoportal.org/web/eoportal/satellite-missions/q/quickbird-2.

[39] "Ikonos-2 - eoPortal Directory - Satellite Missions," [Online]. Available: https://directory.eoportal.org/web/eoportal/satellite-missions/i/ikonos-2.

[40] "GeoEye-1 - eoPortal Directory - Satellite Missions," [Online]. Available: https://directory.eoportal.org/web/eoportal/satellite-missions/g/geoeye-1.

[41] "DigitalGlobe | WorldView-3," [Online]. Available: http://worldview3.digitalglobe.com/.

[42] "WorldView-2 - eoPortal Directory - Satellite Missions," [Online]. Available: https://directory.eoportal.org/web/eoportal/satellite-missions/v-w-x-y-z/worldview-2.

[43] "WorldView-3 - eoPortal Directory - Satellite Missions," [Online]. Available: https://directory.eoportal.org/web/eoportal/satellite-missions/v-w-x-y-z/worldview-3.

[44] "Landsat-7 - eoPortal Directory - Satellite Missions," [Online]. Available: https://directory.eoportal.org/web/eoportal/satellite-missions/l/landsat-7.

[45] "Landsat-8 - eoPortal Directory - Satellite Missions," [Online]. Available: https://directory.eoportal.org/web/eoportal/satellite-missions/l/landsat-8-ldcm.

[46] "Landsat-9 - eoPortal Directory - Satellite Missions," [Online]. Available: https://directory.eoportal.org/web/eoportal/satellite-missions/l/landsat-9.

[47] "Spot-5 - eoPortal Directory - Satellite Missions," [Online]. Available: https://directory.eoportal.org/web/eoportal/satellite-missions/s/spot-5.

[48] Z. Katona, C. Kourogiorgas, A. D. Panagopoulos, and N. Jeannin, "Capacity analysis of high-throughput satellite links for Earth observation missions," *International Journal of Satellite Communications and Networking*, vol. 33, no. 5, pp. 429–449, 2015, ISSN: 1542-0973. DOI: 10.1002/sat.1125.

[49] Z. Katona, M. Grasslin, A. Donner, *et al.*, "A flexible LEO satellite modem with Ka-band RF frontend for a data relay satellite system," *International Journal of Satellite Communications and Networking*, 2018, ISSN: 1542-0973. DOI: 10.1002/sat.1333.

[50] Planet Labs, "Planet Labs 0143-EX-ST-2019 FCC Experimental License," 2019. [Online]. Available: https://fcc.report/ELS/Planet-Labs/0143-EX-ST-2019.

[51] E. Peral, S. Statham, S. Taneli, *et al.*, "Raincube, a Ka-band precipitation radar in a 6U CubeSat," 2017.

[52] Web Page, 2019. [Online]. Available: https://www.fleet.space/.

[53] Kepler Communications Inc., "Application for Fixed Satellite Service by Kepler Communications Inc. [SAT-PDR-20161115-00114]," 2016. [Online]. Available: https://fcc.report/IBFS/SAT-PDR-20161115-00114.

[54] Hiber Inc., "Application for Mobile Satellite Service by Hiber Inc. [SAT-LOI-20180910-00069]," 2018. [Online]. Available: https://fcc.report/IBFS/SAT-LOI-20180910-00069.

[55] Lacuna Space, "Lacuna Space Achieves Major Milestone for LoRa® in Space.," 2019. [Online]. Available: http://www.parabolicarc.com/2019/08/15/lacuna-space-achieves-major-milestone-for-lora-in-space.

[56] Premium.nl, "IOT CONNECTIVITEIT LPWAN UPDATE 2019: WAT IS BESCHIKBAAR IN NEDERLAND EN DAARBUITEN ?," 2019. [Online]. Available: https://premium.nl/wp-content/uploads/2019/01/20190124-IoT-whitepaper-LPWAN.pdf.

[57] Astrocast, “Products - Astrocast - Astronode™ S Development Kit,” *Astrocast*, [Online]. Available: https://www.astrocast.com/products-astronode-s/.

[58] D. Mohney, “Astrocast secures dedicated ground network for IoT satellites – Space IT Bridge,” [Online]. Available: https://www.spaceitbridge.com/astrocast-secures-dedicated-ground-network-for-iot-satellites.htm.

[59] G. D. Krebs, “Astrocast 0.1, 0.2 (Kiwi, Hawaii),” [Online]. Available: https://space.skyrocket.de/doc_sdat/astrocast-0.htm.

[60] G. D. Krebs, “AprizeSat – Spacecraft and Satellites,” [Online]. Available: https://spaceflight101.com/spacecraft/aprizesat/.

[61] “AprizeSat-3 and 4 - eoPortal Directory - Satellite Missions,” [Online]. Available: https://earth.esa.int/web/eoportal/satellite-missions/a/aprizesat-3-4.

[62] G. D. Krebs, “Orbcomm FM101, ..., FM119 (OG2),” [Online]. Available: https://space.skyrocket.de/doc_sdat/orbcomm-2.htm.

[63] G. D. Krebs, “Proxima 1, 2,” [Online]. Available: https://space.skyrocket.de/doc_sdat/proxima-1.htm.

[64] G. D. Krebs, “Centauri 1, 2,” [Online]. Available: https://space.skyrocket.de/doc_sdat/centauri-1.htm.

[65] NanoAvionics, “High-Performance Multi-Purpose 6U Nano-Satellite Bus Datasheet,” 2020. [Online]. Available: https://nanoavionics.com/wp-content/uploads/2020/03/M6P-2020-03-22-web.pdf.

[66] spaceflight101.com, “Orbcomm G2 – Spacecraft and Satellites,” [Online]. Available: https://spaceflight101.com/spacecraft/orbcomm-g2/.

[67] ORBCOMM, “Application for Mobile Satellite Service by ORBCOMM License Corp. [SAT-MOD-20111021-00207],” 2011. [Online]. Available: https://fcc.report/IBFS/SAT-MOD-20111021-00207.

[68] G. D. Krebs, “Iridium-NEXT,” [Online]. Available: https://space.skyrocket.de/doc_sdat/iridium-next.htm.

[69] F. J. Dietrich, P. Metzen, and P. Monte, “The Globalstar cellular satellite system,” *IEEE Transactions on Antennas and Propagation*, vol. 46, no. 6, pp. 935–942, 1998, ISSN: 1558-2221. DOI: 10.1109/8.686783.

[70] C. D. Jilla and D. Miller, “A multiobjective, multidisciplinary design optimization methodology for the conceptual design of distributed satellite systems,” in *9th AIAA/ISSMO Symposium on Multidisciplinary Analysis and Optimization*, p. 5491.

[71] “Stara: Space infrastructure as a service,” [Online]. Available: https://www.stara.space/.

[72] “Alba Orbital sell first two Unicorns to Stealth startup Stara Space,” *Alba Orbital*, [Online]. Available: http://www.albaorbital.com/new-blog/2019/1/15/alba-orbital-sell-first-two-unicorns-to-stealth-startup-stara-space.

[73] “Unicorn 2 Features and Specifications,” *Alba Orbital*, [Online]. Available: http://www.albaorbital.com/unicorn-2-features-and-specifications.

[74] Analytical Space, “Analytical Space WL9XLY 0044-EX-ST-2017 FCC Experimental License,” [Online]. Available: https://fcc.report/ELS/Analytical-Space/0044-EX-ST-2017.

[75] Analytical Space, “Analytical Space WO9XBG 1560-EX-ST-2019 FCC Experimental License,” [Online]. Available: https://fcc.report/ELS/Analytical-Space/1560-EX-ST-2019.

[76] Audacy Corporation, “Application for Fixed Satellite Service Other by Audacy Corporation [SAT-LOA-20161115-00117],” 2016. [Online]. Available: https://fcc.report/IBFS/SAT-LOA-20161115-00117.

[77] SpaceNews.com, “Audacy defaulted on debt, shut doors in 2019,” 2020. [Online]. Available: https://spacenews.com/audacy-shuts-down/.

[78] Ames Research Center, “State of the Art of Small Spacecraft Technology,” *NASA*, 2020. [Online]. Available: http://www.nasa.gov/smallsat-institute/sst-soa.

[79] D. White, C. Shields, P. Papadeas, *et al.*, “Overview of the satellite networked open ground stations (satNOGS) project,” in *Proc. AIAA/USU Conf. Small Satellites*.

[80] “AWS Ground Station,” *Amazon Web Services, Inc.*, [Online]. Available: https://aws.amazon.com/ground-station/.

[81] R. Gedney, “Low-Cost, High-Speed Modems for Small LEO-to-Ground and LEO-to-LEO Data Links,” 2015.

[82] M. Reibe, K. Jäckel, M. F. Barschke, and C. Jonglez, “A Modular Family of High Data Rate SDR Transceivers,” 2019.

[83] GOMSpace, “NanoCom SDR Datasheet,” [Online]. Available: https://gomspace.com/UserFiles/Subsystems/datasheet/gs-ds-nanocom-sdr-10.pdf.

[84] M. Mcnicholas, J. Deluna, R. Manno, and Y. Shu, “Low cost Ka-band transmitter for CubeSat systems,” in *2017 Topical Workshop on Internet of Space (TWIOS)*, pp. 1–4, ISBN: null. DOI: 10.1109/TWIOS.2017.7869770. [Online]. Available: https://ieeexplore.ieee.org/ielx7/7869213/7869753/07869770.pdf?tp=&arnumber=7869770&isnumber=7869753&ref=.

[85] H. Wang, F. Wang, S. Li, *et al.*, “Power Amplifiers Performance Survey 2000-Present,” [Online]. Available: https://gems.ece.gatech.edu/PA_survey.html.

[86] T. Rose, D. Rowen, S. LaLumondiere, *et al.*, Optical communications downlink from a 1.5U Cubesat: OCSD program, ser. International Conference on Space Optics - ICSO 2018. SPIE, 2019, vol. 11180. [Online]. Available: https://doi.org/10.1117/12.2535938.

[87] ETSI DVB, “Digital Video Broadcasting (DVB); Implementation guidelines for the second generation system for Broadcasting, Interactive Services, News Gathering and other broadband satellite applications; Part 1: DVB-S2,” 2015. [Online]. Available: https://www.etsi.org/deliver/etsi_tr/102300_102399/10237601/01.02.01_60/tr_10237601v010201p.pdf.

[88] Digital Video Broadcasting (DVB), “Digital Video Broadcasting (DVB); Implementation guidelines for the second generation system for Broadcasting, Interactive Services, News Gathering and other broadband satellite applications; Part I (DVB-S2),” 2019. [Online]. Available: https://dvb.org/wp-content/uploads/2019/12/a171-1_s2_guide.pdf.

[89] CCSDS, “TM Synchronization and Channel Coding–Summary of Concept and Rationale.,” [Online]. Available: https://public.ccsds.org/Pubs/130x1g2.pdf.

[90] University of South Hampton, “ELEC3028 Digital Transmission – Overview and Information Theory - Lecture 4,” [Online]. Available: https://www.southampton.ac.uk/~sqc/EL334N/InfThe-L5.pdf.

[91] CCSDS, “Flexible Advanced Coding and Modulation scheme for High Rate Telemetry Applications,” 2012. [Online]. Available: https://public.ccsds.org/Pubs/131x2b1e1.pdf.

[92] CCSDS, “SCCC - Summary of Definition and Performance,” 2019.

[93] CCSDS, “CCSDS Space Link Protocols over ETSI DVB-S2 Standard,” 2013. [Online]. Available: https://public.ccsds.org/Pubs/131x3b1.pdf.

[94] CCSDS, “CCSDS Protocols over DVB-S2–Summary of Definition, Implementation, and Performance.,” 2016. [Online]. Available: https://public.ccsds.org/Pubs/130x12g1.pdf.

[95] CCSDS, “Radio Frequency and Modulation Systems–Part 1: Earth Stations and Spacecraft,” [Online]. Available: https://public.ccsds.org/Pubs/401x0b30.pdf.

[96] CCSDS, “Bandwidth-Efficient Modulations–Summary of Definition, Implementation, and Performance,” [Online]. Available: https://public.ccsds.org/Pubs/413x0g3e1.pdf.

[97] CCSDS, “TM Synchronization and Channel Coding,” [Online]. Available: https://public.ccsds.org/Pubs/131x0b3e1.pdf.

[98] "ECSS-E-ST-50-01C – Space data links – Telemetry synchronization and channel coding (31 July 2008) | European Cooperation for Space Standardization," [Online]. Available: https://ecss.nl/standard/ecss-e-st-50-01c-space-data-links-telemetry-synchronization-and-channel-coding/.

[99] "ECSS-E-ST-50-05C Rev.2 – Radio frequency and modulation (4 October 2011) | European Cooperation for Space Standardization," [Online]. Available: https://ecss.nl/standard/ecss-e-st-50-05c-rev2-radio-frequency-and-modulation-4-october-2011/.

[100] "ECSS-E-ST-50C – Communications (31 July 2008) | European Cooperation for Space Standardization," [Online]. Available: https://ecss.nl/standard/ecss-e-st-50c-communications/.

[101] "ECSS-E-HB-50A – Communications guidelines (18 November 2008) | European Cooperation for Space Standardization," [Online]. Available: https://ecss.nl/hbstms/ecss-e-hb-50a-communications-guidelines/.

[102] ETSI DVB, "ETSI EN 302 307-1 V1.4.1 (2014-11) Digital Video Broadcasting (DVB); Second generation framing structure, channel coding and modulation systems for Broadcasting, Interactive Services, News Gathering and other broadband satellite applications; Part 1: DVB-S2," 2014.

[103] ETSI DVB, "ETSI EN 302 307-2 V1.2.1 (2020-05) Digital Video Broadcasting (DVB); Second generation framing structure, channel coding and modulation systems for Broadcasting, Interactive Services, News Gathering and other broadband satellite applications; Part 2: DVB-S2 Extensions (DVB-S2X)," 2020.

[104] ETSI DVB, "Digital Video Broadcasting (DVB); Implementation guidelines for the second generation system for Broadcasting, Interactive Services, News Gathering and other broadband satellite applications; Part 2: S2 Extensions (DVB-S2X)," 2015. [Online]. Available: https://www.etsi.org/deliver/etsi_tr/102300_102399/10237602/01.01.01_60/tr_10237602v010101p.pdf.

[105] Digital Video Broadcasting (DVB), "Digital Video Broadcasting (DVB); Implementation guidelines for the second generation system for Broadcasting, Interactive Services, News Gathering and other broadband satellite applications; Part 2: S2 Extensions (DVB-S2X)," 2020. [Online]. Available: https://dvb.org/wp-content/uploads/2020/02/A171-2_DVB-S2X_Implementation-Guidelines_Draft-TR-102-376-2_v121_Apr-2020.pdf.

[106] Ames Research Center, "State of the Art Small Spacecraft Technology," 2018.

[107] "PULSAR-XTX Datasheet," [Online]. Available: https://www.aac-clyde.space/assets/000/000/105/PULSAR-DATA_original.pdf?1565702890.

[108] GOMSpace, "Flyer NanoCom XT8250," [Online]. Available: https://gomspace.com/UserFiles/Flyer_NanoCom_XT8250.pdf.

[109] H. Saito, A. Tomiki, T. Mizuno, *et al.*, "High bit-rate communication in X band for small earth observation satellites-Result of 505 Mbps demonstration and plan for 2 Gbps link," 2016.

[110] M. Kobayashi, "Iris Deep-Space Transponder for SLS EM-1 CubeSat Missions," 2017.

[111] J. A. King, K. Leveque, M. Bertino, J. Kim, and H. Aghahassan, "Ka-band for cubesats," 2015.

[112] I. SAGE Millimeter, "Ka-Band Circular Polarized Lens Corrected Antenna - Datasheet," 2019. [Online]. Available: https://sftp.eravant.com/content/datasheets/SAL-2632732410-28-C1.pdf.

[113] "Switft-KTX High-Performance Software-Defined K/Ka-Band Transmitter," [Online]. Available: www.tethers.com/wp-content/uploads/2019/09/2019-KTX.pdf.

[114] New Space Systems, "New Space Systems SDR Transciever Datasheet," 2018. [Online]. Available: http://www.newspacesystems.com/wp-content/uploads/2018/02/NewSpace-Communication_5b.pdf.

[115] F. Aguirre, B. Custodero, and B. Shah, “Ka-band tone generator for the ISARA Cubesat,” in *2015 IEEE Aerospace Conference*, pp. 1–6, ISBN: 1095-323X. DOI: 10.1109/AERO.2015.7119294.

[116] E. McCune, “A Comprehensive View of Wireless Link Energy Efficiency,” in *2019 IEEE Global Communications Conference (GLOBECOM)*, pp. 1–5, ISBN: 1930-529X. DOI: 10.1109/GLOBECOM38437.2019.9014174. [Online]. Available: https://ieeexplore.ieee.org/document/9014174/%20https://ieeexplore.ieee.org/ielx7/8968653/9013108/09014174.pdf?tp=&arnumber=9014174&isnumber=9013108&ref=.

[117] S. Gao, Y. Rahmat-Samii, R. E. Hodges, and X. Yang, “Advanced Antennas for Small Satellites,” *Proceedings of the IEEE*, vol. 106, no. 3, pp. 391–403, 2018, ISSN: 1558-2256. DOI: 10.1109/JPROC.2018.2804664. [Online]. Available: https://ieeexplore.ieee.org/ielx7/5/8303007/08303877.pdf?tp=&arnumber=8303877&isnumber=8303007&ref=.

[118] Y. Rahmat-Samii, V. Manohar, and J. M. Kovitz, “For Satellites, Think Small, Dream Big: A review of recent antenna developments for CubeSats,” *IEEE Antennas and Propagation Magazine*, vol. 59, no. 2, pp. 22–30, 2017, ISSN: 1558-4143. DOI: 10.1109/MAP.2017.2655582.

[119] J. Budinger, C. Niederhaus, R. Reinhart, J. Downey, and A. Roberts, “Ka-band technologies for small spacecraft communications via relays and direct data downlink,” 2016.

[120] R. E. Hodges, N. Chahat, D. J. Hoppe, and J. D. Vacchione, “A Deployable High-Gain Antenna Bound for Mars: Developing a new folded-panel reflectarray for the first CubeSat mission to Mars,” *IEEE Antennas and Propagation Magazine*, vol. 59, no. 2, pp. 39–49, 2017, ISSN: 1045-9243.

[121] N. Chahat, R. E. Hodges, J. Sauder, M. Thomson, and Y. Rahmat-Samii, “The Deep-Space Network Telecommunication CubeSat Antenna: Using the deployable Ka-band mesh reflector antenna,” *IEEE Antennas and Propagation Magazine*, vol. 59, no. 2, pp. 31–38, 2017, ISSN: 1045-9243. DOI: 10.1109/map.2017.2655576.

[122] R. E. Freeland, G. D. Bilyeu, G. R. Veal, M. D. Steiner, and D. E. Carson, “Large inflatable deployable antenna flight experiment results,” *Acta Astronautica*, vol. 41, no. 4, pp. 267–277, 1997, ISSN: 0094-5765. DOI: https://doi.org/10.1016/S0094-5765(98)00057-5.

[123] C. J. Vourch and T. D. Drysdale, “V-Band “Bull’s Eye” Antenna for CubeSat Applications,” *IEEE Antennas and Wireless Propagation Letters*, vol. 13, pp. 1092–1095, 2014, ISSN: 1548-5757. DOI: 10.1109/LAWP.2014.2327852.

[124] F. Qin, S. Gao, G. Wei, *et al.*, “Wideband Circularly Polarized Fabry-Perot Antenna [Antenna Applications Corner],” *IEEE Antennas and Propagation Magazine*, vol. 57, no. 5, pp. 127–135, 2015, ISSN: 1045-9243. DOI: 10.1109/map.2015.2470678.

[125] T. Fujishige, A. Ohta, M. Tamamoto, *et al.*, “Active antennas for cubesat applications,” 2002.

[126] M. Patriotis, F. N. Ayoub, C. G. Christodoulou, and S. Jayaweera, “A K/Ka Band Frequency Reconfigurable Transmit/Receive Antenna Array,” in *2019 13th European Conference on Antennas and Propagation (EuCAP)*, pp. 1–4, ISBN: null.

[127] G. Buttazzoni, F. Pelusi, and R. Vescovo, “On the Design of a Circularly Polarized Microstrip Antenna Array for CubeSat in the Ka-Band,” in *2019 13th European Conference on Antennas and Propagation (EuCAP)*, pp. 1–4, ISBN: null.

[128] G. Buttazzoni, M. Comisso, A. Cuttin, M. Fragiacomo, R. Vescovo, and R. Vincenti Gatti, “Reconfigurable phased antenna array for extending cubesat operations to Ka-band: Design and feasibility,” *Acta Astronautica*, vol. 137, pp. 114–121, 2017, ISSN: 0094-5765. DOI: https://doi.org/10.1016/j.actaastro.2017.04.012.

[129] N. J. G. Fonseca and O. Quevedo-Teruel, “The Water Drop Lens: a Low-Profile Geodesic Parallel Plate Waveguide Lens Antenna for Space Applications,” in *2019 13th European Conference on Antennas and Propagation (EuCAP)*, pp. 1–5, ISBN: null.

[130] M. Ferris and N. Phillips, “The use and advancement of an affordable adaptable antenna pointing mechanism,” in *Proc. 14th Eur. Space Mech. Tribol. Symp*, pp. 227–234.

[131] P. K. Kelly, “A Scalable Deployable High Gain Antenna-DaHGR,” 2016.

[132] A. Klesh, B. Clement, C. Colley, *et al.*, “MarCO: Early operations of the first CubeSats to Mars,” 2018.

[133] R. Hodges, B. Shah, D. Muthulingham, and T. Freeman, “ISARA–Integrated Solar Array and Reflectarray Mission Overview,” 2013.

[134] R. E. Hodges, D. J. Hoppe, M. J. Radway, and N. E. Chahat, “Novel deployable reflectarray antennas for CubeSat communications,” in *2015 IEEE MTT-S International Microwave Symposium*, pp. 1–4, ISBN: 0149-645X. DOI: 10.1109/MWSYM.2015.7167153.

[135] M. Ovchinnikov, D. Ivanov, O. Pansyrnyi, *et al.*, “Technological NanoSatellite TNS-0 2 connected via global communication system,” *Acta Astronautica*, vol. 170, pp. 1–5, 2020, ISSN: 0094-5765. DOI: https://doi.org/10.1016/j.actaastro.2020.01.027.

[136] A. Babuscia, M. Van de Loo, M. Knapp, R. Jensen-Celm, and S. Seager, “Inflatable antenna for cubesat: Motivation for development and initial trade study,” in *iCubeSat*, MIT.

[137] A. Babuscia, B. Corbin, M. Knapp, R. Jensen-Clem, M. Van de Loo, and S. Seager, “Inflatable antenna for cubesats: Motivation for development and antenna design,” *Acta Astronautica*, vol. 91, pp. 322–332, 2013, ISSN: 0094-5765.

[138] A. Babuscia, B. Corbin, R. Jensen-Clem, *et al.*, “CommCube 1 and 2: A CubeSat Series of Missions to Enhance Communication Capabilities for CubeSat,” *2013 IEEE Aerospace Conference*, 2013, ISSN: 978-1-4673-1811-2.

[139] A. Babuscia, J. Sauder, A. Chandra, J. Thangavelautham, L. Feruglio, and N. Bienert, “Inflatable antenna for CubeSat: A new spherical design for increased X-band gain,” in *2017 IEEE Aerospace Conference*, pp. 1–10, ISBN: null. DOI: 10.1109/AERO.2017.7943897.

[140] A. Babuscia, T. Choi, J. Sauder, A. Chandra, and J. Thangavelautham, “Inflatable antenna for CubeSats: Development of the X-band prototype,” in *2016 IEEE Aerospace Conference*, pp. 1–11, ISBN: null. DOI: 10.1109/AERO.2016.7500679.

[141] C. G. Cassapakis, A. W. Love, and A. L. Palisoc, “Inflatable space antennas-a brief overview,” in *1998 IEEE Aerospace Conference Proceedings (Cat. No.98TH8339)*, vol. 3, 453–459 vol.3, ISBN: 1095-323X. DOI: 10.1109/AERO.1998.685855. [Online]. Available: https://ieeexplore.ieee.org/ielx4/5608/15026/00685855.pdf?tp=&arnumber=685855&isnumber=15026&ref=.

[142] N. J. G. Fonseca, Q. Liao, and O. Quevedo-Teruel, “The Water Drop Lens: a Modulated Geodesic Lens Antenna Based on Parallel Curves,” in *2018 International Symposium on Antennas and Propagation (ISAP)*, pp. 1–2.

[143] K. K. W. Low, A. Nafe, S. Zihir, T. Kanar, and G. M. Rebeiz, “A Scalable Circularly-Polarized 256-Element Ka-Band Phased-Array SATCOM Transmitter with ±60° Beam Scanning and 34.5 dBW EIRP,” in *2019 IEEE MTT-S International Microwave Symposium (IMS)*, pp. 1064–1067, ISBN: 0149-645X. DOI: 10.1109/MWSYM.2019.8701112.

[144] Q. Luo, S. Gao, and L. Zhang, “Wideband multilayer dual circularly-polarised antenna for array application,” *Electronics Letters*, vol. 51, no. 25, pp. 2087–2089, 2015, ISSN: 0013-5194. DOI: 10.1049/el.2015.3343. [Online]. Available: https://digital-library.theiet.org/content/journals/10.1049/el.2015.3343.

[145] Q. Luo, L. Zhang, S. Gao, *et al.*, “Interleaved dual-band circularly polarized active array antenna for satellite communications,” in *2015 9th European Conference on Antennas and Propagation (EuCAP)*, pp. 1–5, ISBN: 2164-3342.

[146] N. Chahat, R. E. Hodges, J. Sauder, M. Thomson, E. Peral, and Y. Rahmat-Samii, “CubeSat Deployable Ka-Band Mesh Reflector Antenna Development for Earth Science Missions,” *IEEE Transactions on Antennas and Propagation*, vol. 64, no. 6, pp. 2083–2093, 2016, ISSN: 1558-2221. DOI: 10.1109/TAP.2016.2546306. [Online]. Available: https://ieeexplore.ieee.org/document/7440821/.

[147] N. Chahat, J. Sauder, M. Mitchell, N. Beidleman, and G. Freebury, “One-Meter Deployable Mesh Reflector for Deep-Space Network Telecommunication at X-Band and Ka-Band,” *IEEE Transactions on Antennas and Propagation*, vol. 68, no. 2, pp. 727–735, 2020, ISSN: 1558-2221. DOI: 10.1109/TAP.2019.2943394. [Online]. Available: https://ieeexplore.ieee.org/document/8852830/.

[148] D. L. Brandel, W. A. Watson, and A. Weinberg, “NASA’s Advanced Tracking and Data Relay Satellite System for the Years 2000 and Beyond,” *Proceedings of the IEEE*, vol. 78, no. 7, pp. 1141–1151, 1990. DOI: 10.1109/5.56928.

[149] F. Heine, H. K. Kampfner, R. Lange, R. Czichy, M. Lutzer, and R. Meyer, “Laser communication applied for EDRS, the European data relay system,” *Ceas Space Journal*, vol. 2, no. 1-4, pp. 85–90, 2011, ISSN: 1868-2502. DOI: 10.1007/s12567-011-0015-9.

[150] C. Dudal and C. Loisel, “Rosetta-Philae RF link, challenging communications from a comet,” *Acta Astronautica*, vol. 125, pp. 137–148, 2016, ISSN: 0094-5765. DOI: 10.1016/j.actaastro.2015.12.010.

[151] B. Kopp, J. Harris, and C. Lauand, “Utilizing Existing Commercial Geostationary Earth Orbit Fixed Satellite Services for Low Earth Orbit Satellite Communication Relays with Earth,” *New Space-the Journal of Space Entrepreneurship and Innovation*, vol. 7, no. 1, pp. 19–30, 2019, ISSN: 2168-0256. DOI: 10.1089/space.2018.0035. [Online]. Available: %3CGo%20to%20ISI%3E://WOS:000461798000004.

[152] Z. Yoon, W. Frese, and K. Briess, “Design and Implementation of a Narrow-Band Intersatellite Network with Limited Onboard Resources for IoT,” *Sensors*, vol. 19, no. 19, p. 4212, 2019. DOI: 10.3390/s19194212. [Online]. Available: https://doi.org/10.3390/s19194212.

[153] C. Rodriguez, H. Boiardt, and S. Bolooki, “CubeSat to commercial intersatellite communications: Past, present and future,” in *2016 IEEE Aerospace Conference*, pp. 1–15, ISBN: null. DOI: 10.1109/AERO.2016.7500525. [Online]. Available: https://ieeexplore.ieee.org/document/7500525/%20https://ieeexplore.ieee.org/ielx7/7494113/7500496/07500525.pdf?tp=&arnumber=7500525&isnumber=7500496&ref=.

[154] H. Voss, J. Dailey, J. Crowley, B. Bennett, and A. White, “TSAT Globalstar ELaNa-5 Extremely Low-Earth Orbit (ELEO) Satellite,” 2014.

[155] J. Dailey, H. D. Voss, A. White, and S. Brandle, “Globalstar Communication Link for CubeSats,” 2015.

[156] A. Santangelo and P. Skentzos, “Linkstar, a Globalstar Based Duplex Radio for Satellites In LEO-Architecture and Test Results,” 2016.

[157] Online Multimedia, 2020 2020. [Online]. Available: https://en.wikipedia.org/w/index.php?title=TechEdSat&oldid=957266652.

[158] R. Lundin, N. Nathrath, D. Fasold, *et al.*, Performance evaluation of a Lightweight Inter-Satellite Antenna (LISA) breadboard model, ser. 2007 2nd International Itg Conference on Antennas. 2007, pp. 134–138, ISBN: 978-3-00-021644-2. DOI: 10.1109/inica.2007.4353948.

[159] H. Hauschildt, F. Garat, H. Greus, *et al.*, “European Data Relay System–one year to go!” In *Proceedings of the International Conference on Space Optical Systems and Applications (ICSOS)*.

[160] “Argo Modem Datasheet,” [Online]. Available: https://assets.aversio.com/resources/ckfinder/userfiles/154/files/AS-DCM-180191-02-00-ARGO.pdf.

[161] “ARGO Modem | Antwerp Space,” [Online]. Available: https://www.antwerpspace.be/en/products/flight-products/argo-modem-1.

[162] “OneWeb Files for Chapter 11 Restructuring to Execute Sale Process,” [Online]. Available: https://www.oneweb.world/media-center/oneweb-files-for-chapter-11-restructuring-to-execute-sale-process.

[163] Space Exploration Holdings, “Application for Fixed Satellite Service by Space Exploration Holdings, LLC [SAT-MOD-20200417-00037],” 2020. [Online]. Available: https://fcc.report/IBFS/SAT-MOD-20200417-00037.

[164] Telesat Canada, “Application for Fixed Satellite Service by Telesat Canada [SAT-PDR-20161115-00108],” 2016. [Online]. Available: https://fcc.report/IBFS/SAT-PDR-20161115-00108.

[165] Telesat Canada, “Application for Fixed Satellite Service by Telesat Canada [SAT-PDR-20170301-00023],” 2017. [Online]. Available: https://fcc.report/IBFS/SAT-PDR-20170301-00023.

[166] Telesat Canada, “Application for Fixed Satellite Service by Telesat Canada [SAT-MPL-20200526-00053],” 2020. [Online]. Available: https://fcc.report/IBFS/SAT-MPL-20200526-00053.

[167] OneWeb, “Application for Fixed Satellite Service by WorldVu Satellites Limited [SAT-LOI-20160428-00041],” 2016. [Online]. Available: https://fcc.report/IBFS/SAT-LOI-20160428-00041.

[168] OneWeb, “Application for Fixed Satellite Service by WorldVu Satellites Limited [SAT-LOI-20170301-00031],” 2017. [Online]. Available: https://fcc.report/IBFS/SAT-LOI-20170301-00031.

[169] OneWeb, “Application for Fixed Satellite Service by WorldVu Satellites Limited [SAT-MOD-20180319-00022],” 2018. [Online]. Available: https://fcc.report/IBFS/SAT-MOD-20180319-00022.

[170] SpaceNews.com, “OneWeb scales back baseline constellation by 300 satellites - SpaceNews.com,” 2018. [Online]. Available: https://spacenews.com/oneweb-scales-back-constellation-by-300-satellites/.

[171] SpaceNews.com, “Eutelsat buys a quarter of OneWeb to get a LEO broadband growth engine,” *SpaceNews*, 2021. [Online]. Available: https://spacenews.com/eutelsat-buys-a-quarter-of-oneweb-to-get-a-leo-broadband-growth-engine/.

[172] Space Exploration Holdings, “Application for Fixed Satellite Service by Space Exploration Holdings, LLC [SAT-LOA-20161115-00118],” 2016. [Online]. Available: https://fcc.report/IBFS/SAT-LOA-20161115-00118.

[173] Space Exploration Holdings, “Application for Fixed Satellite Service by Space Exploration Holdings, LLC [SAT-LOA-20170301-00027],” 2017. [Online]. Available: https://fcc.report/IBFS/SAT-LOA-20170301-00027.

[174] Space Exploration Holdings, “Application for Fixed Satellite Service by Space Exploration Holdings, LLC [SAT-MOD-20181108-00083],” 2018. [Online]. Available: https://fcc.report/IBFS/SAT-MOD-20181108-00083.

[175] Space Exploration Holdings, “Application for Fixed Satellite Service by Space Exploration Holdings, LLC [SAT-MOD-20190830-00087],” 2019. [Online]. Available: https://fcc.report/IBFS/SAT-MOD-20190830-00087.

[176] SpaceNews.com, “SpaceX sets new Falcon 9 reuse milestone on Starlink launch,” *SpaceNews*, 2020. [Online]. Available: https://spacenews.com/spacex-sets-new-falcon-9-reuse-milestone-on-starlink-launch/.

[177] Space Exploration Holdings, “Application for Fixed Satellite Service by Space Exploration Holdings, LLC [SAT-LOA-20200526-00055],” 2020. [Online]. Available: https://fcc.report/IBFS/SAT-LOA-20200526-00055.

[178] Kuiper Systems LCC, “Application for Fixed Satellite Service by Kuiper Systems LLC [SAT-LOA-20190704-00057],” 2019. [Online]. Available: https://fcc.report/IBFS/SAT-LOA-20190704-00057.

[179] Astrome Space Technologies SARL, “Astrome: SpaceNet Constellation Design Yellow Paper,” 2019. [Online]. Available: https://astrome.io/wp-content/uploads/2019/07/Astrome-YellowPaper.pdf.

[180] Astrome Space Technologies SARL, “Astrome’s SpaceNet: Ubiquitous Internet For Real,” 2019. [Online]. Available: https://astrome.co/publications/white-paper.pdf.

[181] O3b Limited, “Attachment Sched S Tech Report SAT-AMD-20171109-00154,” [Online]. Available: https://fcc.report/IBFS/SAT-AMD-20171109-00154/1303121.

[182] “O3b mPOWER: Technology,” *SES*, [Online]. Available: https://www.ses.com/blog/o3b-mpower-technology.

[183] O3b Limited, “Application for Fixed Satellite Service Mobile Satellite Service by O3b Limited [SAT-MOD-20200526-00058],” [Online]. Available: https://fcc.report/IBFS/SAT-MOD-20200526-00058.

[184] W. Frese, Z. Yoon, H. Q. Vu, and K. Brie□, “TUBiX-10 —Design and Flight Experience of a Nanosatellite Bus for Distributed Missions,”

[185] Innovative Solutions In Space, “TXS S-band Transmitter Datasheet,” 2019. [Online]. Available: https://www.isispace.nl/wp-content/uploads/2016/02/ISIS.TXS_.DS_.001_v1.0-Datasheet.pdf.

[186] A. Price-Whelan, B. Sipőcz, H. Günther, *et al.*, “The Astropy Project: Building an inclusive, open-science project and status of the v2. 0 core package,” *arXiv preprint arXiv:1801.02634*, 2018.

[187] J. L. Cano Rodríguez, A. Hidalgo, S. Bapat, *et al.*, “poliastro/poliastro: poliastro 0.13.0 (late PyAstro ’19 edition),” 2019. DOI: 10.5281/zenodo.3360886. [Online]. Available: https://zenodo.org/record/3360886.

[188] S. K. Lam, A. Pitrou, and S. Seibert, “Numba: a LLVM-based Python JIT compiler,” *Proceedings of the Second Workshop on the LLVM Compiler Infrastructure in HPC*, Article 7, 2015. DOI: 10.1145/2833157.2833162. [Online]. Available: https://doi.org/10.1145/2833157.2833162.

[189] C. A. Balanis, Antenna theory: analysis and design. John Wiley & sons, 2016, ISBN: 1118642066.

[190] H. D. Curtis, Orbital mechanics for engineering students. Butterworth-Heinemann, 2013, ISBN: 0080977480.

[191] “Data types — NumPy v1.21.dev0 Manual,” [Online]. Available: https://numpy.org/devdocs/user/basics.types.html.

[192] E. McCune, Dynamic power supply transmitters: Envelope tracking, direct polar, and hybrid combinations. Cambridge University Press, 2015, ISBN: 131629918X.

[193] F. L. Markley, “Kepler Equation solver,” *Celestial Mechanics & Dynamical Astronomy*, vol. 63, no. 1, pp. 101–111, 1995, ISSN: 0923-2958 1572-9478. DOI: 10.1007/bf00691917. [Online]. Available: https://doi.org/10.1007/BF00691917%20https://link.springer.com/content/pdf/10.1007%2FBF00691917.pdf.

[194] H. Jos van ’t, “Minor change removing if-statement allows for the markley_coe propagator to be called using 1-N arrays. by Josvth · Pull Request #1044 · poliastro/poliastro,” *GitHub*, [Online]. Available: https://github.com/poliastro/poliastro/pull/1044.

[195] H. D. Curtis, Orbital mechanics for engineering students, Fourth Edition. Butterworth-Heinemann, 2020, ISBN: 978-0-08-102133-0.

[196] K. F. Wakker, Fundamentals of Astrodynamics, ser. AE4874. Delft: Faculty of Aerospace Engineering, 2015.

[197] P. Bourke, “Intersection of a Line and a Sphere (or circle),” 1992. [Online]. Available: http://paulbourke.net/geometry/circlesphere/.

[198] “pandas-dev/pandas: Pandas 1.0.3,” 2020. [Online]. Available: https://zenodo.org/record/3715232.

[199] The HDF Group, “Hierarchical Data Format, version 5,” 1997-2021. [Online]. Available: https://www.hdfgroup.org/HDF5/.

[200] M. Boyle, “moble/quaternionic,” 2021. [Online]. Available: https://github.com/moble/quaternionic.

[201] J. L. C. Rodríguez, “Development of Open Source tools for SatCom constellation analysis,” *OpenSatCom*, 2020. [Online]. Available: https://opensatcom.org/wp-content/uploads/sites/5/2020/12/OpenSatCom-Open-Source-tools-for-SatCom-constellation-analysis-2nd-deliverable.pdf.

[202] SpaceNews.com, “FCC approves Starlink license modification,” *SpaceNews*, 2021. [Online]. Available: https://spacenews.com/fcc-approves-starlink-license-modification/.

[203] J. Blank and K. Deb, “Pymoo: Multi-Objective Optimization in Python,” *IEEE Access*, vol. 8, pp. 89 497–89 509, 2020, ISSN: 2169-3536. DOI: 10.1109/ACCESS.2020.2990567.

[204] Computer Program, 2020. [Online]. Available: https://github.com/Josvth/hermes-optimization.

[205] “pymoo - Genetic Algorithm,” [Online]. Available: https://pymoo.org/algorithms/genetic_algorithm.html.

[206] E. McCune, Practical digital wireless signals. Cambridge University Press, 2010, ISBN: 1139484737.

[207] N. Chi, M. Zhang, J. Shi, and Y. Zhao, “Spectrally efficient multi-band visible light communication system based on Nyquist PAM-8 modulation,” *Photonics Research*, vol. 5, no. 6, pp. 588–597, 2017. DOI: 10.1364/PRJ.5.000588. [Online]. Available: http://www.osapublishing.org/prj/abstract.cfm?URI=prj-5-6-588.

[208] K. Deb, A. Pratap, S. Agarwal, and T. Meyarivan, “A fast and elitist multiobjective genetic algorithm: NSGA-II,” *IEEE Transactions on Evolutionary Computation*, vol. 6, no. 2, pp. 182–197, 2002, ISSN: 1941-0026. DOI: 10.1109/4235.996017.

[209] C. M. Fonseca, L. Paquete, and M. Lopez-Ibanez, “An Improved Dimension-Sweep Algorithm for the Hypervolume Indicator,” in *2006 IEEE International Conference on Evolutionary Computation*, pp. 1157–1163, ISBN: 1941-0026. DOI: 10.1109/CEC.2006.1688440.

[210] E. McCune, “Power amplifier efficiency ceilings due to signal modulation type,” in *2017 12th European Microwave Integrated Circuits Conference (EuMIC)*, pp. 392–395, ISBN: null. DOI: 10.23919/EuMIC.2017.8230741.

[211] S. R. Biyabani, R. Khan, M. M. Alam, A. A. Biyabani, and E. McCune, “Energy Efficiency Evaluation of Linear Transmitters for 5G NR Wireless Waveforms,” *IEEE Transactions on Green Communications and Networking*, vol. 3, no. 2, pp. 446–454, 2019, ISSN: 2473-2400. DOI: 10.1109/TGCN.2019.2902179. [Online]. Available: https://ieeexplore.ieee.org/document/8654701/.

[212] J. D. Kraus, “Antennas,” 1988.

[213] T. Chen-To and C. Pereira, “An approximate formula for calculating the directivity of an antenna,” *IEEE Transactions on Antennas and Propagation*, vol. 24, no. 2, pp. 235–236, 1976, ISSN: 1558-2221. DOI: 10.1109/TAP.1976.1141313.

[214] K. Deb and H. Jain, “An Evolutionary Many-Objective Optimization Algorithm Using Reference-Point-Based Nondominated Sorting Approach, Part I: Solving Problems With Box Constraints,” *IEEE Transactions on Evolutionary Computation*, vol. 18, no. 4, pp. 577–601, 2014, ISSN: 1941-0026. DOI: 10.1109/TEVC.2013.2281535.

[215] H. Jain and K. Deb, “An Evolutionary Many-Objective Optimization Algorithm Using Reference-Point Based Nondominated Sorting Approach, Part II: Handling Constraints and Extending to an Adaptive Approach,” *IEEE Transactions on Evolutionary Computation*, vol. 18, no. 4, pp. 602–622, 2014, ISSN: 1941-0026. DOI: 10.1109/TEVC.2013.2281534.

[216] K. Deb and J. Sundar, “Reference point based multi-objective optimization using evolutionary algorithms,” *Proceedings of the 8th annual conference on Genetic and evolutionary computation*, pp. 635–642, 2006. DOI: 10.1145/1143997.1144112. [Online]. Available: https://doi.org/10.1145/1143997.1144112.

[217] I. Das and J. E. Dennis, “Normal-Boundary Intersection: A New Method for Generating the Pareto Surface in Nonlinear Multicriteria Optimization Problems,” vol. 8, no. 3, pp. 631–657, 1998. DOI: 10.1137/s1052623496307510. [Online]. Available: https://epubs.siam.org/doi/abs/10.1137/S1052623496307510.

[218] I. d. Portillo, B. Cameron, and E. Crawley, “Ground segment architectures for large LEO constellations with feeder links in EHF-bands,” in *2018 IEEE Aerospace Conference*, pp. 1–14. DOI: 10.1109/AERO.2018.8396576. [Online]. Available: https://ieeexplore.ieee.org/document/8396576/.

[219] K. Deb, K. Sindhya, and T. Okabe, “Self-adaptive simulated binary crossover for real-parameter optimization,” pp. 1187–1194, 2007, ISSN: 9781595936974. DOI: 10.1145/1276958.1277190. [Online]. Available: https://doi.org/10.1145/1276958.1277190.

[220] H. Seada and K. Deb, “A Unified Evolutionary Optimization Procedure for Single, Multiple, and Many Objectives,” *IEEE Transactions on Evolutionary Computation*, vol. 20, no. 3, pp. 358–369, 2016, ISSN: 1089-778X, 1089-778X, 1941-0026. DOI: 10.1109/TEVC.2015.2459718. [Online]. Available: http://ieeexplore.ieee.org/document/7164289/.

[221] J. van ’t Hof, “Enhanced characterization and calibration techniques for millimeter-wave active devices,” 2020. [Online]. Available: https://repository.tudelft.nl/islandora/object/uuid%3Aa3ef2eec-265f-47fb-a854-916f96499e47.

[222] J. van ’t Hof, V. Karunanithi, and S. Speretta, “Low Latency IoT/M2M Using Nano-Satellites,” *Proceedings of IAC 2019*, 2019.

[223] C. D. Jilla, D. W. Miller, and R. J. Sedwick, “Application of multidisciplinary design optimization techniques to distributed satellite systems,” vol. 37, no. 4, pp. 481–490, 2000, ISSN: 0022-4650.

[224] C. D. Jilla, “A Multiobjective, Multidisciplinary Design Optimization Methodology for the Conceptual Design of Distributed Satellite Systems,” Thesis.